



HAL
open science

Novel interfacial electronic states between correlated insulators

Mathieu Grisolia

► **To cite this version:**

Mathieu Grisolia. Novel interfacial electronic states between correlated insulators. Materials Science [cond-mat.mtrl-sci]. Université Paris Saclay (COMUE), 2016. English. NNT : 2016SACLS239 . tel-01773207v2

HAL Id: tel-01773207

<https://theses.hal.science/tel-01773207v2>

Submitted on 14 May 2018

HAL is a multi-disciplinary open access archive for the deposit and dissemination of scientific research documents, whether they are published or not. The documents may come from teaching and research institutions in France or abroad, or from public or private research centers.

L'archive ouverte pluridisciplinaire **HAL**, est destinée au dépôt et à la diffusion de documents scientifiques de niveau recherche, publiés ou non, émanant des établissements d'enseignement et de recherche français ou étrangers, des laboratoires publics ou privés.

NNT : 2016SACLS239

THESE DE DOCTORAT
DE
L'UNIVERSITE PARIS-SACLAY
PREPAREE A
L'UNIVERSITE PARIS-SUD, AU SEIN DE
"L'UNITE MIXTE DE PHYSIQUE CNRS-THALES"

ECOLE DOCTORALE N° 564
ECOLE DOCTORALE DE PHYSIQUE EN ILE-DE-FRANCE

Spécialité de doctorat : Physique

Par

MATHIEU GRISOLIA

Nouveaux états électroniques d'interface à partir d'isolants corrélés.

Novel interfacial electronic states between correlated insulators

Thèse présentée et soutenue à Palaiseau, le 26/09/2016

Composition du Jury

Mr. Antoine Georges	Professeur à l'école Polytechnique et au collège de France	Examineur
Mr. Bernhard Keimer	Directeur, Max Planck Institute for Solid State Research	Rapporteur
Mr. Gertjan Koster	Professeur, University of Twente	Rapporteur
Mr. Manuel Bibes	Directeur de recherche, UMP-CNRS/THALES, CNRS,	Directeur de thèse
Mr. Marc Gabay	Professeur, Université Paris-Sud	Président
Mme Agnès Barthélémy	Professeur, UMP-CNRS/THALES, Université Paris-Sud	Examineur
Mr. Jacobo Santamaria	Professeur, Universidad Complutense de Madrid	Examineur
Mr. Sergio Valencia Molina	Chercheur, Helmholtz Zentrum Berlin	Examineur
Mr. Frédéric Nguyen Van Dau	Directeur, UMP-CNRS/THALES, Thales	Invité

Titre : Nouveaux  tats  lectroniques d'interface   partir d'isolants corr l s

Mots cl s : Nickelates, titanates, isolant de Mott, isolant   transfert de charge, spectroscopie, interfaces d'oxydes

R sum  :

Les oxydes de m taux de transition (Ti, Fe, Mn, Cu, etc) pr sentent une multitude de fonctionnalit s tout en cristallisant dans un nombre r duit de structures. C'est le cas par exemple dans la famille des p rovskites qui arborent de nombreux ordres  lectroniques (isolants, m taux, supraconducteurs) et magn tiques (ferro- et antiferromagn tiques). La compatibilit  structurale de ces diff rents compos s permet de les combiner au sein d'h t rostructures multifonctionnelles mais aussi, dans certains cas, de faire  merger de nouvelles propri t s aux interfaces. Un exemple typique d couvert en 2004 est celui du gaz  lectronique bidimensionnel se formant   l'interface entre deux isolants de bande, LaAlO₃ et SrTiO₃.

S'inspirant de ce r sultat majeur, ce travail de th se a pour but de g n rer de nouvelles phases  lectroniques et magn tiques aux interfaces, non   partir d'isolants de bande mais d'isolants de Mott et d'isolants   transfert de charge.   l'interface entre ces deux types de compos s, l'alignement de bande est rendu plus complexe par la pr sence de fortes corr lations  lectroniques.

Ainsi, les reconstructions d'interface peuvent donner lieu   une d stabilisation de l' tat fondamental, et   la g n ration de nouvelles phases magn tiques, conductrices ou supraconductrices absentes du diagramme de phase du mat riau massif.

Dans un premier temps, lors de ce travail nous avons synth tis , par ablation laser puls  des couches minces d'isolants de Mott, les titanates de terre-rare (RTiO₃). Nous avons caract ris  leurs propri t s magn tiques, optiques et  lectroniques.

Dans un second temps, nous avons  galement optimis  des couches minces d'isolants   transfert de charge, les nickelates de terre-rare (RNiO₃). Nous avons  tudi  en d tail l'effet du rayon ionique de la terre-rare sur la structure  lectronique   basse temp rature de ces compos s.

Le c ur de ce travail de th se a  t  l' tude des propri t s de l'interface form e par ces deux constituants via une combinaison de plusieurs techniques de spectroscopie (absorption de rayonnement synchrotron, XAS, dichroisme lin aire et circulaire, XMCD, et spectroscopie de perte d' nergie, STEM-EELS) en lien avec des calculs *ab-initio*.

Apr s avoir d montr  l'apparition d'une nouvelle phase ferromagn tique dans les nickelates, nous discutons du r le des corr lations dans les nickelates sur le transfert de charge et sur la reconstruction magn tique, observ s   l'interface avec GdTlO₃.

Enfin, nous mettons en  vidence la possibilit  d'utiliser un param tre de contr le externe comme la lumi re pour alt rer le niveau de covalence dans les nickelates sans modifier la terre-rare. Ces r sultats ouvrent la voie   de nouveaux dispositifs tirant partie du contr le actif du niveau de covalence dans les isolants   transfert de charge.

Title : Novel interfacial electronic states between correlated insulators

Keywords : Nickelates, titanates, Mott Insulator, charge transfer insulator, spectroscopy, oxide interfaces

Abstract :

Transition metal oxides (Ti, Fe, Mn, Cu, etc.) display a multitude of features while crystallizing in a reduced number of structures. This is the case for example of perovskites which exhibit many electronic (insulators, metals, superconductors) and magnetic (ferro- and antiferromagnetic) orders. Their structural compatibility offers a unique playground for combining them in the search for new interfacial properties. A typical example discovered in 2004 is LaAlO_3 and SrTiO_3 whose interface reveals a high-mobility electron gas although the parent constituents are two conventional band insulators. Following-up on this major achievement, this thesis aims at generating new electronic interfacial phases, not from band insulators but rather from Mott and charge transfer insulators. At the interface between these types of compounds, band alignment is made more complex by the presence of strong correlations between electrons. Hence, interfacial reconstructions can destabilize the ground state, and generate new phases absent from the phase diagrams of the two building blocks.

Initially, we synthesized, by pulsed laser deposition, a typical Mott insulator, rare earth titanates (RTiO_3) in the form of thin layers, which were optimized and characterized on different substrates.

Secondly, we also grew charge transfer insulators, rare earth nickelates (RNiO_3). We specifically studied the effect of the ionic radius of the rare earth on the electronic structure of these compounds at low temperature.

The core of this thesis is to study the interface formed by these two constituents via a combination of spectroscopic techniques (synchrotron radiation-based absorption, XAS, linear and circular dichroism XMCD and energy loss spectroscopy, STEM-EELS) in connection with *ab-initio* calculations.

After demonstrating the emergence of a new ferromagnetic phase in nickelates, absent of the bulk phase diagram, we discuss in particular the role of correlations in nickelates on the charge transfer and magnetic reconstruction, observed at the interface with GdTiO_3 .

Finally, we will propose a new external knob, light, to alter the level of covalence in nickelates without changing the rare earth. These results open the way for new devices taking advantage of the active control of the level of covalence in charge transfer insulators.

Remerciements

Je voudrais tout d'abord remercier mes deux rapporteurs, Pr. Keimer and Pr. Koster, d'avoir accepté de relire ce travail. Thank you so very much Pr. Keimer and Pr. Koster for your help in reviewing and judging this manuscript. Je tiens aussi à remercier tout particulièrement mes deux anciens professeurs, Pr. Antoine Georges, et Pr. Marc Gabay, pour avoir accepté de participer à ce jury. Antoine Georges, je vous remercie de m'avoir fait découvrir les joies de la physique du solide et des corrélations lorsque j'étais encore étudiant à l'école Polytechnique. C'est probablement grâce à vous que j'ai poursuivi dans ce domaine si beau et mystérieux. Merci aussi à Marc Gabay pour sa passion sans faille et pour son amour transparent de la science et de l'enseignement.

Evidemment je remercie Agnès pour son aide tout au long de mon travail et sa connaissance infinie des subtilités du magnétisme et des oxydes. Frédéric, merci pour tes conseils dans mes réflexions personnelles et professionnelles : ton soutien m'a beaucoup apporté et touché. Je retiendrai pour toujours certaines des leçons que tu m'as enseignées.

Merci mille fois à Sergio pour son aide durant les nombreuses heures passées au synchrotron Bessy. Non seulement, j'ai énormément appris de toi, mais j'ai aussi toujours passé de formidables moments en ta compagnie. Un peacho de abrazo a Sergio por su ayuda en todas mis noches (o días) de synchrotron y por todos los buenos momentos que hemos pasado juntos.

Il faut ici que je dise combien cette thèse doit au Pr. Jacobo Santamaria. Non seulement il m'a permis par ses discussions de comprendre les mécanismes en jeu dans les interfaces Ti-Ni, mais il m'a surtout permis de voir travailler, au jour le jour, un grand physicien. Je n'oublierai jamais tout ce que j'ai appris pendant ces quelques semaines à tes côtés. Professor ha sido un placer inmenso de poder trabajar junto a ti durante estos meses. Me ensañaste tantas cosas que guardaré hasta el fin. Tu y yo sabemos que en estas cosas se encuentran mucho más que física.

Manuel, je ne peux te remercier assez, ici, pour ton aide, ton soutien, ta confiance. Merci pour ce merveilleux sujet que tu m'as proposé, merci de m'avoir laissé la liberté de papillonner par moment sur des sujets un peu différents, merci d'avoir su me recadrer quand j'en avais besoin, merci d'avoir su souvent trouver les mots justes. Merci pour nos échanges et ta disponibilité toujours infaillible que ce soit pour parler de physique, de nos passions communes ou de choses plus personnelles. Je suis heureux d'avoir passé ces trois années à tes côtés.

Je remercie aussi mes différentes sources de financement et l'école doctorale, le ministère de l'enseignement et de la recherche, l'ERC, et la région pour le soutien dans ce projet de thèse.

Je tiens aussi à saluer Dr. Flavio Bruno pour tout ce qu'il m'a appris. C'est lui qui m'a montré et appris

l'exigence permanente du scientifique, la rigueur (qui m'a manqué, parfois) et la persévérance. Merci pour toutes ces choses que tu m'as transmises. Dr. Bruno, muchísimas gracias por todo lo que aprendiste de ti. Si logre algo en esta tesis, lo debo por mucho a ti. Con tu ayuda, vi lo que ciencia pide de rigor, perseverancia, y exigencia. También muchas gracias por todo los buenos momentos que hemos pasado juntos.

J'ai eu la chance d'être accueilli à deux reprises par deux formidables chercheurs : Pr. Laurent Bellaïche de l'Université d'Arkansas, et Dr. Jorge Íñiguez, à l'université Autonoma de Barcelona. Grâce à vous, j'ai découvert le miracle des symétries qui a profondément influencé ma vision de la physique et des matériaux. Vous m'avez fait découvrir le monde merveilleux des calculs et de l'*ab-initio*, je n'oublierai pas votre aide, votre accueil et votre soutien dans mon apprentissage (souvent lent) de la théorie des invariants. Jorge, ya sabes que fue mas que unos invariantes ! Muchas gracias por todo !

J'ai bien conscience que ce travail est le fruit de l'aide formidable que j'ai reçue : Merci à Julien Rault, Julien Varignon, Jean-Pascal Rueff, Richard Mattana, Fadi Chouekani, Enrico Schierle, Eugen Weschke, Gabriel Sanchez, Maria Varela, Gervasi Herranz, Blai Casals, Tobias Froehlich, Markus Braden, Alexandra Mougin, Jens Kreisel, Ingrid Carnero Infante, Brahim Dkhil, Hong-Ziang Zhao, Cecile Carrétéro, Renato Bisaro, Eric Jacquet, Radu Abrudan, Anke Sander, Edouard Lesnes, Nicolas Reyren, Flavio Bruno, Dan Sando, Karim Bouzehouane.

Merci à Laurence pour les premières années passées ensemble dans notre bureau. Merci aussi à mes nouveaux collègues : Daniele, Diogo, Julien, Hiro-san.

Enfin, tous ceux qui ont eu la chance de mettre un pied dans les couloirs de l'UMR vous diront qu'il s'agit d'un petit havre de paix, peuplés de gens, plus merveilleux les uns que les autres, où règne une convivialité, une entre-aide et une joie de vivre rare. Evidemment, cette atmosphère si particulière n'est que le résultat des gens qui l'ont construite depuis le premier jour, merci à tous les permanents (avec une mention spéciale à leurs deux capitaines les Fréds², à Christine et Anne).

Moi, qui ai toujours aimé vagabonder de sujets en sujets, je remercie tout particulièrement le groupe spintronique, notamment Vincent, Paolo et Albert, Alex, Romain, de m'avoir laissé si gentiment travailler avec eux sur des projets passionnants. Merci aussi à Daniel Dolfi pour son soutien sans faille et pour les discussions enflammées et passionnantes sur la suite de ma carrière, le foot, le rugby (et bien-sûr la physique). Merci aussi à toutes les personnes que j'ai eu la chance de rencontrer au sein de THALES RT ou ailleurs, et avec qui mes discussions ont toujours été passionnantes et enrichissantes.

Merci enfin, à tous les docteurs, et stagiaires du labo pour votre humour, votre aide dans les manip (Soeren, Edouard, merci pour tout), votre gentillesse. Un immense merci au groupe oxyde dans son ensemble. Une pensée particulière à Vince pour tout ce qu'il m'a apporté de sagesse, de clarté, et de

rires !

Je profite de ces quelques lignes pour remercier très chaleureusement les gens qui m'ont fait découvrir les joies de la recherche : Dr. Davide Boschetto, Pr. Tony Heinz, Dr. Yanina Fasano, et bien entendu Kees Van der Beek, qui a suivi et soutenu mes premiers pas de jeune chercheur.

J'ai la chance d'être entouré d'amis tous plus merveilleux les uns que les autres qui m'ont toujours soutenu dans mes moments de colère, de folie, de fatigue, et de joie. Merci à tous d'être là, pour tout partager avec moi : Loïc, Cyprien, Arnaud, Paula, Julien, PA, Jojo, Marion, Boiss', Max, Guillaume, Luc, Lucas, Julia, La corze, Pierre, et tous les autres...

Enfin, si j'ai des amis extraordinaires, je suis comblé par une famille merveilleuse, qui, durant ces dernières années, s'est encore agrandie. Merci à mes belles-familles, merci infiniment à mes chers parents, à mes frères et sœurs, à mes grands-parents, à mes oncles et tantes.

Merci enfin à toi, Claire, parce que tu es là, parce que tu remplis mon existence d'un bonheur sans limite. Je te dédie cette thèse, tendrement...

*“Impose ta chance,
Serre ton bonheur et va vers ton risque.
À te regarder, ils s’habitueront.”*

René Char

Résumé du manuscrit de thèse en français :

Les oxydes de métaux de transition (Ti, Fe, Mn, Co, *etc*) présentent une multitude de fonctionnalités tout en cristallisant dans un nombre réduit de structures. C'est le cas par exemple dans la famille des pérovskites qui arbore de nombreux ordres électroniques (isolants, métaux, supraconducteurs) et magnétiques (ferromagnétiques et antiferromagnétiques). La structure pérovskite, ABO_3 , est composée d'un atome, A, placé au centre d'une maille cubique, au sommet de laquelle siègent des atomes, B, eux-mêmes entourés d'octaèdres d'oxygènes. La compatibilité structurale de ces différents composés permet de les combiner au sein d'hétérostructures multifonctionnelles mais aussi, dans certains cas, de faire émerger de nouvelles propriétés aux interfaces. Un exemple typique découvert en 2004 est celui du gaz électronique bidimensionnel se formant à l'interface entre deux isolants de bande, $LaAlO_3$ et $SrTiO_3$.

S'inspirant de ce résultat majeur, ce travail de thèse a pour but de générer de nouvelles phases électroniques et magnétiques aux interfaces, non à partir d'isolants de bande mais d'isolants de Mott et d'isolants à transfert de charge.

Ces systèmes, bien que classiquement supposés métalliques par leur structure de bande, sont en réalité d'excellents isolants du fait des fortes corrélations électroniques provenant des électrons de valence des métaux de transition. Mott et Hubbard ont proposé les premiers un modèle qui permet de donner une description élégante du caractère isolant d'un système corrélé d'électrons de couches, d , demi-remplies, en s'appuyant notamment sur la compétition entre un terme de répulsion coulombienne, U – équivalent à une excitation entre deux orbitales d'une couche d du métal de transition – et le terme classique de saut, t . Un système pour lequel le terme de répulsion coulombienne, U , domine sur le terme de saut est ainsi qualifié d'isolant de Mott. Anderson et d'autres ont ensuite élargi ce modèle au cas des électrons, p , de l'oxygène, proposant un nouveau paramètre : l'énergie nécessaire pour promouvoir un électron d'une couche, p , de l'oxygène vers une couche, d , d'un métal de transition. Cette énergie est appelée énergie de transfert de charge, Δ . Dans le

cas où le terme de plus basse énergie correspond à une telle transition, on qualifie le système d'isolant à transfert de charge.

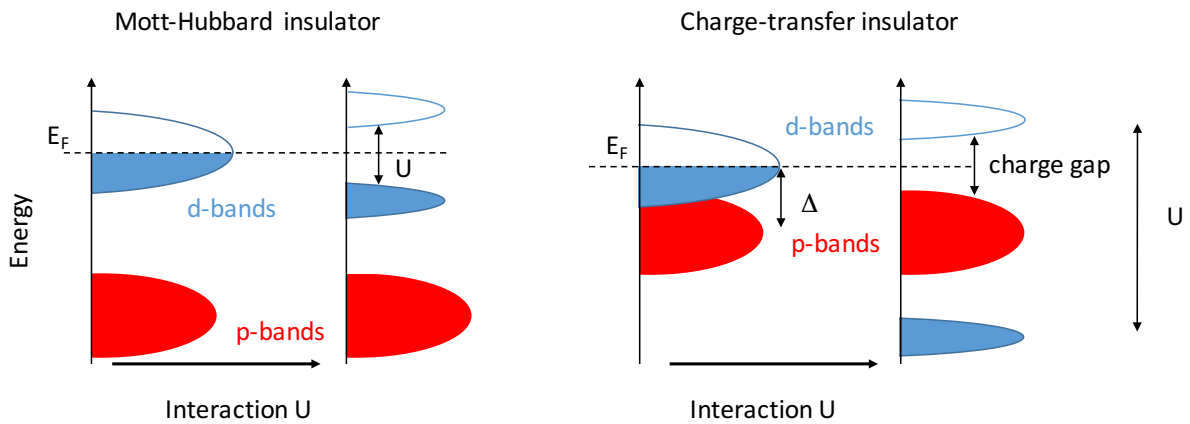


Figure 1 : Structure de bande d'un isolant de Mott (gauche) et d'un isolant à transfert de charge (droite) dans une configuration de demi-remplissage avant et après interaction électronique U .

Aux interfaces entre oxydes corrélés, la question de savoir comment passer continûment d'un système dont la description dépend essentiellement d'une excitation de type $d-d$ à un système dont l'excitation de plus basse énergie est une excitation de type $p-d$, demeure une question ouverte. Non seulement, l'alignement de bande est complexifié par la présence de fortes corrélations électroniques. Mais, les reconstructions d'interface peuvent aussi donner lieu à une déstabilisation de l'état fondamental, et ainsi, du fait du fort couplage entre les différents degrés de liberté (spin, orbitales, charge, ...), à la génération de nouvelles phases magnétiques, conductrices ou supraconductrices absentes du diagramme de phase des matériaux massifs, pris séparément. Afin de parvenir à la synthèse d'une telle interface, nous avons commencé par étudier indépendamment chacun des deux types de systèmes corrélés, décrits précédemment.

Dans un premier temps, nous avons synthétisé, pour la première fois par ablation laser pulsé, des couches minces d'un isolant de Mott, les titanates de terre-rare (RTiO_3). Ces isolants font partie des rares structures pérovskites à présenter un ordre ferromagnétique tout en conservant un caractère isolant. Toutefois, cet ordre magnétique est très sensible au rayon ionique de la terre-rare et passe ainsi d'un ordre ferromagnétique pour $R < \text{Gd}$ à un

ordre antiferromagnétique pour $R > \text{Sm}$.

Nous avons caractérisé les propriétés magnétiques (ferromagnétiques pour des températures inférieures à 30 K), optiques et électroniques (isolants à faible gap) du composé GdTiO_3 . Nous avons pu démontrer qu'elles étaient en bon accord avec celles du matériau dans l'état massif, que nous avons aussi préalablement caractérisé.

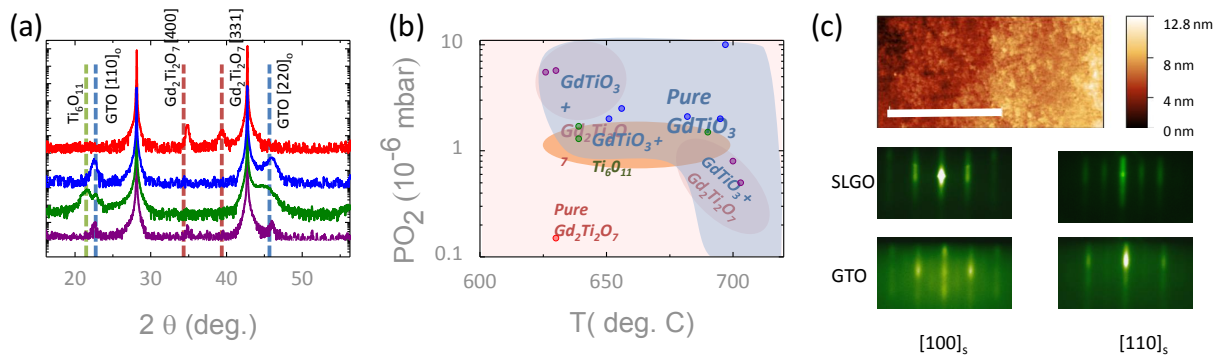


Figure 2 : (a) diagrammes XRD de différentes phases identifiées durant le processus d'optimisation. Les conditions de croissance de haut en bas sont : $\text{PO}_2=0.15 \cdot 10^{-6}$ mbar $T=630$ °C, $\text{PO}_2=2 \cdot 10^{-6}$ mbar $T=660$ °C, $\text{PO}_2=2 \cdot 10^{-6}$ mbar $T=640$ °C, $\text{PO}_2=5.5 \cdot 10^{-6}$ mbar $T=630$ °C. (b) Diagramme de phase décrivant le processus d'optimisation à une fluence de 1.1 J/cm^2 . (c) Microscopie à force atomique d'un film mince de 15 nm et image RHEED d'un substrat de SLGO avant et après dépôt d'un film mince de GTO à 0° et à 45° par rapport à la direction $[100]$ de GdTiO_3 .

Nous avons étudié en détail l'orientation de la couche en combinant des mesures par diffraction de rayons X dans différentes configurations. En effet, les titanates sont des structures très distordues qui peuvent ainsi présenter différentes orientations de croissance lorsqu'elles sont déposées sur un substrat cubique. Les deux orientations sont présentées ci-dessous :

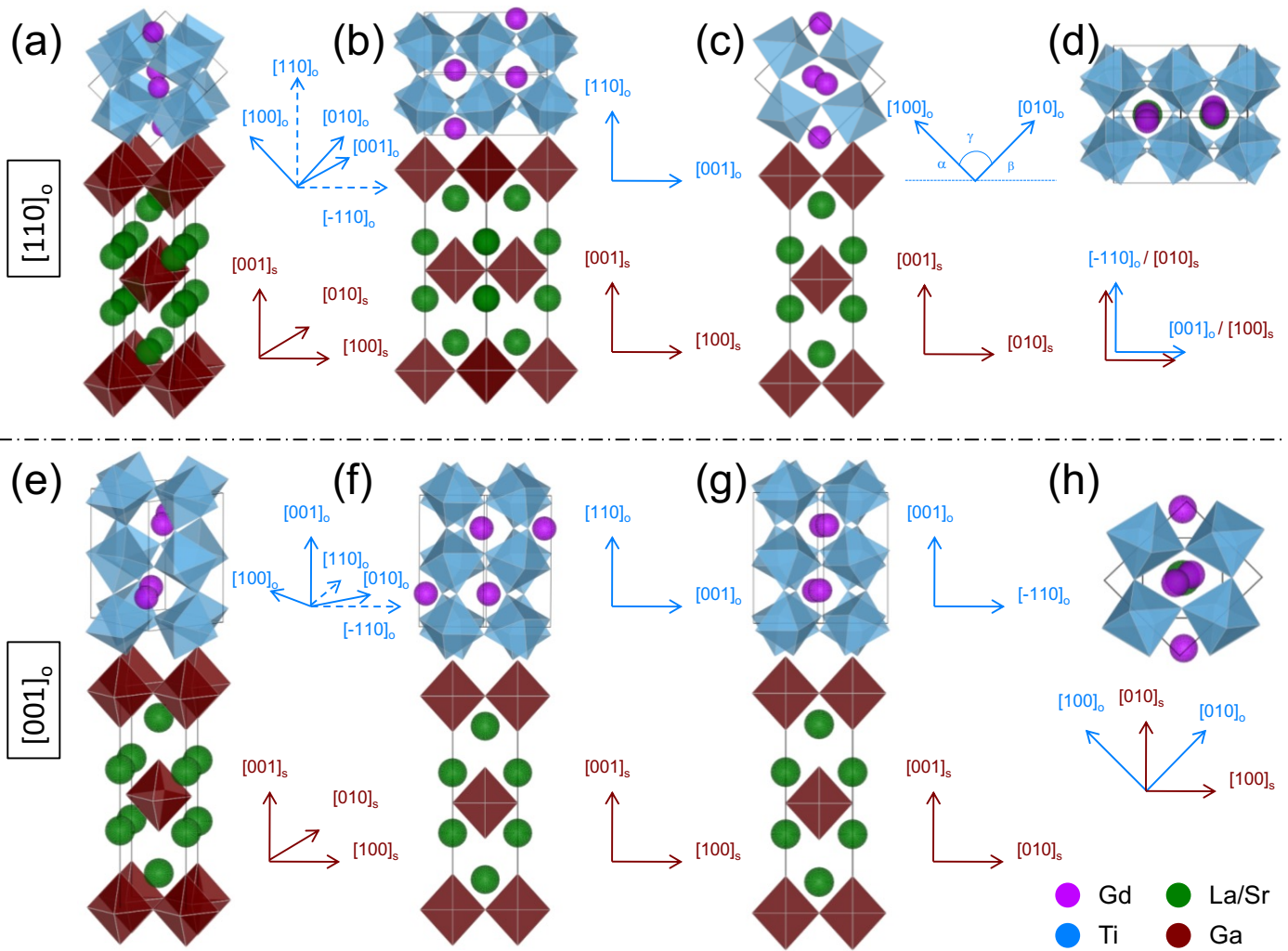


Figure 3 : Représentation des deux orientations possibles de GTO sur SLGO soit *ab*-Pbnm (panneau du haut) soit *c*-Pbnm (panneau du bas) vues selon plusieurs projections.

Grâce à la combinaison des mesures de rayons X selon différentes orientations de la couche, nous avons pu montrer que sur SLGO la couche avait tendance à s'orienter selon la direction $\langle 110 \rangle$. Toutefois, cette orientation ne peut s'apparenter directement à celle de la structure *ab*-Pbnm puisque sous l'effet de la contrainte, la symétrie est réduite, d'une symétrie orthorhombique, à une symétrie monoclinique.

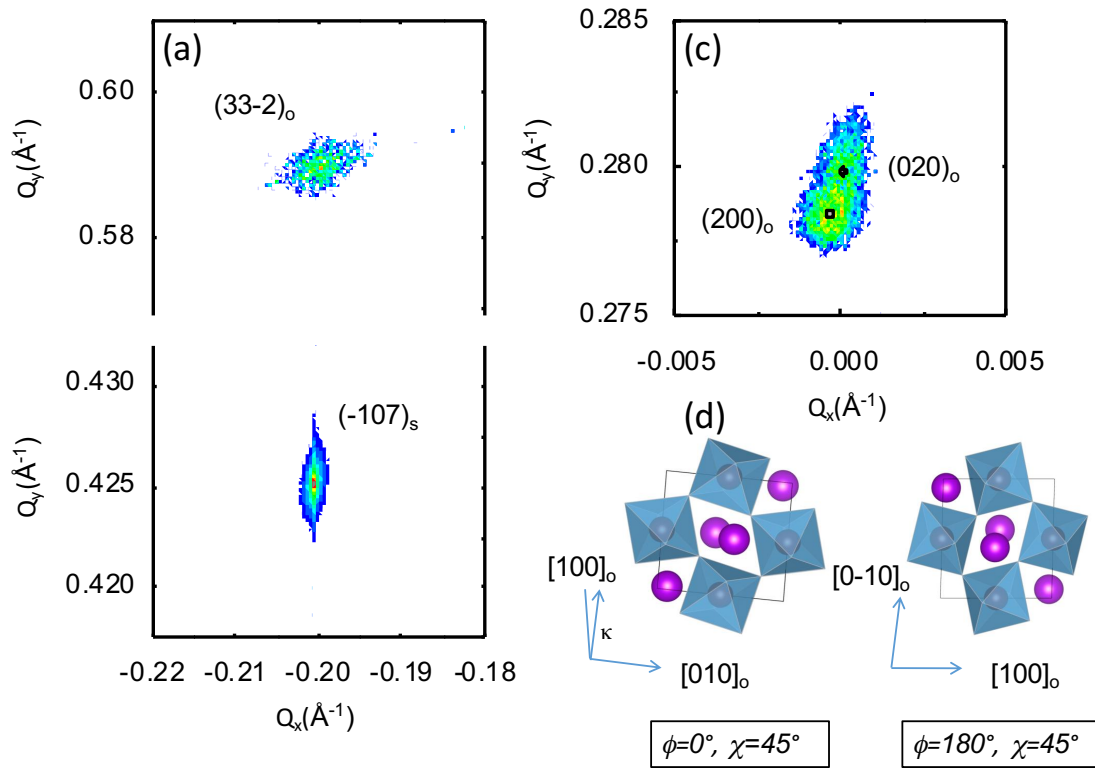


Figure 4 : (a) Carte de réseau réciproque près des pics $[-107]_s$ du SLGO et des pics $[33-2]_o$ du GTO en couche mince (b) Carte de réseau réciproque autour du pic $\langle 200 \rangle_o$ à $\chi=45^\circ$. (c) représentations schématiques des deux orientations possibles vues à 45° .

Afin de tirer profit de l'instabilité magnétique de RTiO_3 , nous avons étudié l'effet des contraintes épitaxiales, en déposant les couches minces sur différents substrats (SrLaAlO_4 , SrLaGaO_4 , LaAlO_3 , SrTiO_3 , PrScO_3 , DyScO_3 , ...). Même si les propriétés magnétiques restent encore à déterminer, nous avons pu observer que les contraintes épitaxiales entraînent un changement de l'orientation de croissance avec une rotation du grand axe de la maille orthorhombique : il est dirigé hors du plan pour les contraintes compressives ($ab\text{-Pbnm}$), mais parallèle au plan du substrat pour de fortes valeurs de contraintes en tension ($c\text{-Pbnm}$).

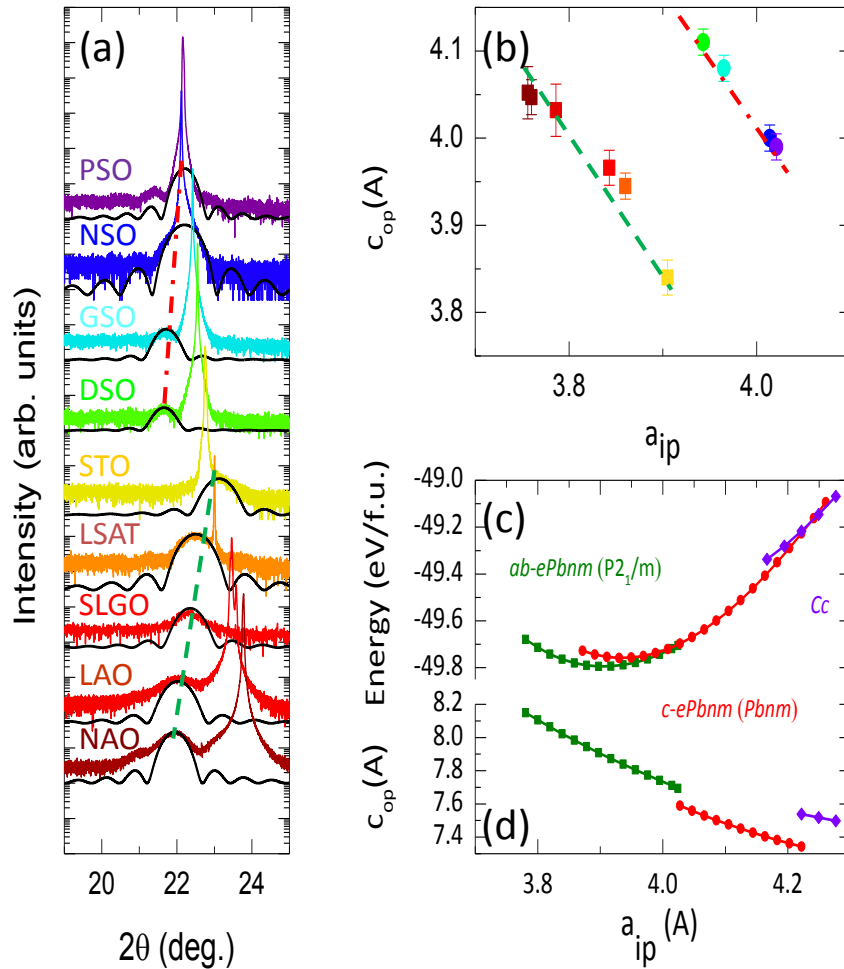


Figure 5 : (a) Diffraction de rayons X pour le pic $[001]_{pc}$ de GTO sur différents substrats. La ligne noire est un fit des oscillations d'épaisseur finie de Laue. (b) Le paramètre hors-plan extrait en fonction du paramètre dans le plan du substrat. (c) Calcul DFT de l'énergie des différents états fondamentaux en fonction du paramètre dans le plan du substrat. (d) Paramètre hors-plan calculé en fonction du paramètre dans le plan du substrat.

Nous avons pu corréliser ce changement d'orientation avec une modification de la rugosité des couches observées par microscopie de champs proche. La rugosité est mesurée comme étant plus faible lorsque le grand axe est parallèle au plan du substrat. Nous expliquons ce phénomène par une monoclinicité plus importante des couches en compression entraînant une tendance plus forte à former des défauts du type parois de macles, ou défauts d'empilement, que nous avons identifiés par microscopie électronique en transmission.

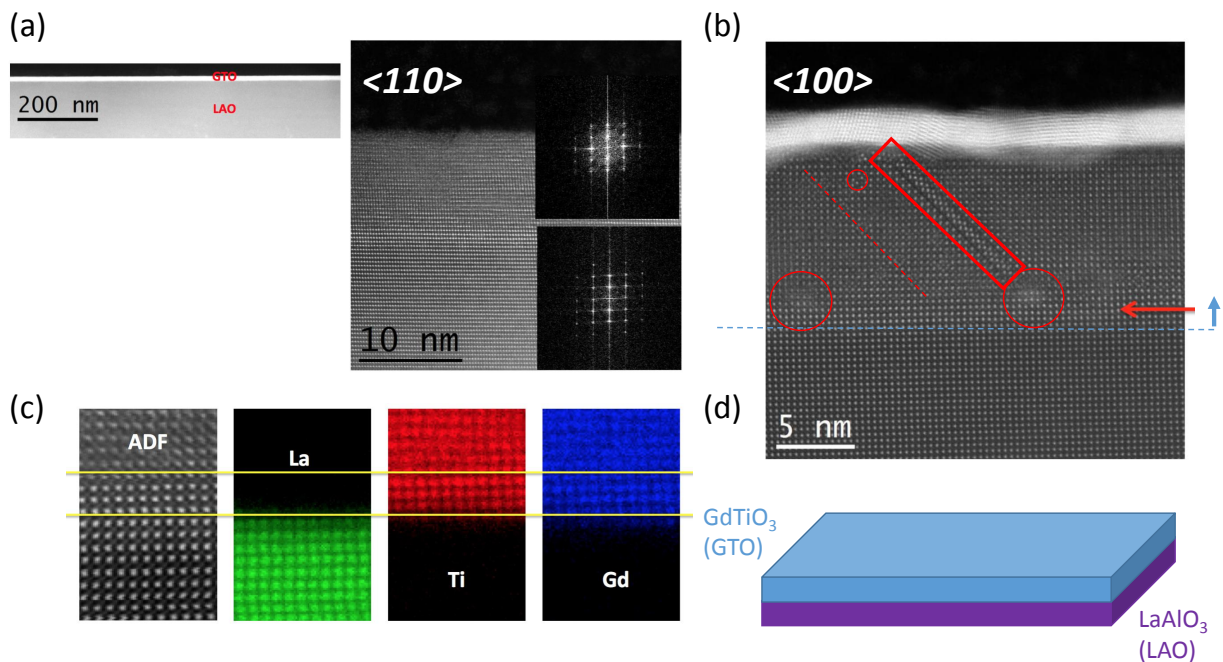


Figure 6 : Différentes vues en TEM d'un échantillon de GTO déposé sur LAO ainsi que sa caractérisation chimique en EELS. Les défauts mentionnés précédemment sont mis en valeur par l'encadrement en rouge dans l'image (b).

Dans un second temps, nous avons également optimisé des couches minces d'isolants à transfert de charge, les nickelates de terre-rare (RNiO_3). Nous avons étudié en détail l'effet du rayon ionique de la terre-rare sur la structure électronique à basse température de ces composés. En effet, ces composés sont connus pour présenter une transition métal-isolant dont la température de transition dépend de la terre-rare. A cette transition s'ajoute, une transition magnétique (vers un ordre antiferromagnétique) à plus basse température.

Nous avons donc déposé sur un même substrat, en l'occurrence LaAlO_3 , différents nickelates de terre-rare (LaNiO_3 , NdNiO_3 , SmNiO_3). Nous avons montré que la température de transition métal-isolant varie effectivement avec la terre-rare. Nous avons mis ces résultats en regard d'une description théorique applicable à l'ensemble des nickelates de terre-rare et en excellent accord avec nos mesures expérimentales. Cette étude théorique a permis de montrer que la structure électronique des nickelates (y compris à hautes températures) ne peut être décrite en considérant les électrons de valence issus des

électrons du métal de transition et ceux de l'oxygène comme étant indépendants les uns des autres. En effet, les niveaux électroniques p et d sont si proches en énergie que les orbitales sont fortement hybridées, présentant ainsi un fort niveau de covalence. A basses températures, l'état isolant résulte d'un transfert de charge interne où : (i) un site de nickel sur deux voit son électron non apparié de valence transféré vers le site de nickel voisin (ii) et ces niveaux, ainsi, laissés libres, permettent l'apparition d'un singlet formé par les électrons de valence de l'oxygène présents dans la liaison covalente. Les calculs théoriques, menés conjointement à cette thèse, indiquent que le degré de covalence est étroitement lié aux distorsions de la nickelate (notamment les rotations des cages d'oxygènes entourant l'atome de nickel), elles-mêmes directement liées au rayon ionique de la terre-rare. Ainsi, le degré de covalence augmente fortement à mesure que le rayon ionique de la terre-rare augmente (de Lu à La).

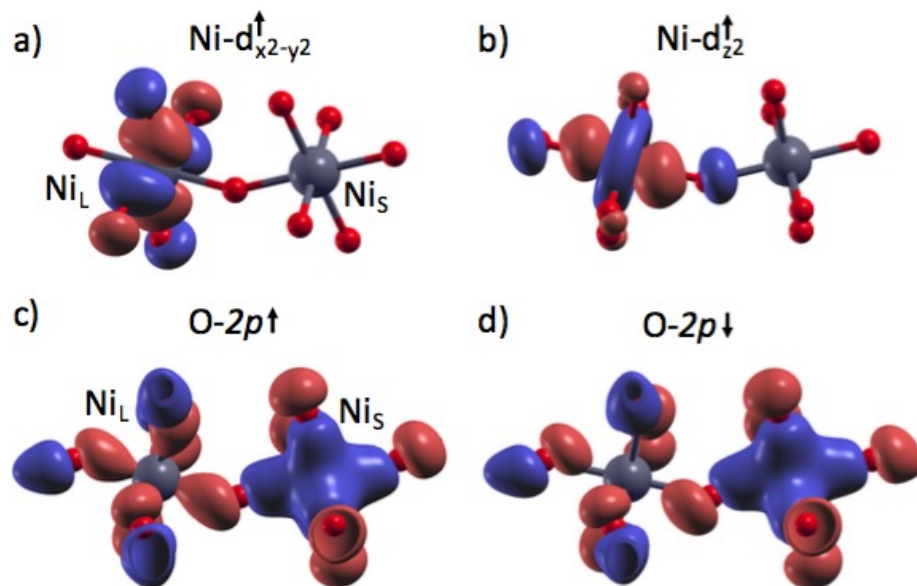


Figure 7 : Occupation orbitale dans les nickelates (a) fonctions de Wannier $d_{x^2-y^2}^{\uparrow}$ sur deux sites consécutifs de Nickel. Le site Ni_L porte un spin \uparrow (b) fonctions de Wannier $d_{z^2}^{\uparrow}$ sur deux sites consécutifs de Nickel. Le site Ni_L porte un spin \uparrow . Fonctions de Wannier O 2p orientée selon la liaison Ni-O sur deux sites consécutifs de Ni dans le canal de spin \uparrow (c) et pour le canal de spin \downarrow . (d)

En utilisant des techniques d'absorption de rayons X en synchrotron, sous différentes polarisations (verticale, horizontale, circulaire), nous avons pu apporter un certain nombre de faits expérimentaux, en accord avec cette description. Notamment, un résultat majeur de

notre étude expérimentale est de promouvoir l'idée que les électrons de l'oxygène se lient préférentiellement à un site sur deux de nickel avec des spins opposés résultant en un moment magnétique de $S=0$, comme prédit par la description théorique et de nombreux autres modèles. Par ailleurs, cette étude met en évidence de nombreux autres paramètres expérimentaux permettant de mesurer l'apparition de l'état singlet formé par les électrons de l'oxygène sur les sites de nickel.

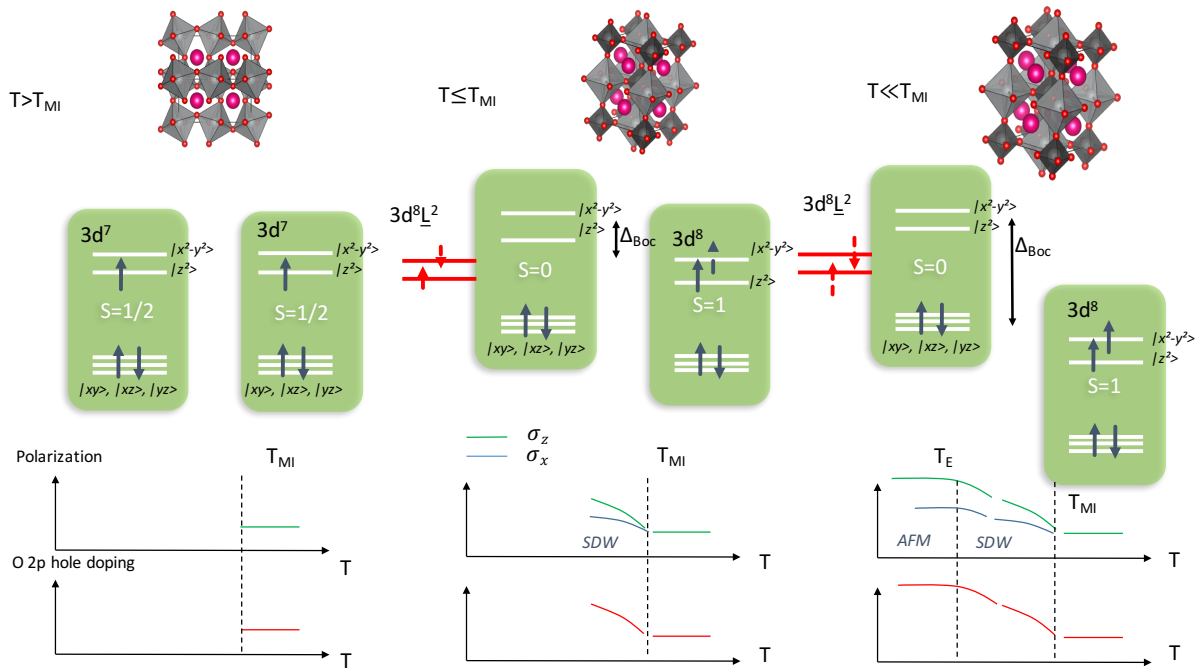


Figure 8 : Représentation simplifiée de l'évolution de l'état fondamental des nickelates. Les figures en haut représentent la structure cristallographique et électronique des nickelates à des températures intermédiaires. La ligne du bas représente schématiquement l'évolution des grandeurs expérimentales obtenues à partir de mesures en absorption de rayons X sous lumière synchrotron

Finalement, le cœur de ce travail de thèse a été l'étude des propriétés de l'interface formée par ces deux constituants via une combinaison de plusieurs techniques de spectroscopie (absorption de rayonnement synchrotron, XAS, dichroïsme linéaire et circulaire, XMCD, et spectroscopie de perte d'énergie, STEM-EELS) en lien avec des calculs *ab-initio*.

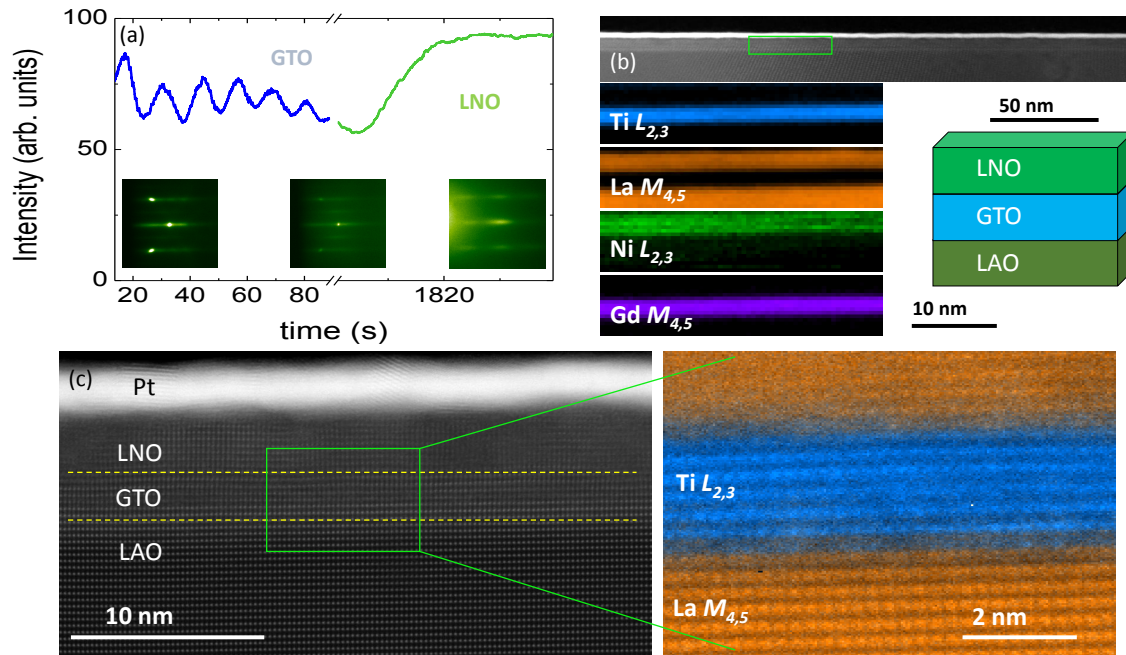


Figure 9 : (a) Variation du signal RHEED pendant la croissance avec des extraits d'images RHEED sur LAO (gauche), GTO (milieu), et LNO (droite). (b) Image TEM basse résolution d'une heterostructure de LNO/GTO (en haute), et cartes EELS d'une zone encadrée par un rectangle vert. De haut en bas, les cartes correspondant aux seuils $Ti L_{2,3}$, $La M_{4,5}$, $Ni L_{2,3}$ and $Gd M_{4,5}$ are (c) Image TEM avec résolution atomique. Cartes EELS dans au seuil du $Ti L_{2,3}$ en bleu et au seuil du $La M_{4,5}$, en orange dans la zone délimitée par le rectangle vert

Le premier résultat marquant de ces caractérisations est l'apparition d'une nouvelle phase ferromagnétique dans les nickelates, absente du diagramme de phase des nickelates pris séparément. Cette phase ferromagnétique est accompagnée d'un autre système de spin polarisé, indépendant du champs magnétique, mais qui présente pourtant un fort signal dichroïque.

On notera sur la figure ci-dessous que le cycle ferromagnétique est déplacé vers le haut et vers la gauche, ce qui rappelle le mécanisme "d'échange-bias". Puisque certains spins semblent boqués dans une direction donnée de champs, on peut légitimement supposer que ce sont ces spins qui sont responsables du décalage du cycle ferromagnétique observé.

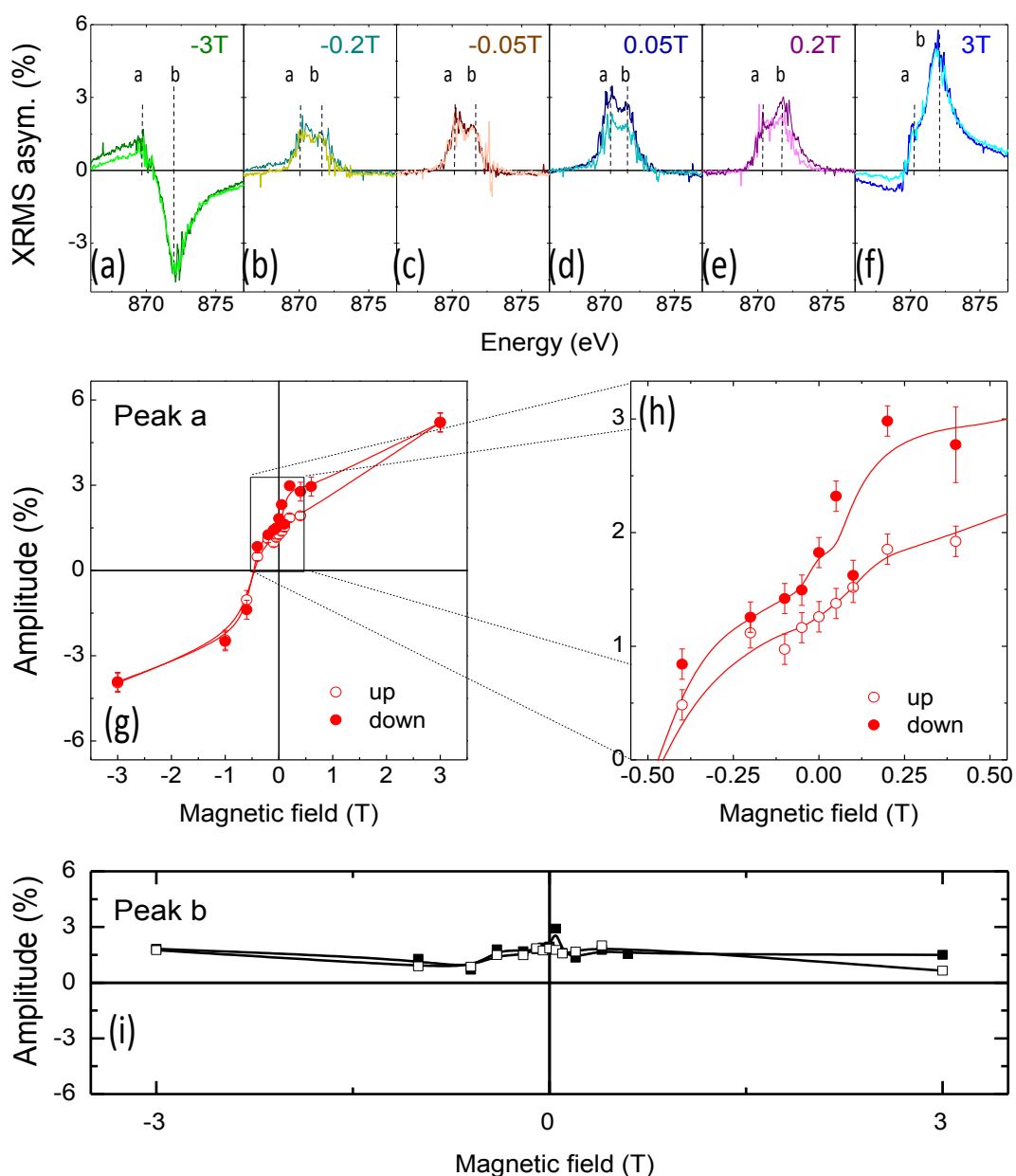


Figure 10 : (a-f) Spectres XRMS mesurés à différents champs de 3T à -3T (traits couleurs sombres) et de -3T à 3T (couleurs claires). L'amplitude du pic "a" (g) et "b" (i) extrait des spectres XRMS en fonction du champs magnétique (h) Zoom sur la région à bas champs du graphe (g).

Cette phase ferromagnétique est accompagnée d'un fort transfert de charge du titanate vers la nickelate que nous pouvons mesurer en caractérisant la valence de chaque élément par des techniques de spectroscopie. Considérant la différence entre les affinités électroniques (~ 1.6 eV) de ces deux systèmes, un tel transfert de charge (~ 1 e⁻/u.c) n'est pas surprenant. Toutefois, lorsque la terre-rare de la nickelate est modifiée de La à Nd puis à

Sm, le transfert de charge est très largement affecté et va en diminuant à mesure qu'on augmente le rayon ionique de la terre-rare (de Sm à Nd à La), et donc le degré de covalence de la liaison Ni-O. Il est important de rappeler ici que si la terre-rare modifie le niveau de covalence, elle n'altère en rien (au premier ordre) les affinités électroniques et ne devrait donc pas modifier le transfert de charge, attendu dans une vision de bandes conventionnelles.

Nous avons aussi observé que le niveau de covalence, accessible par des mesures simultanées au seuil de l'oxygène et du nickel, reste inchangé quel que soit l'état dans lequel se trouve les nickelates, aussi bien sous forme de matériaux massifs, que de couches minces, ou sous formes de bicouches après transfert de charge. Ceci renforce l'idée que le niveau d'hybridation (et donc l'énergie requise pour exciter un électron p vers un électron d) est indépendant de l'état électronique global dans lequel se trouve la nickelate et qu'il est une propriété intrinsèque de la liaison Ni-O.

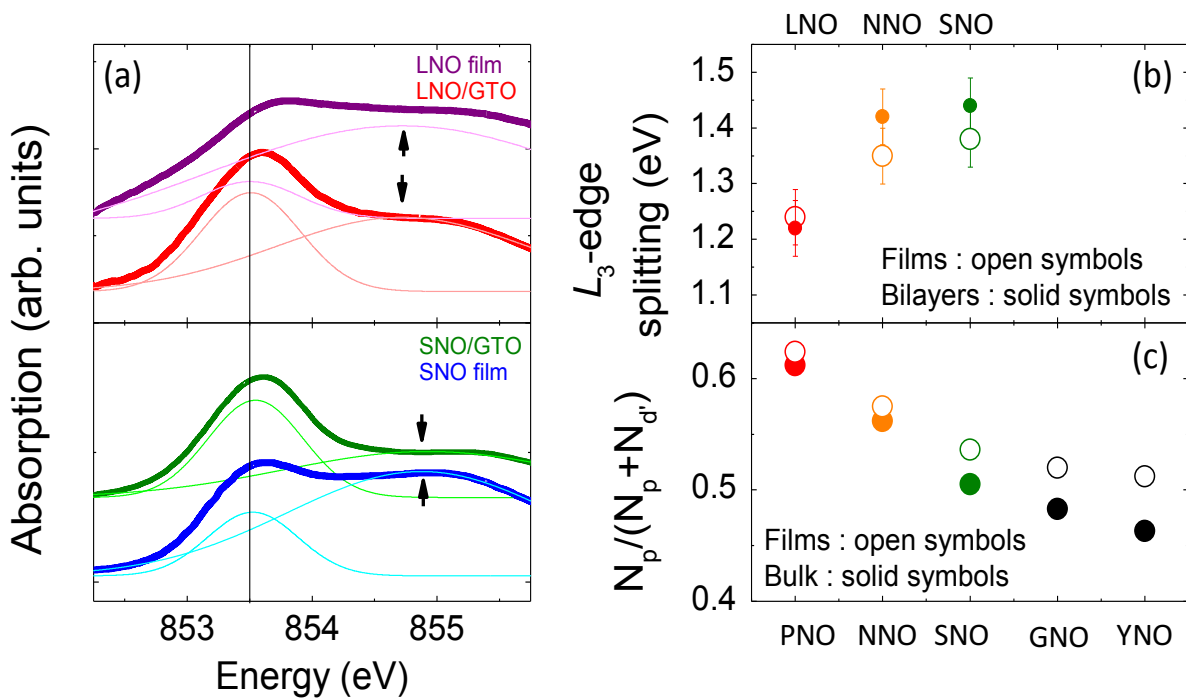


Figure 11 : spectres au seuil du Ni L₃ pour un film de LNO et une bicouche de LNO/GTO (a) et de SNO et de SNO/GTO (b). Tous les spectres sont reproduits par deux pics (lignes fines) et décalés en énergie pour aligner la première composante à 853.5 eV. La flèche indique la position du second pic. (c) La différence d'énergie entre les deux composantes pour (a), (b), et pour un film de NNO, et une bicouche de NNO/GTO. (d) Covalence extraite des calculs DFT pour des nickelates sous contraintes et sous forme massive.

Sur la base de ces deux observations, nous avons proposé que la variation du transfert de charge avec la terre-rare s'explique de la façon suivante: (i) l'électron sur le site de la titanate est transféré vers la nickelate pour équilibrer les affinités électroniques ; (ii) toutefois, une fois sur le site de Ni, le niveau d'hybridation est localement modifié ; (iii) pour maintenir constant le niveau d'hybridation localement, la liaison redistribue les charges entre les Ni et les O dans son environnement proche de telle sorte que le niveau d'hybridation reste constant. Ce mécanisme s'effectue en proportion du niveau de covalence. De sorte que les affinités électroniques dans les nickelates interfacées ne sont que des affinités « effectives » car fonction du niveau de covalence de la liaison et donc de la terre-rare. Ainsi, la différence d'affinités électroniques augmente à mesure que le niveau de covalence devient faible, se traduisant par un plus grand transfert de charge pour les terres-rares de faibles rayons ioniques comme le Nd ou le Sm. Ce scénario a été renforcé par les calculs théoriques qui prédisent une évolution du transfert de charge en accord parfait avec celui observé expérimentalement.

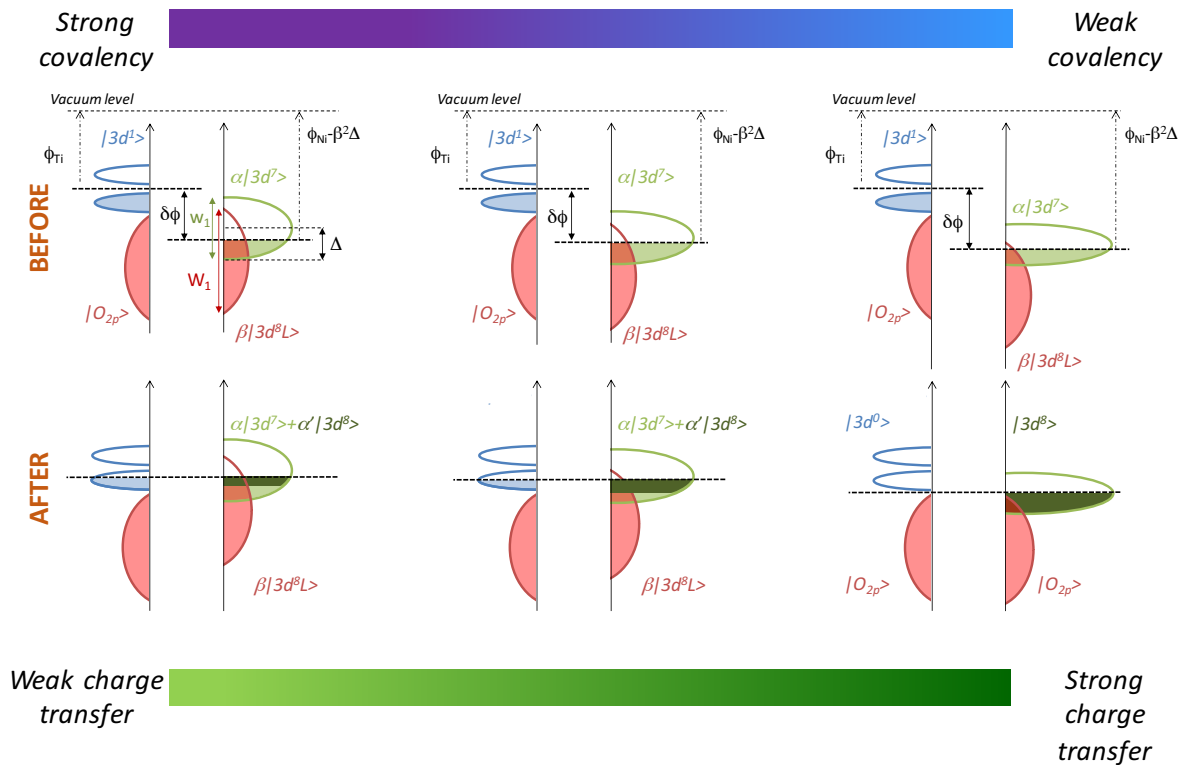


Figure 12 : Représentation schématique du transfert de charge inter facial et du processus de ré-hybridization dans les bandes covalentes. (En haut) avant le transfert de charge (en bas) après le transfert de charge.

Dans l'optique d'utiliser ces observations dans le cadre de dispositifs actifs, nous souhaitons pouvoir altérer la covalence des nickelates sans avoir à changer la terre-rare. Ainsi, les derniers développements de ces travaux de thèse ont consisté à démontrer la possibilité d'utiliser un paramètre de contrôle externe comme la lumière pour altérer le niveau de covalence dans les nickelates sans modifier la terre-rare.

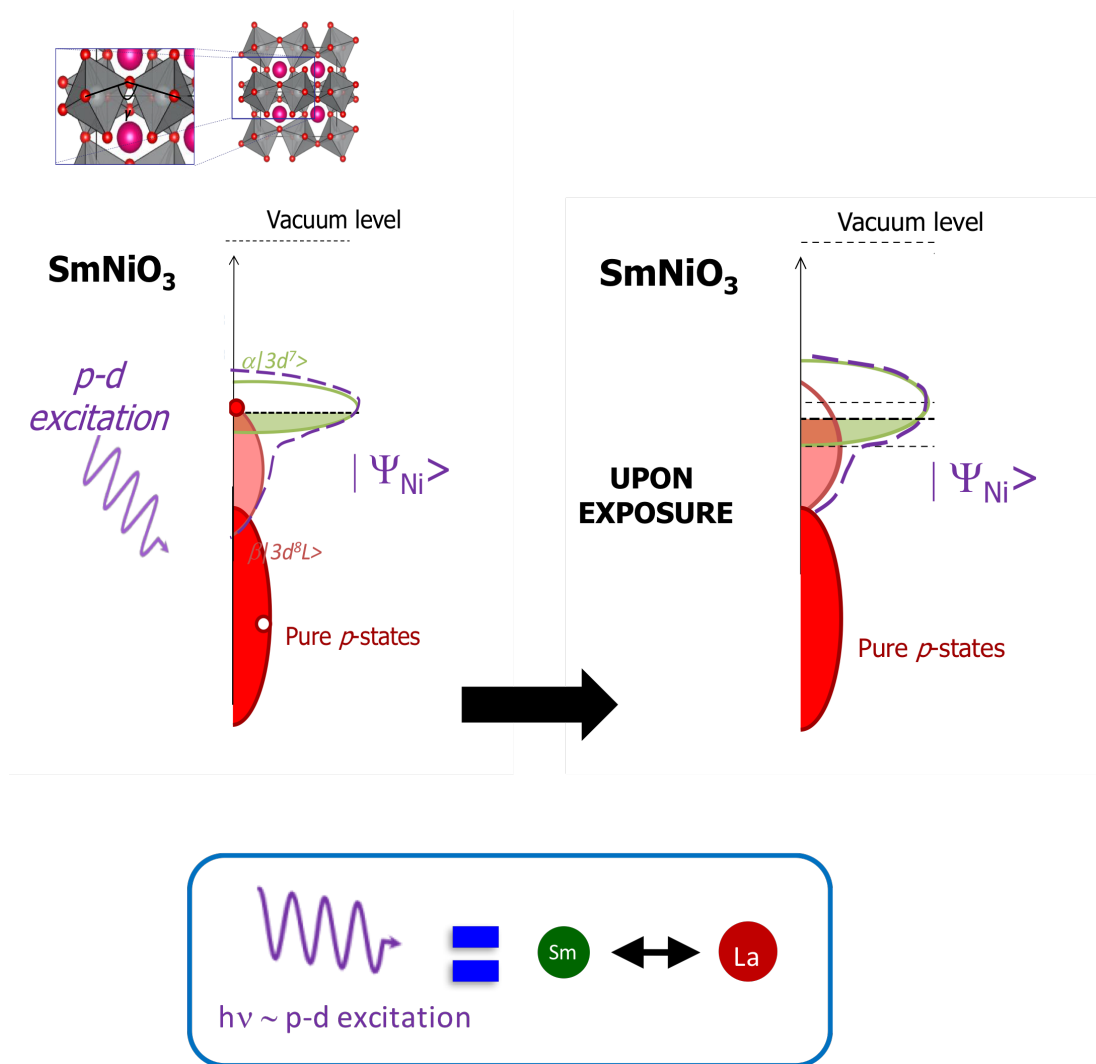


Figure 13 : Schéma d'explications de l'effet d'illumination sur une nickelates peu covalente

En effet, puisque la covalence peut être vue comme un phénomène de dopage *in situ* entre l'oxygène et le nickel, il devrait être possible de le reproduire en utilisant la transition p-d autour de 2.7 eV. Nous avons donc développé de nouveaux dispositifs expérimentaux pour caractériser les propriétés en transport et en structure des nickelates de terre-rare sous

illumination à différentes longueurs d'onde. Nous avons pu démontrer des effets de photoconductivité géants à la transition $p-d$, comme attendu. Les systèmes isolants sont en effet rendus plus métalliques sous l'effet de l'excitation lumineuse comme si on avait altéré le niveau d'hybridation en modifiant la terre-rare.

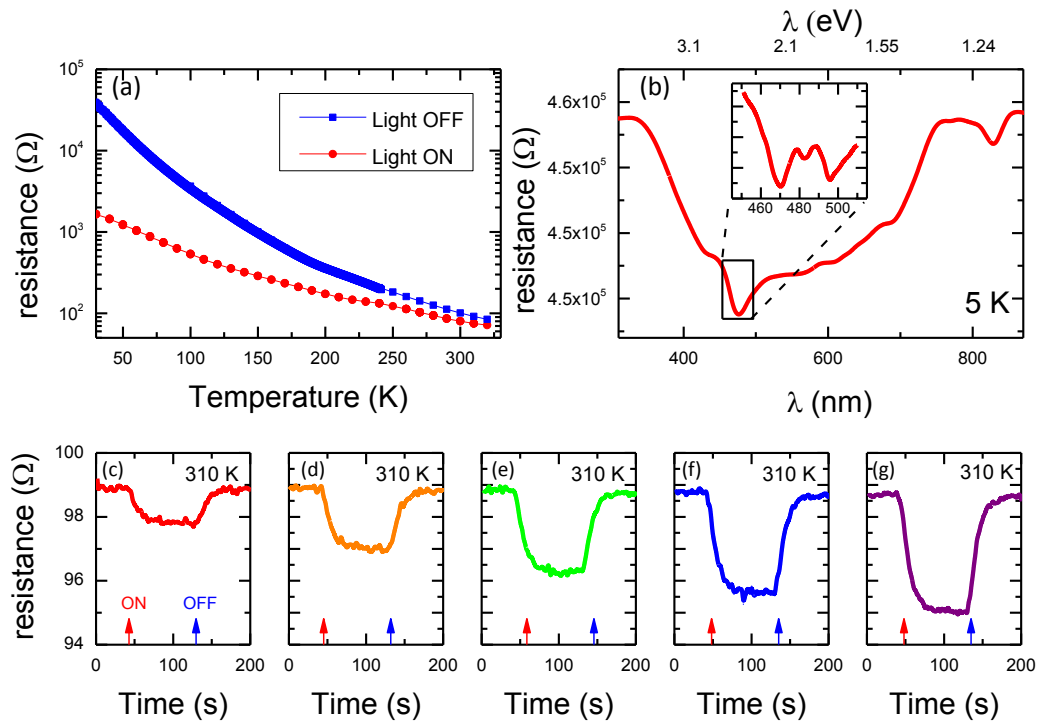


Figure 14 : (a) dépendance de la résistance en température d'un échantillon de SNO sur LAO de 23 nm sans éclairage (bleu) et avec (rouge) un éclairage en lumière blanche de 0.5 W. (b) variation de la résistance en fonction de la longueur d'onde de l'éclairage. (Inset) Zoom entre 450 et 550 nm. (c-g). Variation de résistance en fonction du temps d'illumination à 470 nm de 20 s à 120 s (flèche rouge) et sans lumière après 120 s (flèche bleue) pour différente puissance de 0.2 A à 1 A dans une diode bleue avec un pas de 0.2 A.

Par ailleurs, la conductivité n'est pas le seul paramètre affecté par la variation de covalence. En effet, dans les nickelates, la phase métallique de haute température est connue pour être orthorhombique alors que la phase isolante est associée à une phase monoclinique de plus grand volume. Ainsi, simuler le dopage *in situ* ayant lieu en fonction de la température, par l'impulsion lumineuse devrait induire une variation de la monoclinicité.

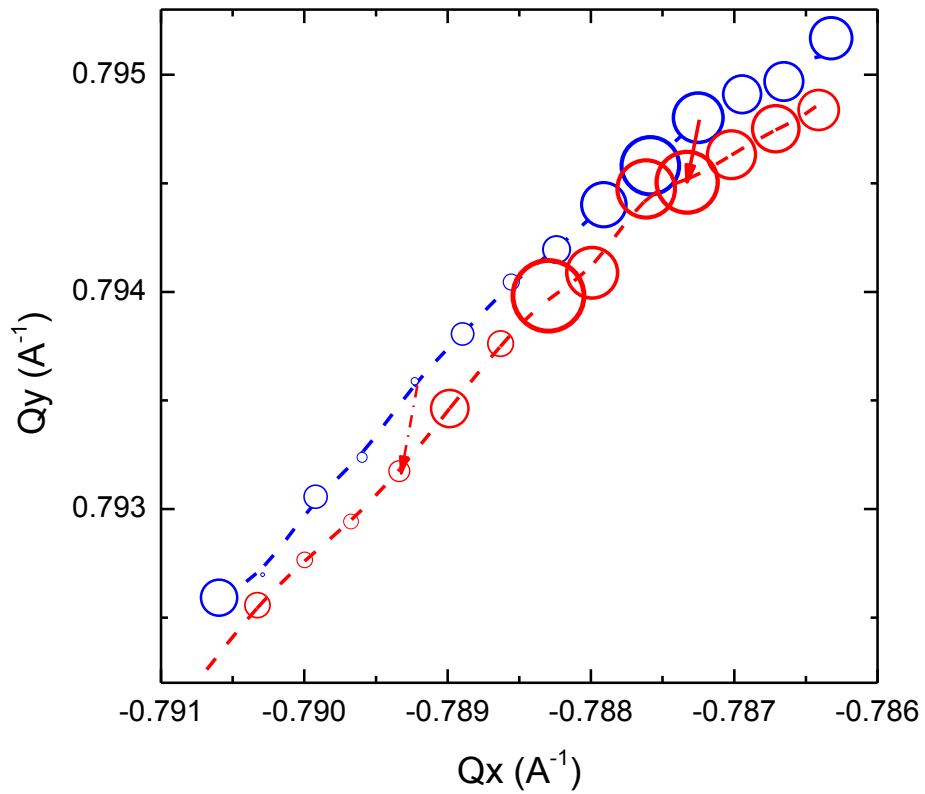


Figure 15 : Scans dans l'espace réciproque du pic [-303]pc pour un échantillon de 50 nm de SmNiO_3 déposé sur SLGO éclairé à 470 nm (rouge) et sans éclairage (bleu) à température ambiante.

Nous avons ainsi observé une réduction de l'angle monoclinique de 0.012 degrés associée à une augmentation de la conductivité électronique (en direction de la phase métallique).

Résumé du manuscrit de thèse en français :	8
I. Introduction to correlated oxide interfaces	29
A - The oxide perovskite world	29
1 - The crystal structure	30
2 - The electronic structure	31
B - A perfect playground for studying correlated matter	34
1 - The Mott-Hubbard insulator	34
2 - Mott-Hubbard versus Charge-Transfer insulator	35
C - Organization of this manuscript	39
II. Experimental techniques	40
A - Sample fabrication	40
1 - Substrate preparation	40
2 - Pulsed-Laser Deposition	43
3 - In-situ monitoring.....	45
B - Structural characterizations	46
1 - X-ray reflectivity	46
2 - X-ray diffraction.....	47
C - Physical characterizations	49
D - Synchrotron radiation-based techniques	50
1 - X-ray absorption spectroscopy.....	51
2 - Sum rules.....	52
a) For X-ray magnetic circular dichroism.....	52
b) For X-ray linear dichroism	53
3 - X-ray photoemission spectroscopy	54
III. Rare-earth titanates	57
A - State-of-the art.....	57
1 - Bulk single crystals	57
a) Structural properties	57
b) Transport properties.....	59
c) Magnetic properties.....	60
2 - Thin films of GdTiO ₃	63
a) Thin films grown by hybrid MBE	63
b) Properties under doping	64

c) Confinement and thickness-dependent effect in RTO thin films	66
B - Orbital and spin structure of the ferromagnetic GdTiO₃ single crystal	67
1 - Crystal structure	67
2 - Magnetism at low temperature	70
3 - Electronic structure	72
4 - Field dependence of Ti magnetism	73
C - Pulsed laser deposition of GdTiO₃ thin films and its characterization	75
1 - Growing titanate thin films	75
2 - Growth orientation	78
3 - Transport properties	81
4 - Magnetic properties	82
5 - Numerical confirmation	83
6 - Effect of defects and oxidation	83
D - A strain engineering study	85
1 - Effect of strain on the growth orientation	86
2 - Effect of strain on surface morphology	88
IV. Rare-earth nickelates	92
A - Electronic and magnetic properties of RNiO₃:	92
1 - Bulk crystals	92
a) Structural properties	93
b) Magnetic properties	94
c) Transport properties	95
d) Electronic structure	96
e) Effect of hydrostatic pressure on rare-earth nickelates	98
2 - Thin films	99
a) Growth parameters and variability	99
b) Strain-engineering in rare-earth nickelates	101
c) Confinement effects	102
d) A debated ground state	104
e) Crossing from ionicity towards covalence	106
1) Structure of the ground state	107
2) Electrostatic properties of the ground state	108
3) Imaging orbital occupancy in the ground state	110
4) Reconciling ionic and covalent scenarios	112
5) Role of the covalence	113
B - Probing the metal-insulator transition in SmNiO₃	113

1 - Sample characterizations	114
2 - Temperature dependence of isotropic XAS	115
3 - Temperature dependence of resonant X-ray diffraction	116
4 - Temperature dependence of linearly polarized XAS	117
5 - Discussion and conclusions	119
V. Correlated interfaces.....	125
A - Interfaces in oxides	125
1 - The canonical oxide interface: LaAlO ₃ /SrTiO ₃	126
2- Interfacing nickelates or titanates.....	127
a) Nickelates interfaces	127
1) With a band insulator	127
2) With other charge-transfer insulators.....	129
b) Titanates interfaces	131
1) With a band insulator	131
2) With other correlated oxides.....	134
B - Titanate-Nickelate bilayers	136
1 - Growing the bilayer.....	136
2 - Interfacial charge transfer.....	141
a) In LNO/GTO	141
b) In RNO/GTO	147
c) Effect of polar termination	150
3 - ferromagnetic phase in RNO	152
a) Magnetism in NNO/GTO	152
b) Magnetism in RNO/GTO	156
4 - A new knob for tuning oxide properties: Covalence	157
a) Measuring covalence in RNO/GTO.....	157
b) Charge transfer in RNO/GTO at the O K-edge.....	160
c) Origin of the covalence in RNO/GTO bilayer	162
d) Role of the covalence on magnetism in RNO/GTO	164
VI. Versatile manipulation of covalence in rare-earth nickelates	167
A - Illumination experiment in oxides	167
1 - In cuprates.....	168
2 - In other oxides.....	170
B - Illumination properties in nickelates.....	171
1 - Photo-excited transport properties in SNO.....	171

a) Experimental setup	172
b) Transport measurements under illumination	173
1) Photo-conductivity	173
2) Spectral dependence	175
3) Power dependence	176
4) Relaxation times	179
2 - Photo-excited structural properties in SNO	180
a) X-ray reflectivity under illumination	180
b) Reciprocal space maps under illumination	182
VII. Conclusions, and perspectives	185
A - Conclusions and summary	185
B - Perspectives	188
1 - Future research	188
a) Other titanates and nickelates	188
b) Strain engineering physical properties in titanates	188
c) Growing superlattices	189
d) Octahedral control	189
e) Looking for topological properties	189
2 - New “covalentronic” architectures	190
Bibliography	192

I. Introduction to correlated oxide interfaces

A - The oxide perovskite world

In the bulk, transition-metal oxides and in particular perovskites (with chemical formula ABO_3) display an amazingly large range of functionalities [1] (insulator, metallic or superconducting, ferroelectric, magnetic, etc.). Their sensitivity to external stimuli (electric field, light) and their various tunable order parameters (charge, orbital and spin) make them ideal candidates for information processing.

Their investigation started in the 1950's when Wollan et al. first discovered and studied different types of magnetic orders in manganites [2]. Soon after, ferroelectricity, which is the presence of a spontaneous electric polarization, was first established in $BaTiO_3$ [3]. The potentiality of the oxide world was then revealed by John Goodenough's pioneering work on their complex phase diagrams and the discovery of their many order parameters [4]. Finally, the late 1980's was marked by a huge achievement for the community with the discovery of high-temperature superconductivity in layered cuprates [5,6].

All these amazing properties arise both from the complex crystal structure – that offers many possible degrees of freedom – and from the intertwined electronic and spin degrees of freedom – that develop from the hybridization between ligand p-orbitals and transition metal d-orbitals.

1 - The crystal structure

The perovskite structure (ABO_3) is indeed described by a cubic unit cell (u.c), with the $Pm-3m$ space group (cf. Figure A-1). This unit cell is composed of large A cations – often alkaline or lanthanide, in red in Figure A-1 – sitting in the middle of a cube formed by B cations – often transition metals in green in Figure A-1 – surrounded by ligand (often oxygens) octahedra. Along any primary directions ($\langle 100 \rangle$, $\langle 010 \rangle$, $\langle 001 \rangle$), AO and BO_2 planes are stacked in an alternating fashion.

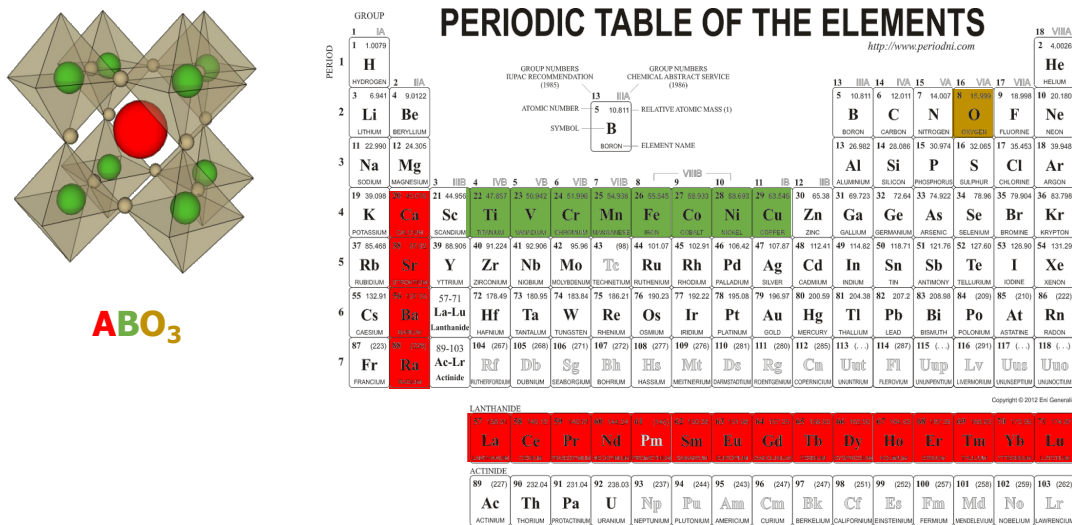


Figure A-1: Schematic representation of an oxide perovskite with the location of A (red), B (green) and O in the periodic table (left)

The existence and stability of such a structure is based only on steric considerations for a large range of ionic radii. Indeed, the size of the B cation must be sufficiently large to accommodate the presence of oxygen cages, themselves strained by the size of the A cation. The induced strain cannot always be sustained by the oxygen skeleton that in turn rotates and reduces the symmetry of the system. In 1926, V. M. Goldschmidt [7] proposed to study the stability of the perovskite structure as a function of an intrinsic parameter, now called, the Goldschmidt factor or the tolerance factor. This latest relates all the ionic radii present in the u.c. according to the following equation: $t = \frac{r_A+r_O}{\sqrt{2}(r_B+r_O)}$, where r_A , r_B , r_O correspond to the ionic radii of each species. Naturally, this formula, which follows the stoichiometry and neutrality of the unit cell, illustrates the equilibrium between the A-O and B-O bonds, and can give some insights on the many distortions that the structure can undertake. Those can be either rotations, tilts, or structural distortions of the coordination polyhedra of the A and/or B cations, yielding either compression, or elongation of the unit cell. As an example, when $t=1$, the structure is perfectly cubic. However, as soon as t is no longer equal to 1, the unit cell is

distorted:

- $t > 1$, the unit cell becomes hexagonal: BaTiO_3 , NaNbO_3 , BaNiO_3
- $0.95 < t < 1$, the unit cell is back to cubic: BaZrO_3 , SrTiO_3
- $0.9 < t < 0.95$, distortions are rhombohedral: RbTaO_3 , KNbO_3 , LaNiO_3
- $0.8 < t < 0.9$, distortions are in that case – the most common – orthorhombic: PbTiO_3 , GdFeO_3 , GdTlO_3 , NdNiO_3 , LaMnO_3
- $t < 0.71$, the structure is totally different: it can be ilmenite for example in FeTiO_3

These distortions have a dramatic influence on the electronic properties of perovskite oxides as the ligand interact with the transition metal ions to give the oxide its electronic structure.

2 - The electronic structure

The structural distortions of oxide perovskites are due, as we have just seen, to steric considerations that result in modifications of the electronic structure.

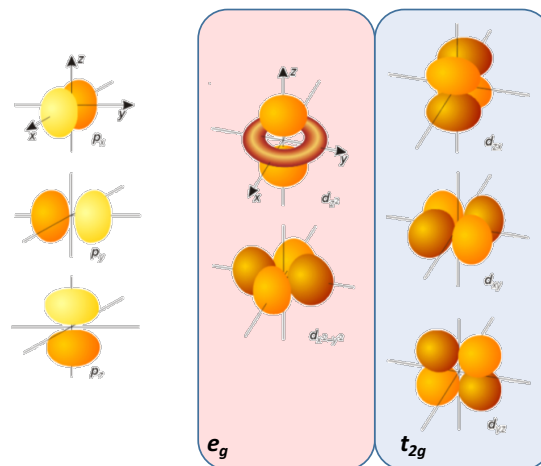


Figure A-2: representation of the three p-orbitals (left) of the oxygen and (right) of the five d orbitals of the transition metal ion split up in e_g (red) and t_{2g} (blue) orbitals

To understand how and why structure and electronic degrees of freedom interact so much in oxide perovskites, the peculiar nature and symmetries of the orbitals are keys. For isolated atoms or ions in vacuum, the orbitals adopt a spherical symmetry with typical quantum numbers (n , l , and j – when the spin-orbit coupling needs to be included). However, as soon as these atoms are placed in a crystal structure, the symmetry is changed and the resulting symmetry is determined by the proper symmetry of the crystal.

In oxides perovskites, when a transition metal (TM) ion is placed in an O^{2-} anions oxygen

octahedral cage, the non-degenerated fivefold $3d$ orbitals split into a lower triplet t_{2g} and an upper doublet e_g (cf. Figure A-2). The splitting of the orbital is caused by the electrostatic interactions of d -electrons of the transition metal ions with electrons of the surrounding O anions and is called the crystal field (CF) splitting. The splitting of the orbitals arises once again from pure symmetry. Indeed, for the e_g states electronic charge distribution points directly to the negatively charged anions surrounding the TM (cf. Figure A-2). As a result, e_g states feel a much stronger coulomb repulsion than t_{2g} states whose electronic density lies exactly in between the anions charge distribution. This contribution is known as the point-charge contribution. Nevertheless, this contribution is not the only one that matters.

One that will reveal particularly important for the rest of this work, is the level of covalence between the TM ions and the surrounding ligands (in the following we will speak of O anions, but this could be further applied to other halogens such as F, S or Se...). The d orbitals of the TM ions overlap with the p orbitals of the oxygen resulting in a hybridization between the oxygens and the TM ions (and the creation of bonding and antibonding states- cf. Figure A-3). A description as pure d or pure p electrons does no longer apply as the d and p levels are mixed by hybridization. One can show that this hybridization is different throughout all the $3d$ orbitals depending on the respective symmetry and filling of the considered orbitals. Since the covalence is stronger between e_g and oxygen- p orbitals than between t_{2g} and p -orbitals, the resulting splitting is stronger for e_g than for t_{2g} . This contribution is also called the ligand-field contribution.

Haverkort et al. discussed the role of both contributions in the context of NiO in [8]. We reproduced the sketch summarizing the different contribution (cf. Figure A-3).

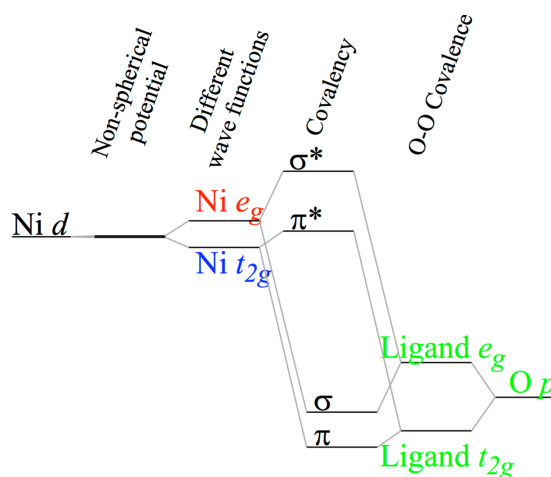


Figure A-3: One particle description of orbital energy levels diagram for NiO₆ cluster in NiO, adapted from [8].

We will discuss in chapter IV the effect of this contribution to absorption spectra for instance. For now, we have only discussed cubic systems with octahedral symmetries, nonetheless, other

contributions to the crystal field can eventually occur. Based on what was just discussed, one can easily figure that any distortion or symmetry lowering of the O octahedral surrounding the TM ions will result in changes of the crystal field.

For example, a tetragonal elongation (coming from a Jahn-Teller distortion [9] for example), leading the oxygens to move by a small displacement, d as $z = z + 2d$, $x = x - d$, $y = y - d$ (so that the volume remains unchanged in first order approximation- cf. Figure A-4.) would split the z^2 and x^2-y^2 , with z^2 being lower in energy (Figure A-4). Indeed, the z^2 -lobes point in the z-direction in which the TM-O distance increases. Additionally, the spin-orbit coupling may also separate the levels depending on the total orbital moments of the different non degenerated orbitals.

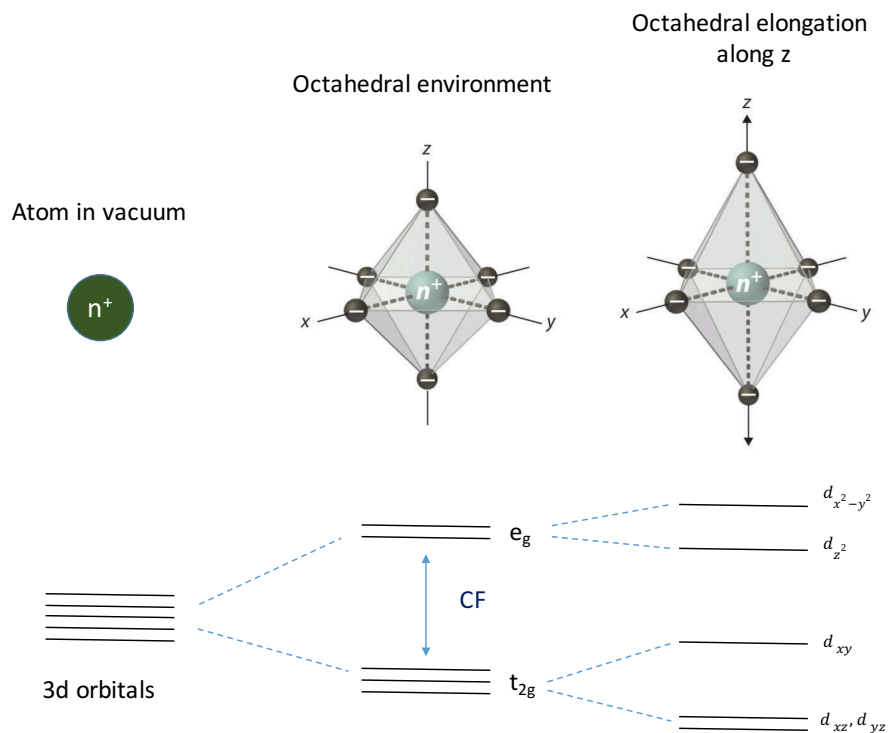


Figure A-4: orbital splitting of the B-cation 3d-orbitals as a function of the crystal field (CF) or Jahn-Teller effect (JT) for elongation along the z-direction

This orbital splitting then results in the formation of bands, which are often close to the Fermi level (either valence band if the level is filled or conduction in case it is not). If the physics of crystal field splitting is shared among all perovskite oxides, many oxides present a certain originality arising from the presence of strongly interacting d-electrons. We will discuss that in more depth in the next section of this introduction.

B - A perfect playground for studying correlated matter

1 - The Mott-Hubbard insulator

In 1937, de Boer and Verwey reported that NiO is an insulator [9]. This compound adopts the cubic NaCl structure, with octahedral Ni ($3d^8$) and O^{2-} sites. The $3d^8$ configuration can be decomposed in 3d: $t_{2g}^6 e_g^2$. e_g can host up to 4 electrons in total (spin up and spin down in the z^2 and x^2-y^2 orbitals). According to conventional band theory, NiO should thus be metallic because it presents half-filled e_g band. This insulating behavior at half-filling – thought to be extraordinary at that time – is actually not that unusual among other oxide perovskites. It can be observed in perovskite nickelates, titanates, manganites and in many other oxides.

The first to propose a qualitative explanation of this unusual phenomenon were Mott and Peierls in their discussion of De Boer's seminal paper [11]. Mott, followed by Hubbard [12–14], came out with the idea of adding an extra repulsive term to the common tight-binding Hamiltonian that describes the conventional band picture. This model was named the Mott-Hubbard Hamiltonian and reads as follows:

$$H = \varepsilon_d \sum d_i^\dagger d_i + t \sum (d_i^\dagger d_j + h.c.) + U \sum n_{i,\uparrow} n_{i,\downarrow}$$

where ε_d is the d-orbital energy, t is the hopping energy, n is the electronic density and U is the on-site coulomb repulsion term.

When $U = 0$, the conventional tight binding Hamiltonian is recovered. The unusual insulating behavior observed by de Boer and Verwey comes from the additional energy provided by Hubbard U term. If U is positive, the extra-energy cost further splits off the d-band into so-called “lower” and “upper” Hubbard bands. For NiO, the Hubbard term dominates the hopping term and the bandwidth W of the d-electrons (which is somehow related to the hopping term by $W \sim 2 n t$, where n is the number of neighboring sites), leading to a localized behavior (and thus an insulating character). It follows indeed from the above expression that :

- If $U/W \ll 1$, the tight-binding Hamiltonian applies, the band is partially filled and the system is metallic.
- Whereas when $U/W \gg 1$, the system is dominated by on-site coulomb interactions, which leads to an insulating behavior.

Strongly correlated Mott materials are very often found in transition metal oxides with partially filled d-bands. Indeed, d-orbitals are particularly localized in space with bandwidths of only a

few eVs whereas the Hubbard term U is typically of the order of 5 eVs for Ti to 8 eVs for Cu. This places TM oxides in the $U/W \gg 1$ category and explains their often insulating behavior, even for partially filled bands.

The Mott-Hubbard paradigm is enough to account for some non-trivial phase diagrams describing the electronic behavior of doped early TM-oxides as titanates, vanadates. Nonetheless, it is clearly not enough to account for the tremendous variety of complex phase diagrams as discussed by Dagotto for instance in [15] (some of which are reported in Figure B-1).

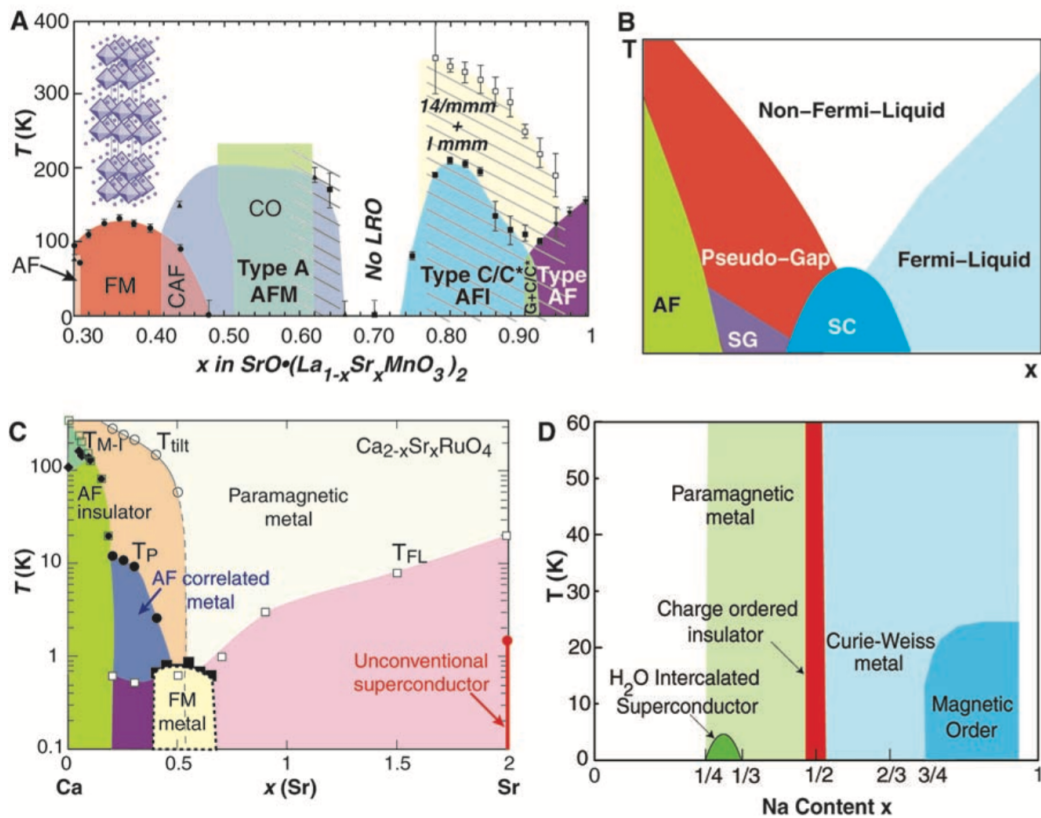


Figure B-1: Phase diagrams of representative materials of the strongly correlated electron family (notations are standard and details can be found in the original references). (A) Temperature versus hole density phase diagram of bilayer manganites [16] (B) Generic phase diagram for high- T_c superconductors (HTSC). (C) Phase diagram of single layered ruthenates [17,18] (D) Phase diagram of Co oxides [77] This figure is adapted from [15]

2 - Mott-Hubbard versus Charge-Transfer insulator

As we already saw when explaining specific contributions of the crystal field splitting, it is often necessary to include both d and p-electrons. In some cases, one can neglect these electrons and find a convenient description reduced only to the d-electrons, similar to the Mott-Hubbard description, for example in the case of titanates or vanadates.

However, it is often required to include all the electrons, particularly if the d and p levels lie

close to each other as in nickelates or cuprates. The simplest theoretical model, generalizing the Mott-Hubbard model, is called the “d-p model”. Here, we consider only non-degenerate d levels hybridizing with p levels through the t_{pd} hopping term.

$$H = \varepsilon_d \sum d_i^\dagger d_i + \varepsilon_p \sum p_i^\dagger p_i + t_{pd} \sum (d_i^\dagger p_j + h.c.) + U_{dd} \sum n_{d,i,\uparrow} n_{d,i,\downarrow} + U_{pp} \sum n_{p,i,\uparrow} n_{p,i,\downarrow} + U_{dp} \sum n_{d,i,\uparrow} n_{p,j,\downarrow}$$

where ε_d , and ε_p are the energy of d and p orbitals, t_{pd} is the hopping term between d and p orbitals, and U states for the coulomb interaction either on-site on a same orbital (U_{dd} , U_{pp}) or between electrons coming from different orbitals (U_{dp}).

The first observation is that this Hamiltonian is much more complex than the previous one but can be considered for example as a good description of the physics of the parent compounds of High- T_c cuprate superconductors [19,20]. For simplicity, and because it is most relevant to this work, we will discuss this model in the case of only one e_g electron (which is ideally realized in the case of Ni^{3+}). In typical cases, the position of the d and p levels are well separated and the p levels rest well below d levels. This model has thus two types of excitations: one corresponding to an excitation of localized d-electrons to neighboring d-sites, and the other consisting of an excitation of an electron from occupied $2p$ bands to $3d$ bands [20]. These two excitations happen at certain energies that we would refer in the following as the on-site energy U and the charge-transfer energy, Δ_{CT} respectively. The d - p model differs from the famous Mott-Hubbard model essentially by providing another source of excitations through the ligand p-states.

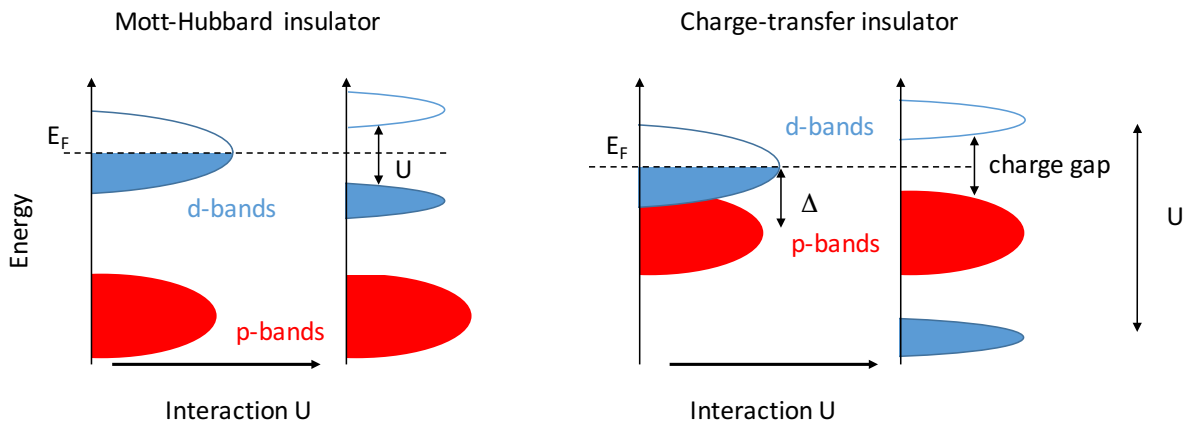


Figure B-2: Band structure for Mott-Hubbard insulators (left) and charge transfer insulators (right) for 1/2-filling before and after U interaction

The second process which will reveal to be fundamental to this work, allows the appearance of an extra electron in the d states and the creation of an oxygen hole. We will later denote this state: $d^{n+1}L$. In the simplest case, where the d band contains no electron, Δ_{CT} is equal to the difference

in energy between d and p levels. This energy would thus increase when moving across the TM ions series of the periodic table (cf. Figure A-1) by an amount proportional to the number of d electrons (providing an additional $n U_{dd}$ energy term where n is the number of d -electrons). Due to geometric arrangements of all ions in perovskite structures, d - d hopping is usually quite rare in oxides. The hopping between d elements can be viewed as a sequential process in which (i) the electron first hops from a p to a d orbital and then, (ii) a neighboring d -electrons coming from a second site hops from the d band to the now vacant p orbital. This results in an effective second-order d - d hopping term which can be written in perturbation as $\frac{t_{pd}^2}{\Delta_{CT}}$. By doing so, the d - p model is actually renormalized into an effective Mott-Hubbard model in which the physics of ligand charge-transfer appears into the rescaled t_{dd} hopping term. Basically, the previous condition between localized and itinerant behavior described by the condition $U/t \ll 1$ in the Mott-Hubbard Hamiltonian becomes a condition between $\frac{U}{t_{pd}}$ and $\frac{\Delta_{CT}}{t_{pd}}$. This leads to the presence of three zones:

- $\frac{U}{t_{pd}} \gg 1$ and $\frac{\Delta_{CT}}{t_{pd}} \ll 1$ ($U > \Delta_{CT}$): the physics is dominated by the charge transfer energy which is the smallest energy excitation (yielding the creation of a ligand hole state, $d^{n+1}L$). These systems are called charge transfer insulators (cf. Figure B-2-right)
- $\frac{U}{t_{pd}} \ll 1$ and $\frac{\Delta_{CT}}{t_{pd}} \gg 1$ ($U < \Delta_{CT}$): the physics is dominated by the on-site Hubbard term, d - d excitations are the smallest energy excitations. These systems are called Mott-Hubbard insulators (cf. Figure B-2-left)
- $\frac{U}{t_{pd}} \ll 1$ and $\frac{\Delta_{CT}}{t_{pd}} \ll 1$: the tight-binding Hamiltonian is recovered and the systems are metals at partial filling

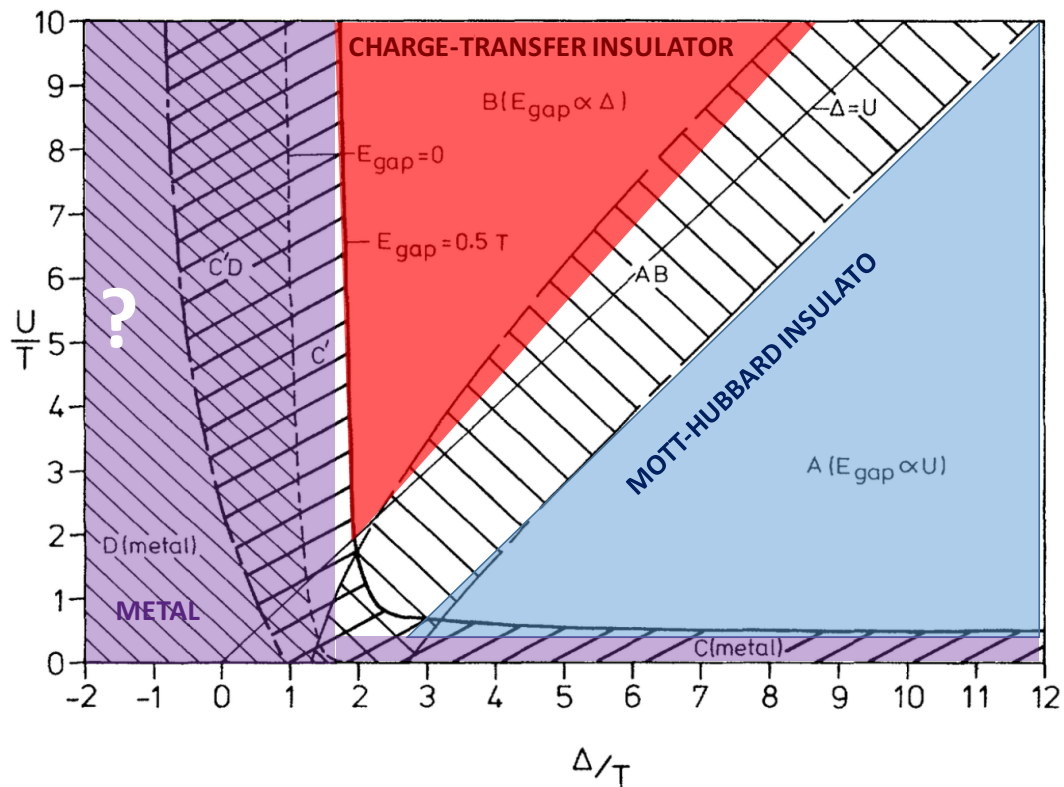


Figure B-3: Zaanen-Sawatsky-Allen phase diagram of the different phases discussed above. Note that certain regions are exhibiting anomalous metallic behaviors with different characteristics depending on the smallest excitation (those are labeled D or C). The figure is adapted from [21]

This has been summarized in the famous Zaanen-Sawatsky-Allen (ZSA) [21] phase diagram (cf. Figure B-3) and can be even complexified by introducing a filling factor describing the physics of doping. An interesting case arise when Δ_{CT} is negative. There, the creation of oxygen holes in the d-band ($d^{n+1}L$) would become energetically favorable resulting in a spontaneous internal charge transfer between oxygen and TM ions sites. We will see later in this manuscript that this special case happens in nickelates and in cuprates. They are called (negative-) charge transfer materials.

As a conclusion, the physics of metal-insulator transition discussed in the previous section becomes now much more exotic as the strength of the hopping terms depends on the d-p energy scale and the direction of the spin of the d-d orbitals leading to a rather unusual and almost unique coupling between the orbitals, the spin, and the electronic degrees of freedom.

C - Organization of this manuscript

In this work, we have been interested in studying the effect of correlations at the interfacial level. Based on the concepts of correlated physics presented in this chapter, we decided to combine the two extreme cases of the ZSA phase diagram: A $U/t \ll 1$ – Mott insulator – GdTiO_3 (GTO) and a $\Delta/t \ll 1$ – (negative) charge-transfer insulator – RNiO_3 (RNO). Combining such extreme cases of correlated matter offers a formidable playground for material physicists and theoreticians as it provides us with a unique way to continuously probe the whole p-d energy landscape present in the oxide world.

Additionally, GTO and RNO present extraordinary properties in themselves (that we will present in chapter III and IV respectively), due to the interplay between their different degrees of freedom (spin, orbital and charge). Interfacing these materials provides a good opportunity to study how continuously these degrees of freedom will evolve upon crossing the interface.

On the way towards this end goal, we will organize the manuscript as follows:

- First, we will describe the growth and characterization of the Mott-Hubbard rare-earth titanates (chapter III)
- Then, we will be interested in probing the rich physics of (negative) charge-transfer rare-earth nickelates (chapter IV)
- Next, we will combine these two materials into a bilayer whose growth will be described and whose unique properties characterized by means of synchrotron-radiation based spectroscopy techniques (chapter V).
- In the last chapter, we will propose new innovative ways to tune the level of covalence in rare-earth nickelates (chapter VI).

II. Experimental techniques

In this chapter, we present the different experimental techniques that we have used during this work from sample fabrication to its characterization. We will also specifically focus on the use of synchrotron-spectroscopy techniques and present absorption spectroscopy and photoemission techniques.

A - Sample fabrication

1 - Substrate preparation

During this Ph.D., we have been working with different substrates. For that purpose, I have learned and performed substrate treatment on all the different types of substrates that are commercially available. I have also been particularly careful on studying their morphology at high temperature (>500 °C) at which we performed most of our material growth. In this section, we will focus on two substrates that I used preferentially during this work: LSAT and LaAlO₃.

LSAT stands for Sr_{1-x}La_xAl_{1-y}Ta_yO₃ solid solutions, with typical values for x and y of x = 0.3 and y = 0.7, respectively, (*i.e.* (LaAlO₃)_{0.3}(Sr₂AlTaO₆)_{0.7} formula). Its lattice constant is 3.868 Å. It has a perovskite structure for temperatures above 150 K and a tetragonal - or slightly orthorhombic - one below [22]. There are very few reports on surface treatment of LSAT [23–25], probably due to difficulty of obtaining an A- or B-site single terminated surface for this solid solution compound.

We thus performed our own substrate treatment study. The best treatment consisted of:

1. Cleaning the substrate during 15 minutes in an ultrasonic acetone bath
2. Cleaning the substrate with optical paper in a bath of isopropanol.
3. Drying the substrate in N₂ flow
4. Annealing in air at different temperatures for different time. The figure below sums up the different results.

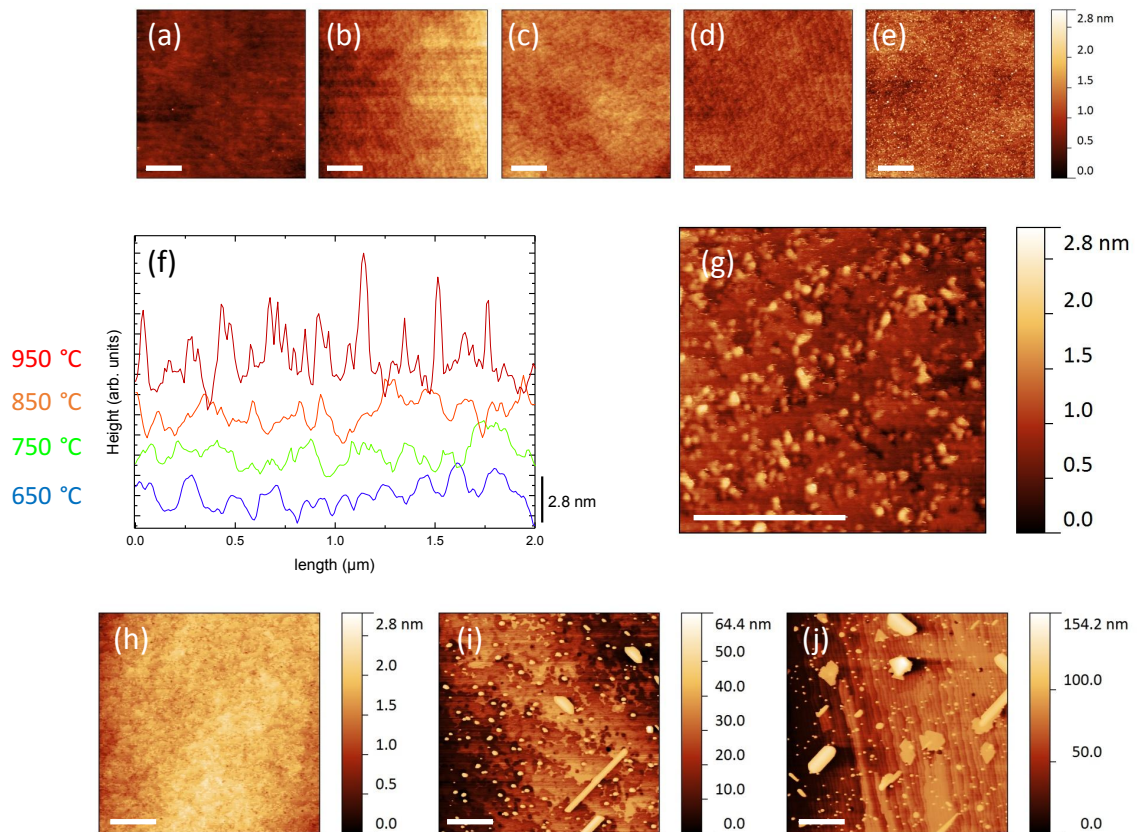


Figure A-1: AFM image of 25 μm² of bare LSAT substrate (a) annealed in air-flow for 3 h at (b) 650 °C (c) 750 °C (d) 850 °C (e) 950 °C. Height profiles of 2 μm-long scans for (b) blue, (c) green (d) orange and (e) red lines. (g) 1 μm² zoom of step terraces in (e). AFM image of 25 μm² of bare LSAT substrate annealed in air for 1 h at 950 °C (h), 1075 °C (i) 1150 °C (j). The white straight line represents 1 μm

The atomic force microscopy (AFM) images, in Figure A-1 (a-e), present small mounts that appear when the annealing temperature is higher than 950 °C. These structures start to segregate at the edges of the step terraces. This is clearly visible in the height profiles (Figure A-1 f) extracted from AFM measurements (cf. Figure A-1 g).

We studied the formation of these mounts by reducing the annealing time from 3 h to 1 h but by increasing the temperature from 950 °C to 1000 °C. We observe that, at higher temperatures, the mounts in Figure A-1 (g) adopt an orientation quasi-perpendicular to the edges of the terraces

and aggregate to form crystallites of about 2 μm in length and 20 nm in width and whose thickness increases with temperature (cf. Figure A-1 h-j). In Figure A-2, Auger spectroscopy confirmed that those crystallites were mainly composed of SrO.

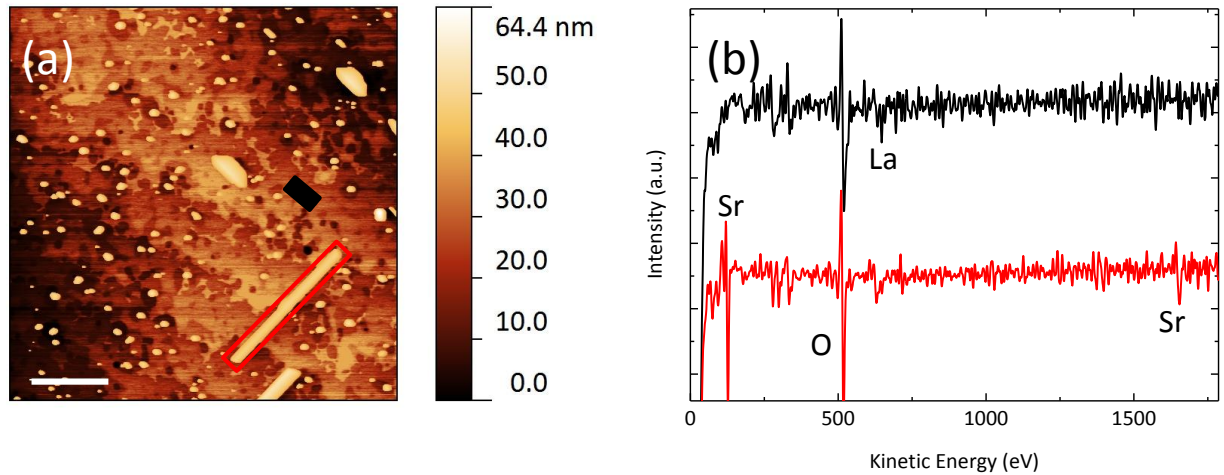


Figure A-2: (a) AFM image of 25 μm^2 of bare LSAT substrate annealed in air for 1 h at 1075 $^\circ\text{C}$. The white straight line represents 1 μm . (b) Auger spectroscopy performed in the red rectangle (red curve) and in the black area (black curve)

Below, we summarize different experiments performed on LSAT substrates as a function of annealing duration and temperature.

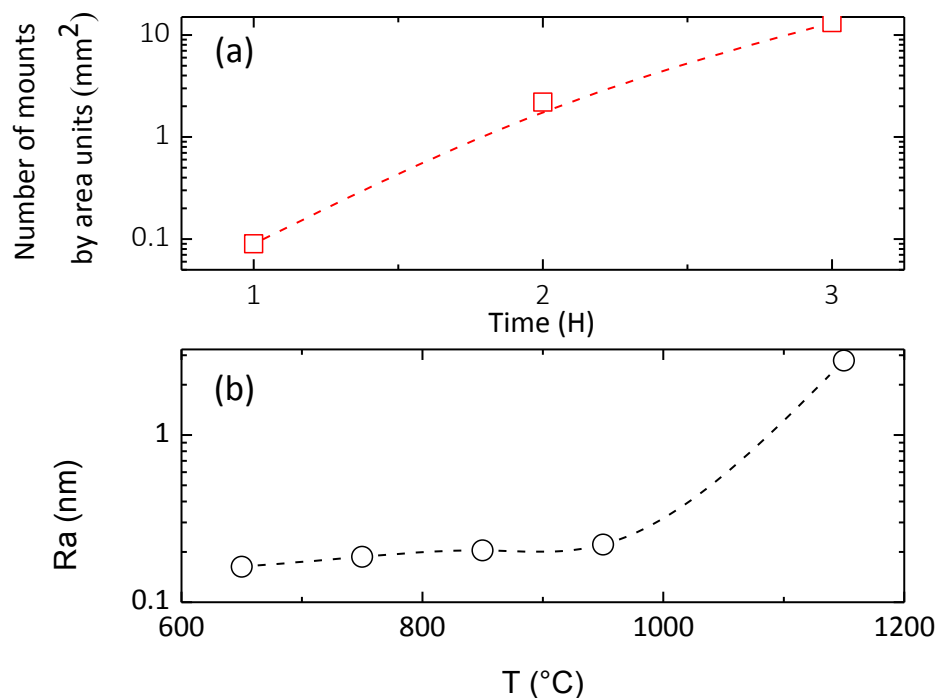


Figure A-3: (a) Density of mounts as a function of the annealing time in hours and (b) roughness as a function of the annealing temperature

Based on Figure A-3 (a) and (b), it is clear that minimizing the annealing time while maximizing the annealing temperature before the formation of SrO-crystallites is the optimal choice. We thus opted for an annealing time of 1 h at a temperature of 950 °C.

Another very important substrate used during this work was LaAlO₃ (LAO). In the case of LAO, the two surface terminations are either LaO or AlO₂. Many studies [24,26,27] have reported on the cleaning of LAO surfaces but only a few have succeeded in having a perfect LaO-termination.

We used a treatment made of etching the substrate in a bath of HNO₃ at 50 °C then rinsing in acetone, and etching again for 30 seconds in a bath made of BE7-1 which is solution of HF/NH₄F. The substrate is finally rinsed in deionized water.

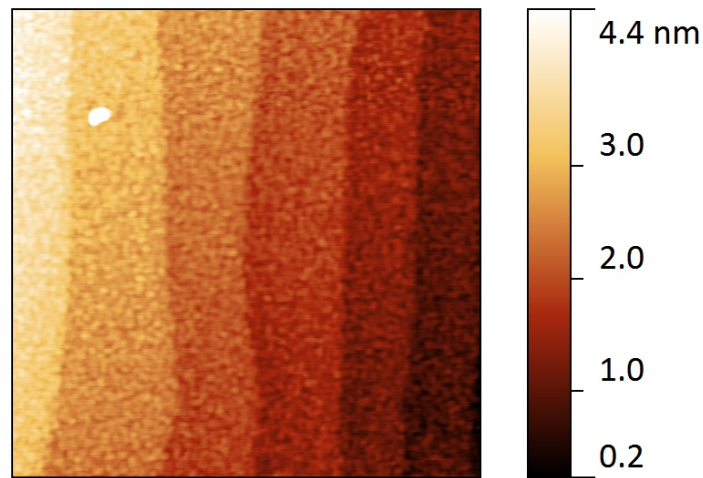


Figure A-4: 1 μm wide-AFM image of the topography of a treated LAO substrate prior to deposition.

Figure A-4 attests the quality of the treatment which enabled nice termination and perfectly defined step edges.

2 - Pulsed-Laser Deposition

The thin films, presented in this manuscript, have been obtained by pulsed laser deposition (PLD) (cf. Figure A-5). Short impulses of a very intense laser ablate a target placed in front of a substrate. The matter ablated by the laser forms an out-of-equilibrium plasma that is projected perpendicularly from the surface of the target onto the substrate. Many parameters control the growth quality. The most important one are the temperature of the substrate, the pressure inside the chamber and the fluence of the laser. Other parameters such as the substrate-to-target distance, and the frequency of the laser also matter.

The process by which matter is ejected from the target onto the substrate can be divided in 3 steps [28,29]:

- *laser-target interaction*: when the laser hits the target, the laser energy is absorbed by the surface of the target, and then converts into thermal energy. Upon heating, particles start to form a plasma in which ions are present either in the form of clusters or as pure ions. The chemical and kinetic characteristics of the plasma depend mainly on the laser itself (wavelength, duration of the impulsion, frequency, power) and on the target (density, thermal conductivity, and absorption coefficient).
- *Adiabatic expansion of the plasma*: The plasma goes then through an anisotropic adiabatic expansion, quasi-perpendicularly to the surface of the target. Then, the plasma, taking the shape of a plume, slowly cools down as energy is lost through the collisions between ionized species. The angular distribution and the orientation of the plasma mainly depend on the parameter of the laser, on the superficial morphology of the target and, above all, on the pressure in the chamber. Indeed, this latest is essential in confining the plume.
- *Interaction plume-substrate*: Species are deposited onto the surface of the substrate and the film grows according to out-of-equilibrium growth mechanisms, mainly dependent on the probability to stick to the surface and the probability to find a nucleation center. Again, the substrate temperature and the frequency, at which the laser hits the the target, controls the quantity of matter that reaches the substrate and thus the growth rate and mode (either 2D, flat terraces, or 3D, with islands forming due to oversaturation).

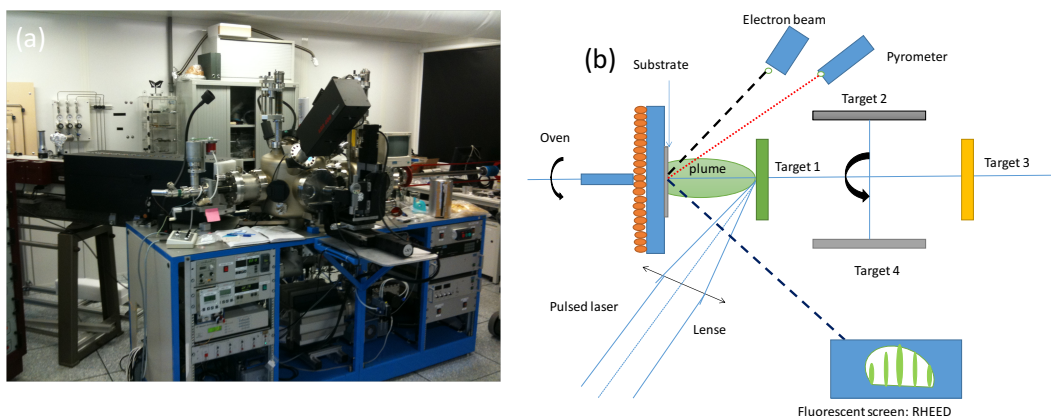


Figure A-5: (a) Pulsed Laser Deposition (PLD) setup used during this Ph.D. (b) schematic representation of the PLD setup with the laser, the RHEED, the target holder, and the substrate placed on a rotating oven, whose temperature is measured through a pyrometer.

In order to grow nickelates and titanates, we used mixed powders of constituting oxides such as $\text{Gd}_2\text{O}_3\text{-TiO}_2$ (for GdTiO_3) and $(\text{R}_2\text{O}_3\text{-NiO})$ for nickelates. Another option consists in using

stoichiometric single phase targets such as pyrochlore titanates of phase $\text{Gd}_2\text{Ti}_2\text{O}_7$. The PLD setup (cf. Figure A-5 a) was made of a solid pulsed laser Nd:YAG. Its fundamental wavelength is around 1065 nm for a maximum energy of 1 J per impulsion. The wavelength is then tripled to reach 355 nm (2.8 eV) which allows to interact with most of the materials of interest. The frequency of the impulsions varies between 1 Hz and 10 Hz and each of them lasts 7 ns, for a maximal energy of 180 mJ. The laser beam reaches the target at 45 degrees and is focalized on a spot size of approximately 5 mm^2 . The maximal energy density, also called fluence, is 3.2 J.cm^{-2} . An attenuator allows to carefully tune the fluence level independently from the frequency or the spot-size. Our PLD setup is composed of one growth chamber that can accommodate 4 targets simultaneously which allows to grow heterostructures comprising up to 4 materials. The targets are moved according to a certain pattern of consecutive lines that insures a homogeneous interaction with the laser. The growth chamber reaches a base pressure of about $5 \cdot 10^{-7}$ mbar and the substrate can be heated up to approximately 800 °C. Finally, the temperature of the substrates is controlled by means of an external pyrometer. The samples are introduced and removed without breaking vacuum in the growth chamber through an introduction cluster attached to the growth chamber.

3 - In-situ monitoring

Reflection high energy electron diffraction (RHEED) is an “in-situ” growth monitoring technique that enables to follow in real time the growth, the morphology and the superficial reconstruction of the as-grown thin film. RHEED is providing with real time information about the superficial reciprocal space.

To do so, a high energy electron beam (cf. Figure A-5 b), accelerated at 25 keV, is directed, at grazing incidence, towards the surface of the sample (typically a few degrees) and a chosen direction (typically $\langle 100 \rangle$, $\langle 010 \rangle$, $\langle 110 \rangle$). Part of the beam is reflected by the sample surface and another part is diffracted and intercepted by a fluorescent screen. Those diffraction patterns are then recorded on a CCD camera to enable numerical post-treatment. One can thus follow and quantitatively treat the intensity of the spots visible on the inset of Figure A-6 (b).

The condition to obtain constructive interferences may be deduced from the intersection of the reciprocal space with the Ewald sphere. For an ideally plane surface, the reciprocal space is a two-dimensional network of lines perpendicular to the real surface (cf. Figure A-6 a). The intersection of these lines with the Ewald sphere creates dots placed onto a circle. In non-ideal samples, the roughness of the as-grown films broadens the width of the lines and thus increases the intersection between the now thicker lines and the Ewald sphere, leading to more conventional RHEED fringes (cf. insets in Figure A-6 b)

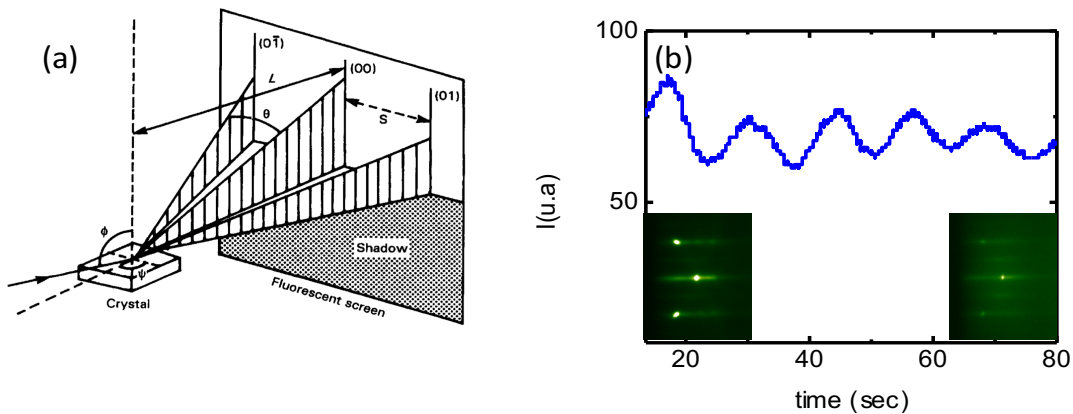


Figure A-6: (a) diagram describing the principle behind reflection high energy electron diffraction (RHEED) (b) example of a RHEED pattern of a 7 unit cells GdTiO_3 with as inset the recorded 2D RHEED pattern for the substrate LaAlO_3 right prior to the growth (left) and right after for a 7unit cells GdTiO_3 thin film (right).

The shape of these fringes can give us insights on the quality of the growth. Fringes that are all over the recorded area and regularly spaced in both directions are often due to 3D growth, while fringes looking like cones, generally indicate polycrystalline growth.

Finally, following the intensity of a bright spot in the diffraction fringes allows to inquire on the growth rate. When the surface is not homogenous most of the beam is scattered and intensity is lost. This is what happens when a monolayer is not yet fully completed. The RHEED intensity is indeed the smallest at half-coverage. It then recovers when a monolayer is fully deposited. In an ideal case, the intensity should come back to the same original value, at the beginning of the growth (cf. Figure A-6 b). Following the intensity variations, as in Figure A-6 (b), it can be decided in real time how many unit cells of a certain materials need to be deposited. Figure A-6 (b) also gives an idea of the growth speed of GTO grown onto LAO: 4 oscillations last approximately 50 seconds, 4 oscillations equal to 4 unit cells, the growth speed is thus approximately 12.5 seconds per unit cell.

B - Structural characterizations

1 - X-ray reflectivity

Next, crystal characterizations have been carried out by means of X-ray reflectivity (XRR). θ - 2θ scans in reflectivity mode (at grazing incidence) allows to determine the thickness of the films if the film-substrate and the film-surface interface are not too rough. The “low angle Kiessig fringes” apparent in Figure B-1 (a) result from the presence of parallel interfaces with different refraction indices. We call low angles, values typically below 4-5 degrees.

Below an angle, called the critical angle θ_c , the beam is fully reflected. This angle is essentially function of the electronic density of the film. Above θ_c , the X-rays partially penetrate the sample and

may interfere with in-coming X-rays and/or X-rays scattered from a deeper interface. In thin films, there are mainly two interfaces: air / film and film / substrate. Considering the small penetration of lab X-rays (few tens of microns), the contribution from the substrate / air interface can be neglected. Interferences are then directly related to the optical path difference for X-rays reflected at the film / substrate interface and X-rays reflected at the surface of the film.

The optical path difference is $m \lambda = 2 t \sin \omega$ where t is the thickness and ω is the incident angle, m are interference orders. The methodology consists then in subtracting to the bare X-ray reflectivity signal from Figure B-1 (a) a background which can be related to the Fourier transform of the index profile in the heterostructure (cf. Figure B-1 b). Finally, linear interpolation of the interference orders with ω -values enables to extract the actual thickness of the film which was estimated in that specific case (GTO grown on SrLaAlO₄-SLAO) to be 13.9 nm.

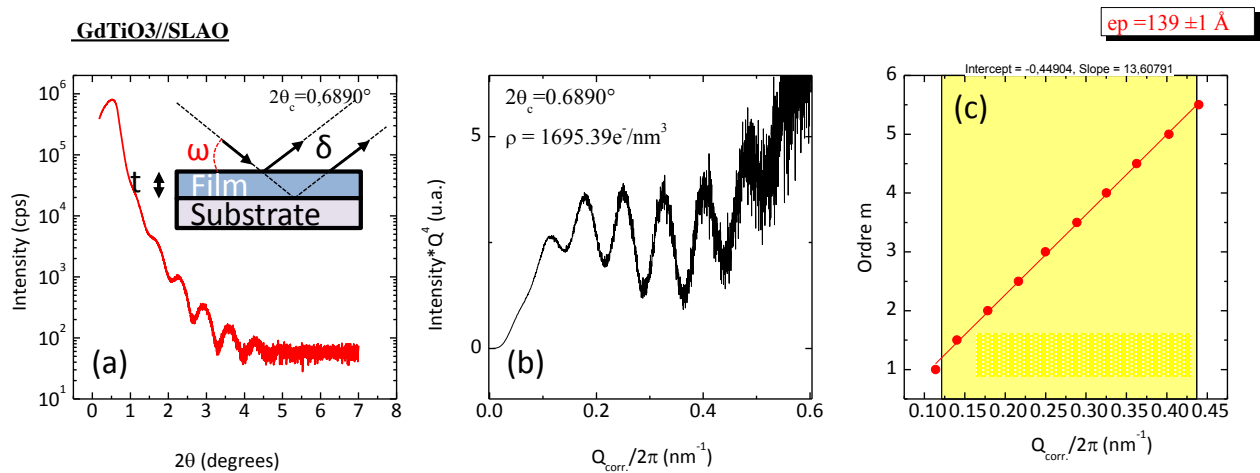


Figure B-1: X-ray reflectivity of a GdTiO₃-thick sample grown on top of SLAO substrate. (b) Extraction of the background intensity decay for an electronic density ρ and a critical angle of 0.689 degrees. (c) fitting of the oscillations for thickness extraction which in case yields 13.9 nm.

2 - X-ray diffraction

At higher angles, the diffraction peak of the film allows one to extract its c-axis parameter using Bragg's law $c_{op} = n \frac{\lambda}{2 \sin \theta_n}$, where n is the order of diffraction and λ , the Cu K- α_1 wavelength, is equal to 1.5406 Å. In Figure B-2 (b), we present an example of different x-ray diffraction patterns of GTO thin films of approximately the same thickness (~ 10 nm). One can see that the substrate peaks are localized at different θ values due to their different out-of-plane lattice constant. This affects the thin-film out-of-plane peak whose value shifts accordingly. This is characteristic of strained films. We can distinguish the 1st order and 2nd order peaks ([001] and [002] reflections), but even more accurate results can be obtained by looking at higher orders (3rd or 4th).

During this Ph.D., X-ray characterizations were performed on a Panalytical Empyrean equipped of a PIXCel detector, and a Ge (220) monochromator. A picture of the set-up is presented in Figure B-2 (a). In order to reach reflections with specific in-plane components the sample stage can rotate along two main directions: χ for tilts perpendicular to the sample holder plane and φ for rotations in the sample holder plane.

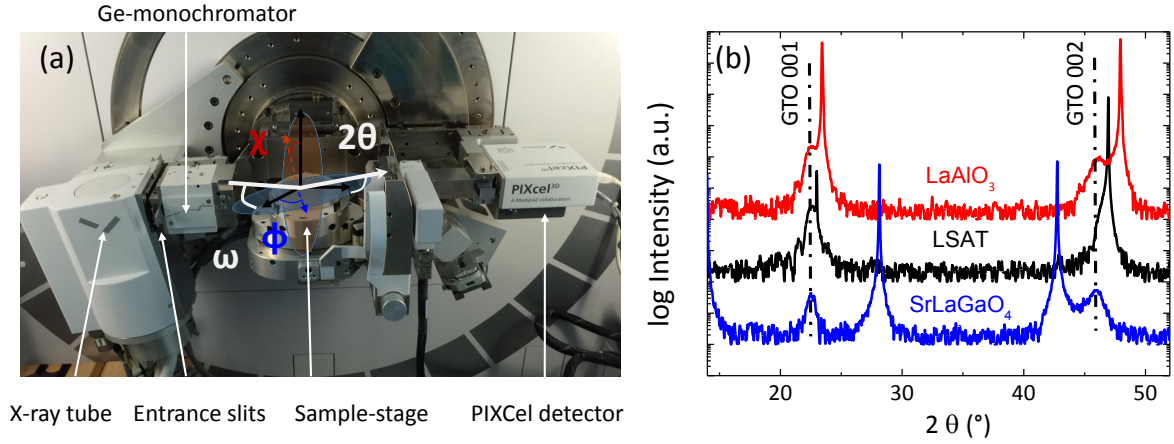


Figure B-2: (a) schematic representation of the angle configuration and presentation of the Empyrean PIXCel diffractometer (b) examples of x-ray diffraction patterns for GdTiO₃ thin films grown onto respectively SLGO (blue), LSAT (black) and LAO (red) substrates.

In order to check whether films are coherently strained on a specific substrate, reciprocal space maps (RSM) are required.

They characterize portions of the reciprocal space displaying reflections with both in-plane and out-of-plane components. These areas are obtained from θ - 2θ scans at different ω values. From this map in (θ, ω) -coordinates, one can represent the reciprocal space by transforming (θ, ω) -coordinates in $(q_{\parallel}, q_{\perp})$ -coordinates according to:

$$q_{\parallel} = \sin \theta \sin (\theta - \omega)$$

$$q_{\perp} = \sin \theta \cos (\theta - \omega)$$

In Figure B-3 (b), we see an example of a reciprocal space map for a SLGO substrate (lower part) and a GTO thin film (upper part). The in-plane lattice parameter of the film (Q_x value) is identical in both. This indicates that the film is fully strained to the substrate.

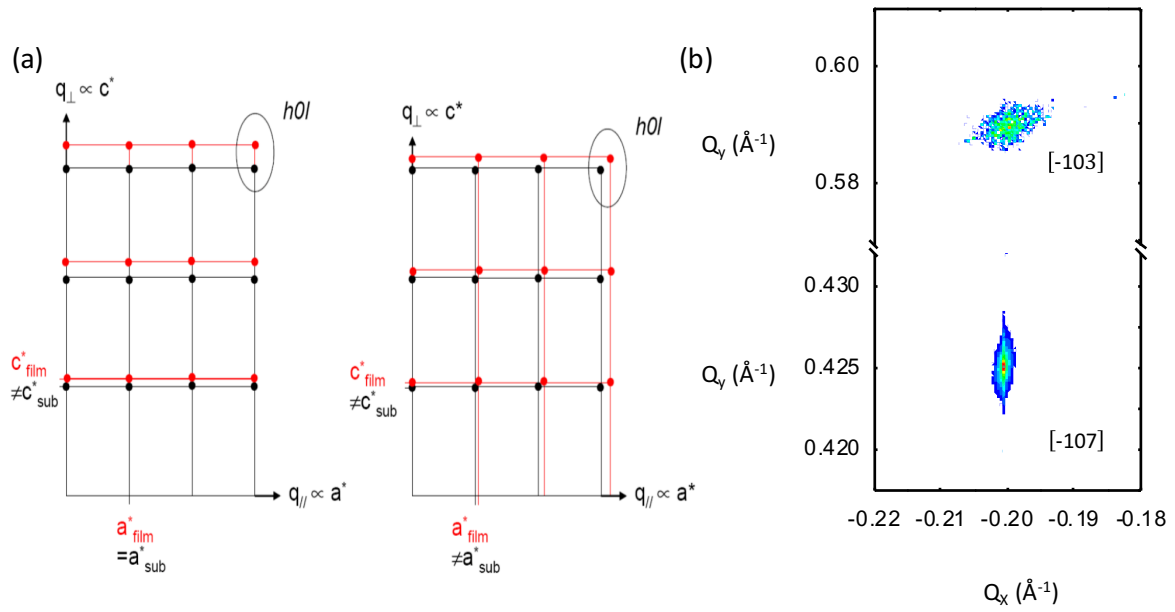


Figure B-3: (a) schematic understanding of strain in terms of reciprocal space maps (b) reciprocal space map of [-107] SLGO peak and [-103] GTO peak

C - Physical characterizations

We performed transport measurements by patterning electrodes following Van-Der-Pauw methodology. The electrode (mostly Au and Pt) were deposited by sputtering. Measurements were carried out using an electrometer and a voltage source because of the high level of resistivity in all our samples of RTiO_3 . We mounted up an entirely new setup in which Labview-interfaced magneto-transport measurements were performed (cf. Figure C-1). The setup is composed of a cryogenic helium gas compressor (allowing temperature ranging from 4 K to 350 K), a current control 1 T-magnet wired around the cryostat with a Gaussmeter feedback-loop. The magnet can be oriented in all directions in a plane parallel to the sample surface thanks to a step-by-step motor. The probe allows Hall, and longitudinal magneto-transport up to 1 T.

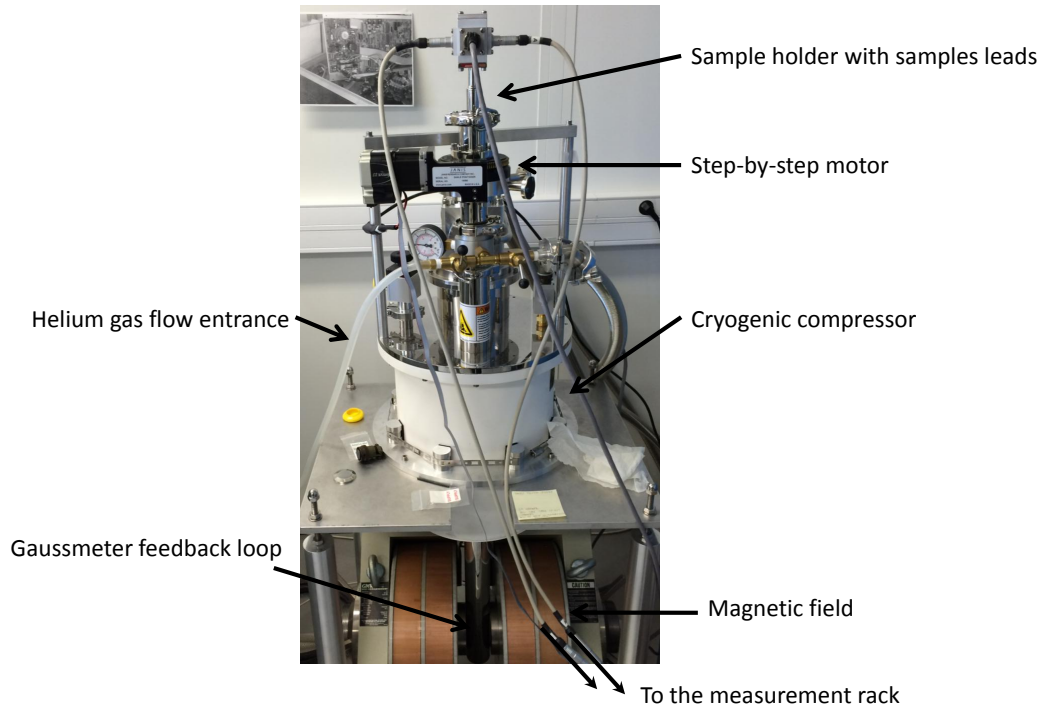


Figure C-1: cryogenic magneto-transport measurement setup mounted and used during the Ph.D.

Magnetometry was performed in a conventional Quantum Design 5 T-SQUID magnetometer.

D - Synchrotron radiation-based techniques

During this Ph.D., we have been using extensively synchrotron radiation-based spectroscopy techniques. The first one is X-ray absorption spectroscopy (XAS) and the second is photoemission spectroscopy (PES).

X-ray spectroscopy is one of the best techniques to determine the electronic, chemical and crystallographic structure of materials. In spectroscopic experiments, a monochromatic light is shined onto the sample. X-ray photoemission (XPS) or X-ray absorption spectroscopy (XAS) use x-rays with energies of several hundred eV or keV.

In order to obtain reliable results, a spectroscopic experiment requires an ultra-high vacuum environment ($\approx 10^{-10}$ mbar), as the surface of the sample can easily react with the residual gas in the chamber. Other options are either to clean or cleave *in situ* the sample, or to protect the sample with ultrathin capping layers (Au, Pt, amorphous LAO, were preferred in our specific case). Higher X-ray energies may be used to penetrate deeper in the sample to probe buried regions. For soft X-rays (from 300 – 1500 eV), the penetration depth is of the order of tens of nanometers.

1 - X-ray absorption spectroscopy

Absorption spectroscopy (XAS) and its derivatives, circular dichroism (XMCD) and linear dichroism (XLD), will be used thoroughly in this manuscript. This spectroscopy enables to probe the chemical and structural environment of our samples. When X-ray beams hit the sample, atoms comprising the samples absorb X-ray photons with sufficient energy: there is absorption of an X-ray photon and emission of an electron. This process yields edges in the absorption spectra for each photon energy that corresponds to the energy difference between the probed level and an upper empty level. These edges are strongly dependent on the absorber but also on its environment and on the multiplet structure (number of electrons, coordination, bonds, symmetries). We call K -edge excitations of $1s$ electron, and L_2 and L_3 excitations from $2p$ electrons. M_4 and M_5 transitions from $3d$ electrons. In this work, we mainly focused on O K -edge, rare-earth M -edges, and transition metal L -edges (cf. left panel Figure D-1).

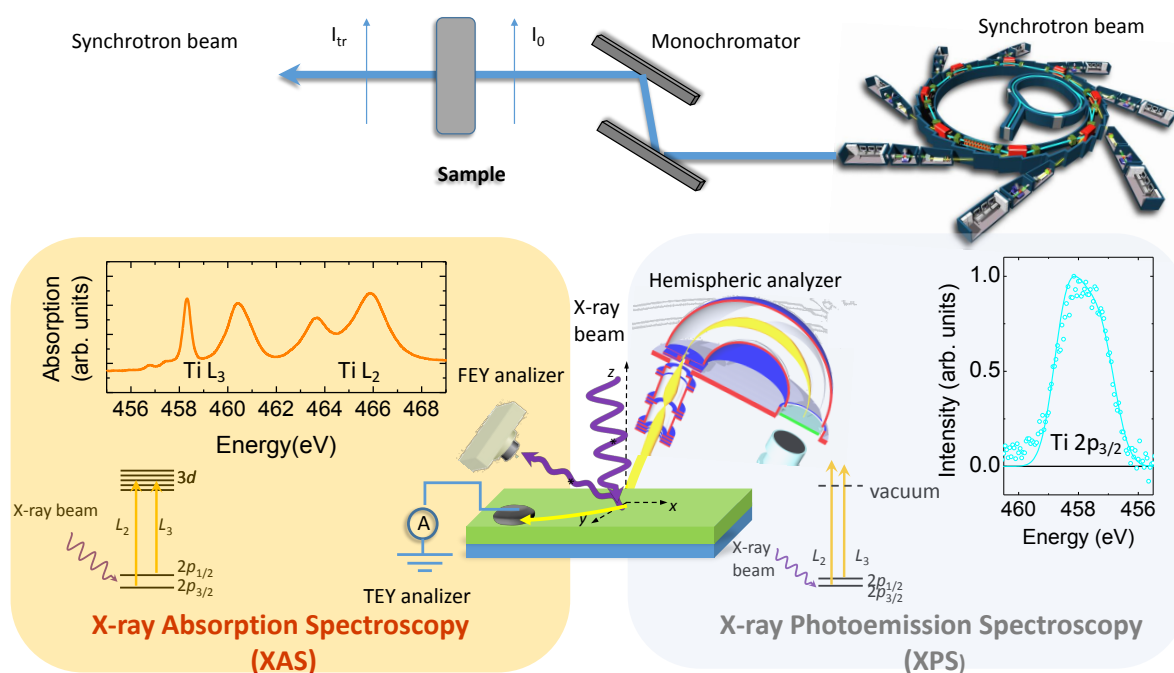


Figure D-1: upper panels: schematic presentation of the synchrotron facility and end stations. Lower panels: sketches of synchrotron radiation-based spectroscopy techniques (left) X-ray absorption spectroscopy with experimental Ti L -edge XAS spectrum and (right) schematic description of X-ray photoemission spectroscopy and experimental Ti $2p_{3/2}$ spectrum.

It is also possible to linearly or circularly polarize the incident light. The difference of left and right-circularly polarized light is called circular dichroism. This difference can give access to the orbital moment and spin moment of the probed element. Linear dichroism between vertical and horizontal polarization probes any anisotropy of the charge distribution.

In this work, the absorption experiments presented in chapter IV and V were performed at the electron storage ring of the Helmholtz-Zentrum Berlin (HZB) by using the 70 kOe high-field end station located at the UE46-PGM1 beamline [30], while those presented in chapter III were acquired at the electron storage ring of SOLEIL in Paris, using the 70 kOe high-field end station located at the DEIMOS beamline [31].

During this work, spectra were obtained across the Ti and Ni $L_{3,2}$ edges as well as across the O K and rare-earth (Gd, La, Nd, Sm) $M_{5,4}$ edges. Absorption experiments (XAS) were performed at normal incidence. The signal can be recorded either by means of total electron yield (TEY) detection, which collects photoelectrons formed upon absorption or by means of reflection experiments (scattering), which collects photons proportional to the recombination of the excitonic states. The probing depth varies depending on the technique used to record the signal. Reflection experiments were done in a $\Theta/2\Theta$ geometry for which the samples (in chapter V) were placed at an incidence angle of $\Theta = 19^\circ$ with respect to the incoming propagation direction. This was used to acquire deeply buried Ni or Ti $L_{2,3}$ edges with increased sensitivity. XAS spectra were background corrected at the pre-edge of the L-edge and then renormalized at the post-edge. The O K -edge signal was also background corrected at the pre-edge and renormalized at its post-edge (550 eV).

2 - Sum rules

a) For X-ray magnetic circular dichroism

By circularly-polarizing the X-ray light, it is possible to qualitatively probe the spin and orbital moment, in certain cases - when the L_2 and L_3 edges are separated enough - it becomes possible to perform quantitative analysis. This is done by applying the so-called “sum-rules” [32,33].

From the absorption cross section for right circularly (μ_+) or left (μ_-) circularly polarization, we can estimate the isotropic cross section according to the following formula:

$$\mu_{iso} = \frac{\mu_+ + \mu_-}{2}$$

which also corresponds to the cross section of non-polarized X-ray light. XMCD signal can be deduced from μ_+ and μ_- by the following formula:

$$\mu_{XMCD} = \frac{\mu_- - \mu_+}{2\tau}$$

where τ accounts for the polarization of the incident beam that we would take equal to 1 in the following (as it is for both beamlines nearly 100 %). At $L_{2,3}$ edges, we can apply sum rules in order to calculate the spin moment M_s and the orbital moment M_o from the μ_+ and μ_- spectra.

The orbital moment is defined by:

$$M_o = -\mu_B \langle L_z \rangle$$

with $\langle L_z \rangle$ being the average value of the orbital moment operator that can be calculated from different absorption spectra according to:

$$\langle L_z \rangle = -2(10 - n) \frac{\int \mu_{XMCD} dE}{\int \mu_{iso} dE}$$

in this expression, the integral runs over L_3 and L_2 edges, n is the number of d electrons on the 3d orbitals, and $10-n$ is thus equivalent to the number of holes on the 3d bands. In the case of Nickelates (RNO), it is equal to 3 because of the $3d^7$ valence state of Ni in a perovskite environment (cf. chapter IV).

The spin moment is defined by:

$$M_s = -2 \mu_B \langle S_z \rangle$$

with $\langle S_z \rangle$ being the average value of the spin moment operator that can be calculated from different absorption spectra according to:

$$\langle S_z \rangle + \frac{7}{2} \langle T_z \rangle = -\frac{3}{2} (10 - n) \frac{\int \mu_{XMCD} dE - 2 \int_{L_2} \mu_{XMCD} dE}{\int \mu_{iso} dE}$$

That formula is also function of $\langle T_z \rangle$ which we will assume to be much smaller than $\langle S_z \rangle$.

In the end, these sum rules, that will be discussed in the following chapters, allows to compute the full magnetic moment $M_{tot} = M_o - M_s$ for less than half-filled systems such as Nickel.

b) For X-ray linear dichroism

For linearly-polarized X-ray light, there also exists sum-rules [34,35] quantifying the orbital occupation of e_g states. We will use them in chapter IV when dealing with orbital occupancy of rare-earth nickelates. This sum rule relates the total integrated intensity of the polarized spectra (along x or z) to the hole occupancy in $d_{x^2-y^2}$ and d_{z^2} e_g -orbitals:

$$R = \frac{h_{z^2}}{h_{x^2-y^2}} = \frac{3 \int I_z dE}{4 \int I_x dE - \int I_z dE}$$

In this expression, h designates the number of holes in $d_{x^2-y^2}$ and d_{z^2} orbitals. The integral in the previous expression runs over L_2+L_3 edge. The polarization of the number of electrons occupying the e_g -orbitals, $P = \frac{n_{x^2-y^2} - n_{z^2}}{n_{x^2-y^2} + n_{z^2}}$, is then expressed following:

$$P = \left(\frac{4}{n_{e_g}} - 1 \right) \frac{R - 1}{R + 1}$$

Here, n designates the number of electrons in e_g -orbitals.

3 - X-ray photoemission spectroscopy

Photoemission spectroscopy (PES), contrary to XAS, is a measure of emitted electrons that are ejected from electronic levels of the sample to the vacuum. This happens only if the photon energy is equal to or greater than the binding energy. The measured spectra consist of multiple peaks that correspond either to well-defined core levels or to valence bands. As in XAS, the peak width is a convolution of broadenings due to electron lifetime and instrumental resolution. PES is a powerful technique to study the electronic structure of correlated materials, as it probed excitations of the ground state (cf. previous chapter). By analyzing and comparing spectra in the energy range from several meV up to several hundreds of eV, one can obtain direct information about the valence of core levels electrons, or the valence band structure of the Fermi level electrons, and even, the presence of internal build-in electric fields (cf. chapter V). Throughout the course of this Ph.D., we conducted hard x-ray photoemission spectroscopy (HXPS) experiments at the GALAXIES beamline in SOLEIL, Paris [36]. The photon energy was set at 2300 eV and the binding energy scale was calibrated using the Fermi edge of the sample at 2295 eV. The overall resolution was better than 250 meV and all measurements were done at room temperature. A Shirley background was subtracted from every core-level spectrum. In the angle dependent measurements, the angle versus depth photon field magnitude (cf. chapter V) was computed using YRXO software [37], taking into account the experimental geometry and the bilayer optical properties at 2300 eV for linearly polarized light.

Both absorption or photoemission processes remove electrons from the near surface of the studied sample which consequently charge the sample positively. In metals, this does not affect the measurements as the charge can quickly be screened. This is not the case, however, for insulators in which progressive charging leads to distortions of the spectra or large energy shifts of the expected

core-level peak positions. Therefore, using X-ray spectroscopy experiments to probe oxides, which are often insulating by essence, is not straight-forward. Finally, the non-ideality of our samples, that always present some distributed defects (sometimes created by the beam itself), generally provides a non-zero conduction which is often sufficient to limit the charging of the surface. Again metallic capping (such as Au, or Pt) can help prevent the negative effects of charging mechanism. Although capping layers are useful as oxidation and anti-charging shields, a compromise needs to be found to allow the photon to penetrate deep enough into the sample to probe the relevant properties. This can reveal quite challenging when the desired properties are buried interfacial ones as in our case (cf. chapter V).

After this overview of the experimental techniques used in this manuscript, we go on to the study of rare-earth titanates, RTiO_3 .

III. Rare-earth titanates

In this chapter, we will first perform a short review of the main results concerning rare-earth titanates at the moment where this PhD started. Second, we will present our own study on single crystals of GdTiO_3 . Then, after examining the first results on the growth of titanates thin-films by pulsed laser deposition, we will study how strain engineering is affecting their crystal structure and growth orientation.

A - State-of-the art

In the first section, we will review structural, electronic, and magnetic properties of titanate bulk crystals prior to reviewing thin film properties.

1 - Bulk single crystals

a) Structural properties

The structure of rare-earth titanates differs from the ideal cubic space group $Pm-3m$ by the presence of additional distortions that lower the symmetry from cubic to orthorhombic. As we saw in the first chapter of this manuscript, when the tolerance factor of a material is smaller than 1, the size of the A cation (here the rare-earth) pushes on the oxygen octahedra cages and forces them to

slightly tilt. RTiO_3 (RTO) display tolerance factors from 0.8 to 0.92 depending on the size of the R cation (cf. Figure A-1 b). Following Glazer's pioneering work on distortions in oxides [38], the rare-earth titanates have a specific tilting pattern compatible with the RTO orthorhombic $Pbnm$ space group symmetries, labelled $a^-a^+c^+$. This Glazer's notation means that, along the $\langle 100 \rangle$ and $\langle 010 \rangle$ directions, neighboring TiO_6 octahedra rotate out-of-phase, while they turn in-phase along the $\langle 001 \rangle$ direction (cf. Figure A-1 a). The direct relationship between cubic and orthorhombic coordinates is thus a 45 degrees rotation in the (a,b)-plane, accompanied by a $\sqrt{2}$ -enlargement in the a and b directions and a doubling along the c-direction. Figure A-1 (b) shows that rotations decrease for larger tolerance factors. Indeed, as the tolerance factor is increased, the structure goes more and more cubic forbidding the presence of oxygen distortions. This trend is naturally followed by an increase of the volume (cf. Figure A-1 c) as the R cation becomes bigger from Lu to La.

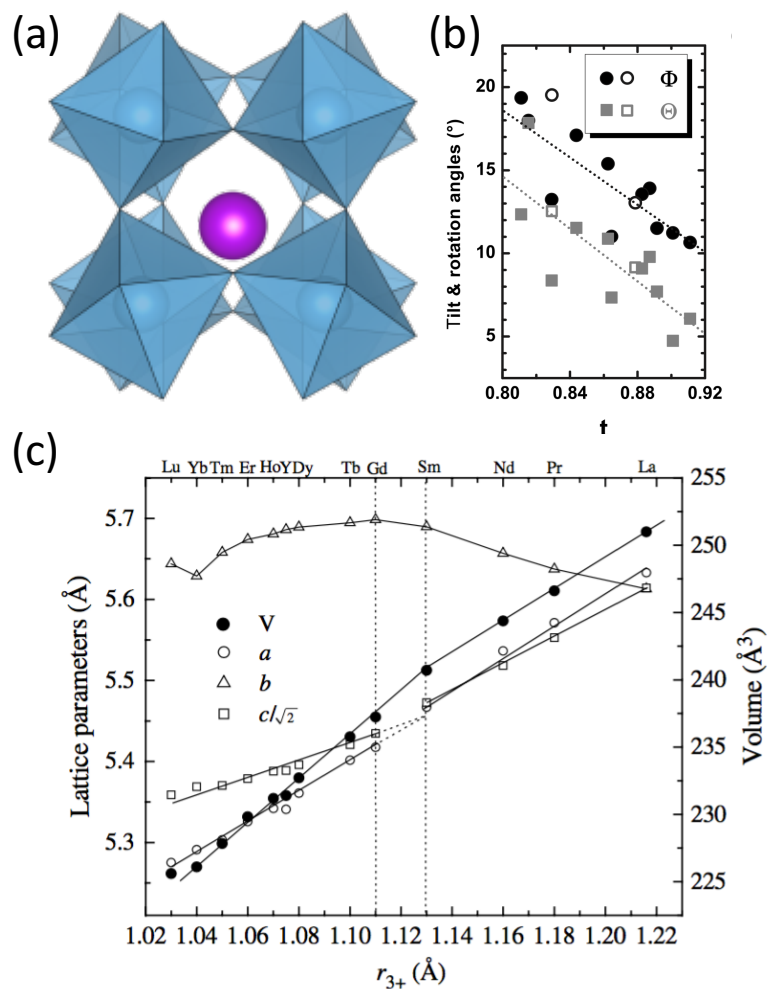


Figure A-1: (a) RTiO_3 typical crystallographic structure (b) tilts and rotation angles as a function of the tolerance factor (c) variation of the crystallographic lattice parameters as a function of the ionic radii. Figure (b) and (c) are adapted from [39,40]

b) Transport properties

From the point of view of its transport properties, RTO is a prototypical Mott insulator (cf. chapter I). In these compounds, Ti is trivalent ($3d^1$) with only one filled t_{2g} band out of the threefold degenerated t_{2g} orbitals.

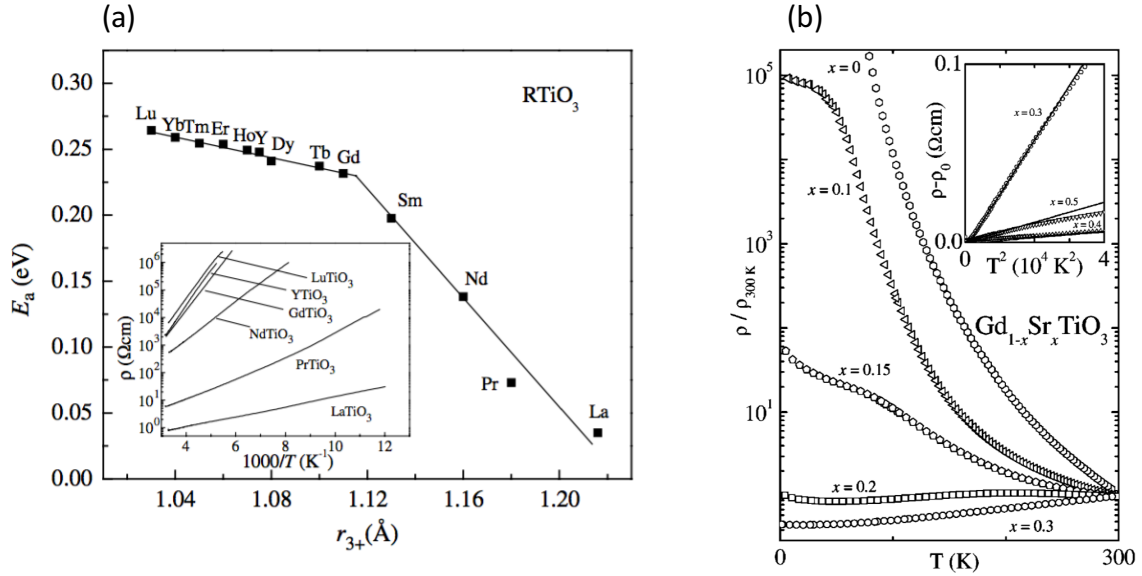


Figure A-2: (a) activation energy as a function of the ionic radius from [40] (b) temperature-dependent resistivity curves as a function of the doping level from [41] Inset present the quadratic temperature-dependence of the resistivity as a function of the doping level

As we explored in the introduction on correlated matter (chapter I), Mott insulators exhibit insulating behaviors even at half-filling. In terms of transport properties, they can be viewed as conventional semiconductors with a thermally-activated resistivity $\rho(T) \sim \exp(E_a/kT)$, where E_a is the activation energy. Goodenough et al. measured this activation energy as a function of the R-cation in [40]. We report their results in Figure A-2 (a). The activation energy decreases from Lu to Gd from 0.26 eV to 0.23 eV. Beyond Gd, the activation energy keeps decreasing with increasing the rare-earth ionic radius but with a larger slope. The activation energy for LaTiO_3 (LTO) is around 0.035 eV.

Noteworthy, the kink in the activation energy reminds the one in the volume data of Figure A-1 (c). Goodenough et al. proposed that that this correlation between the activation energy of the mobile carriers and the volume pointed toward polaronic activation of trapped cation vacancies [40]. From thermoelectric-power measurements [42], they showed that LTO presented a hole-type conduction coupled to clusters comprising multiple Ti atoms. The data presented in Figure A-2 (a) are consistent with a cluster size that decreases progressively with the size of the rare-earth ions and thus with distortions. Interestingly, this also suggests that defects and distortions couple on much

larger scales than one unit-cell.

Following on this idea of distortion-dependent polaronic hole conduction, Figure A-2 (b) reports on the sensitivity of the transport properties in GdTiO_3 upon hole doping [41]. Indeed, under 20 % of Sr-doping in GTO, samples undergo a metal-to-insulator transition (MIT) that is quite abrupt. With increasing the Sr-doping level, the resistivity strongly decreases and a MIT occurs for $x=0.2$. This is typical of the expected filling-dependent MIT in Mott materials (cf. Chapter I). Within a concentration range between $x=0.3$ and $x=0.5$, the resistivity obeys roughly a quadratic temperature dependence, which is demonstrated in the inset of Figure A-2 (b). The observed quadratic temperature dependence, instead of the usual phonon contribution that is scaling with T^5 , is typical of electron-electron scattering and only observable if the effective mass of the electrons is strongly enhanced due to electronic correlations such as in heavy-fermion systems. At Sr-concentrations larger than $x=0.6$, the system becomes gradually insulating, approaching conventional band insulators, like SrTiO_3 .

c) Magnetic properties

Finally, the RTiO_3 family is very unique due to its very peculiar magnetic properties. For small rare-earth ($R < \text{Gd}$), rare-earth titanates present a ferromagnetic behavior. The hysteretic M-H curves in Figure A-3 (a) shows the dependence of the magnetization at 5 K as a function of the rare-earth. If the saturation magnetization is smaller in LuTiO_3 ($0.9 \mu_{\text{B}}/\text{Ti}$) or YTiO_3 ($0.8 \mu_{\text{B}}/\text{Ti}$), than in GdTiO_3 ($6 \mu_{\text{B}}/\text{Ti}$), a puzzling feature of RTiO_3 is that neither the saturation moment nor the Curie temperature T_{C} (Figure A-3 c) varies systematically with the rare-earth size.

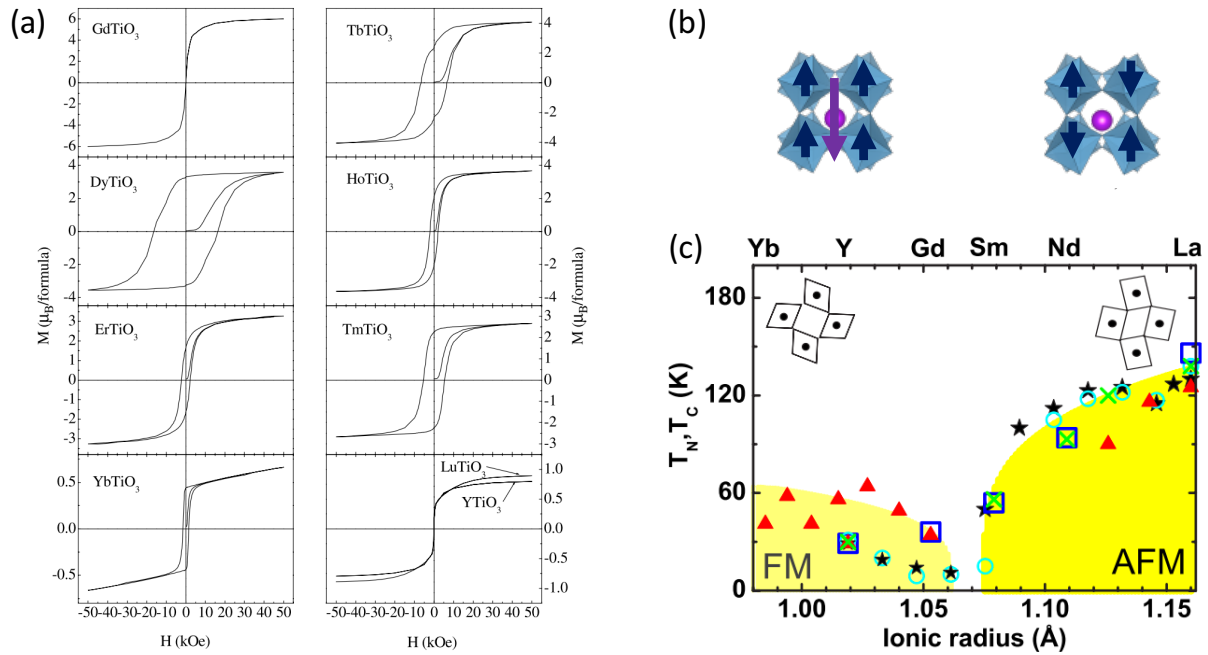


Figure A-3: (a) field-dependent hysteresis curves from [40] (b) GdTiO_3 crystal structure with ferromagnetic (left) and G-type antiferromagnetic (right) structures (c) magnetic phase diagram with the critical temperature (T_N or T_C) as a function of the ionic radius of the rare-earth from [39].

Taking the specific example of GTO, the saturation magnetization would correspond to full spin-only ferrimagnetism, that could originate from a 5d-3d Gd–O–Ti superexchange-interaction [43] that would both raise T_C and fully magnetize the TiO_3 array. But if this scenario applies to all ferromagnetic RTO compounds, one would expect the T_C to follow the distortion amplitude that controls super-exchange paths, which is contradictory to what is observed in Figure A-3. It has been claimed that the absence of trend may be due to the strong orbital moment of the rare-earths [40]. However, M – H curves of polycrystalline samples show no evidence of a large magneto-crystalline anisotropy that would be present in case of a strong orbital moment of the rare-earths coupled to the Ti sub-lattice. Note that this does not hold for DyTiO_3 where the coercive field is around 2 T, with an opposite behavior compared to GTO.

For larger rare-earth ions - thus smaller distortions - the situation is radically different, and the Ti-sublattice is antiferromagnetically ordered. LTO, for example, shows a G-type AFM (AFM G) ground state (cf. Figure A-3 b), in which Ti-spins are aligned antiferromagnetically in all x, y and z directions. The Néel temperature (T_N) is about 130 K. With increasing GdFeO_3 -type distortion, T_N decreases and is strongly suppressed at SmTiO_3 . The magnetic phase diagram is reproduced in Figure A-3 (c). To our knowledge, this volume driven magnetic phase transition is unique among perovskite oxides.

Here again, the origin of this transition, and of both magnetic orders, have remained

controversial over the years. Indeed, magnetic properties in transition metal oxides generally results from the delicate interplay between lattice, charge, spin and orbital degrees of freedom, which has been formalized in the Goodenough-Kanamori-Anderson (GKA) framework. In short, GKA rules are based on the assumptions that the orientation of orbitals on neighboring sites controls the exchange interaction between magnetic ions [4]. While most experiments on transition metal oxides are in accordance with this paradigm, it does not apply to the titanate phase diagram.

Over the last decade, a tremendous amount of work [44–50] has been devoted to measuring the orbital degeneracy and magnetic moment in rare-earth titanates single crystals. Indeed, additionally to the issues raised previously (absence of trend in the magnetization, origin of the magnetic order, etc.), rare-earth titanates can be considered as a perfect playground to study the intriguing interplay between orbital, electronic and spin degrees of freedom.

These open problems are particularly striking in the case of the least distorted titanate, LTO where the appearance of an AFM magnetic state is puzzling if one suspects orbital degeneracy. Two models have been proposed:

- one claims that the t_{2g} splitting is sufficiently small to allow for orbital fluctuations yielding unquenched orbital moment [51]
- the other pretends that these fluctuations are suppressed by distortions, leading to a vanishingly small orbital moment [44,49].

In LTO, the orbital moment was experimentally found to be vanishingly small, supporting the second scenario. However, the ordered spin moment was only $0.46 \mu_B$ [52], which is much smaller than the value of $1 \mu_B$ expected for a single electron with quenched orbital moment. Quantum fluctuations, plus spin orbit coupling, could explain this reduction.

Nevertheless, neutron scattering experiments [53] have shown an isotropic spin-wave spectrum with a small spin-gap, which is incompatible with the expected spin-orbit induced anisotropy. Apart from LTO, the Ti spin moment in the ferromagnetic $YTiO_3$ (YTO) was also estimated by polarized neutron diffraction to be relatively small ($\sim 0.6 \mu_B$) [50] but, again, no orbital moment could be detected. Most studies so far were conducted on RTO compounds in which the ion at the A site does not carry any spin or orbital moment [54–56]. Surprisingly, direct and simultaneous experimental measurements of orbital and spin moments in other RTO compounds have been missing. In the second part of this chapter, we will try to contribute to this debate by making use of XAS combined with X-ray magnetic circular dichroism (XMCD) to characterize the spin and orbital moments of GTO single crystals, which sits at the border of the AFM to FM transition.

2 - Thin films of GdTiO₃

a) Thin films grown by hybrid MBE

At the beginning of this Ph.D. work, very few studies reported the growth of titanate thin films. Only Stemmer's group at U.C Santa Barbara had been able to successfully grow GdTiO₃ thin films [57,58]. In these studies, GTO thin films were grown on [001]-oriented (LaAlO₃)_{0.3}(Sr₂AlTaO₆)_{0.7} (LSAT) substrates and then capped by STO by hybrid MBE. This method combines solid source evaporation as in conventional MBE with metal-organic sources [59–61]. The Sr and Gd cations were provided to the substrate by evaporating metal sources while Ti was supplied with a metal organic precursor, titanium tetraisopropoxide (TTIP, SigmaAldrich99.999%). TTIP was also the only source of oxygen to ensure growth of the perovskite phase rather than pyrochlore (Gd₂Ti₂O₇). The substrate temperature was set to 950 °C.

This method allows to reach a very high growth quality that was probed by means of transmission electron microscopy (TEM). The TEM side view is presented in Figure A-4 (a).

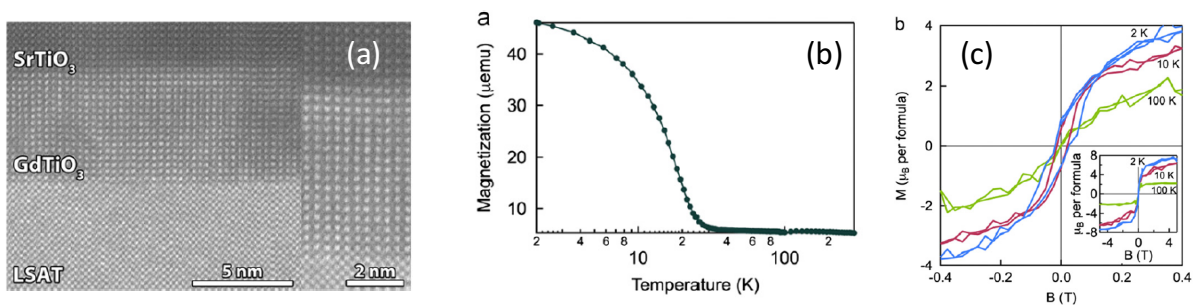


Figure A-4: (a) HAADF-STEM image of an 8 nm-GdTiO₃ film grown on LSAT and capped with SrTiO₃. Magnetic characterization of this film as a function of the temperature (b) as a function of the applied magnetic field (c). Figures (a-c) are adapted from [58].

The magnetic characterizations of the as-grown thin films reveal properties very close to those of the bulk with a T_C of about 32 K. The M-H curves present a saturation values which are much smaller than in the bulk but for larger coercive fields. This may be explained by the presence of superparamagnetic clusters with mixed valence states (Ti⁴⁺-Ti³⁺). Finally, transport properties also recall semiconductor-like activated behavior alike bulk materials.

b) Properties under doping

Stemmer's group then investigated the effect of doping in titanates. Either by doping STO with Gd or the opposite. We report results from various studies in Figure A-5.

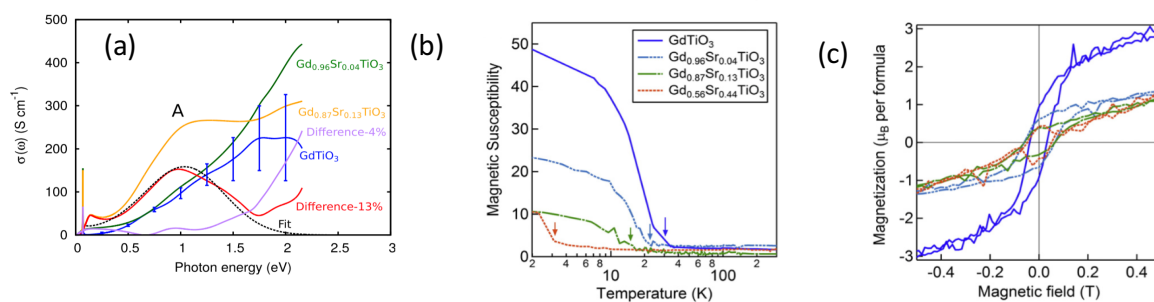


Figure A-5: (a) optical conductivity as a function of photon energy for different doping level adapted from [62]. Temperature (b) and field (c)-dependent magnetization curves for GTO and several Sr-doping level. (b-c) are adapted from [63]

In Figure A-5 (a), one can see that the optical conductivity, that measures the gap, is affected by the presence of Sr-dopants. The gap is reduced by more than 0.5 eV with the presence of only 4 % Sr-dopants. According to the authors, this mechanism arises from the sensitivity of GTO to small polaron hopping that increases dramatically the conductivity of the materials for small defects concentration.

Interestingly, Sr-doping also induces a diminution of the ferromagnetic properties of GTO. The critical temperature and saturation magnetization are killed for less than 50 % Sr-doping (cf. Figure A-5 b-c). Note that STO is expected to present a small ferromagnetic contribution at extremely low temperatures under doping.

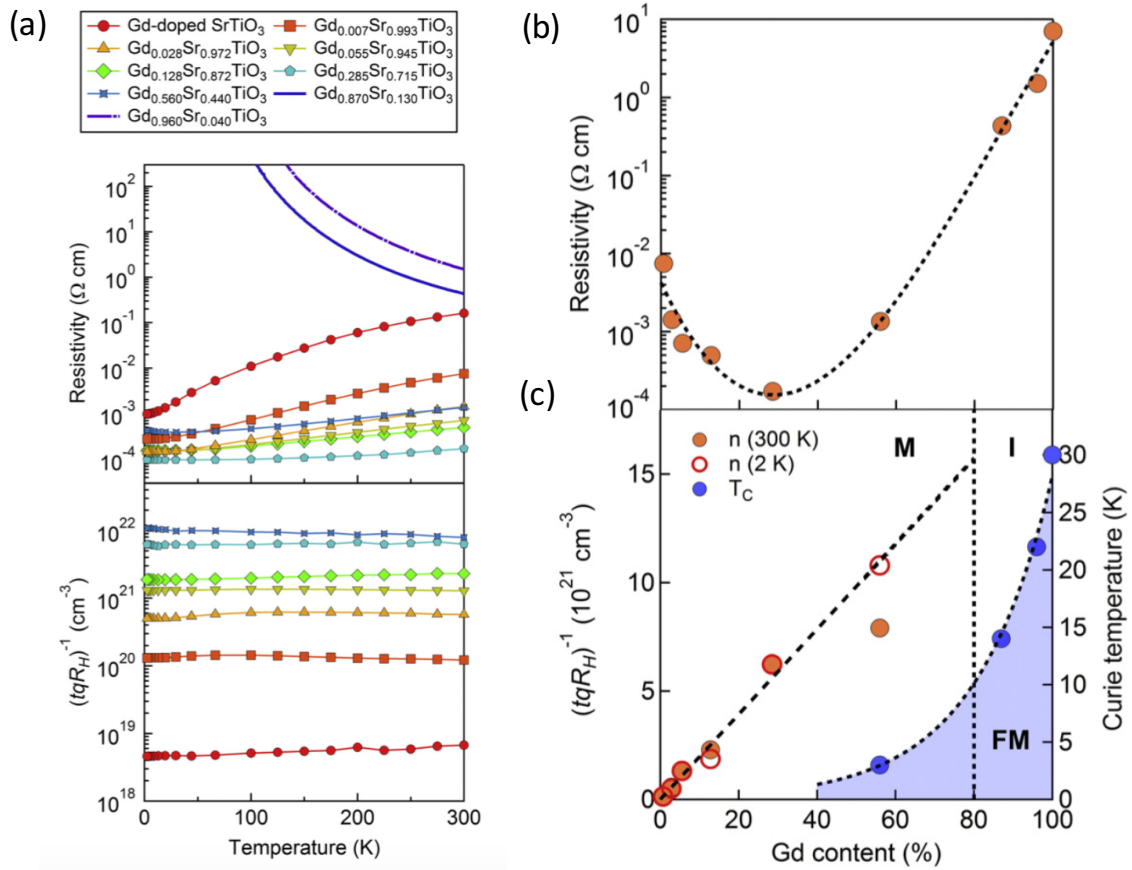


Figure A-6: (a) transport properties for different temperatures and different doping levels. (b) Evolution of the resistivity as a function of the Gd-content (%) (c) mobility and Curie temperature for different Gd content (%) adapted from [63]

Additionally, transport properties are also modified by the presence of Sr-dopants (cf. Figure A-6 a). 20 % of Sr-doping is already enough to go from a strong activated behavior to a bad metallic one. These results remind the ones of the bulk that we reported in Figure A-2 (c). Figure A-6 (b-c) present a phase diagram for different Gd-contents in STO (or oppositely of Sr-content in GTO), we observe that the resistivity drops down by 6 orders of magnitude for 40 % of Gd content before recovering. This effect is a signature of correlated transport in GTO. While for low Sr-doping levels, the system retains the effect of correlation, for high-concentration, it behaves essentially as a band insulator. For intermediate filling level, the system acts as a fermi-liquid with enhanced electron-masses. Figure A-6 (c) reports how magnetism vanishes as the proportion of Sr is increased. This is expected from the paramagnetic Ti^{4+} - nature of Ti ions surrounded by Sr defects. However, one can notice that the magnetic decay is not linear, showing that the interplay between bandwidth, correlation and magnetism is critical in this system.

c) Confinement and thickness-dependent effect in RTO thin films

Finally, confinement and thickness-dependent properties of GTO thin films were also studied by Stemmer's group [64]. They observed that reducing film-thickness induced a strong reduction of the ferromagnetic properties that become vanishingly small for 2 nm-thick sample. Similarly, the magnetization saturation decreases. However, the coercive fields goes oppositely as it increases very strongly with decreasing the thickness of the sample (cf. Figure A-7 a and b).

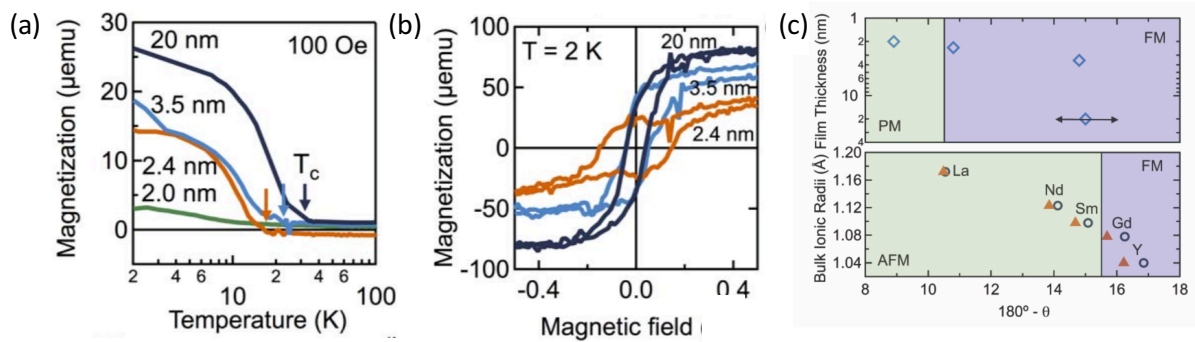


Figure A-7: Magnetization curves as a function of temperature(a) and magnetic field (b) for samples with GTO films of various thicknesses (c) Magnetic phase diagram of GTO thin films for different thicknesses (upper panel) and deviation angle compared with different RTO bulk ionic radii and their corresponding deviation angle (bottom panel). Figure are adapted from [64]

The authors of this study [64] suggest that this reduction of the ferromagnetic properties was linked to a concomitant closing of the deviation angle measured in confined samples between STO-buffer and STO-capping layers. This deviation angle quantifies the GdFeO_3 distortion which is believed to play a major role in the ferromagnetic ground state of large rare-earth. Yet, the paramagnetic phase appears for a deviation angle 6 degrees smaller than bulk values, pointing to the role of other degrees of freedom such as the role of the orbital (which can be modified in very thin samples) under confinement.

In the following, we will concentrate on a specific RTO: GdTiO_3 . We will first present results that we obtained on bulk single crystals. Then we will explain how we grow and characterize GTO thin films. Finally, we will also unveil the first study on strain engineering in GTO thin-films.

B - Orbital and spin structure of the ferromagnetic GdTiO_3 single crystal

We focused this chapter section on GTO single crystals. Our study was carried out on GTO samples. The sample were grown by T. Froehlich from Braden's group using the travelling floating-zone image method, Ref. [39]. We then performed many characterizations that are presented below.

1 - Crystal structure

The samples were first analyzed by means of Raman microscopy which allows to observe large scales of the sample surface. We notice inhomogeneities at the surface of the samples (cf. inset Figure B-1). Each of these crystallites could be clearly identified thanks to their Raman spectra (cf. Figure B-1 a-c). Consistent with previous reports on other RTO compounds [45,65–69], we have found that the surface of GTO tends to over-oxidize. The samples were polycrystalline and included small superficial amounts of tetravalent Ti^{4+} pyrochlore $\text{Gd}_2\text{Ti}_2\text{O}_7$ and anatase TiO_2 , but also contained large, poorly crystallized, yet well-oriented, GTO regions.

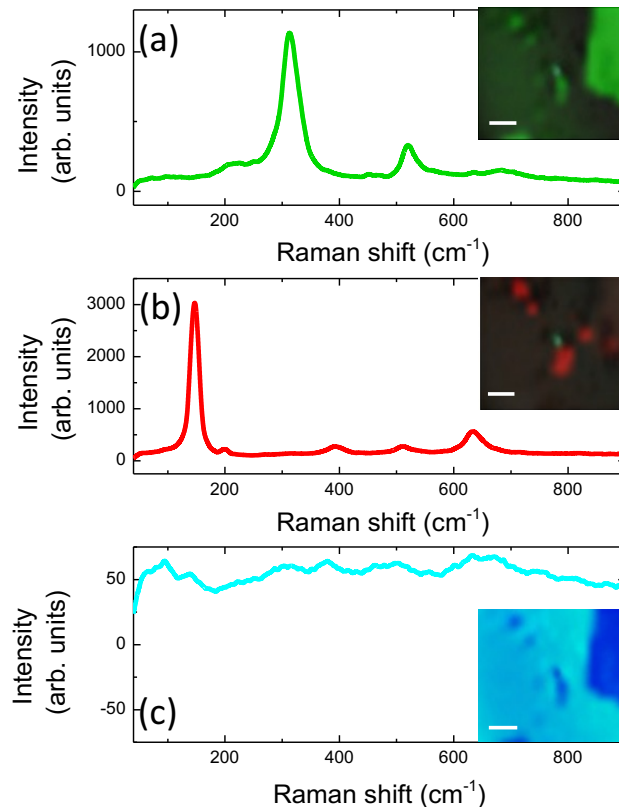


Figure B-1: Raman microscopy scan of the surface of a GTO single crystal (a) $\text{Gd}_2\text{Ti}_2\text{O}_7$ superficial crystallites appearing in green in the inset (b) TiO_2 anatase phase in red in the inset and (c) GTO poorly crystallized in blue in the inset. The white bar stands for $2 \mu\text{m}$.

Next, the zones corresponding to virtually amorphous GTO were characterized by means of high-angle annular dark field (HAADF) imaging and electron energy-loss spectroscopy (EELS) using a JEOL JEM-ARM200cF scanning transmission electron microscope (STEM) operated at 200 kV, and equipped with a probe aberration corrector and a Gatan Quantum EEL spectrometer. The superficial over-oxidation (associated with a lack of crystallinity visible from Raman spectra – Figure B-1 c) was further confirmed. Figure B-2 exhibits spectroscopic data for a region where this effect is particularly pronounced: EEL spectra were acquired as the electron beam was scanned from the edge into the crystal (cf. Figure B-2 a). Figure B-2 (b) displays the Ti $L_{2,3}$ edge down this line scan. A clear, progressive change in spectral shape is noticed when comparing data from well-crystallized GTO below the surface to more defective yet still stoichiometric surface regions (cf. Figure B-2 b).

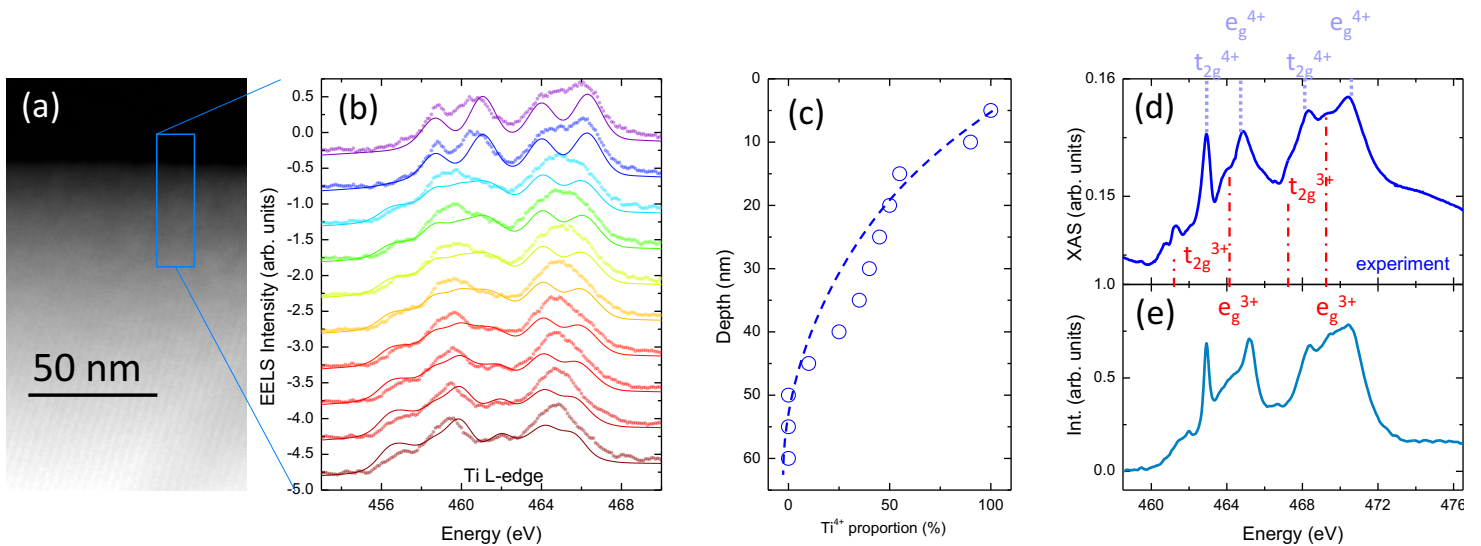


Figure B-2: (a) Low-magnification HAADF image of the GTO crystal. The blue rectangle represents the region where EELS spectra at the Ti $L_{2,3}$ edge (b) were extracted. In (b) the data are shown as symbols and in (b) the fine lines are linear combination of simulations obtained from multiplet calculations. The proportion of Ti^{4+} is shown in (c). A XAS spectrum measured at 10 K is displayed in (d) and its simulation using experimental 3+ and 4+ spectra is presented in (e).

The deepest regions show Ti $L_{2,3}$ spectra resembling those acquired in XAS on $LaTiO_3$ [70,71] and can be well reproduced by simulations, described later in this chapter, using CTM4XAS software [72] (with a spectral broadening of 0.5 eV, accounting for the experimental resolution) and a pure Ti^{3+} state. The most superficial spectra present similarities with data taken on Ti^{4+} compounds such as $SrTiO_3$ [73] and with simulations for a pure Ti^{4+} state. Intermediate spectra can be mimicked by linear combinations of the simulations for Ti^{3+} and Ti^{4+} , yielding estimates of the local Ti valence.

The progressive variation of this Ti oxidation state across the observed area is plotted in Figure B-2 (c). Moreover, the O *K*-edge pre-peak (Figure B-5), whose intensity is proportional to the number of holes in the hybridized Ti-O bond [74], is enhanced at the surface, consistent with a Ti valence closer to 4+ and previous indirect studies [69].

To complement the EELS analysis, we performed XAS in the absence of magnetic field at the DEIMOS beam line of the synchrotron SOLEIL [31]. The sample was cleaved in order to measure a fresh surface prior to introduction in the chamber that was then pumped to reach ultra-high vacuum ($P=10^{-10}$ mbar). The XAS spectrum, reported in Figure B-2 (d), departs from the Ti^{3+} EELS spectrum of Figure B-2 (b) (bottom curves), which, as also found in *e.g.* [65], reflects some over-oxidation of the sample surface after cleaving. Accordingly, the data can be reproduced by a linear combination of a Ti^{3+} reference and the XAS of a STO crystal (Ti^{4+} reference), cf. Figure B-2 (e). The best agreement is found for about 45% of Ti^{4+} and 55% of Ti^{3+} . Remarkably, the position of the t_{2g} and e_g peaks associated to Ti^{4+} are well separated from the Ti^{3+} ones (cf. labels on Figure B-2 d).

From these measurements, we could clearly identify stoichiometric buried zones in which we performed higher resolution HAADF imaging hoping to carefully resolve the intrinsic distortions of GTO.

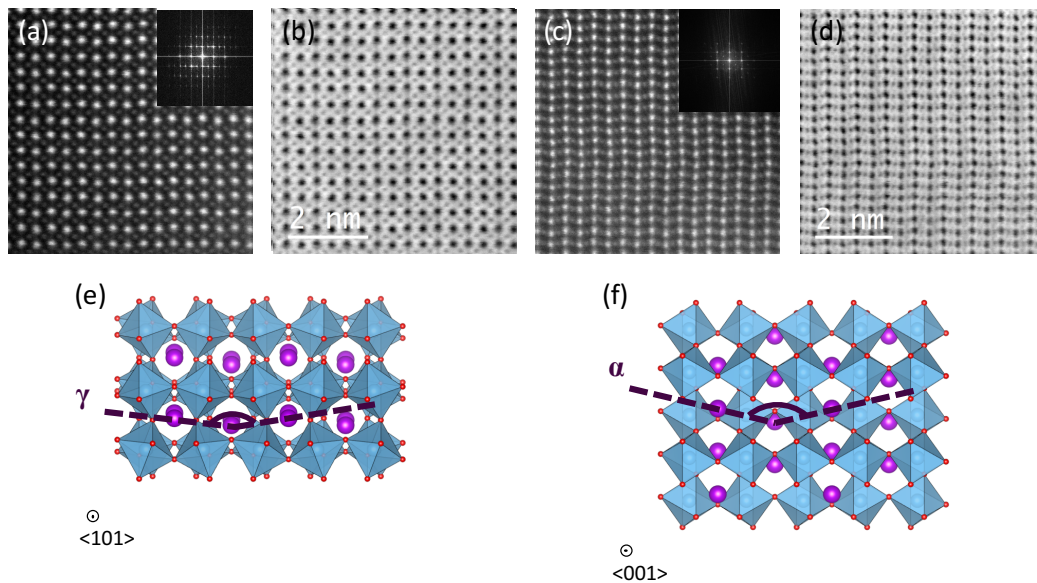


Figure B-3: (a) HAADF images of the GTO crystal oriented along the $\langle 101 \rangle$ direction (a) and the $\langle 001 \rangle$ direction (b) Fast Fourier transform images are shown in inset. Please note that some spatial drift is present. Bottom panels present the GTO crystal structure along the $\langle 101 \rangle$ direction (c) and the $\langle 001 \rangle$ directions (d).

Figure B-3 shows the structural properties of one of such zones. We present observations of the GTO crystal along the $\langle 101 \rangle$ (Figure B-3 a-b) and $\langle 001 \rangle$ (Figure B-3 c-d) directions. Their respective fast Fourier transform (FFT) images extracted from the same regions are shown in the

insets and account for the orthorhombic symmetry lowering with respect to the pseudocubic phase. The tilting of the octahedral cage, corresponding to the complex pattern of the $Pbnm$ structure – $a\bar{a}c^+$ in Glazer's notation [38] – is sketched in Figure B-3 (e) and Figure B-3 (f). The atomic column coordinates were measured using an iterative process, looking for the center of mass of the Gd columns in the HAADF images of Figure B-3 (a) and (c). The extracted averaged values of the deviation angles, $180-\alpha$ and $180-\gamma$, are respectively 18° and 13° . Based on these, we can extract the off-centering of the rare-earth ions to be around 0.25 \AA and conclude that the Ti-O-Ti angle is about 143.7° , close from other values reported in the literature [39,75]. We also acquired EEL spectra including the Ti $L_{2,3}$ and O K edges on the bulk region (cf. Figure B-5). From these spectra we can estimate a relative Ti:O ratio of 1:3 using the routines implemented in the Digital Micrograph suite. This value is in line with the nominal composition of GTO.

2 - Magnetism at low temperature

We now turn to the magnetic properties of our sample. We measured XMCD at 10 K at the Ti $L_{2,3}$ and Gd $M_{4,5}$ edges in total electron yield (TEY). XMCD was recorded from the difference between left (dark curve in Figure B-4 a and c) and right (light curve in Figure B-4 a and c) circularly polarized light at 45 degrees with respect to the normal incidence. The two XMCD spectra are presented in Figure B-4 (b) for Gd and in Figure B-4 (d) for Ti after normalization to the highest intensity in the average XAS signal (shown in Figure B-4 (a) for Gd and in Figure B-4 (c) for Ti).

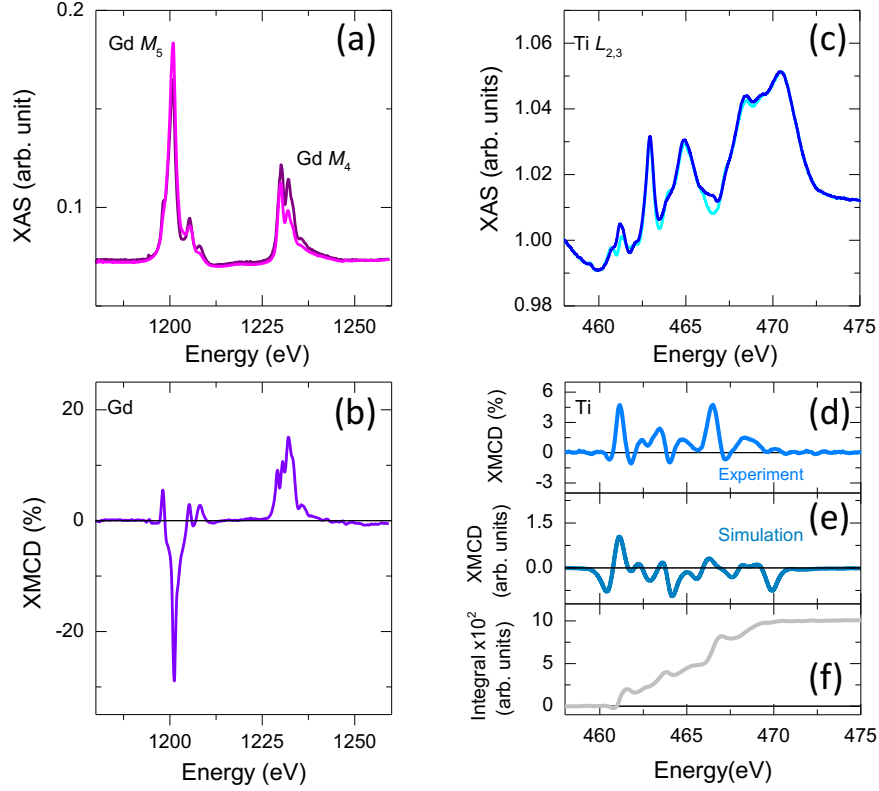


Figure B-4: XAS at the Gd $M_{4,5}$ (a) and Ti $L_{2,3}$ (b) edges recorded in total electron yield (TEY) for left (dark colours) and right (light colours) circularly polarized light. The incoming light is 45 degrees, with respect to the normal incidence of the film. An in-plane magnetic field of 1 T is applied. XMCD signals acquired at the Gd M-edges in (b) and at Ti L-edge in (d) with its integrated signal (f). The XMCD signals are renormalized with the edge jump acquired at 1200 eV for the Gd and at 464 eV for the Ti. Simulation of the XMCD experimental signal is presented in (e).

We note that the shape of the XMCD signal departs from that found at SrTiO₃-based interfaces [76–78], where the polar catastrophe also induces trivalent ferromagnetic-like Ti spins, suggesting that the mechanisms polarizing the Ti spins are different. The opposite sign of the XMCD signal at the L_3 and M_5 edge for both species demonstrates that Ti and Gd are antiferromagnetically coupled, as previously suspected [39,40,43,79–81]. Additionally, the two magnetic ions present strong XMCD (of the order of 7% for Ti and -24% for Gd) consistent with ferromagnetic ordering in both sub-lattices and an alignment of the Gd in the direction of the field.

The Ti XMCD spectra are full of relevant information concerning both the magnetic and electronic structure of titanates, such as the orbital and spin moments, or the energy splitting of the 3d orbitals that can be revealed by using “sum-rules” [82] (cf. chapter II). However, the large overlap between Ti L_3 and L_2 edge does not allow to apply them reliably [83,84] and impedes any accurate determination of the spin moment. Nonetheless, if quantitative analysis of the spin moment seems out of the way, qualitative understanding of the alignment and amplitude of the orbital moment may still rely on the analysis of the XMCD cumulative integral to which it is directly proportional. The

integrated XMCD signal displayed in Figure B-4 (f) is non-zero, which thus clearly indicates the existence of an orbital moment at the Ti ions. Due to both the large charging effects in the absorption experiment, and the sizeable L_2/L_3 -multiplet overlap, any quantitative extraction of the actual orbital moment is impossible.

This orbital moment differs from previous experiments in LTO and YTO, which claimed that the orbital moment was virtually quenched. This also indicates a finite spin-orbit coupling at play in GTO. For symmetry reasons, the matrix element of the orbital momentum operator acting on the t_{2g} orbitals is zero. The presence of an unambiguous orbital moment constitutes direct evidence that orbital degeneracy is not entirely lifted (which would otherwise result in a complete quenching of the orbital moment as argued in [44,71,85]) and confirms some claim found in Ref. [86]. Moreover, an antiparallel alignment of L and S is expected from Hund's third rule, assigning a positive value to the coupling constant and thus a minimum value of the J moment ($J=|L-S|$) to shells that, as it is the case here, are less than half-filled.

3 - Electronic structure

To gain insight into the electronic structure of GTO, we have performed multiplet calculations using CTM4XAS [72]. We find that a reasonable fit of the XMCD data (cf. Figure B-4 (e), light gray curve) is obtained for values of the distorted C_4 crystal field, parameterized by $10Dq = 2.2$ eV, $Dt = -0.007$ eV and $Ds = 0.073$ eV, leading to an orbital splitting of the order of 250 meV, in very close agreement to recent findings obtained from resonant inelastic X-ray scattering, infrared measurements and Raman scattering [45,48,87,88] in YTO. Note that this is surprisingly large considering the presence of a concomitant orbital moment. In [71], Haverkort et al. considered that the crystal field splitting needed to be smaller than 120 meV to explain a orbital moment, a value that would clearly not account for the measured XMCD spectra.

To comfort the simulated energy splitting, we looked at the distortion extracted from HRSTEM in Figure A-4, which yields approximately 15° . Mizokawa et al. [89] predicted that a large $GdFeO_3$ -distortion ($> 10^\circ$) would tend to stabilize a "d-type Jahn-Teller"-like over trigonal distortion, leading precisely to the energy hierarchy observed in our simulation. Finally, the best agreement with experimental data was obtained by introducing a small charge transfer of type $3d^2L$ between the oxygen ligand and the Ti ions characterized by $\Delta = 2.65$ eV and $U_{pd} - U_{dd} = 2$ eV. This ligand hole state is noticeable from the pre-peak of the O K -edge spectra (cf. Figure B-5) that clearly shows the presence of holes in the hybridized Ti-O band.

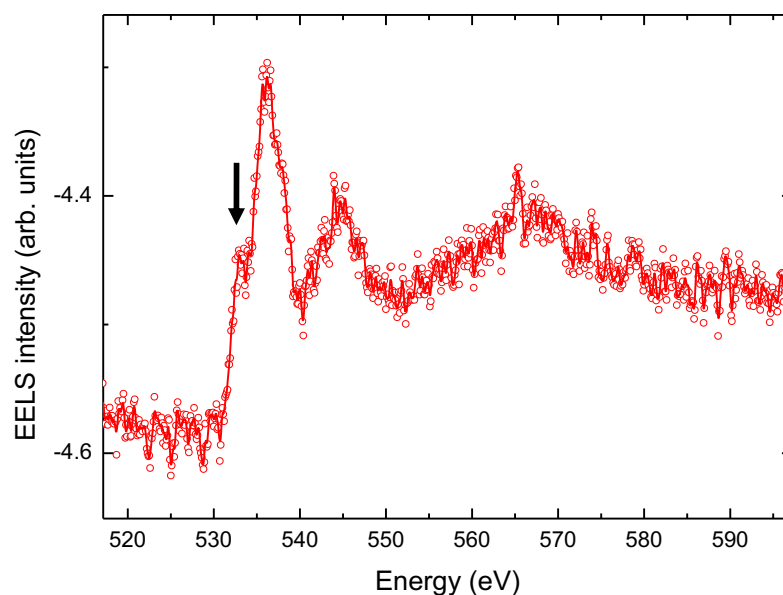


Figure B-5 : EELS at the O K-edge for a buried highly crystalline $GdTiO_3$ region. The O-K edge pre-peak is highlighted by the black arrow.

4 - Field dependence of Ti magnetism

Last, we turn to the field dependence of the Ti XMCD. In Figure B-6 (a-d), we display XMCD spectra at -2 T, -0.1 T, and 0.1 T, 2 T. Spectral features reverse when flipping the field from -2 T to 2 T. In Figure B-6 (e), we present the magnetic field dependence of the Ti XMCD obtained by tracking the most intense peak around 461 eV. The shape of this field dependence resemble the one obtained by previous SQUID studies [43]. The very weak magnetic anisotropy (that did not seem to depend on the sample orientation) of the Ti sub- lattice (< 0.5 T) suggests a small spin-orbit coupling at least weaker than 10 meV, 20 times smaller than the amplitude observed “Jahn-Teller”-like distortion.

In conventional descriptions of the 3d orbitals in octahedral environments, the only reason for the appearance of a orbital moment is that the spin-orbit splitting competes with the structurally-induced one. But considering the relatively weak spin-orbit coupling compared to the amplitude of the “Jahn-Teller” -like distortion, this is clearly not the case here.

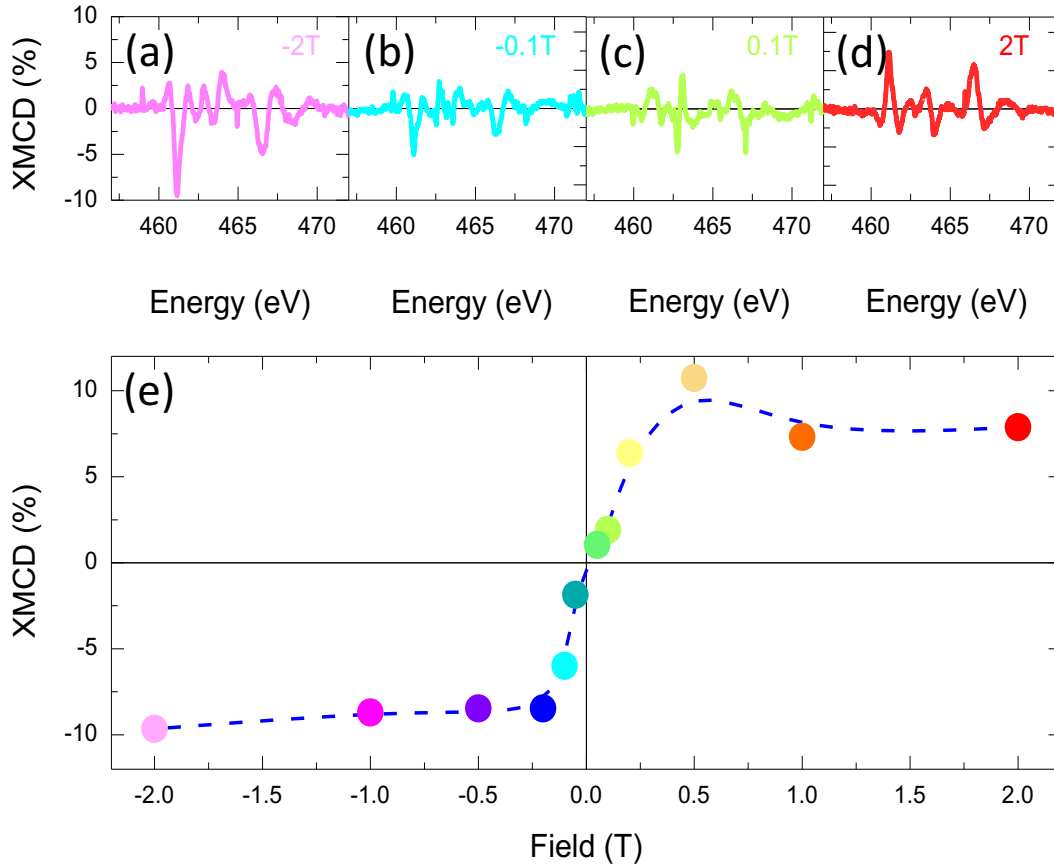


Figure B-6: XMCD acquired at 10 K at the Ti $L_{2,3}$ edge at -2 T (a), -0.1 T (b), 0.1 T (c), and 2 T (d). (e) Field dependence of the Ti XMCD peak at 461 eV. Magnetic field (f) and temperature (g) dependence of the magnetization obtained by SQUID.

Thus, in order to account for the unambiguous presence of an orbital moment, measured through the integration of the XMCD signal, we need to resolve to a more complex orbital structure than the one considered so far. Indeed, unquenched orbital moments may come from strong oxygen hybridization and large rare-earth crystal fields, known to play a crucial role in determining orbital occupancy of the electronic degrees of freedom for smaller rare-earth titanates and for YTiO_3 [44]. The proposed ground state in [44] is an orbitally-unquenched combination of the three t_{2g} orbitals that leads to the formation of a orbital moment. The authors calculated similar energy splittings as the ones we measured, mimicking a “d-Jahn-Teller”-like distortion, although the spin orbit coupling remained very small. This scenario in view of all the experimental evidences seems to be the most plausible.

In summary of this section, we have been able to directly measure the orbital and spin contributions of GTO by means of XMCD. By comparing multiplet simulations and STEM-EELS characterizations, we could emphasize the role of the different distortions on the spin-orbital ordering structure, mimicking the presence of a “d Jahn-Teller” like distortion. We were also able to directly observe the antiferromagnetic coupling between the Gd and Ti sub-lattices. Interestingly, the

small anisotropy of the magnetic field dependence of the XMCD signal points to a virtually vanishing spin-orbit interaction, whereas the XMCD integral supports a rather large one. All this can be eventually reconciled considering a complex orbitally-unquenched combination of the different cubic t_{2g} orbitals, as proposed by Pavarini et al. [44].

These features observed in the single crystal constitutes a good starting point for the study of GTO thin films that will be the main topics of the next sections.

C - Pulsed laser deposition of $GdTiO_3$ thin films and its characterization

Growing GTO thin-films has revealed more complicated than it looked at first. Of course, our own study of the growth of GTO thin film has been in part inspired by Stemmer's group work – that we reported in the second part of this chapter introduction.

However, before describing our own work, we need to highlight a few intrinsic difference between our own growth setup and theirs [58,90]:

- Substrates can be heated to temperatures higher than 1500°C in Stemmer's system, whereas our substrate heater can only reach a maximum 800°C .
- Our ablation laser is a tripled Nd:YAG for ablation and the technique is essentially an out-of-equilibrium, high rate deposition techniques, whereas theirs is a low speed, low energy deposition technique (in shuttered mode).
- Oxygen can be controlled independently (contrary to us) from the other cation sources as oxygen is provided by TTIP only.
- In our PLD setup, the base pressure is limited to 10^{-6} mbar whereas theirs is set by hybrid MEB ultra-high vacuum condition and can be as low as 10^{-10} mbar

1 - Growing titanate thin films

Base pressure is indeed a key parameter, as the growth of stoichiometric $RTiO_3$ thin films is particularly challenging due to the unstable valence of Ti^{3+} ions in an oxygen-rich atmosphere. Typically, the pyrochlore $Gd_2Ti_2O_7$ phase is synthesized more easily than the perovskite GTO. In bulk form, the tendency to superficially oxidized was also observed and presented in the last section of this work.

Here, films were grown first on $\langle 001 \rangle$ -oriented $SrLaGaO_4$ (SLGO) substrates with an in-plane lattice parameter $a_{ip} \sim 3.852 \text{ \AA}$ by PLD from a stoichiometric pyrochlore target using a Nd:YAG laser at 355 nm (cf. chapter II). Prior to deposition, the substrates were cleaned up with acetone in an ultrasound bath for 5 min before being placed in an isopropanol bath for another 5 min. In the

chamber, the SLGO crystals were heated by a resistive wire under an oxygen pressure of 0.4 mbar up to the deposition temperature. Then, the pressure was lowered to the deposition value.

The structure of the films was monitored during growth using in situ reflection high energy electron diffraction (RHEED). After growth, the films were further characterized by XRD using a Panalytical Empyrean equipped with a Ge (220) monochromator and a PIXcel detector.

A series of films were grown at a constant fluence of 1.1 J/cm^2 while changing the temperature and oxygen pressure in order to establish the growth window of single phase GTO. After deposition, the films were cooled down to room temperature at a constant rate in the growth O_2 partial pressure.

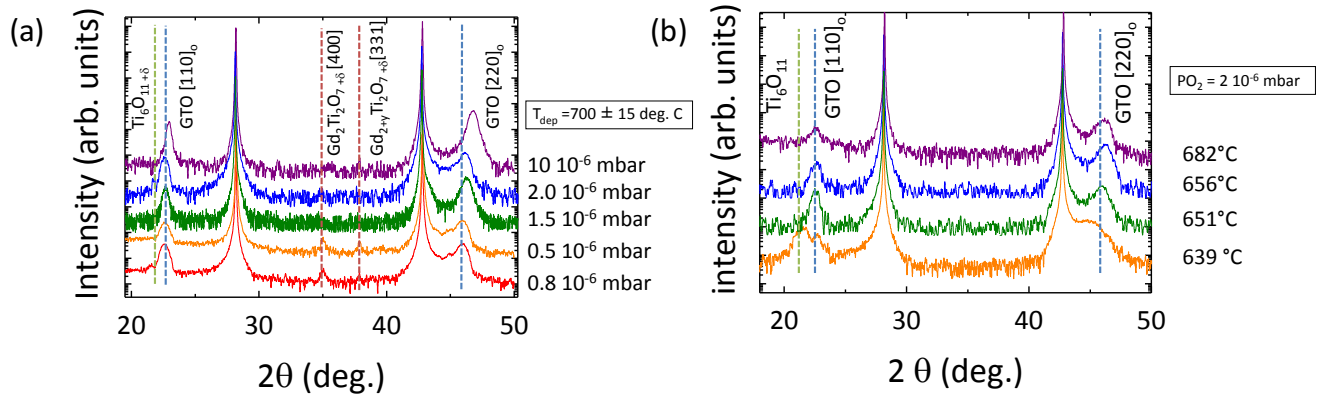


Figure C-1: XRD diagrams of 15 nm thick GTO films grown at 1.1 J/cm^2 and (a) constant temperature and varying pressure, and (b) constant pressure and varying temperature.

Figure C-1 (a) and (b) present XRD spectra for samples grown at constant temperature while varying pressure and at constant pressure while varying temperature, respectively. We find that the pure pyrochlore ($\text{Gd}_2\text{Ti}_2\text{O}_7$) phase is stabilized at low temperature and/or low oxygen partial pressure, as highlighted by the vertical dotted red lines. Upon increasing pressure and temperature to $\text{PO}_2=10^{-6} \text{ mbar}$ and $T=650^\circ\text{C}$, the pure GTO phase is stabilized (vertical blue lines). Spurious Magnnelli phases like Ti_6O_{11} (vertical green lines) are also found near $\text{PO}_2=10^{-6} \text{ mbar}$.

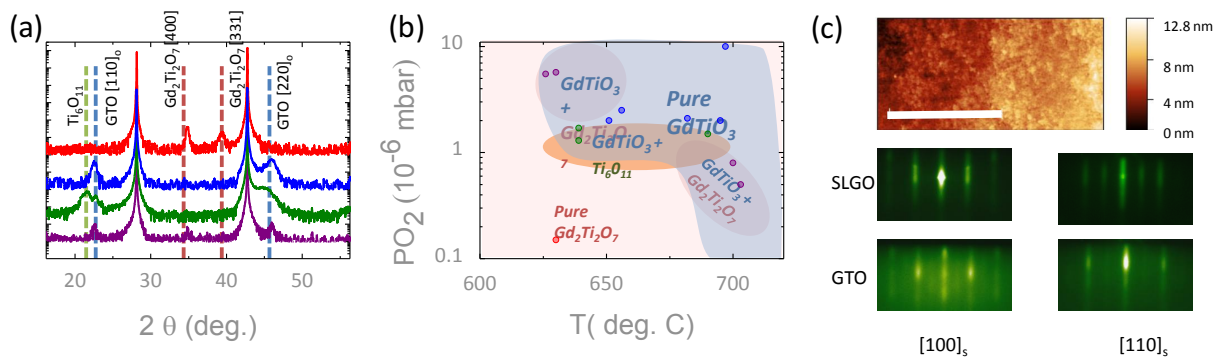


Figure C-2: (a) XRD diagrams of the different phases identified during the growth optimization. Growth conditions from top to bottom: $PO_2=0.15 \cdot 10^{-6}$ mbar $T=630$ °C, $PO_2=2 \cdot 10^{-6}$ mbar $T=660$ °C, $PO_2=2 \cdot 10^{-6}$ mbar $T=640$ °C, $PO_2=5.5 \cdot 10^{-6}$ mbar $T=630$ °C. (b) Phase diagram summarizing the growth optimization as a function of pressure and temperature for a fluence of 1.1 J/cm^2 . (c) atomic force microscopy image of a 15 nm-thick film and RHEED images of the SLGO substrate before and after deposition of a GTO film, at 0° and 45° azimuthal angles from the $[100]$ direction of $GdTiO_3$.

Figure C-2 (a) gathers XRD spectra displaying the whole variety of phases encountered during the optimization. The temperature-pressure phase diagram of Figure C-2 (b) summarizes these results. In Figure C-2 (c), we present some characterizations of the surface quality of our films at the end of the growth. As it can be observed, the RHEED patterns are still clearly visible displaying all the features of a virtually 2D surface for a 15 nm-thick film. The top panel of Figure C-2 (c) shows an atomic force microscopy (AFM) image of a film. Atomic steps and terraces are visible, on top of a wavier structure. The roughness (Ra) of such single phase GTO films is typically 1–2 nm.

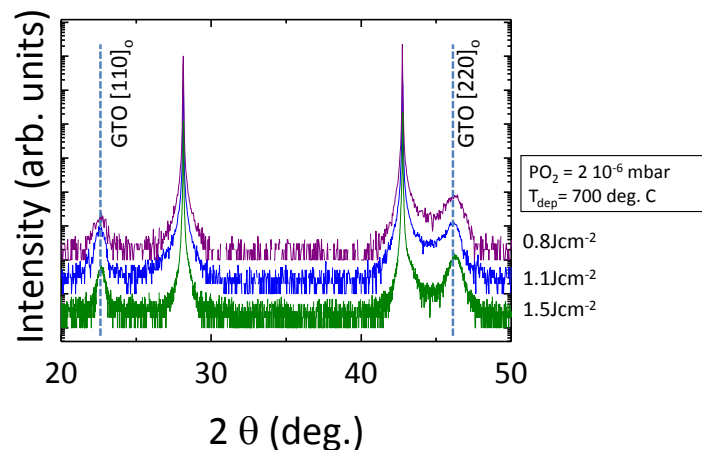


Figure C-3: XRD diagrams of films grown at the same pressure and temperature and different fluence values.

Figure C-3 presents XRD data of films grown at optimal pressure and temperature, while varying the laser fluence. All films are single phase and the out-of-plane parameter remains unchanged. The data thus suggest that, as the stoichiometry of GTO is concerned, pressure and temperature are the main driving parameters, with laser fluence playing a less prominent role.

2 - Growth orientation

Due to the strongly distorted orthorhombic unit cell of GTO, it is not straightforward to predict the most favorable growth orientation on $\langle 001 \rangle_s$ SLGO (where the subscript *s* refers to the substrate). Two possibilities exist with either the $\langle 001 \rangle_o$ or the $\langle 110 \rangle_o$ GTO axis parallel to the substrate normal (here the *o* subscript refers to the orthorhombic unit cell of GTO). In Figure C-4, we present the different growth orientations ($\langle 110 \rangle_o$ and $\langle 001 \rangle_o$ respectively) along with their epitaxial relationships and visualizations. If the film grows along $\langle 110 \rangle_o$ (Figure C-4 a) the $\langle -110 \rangle_o$ and $\langle 001 \rangle_o$ directions lie in the plane of the substrate (Figure C-4 b and d) and in fully-strained films the lattice vector along these directions equal to $2a_{ip}$, where a_{ip} is the in-plane substrate parameter. Although the lattice vector along the diagonal $\langle -110 \rangle_o$ is fixed to the substrate, the ratio a^f/b^f (where the subscript *f* refers to film) is free to change since it can easily be accommodated by the tilting of the TiO_6 octahedra (Figure C-4 a) and a consequent change of the angle α or β as represented in Figure C-4 (c). On the other hand, if the film grows along $\langle 001 \rangle_o$ (Figure C-4 e), the constraints are that a^f and b^f must be equal to $\sqrt{2}a_{ip}$ (Figure C-4 h).

For both growth orientations, two different in-plane strain values can be considered:

- For the $\langle 110 \rangle_o$ -growth direction, one can define a strain state along the *c* direction of the orthorhombic unit cells ($\langle 001 \rangle_o$) as $\epsilon_1 = \frac{2a_{ip}-c}{c}$ and another strain state corresponding to the diagonal direction ($[1-10]_o$) $\epsilon_2 = \frac{2a_{ip}-\sqrt{a^2+b^2}}{(\sqrt{a^2+b^2})}$.
- In the case of the $\langle 001 \rangle_o$ -oriented growth, one obtains the *a* and *b* parameters of the film lying in the plane but rotated by 45 degree with respect to the in-plane parameters of the substrate. This yields the following strain states: $\epsilon_1 = \frac{\sqrt{2}a_{ip}-a}{a}$ and $\epsilon_2 = \frac{\sqrt{2}a_{ip}-b}{b}$.

Calculated in this way, the average in-plane misfit strain is -3% for the $\langle 001 \rangle_o$ -oriented growth and -1% for $\langle 110 \rangle_o$. Thus, to minimize elastic energy the film should grow with the $\langle 110 \rangle_o$ axis parallel to the SLGO substrate normal $\langle 001 \rangle_s$. Such an orientation has already been observed in *Pnma* systems such as CaTiO_3 and is referred to as *ab-ePnma* [91] for which the *c* axis lies in the plane while *a* and *b* are tilted out of the plane, as schematically shown in Figure C-4 (a) and (c).

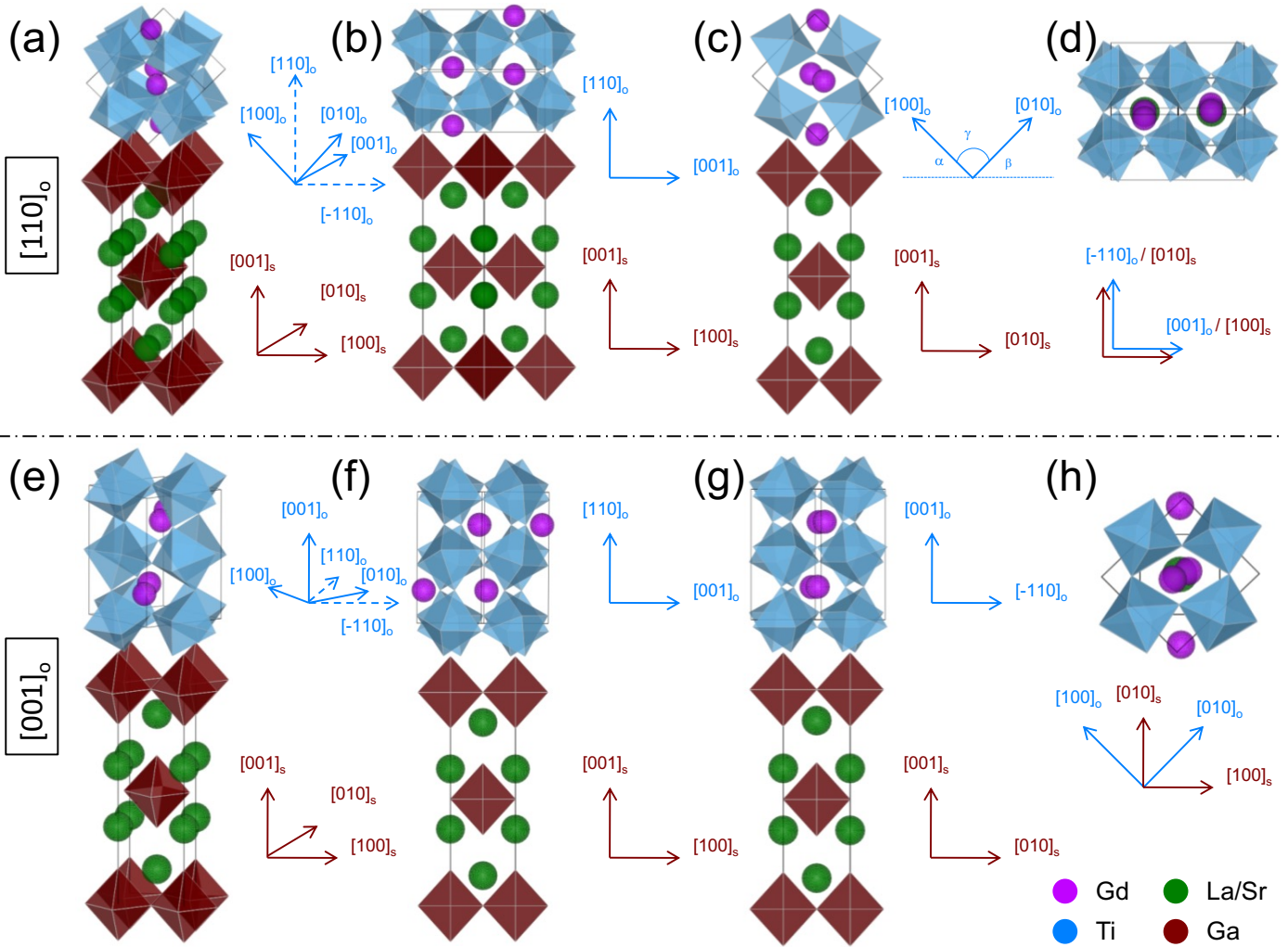


Figure C-4: Sketches of the GTO orthorhombic unit cell growing onto $[001]_s$ -oriented SLGO in the $\langle 110 \rangle_o$ -orientation (a)-(d) or the $\langle 001 \rangle_o$ orientation (e)-(h). (a) and (e) are views in three dimensions. (b) and (f) are projections on the $\langle 101 \rangle_o$ direction. (c) and (g) are projections on the $\langle 010 \rangle_s$ direction. (d) and (h) are views from the top.

To confirm these predictions, we performed reciprocal space mapping (RSM) around the $[33-2]_o$ peak of GTO (which, without taking into account the distortion, may be referred to as the $[-103]_{pc}$ peak in pseudo-cubic notation) and the $[-107]_s$ peak of SLGO. The in-plane components corresponding to the peaks of GTO and SLGO in Figure C-5 (a) coincide, indicating that the film is fully strained (cf. chapter II).

RSMs around $[200]_o$ reflections measured with the sample at $\chi=45$ degrees were also performed to determine the other lattice parameters of the film. As visible from Figure C-5 (b), two peaks are present, corresponding to two structural variants. These two peaks are indeed the superposition of domains rotated by 180 degrees with respect to each other around the $\langle 110 \rangle_o$ direction. In Figure C-5 (c), we display a view of the two structural variants along the $\langle 001 \rangle_o$

direction. Since χ is defined with respect to the substrate and a differs from b , both directions ($\langle 010 \rangle_o$ and $\langle 100 \rangle_o$) cannot simultaneously be perpendicular to the sample holder. The slight tilt will be denoted in what follows as κ and the lattice parameters extracted from Figure C-5 (b) as $a_{[100]_o}^{\chi=45}$, $b_{[010]_o}^{\chi=45}$.

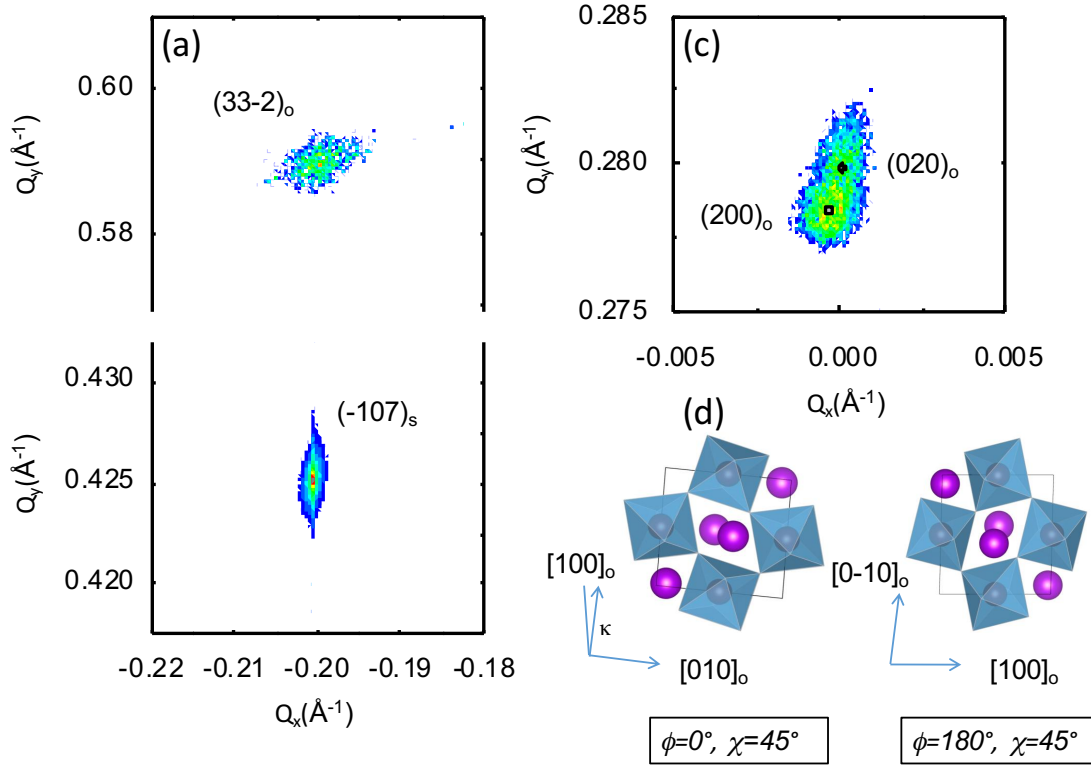


Figure C-5: (a) Reciprocal space map near the $[-107]_s$ peak of SLGO and of $[33-2]_o$ of GTO for a film grown at 0.8 J/cm^2 , 700°C , and $2 \times 10^{-6} \text{ mbar}$. (b) Reciprocal space map near the $\langle 200 \rangle_o$ peak at $\chi=45^\circ$. (c) Sketches displaying the projections of the two variants oriented at 180° with respect to each other at $\chi=45^\circ$ along $\langle 001 \rangle_o$.

Assuming that the orientation of the unit cells is the one described in the diagram Figure C-4 (c), we can find all structural parameters by solving 7 equations simultaneously where c_{out} is calculated from the $2\theta-\theta$ scan shown in Figure C-1 (a), and $a_{[100]_o}^{\chi=45}$, $b_{[010]_o}^{\chi=45}$ are both extracted from Figure C-5 (b).

$$\frac{d_{[110]_o}}{2} \sin \kappa = c_{out} \quad (1)$$

$$a^2 + b^2 - 2ab \cos \gamma = 4a_{ip}^2 \quad (2)$$

$$2 \tan^{-1}\left(\frac{b}{a}\right) = \kappa \quad (3)$$

$$\cos\left(\frac{\pi}{4} - \alpha\right) b = b_{[010]_o}^{\chi=45} \quad (4)$$

$$\cos\left(\frac{\pi}{4} - \beta\right) a = a_{[100]_o}^{\chi=45} \quad (5)$$

$$a^2 + b^2 + 2ab \cos \kappa = d_{[110]_o}^2 \quad (6)$$

$$\alpha + \beta = \pi - \gamma \quad (7)$$

Solving this system numerically yields the following values: $a=5.47 \text{ \AA}$, $b=5.56 \text{ \AA}$, $d_{[110]_o}=7.85 \text{ \AA}$, $\gamma= 88.8^\circ$, $\kappa= 90.3^\circ$. These values confirm that the film is grown in the $\langle 110 \rangle_o$ orientation, lowering its symmetry from the orthorhombic $Pbnm$ to the monoclinic $P2_1/m$ in order to accommodate the in plane strain (similar to the case of SrRuO_3 on SrTiO_3 , see Ref. [92]) imposed by the substrate.

3 - Transport properties

Next, we characterized the physical properties of the single phase GTO films by transport, optical, and magnetic measurements. The electrical resistivity of a GTO film grown on SLGO is shown in Figure C-6 (a). The resistivity increases with decreasing temperature, consistent with a Mott insulating behavior [58]. It is well-known that oxygen-rich rare earth titanate films are metallic [68], thus the insulating nature of our GTO films suggests that no major off-stoichiometry is present [41,93]. At room temperature the resistivity is 19.8 \Omega cm , which is lower than that of bulk GTO (26 \Omega.cm) [94] but higher than the values obtained in previous studies on thin films [58,90]. The inset in Figure C-6 (a) shows the resistivity as a function of the inverse temperature ($1/T$), and a fit of the data using Arrhenius law. The activation energy is found to be 0.094 eV and is comparable to the value of 0.14 eV for thin films found in [58] but lower than the bulk value known to be $0.19\text{-}0.23 \text{ eV}$ (Refs. [40,75]).

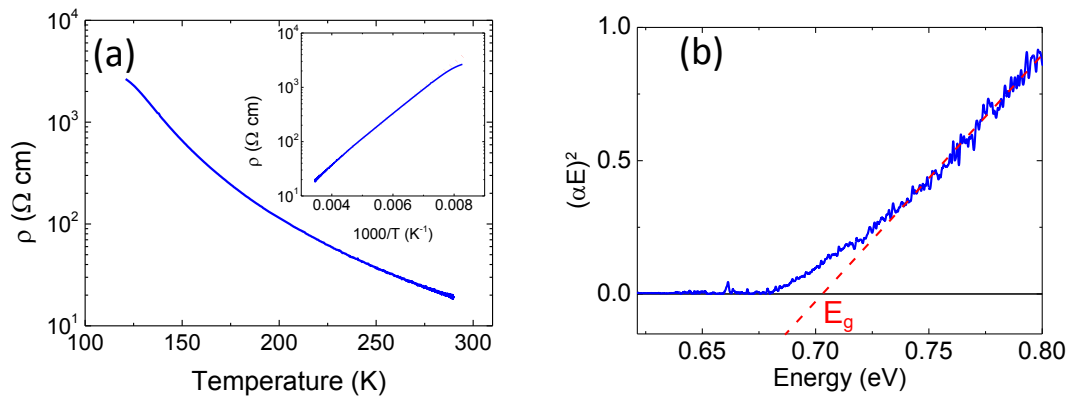


Figure C-6: (a) Electrical resistivity as a function of temperature of a 15 nm GTO film grown at 1.1 J/cm^2 , $2.5 \times 10^{-6} \text{ mbar}$, and $T=660^\circ \text{C}$. Inset: same plotted against the inverse temperature; an activated behavior characteristic of Mott insulating is used to fit the data. (b) UV spectroscopy data performed on the same sample at room temperature.

To determine the optical band gap of our GTO thin films, we performed transmission spectroscopy using a Cary spectrometer over the spectral range 1000-2000 nm (1.24-0.62 eV). The absorption coefficient of the GTO layer, α , was calculated from the transmission of the GTO sample, T , and the substrate, T_0 , using the relation $\alpha = -\frac{1}{t} \ln \left(\frac{T}{T_0} \right)$, where t is the thickness of the GTO layer (determined by X-ray reflectometry). To determine the band gap, a Tauc plot of $(\alpha E)^2$ vs E was constructed, and the linear region extrapolated to the E axis (Figure C-6 b), yielding an optical gap value of ~ 0.7 eV in good agreement with reported values for thin films [58] and bulk [95].

4 - Magnetic properties

Figure C-7 (a) shows the magnetic properties of the GTO films. Magnetization as a function of the magnetic field is hysteretic with a coercive field (~ 370 Oe) at 10 K, consistent with the expected ferrimagnetism of GTO (Ref. [40,80]).

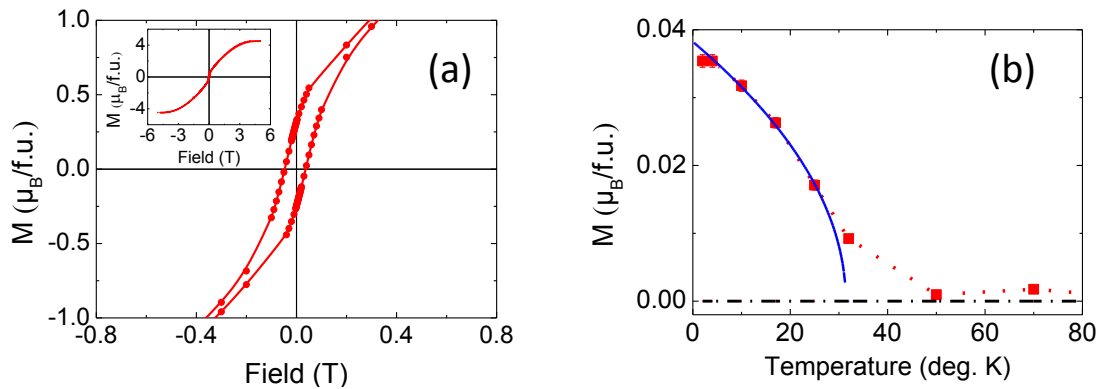


Figure C-7: (a) $M(H)$ hysteresis loop and (d) $M(T)$ for a 15 nm-thick film grown in the same conditions. In (b), the width of the red dots corresponds to the error bars in the measurements; the blue line is a fit to the data in a classical mean field model.

The saturation magnetization at 10 K is about $4.2 \mu_B$ per formula unit (f.u.). This value is lower than the bulk value ($\sim 6 \mu_B/\text{f.u.}$) but is comparable to the value found in [55] for films grown on LSAT. In order to correctly remove the paramagnetic background arising from impurities in the substrate, we determined the $M(T)$ by measuring the remanent magnetization from $M(H)$ hysteresis loops performed at different temperatures after field cooling. The result is shown in Figure C-7 (b). A classical mean field fit of the ferromagnetic cycle gives a T_c of the order of 32 K but the small amount of experimental data only allows to carefully state that T_c is $35 \text{ K} \pm 5 \text{ K}$ close to the corresponding bulk value of 32-34 K (Refs. [40,75]).

5 - Numerical confirmation

To gain further insight into our results, Hongjian Zhao from University of Arkansas in Pr. Bellaiche's group performed theoretical density functional (DFT). We present the results here, as they confirm quite nicely experimental evidences.

Two possible growth orientations $\langle 001 \rangle_o$ and $\langle 110 \rangle_o$ were considered and simulated. Considering the SLGO substrate with in-plane lattice parameter of $\sim 3.852 \text{ \AA}$, the calculation indicates that the $P2_1/m$ phase ($ab\text{-}ePbnm$) is more stable than the $Pbnm$ phase ($c\text{-}ePbnm$). The calculated mean value of the a and b lattice parameters of $P2_1/m$ phase on SLGO substrate is 5.549 \AA . The calculation overestimates the mean value of a and b by $\sim 0.6\%$ compared to the experimental 5.515 \AA . The calculation shows the c lattice parameter of 7.704 \AA and γ angle of 87.9 degree (the atomic positions presented in Figure C-4 and Figure C-5 are the actual atomic positions from the computations). The simulated GTO on SLGO substrate shows a total magnetic moment of $5.99 \mu_B$, and a partial magnetic moment (magnitude) for Gd^{3+} and Ti^{3+} of $6.96 \mu_B$ and $0.94 \mu_B$, respectively. The calculation overestimates the magnetization possibly since the spins are assumed to be collinear, *i.e.* no canting or frustration is considered.

Consistent with the experimental results, the theory predicts that the most favorable growth direction of GTO on SLGO is $\langle 110 \rangle_o$. Although the values of the lattice constants are slightly different, the results agree in showing the monoclinic rearrangement of the atoms in the $P2_1/m$ space group. The theory allows the calculation of the Ti-O-Ti angles in all directions. In the $\langle 110 \rangle_o$ oriented growth the Ti-O-Ti angle along both the a and c direction decreases from 143.7° (calculated bulk value, in agreement from the value found in our own single crystal study) to 141.5° and 141.1° respectively.

We thus argue that the biaxial stress imposed by the epitaxial strain may be responsible for the different experimental behaviors found in films compared to the bulk. The modification of the bandwidth (W defined as $W \propto \cos^2\Theta$ where Θ is the angle of the R-O-R bonds [1]) by epitaxial strain has profound consequences on the physical properties of strongly correlated electronic systems [96]. A heterogeneous decrease in the Ti-O-Ti angle thus results in a decrease of the bandwidth and yields a lower activation energy as observed from Figure C-6.

6 - Effect of defects and oxidation

We also performed some characterizations of eventual structural defects in our slightly off-stoichiometric samples (according to their out-of-plane parameters). To that end, we used

transmission electron microscopy on a 10 nm-thick GTO thin-film grown on top of LaAlO₃ in the same growth condition. The result is presented in Figure C-8.

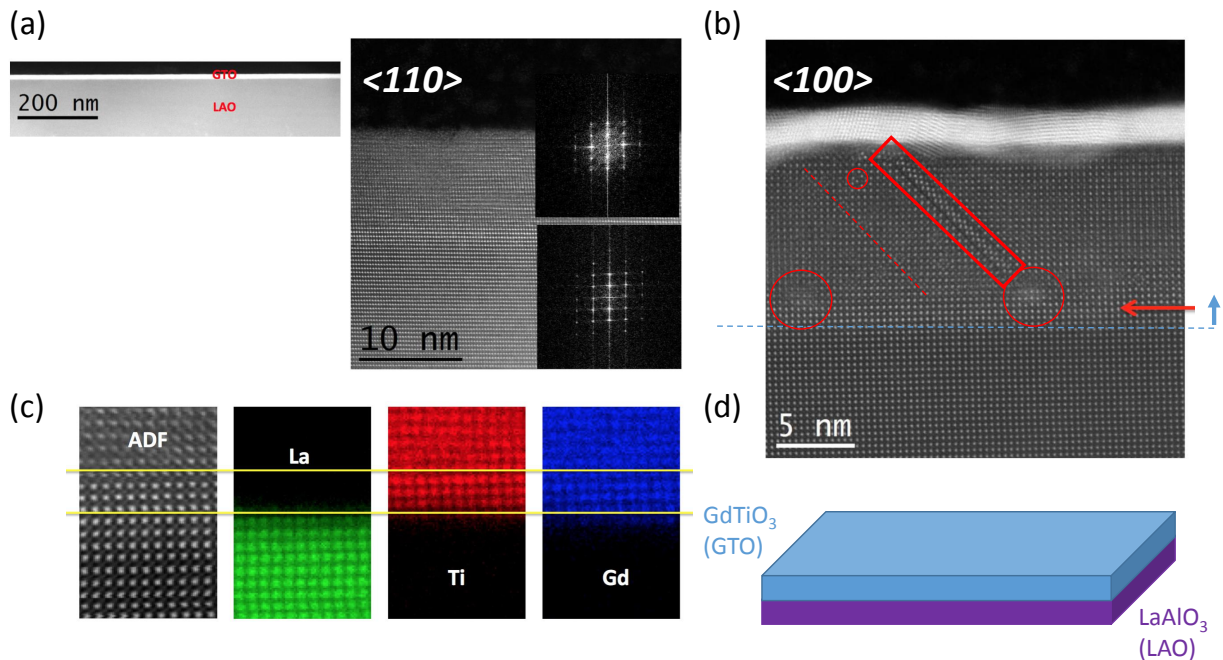


Figure C-8: (a) Pt-capped 10 nm-thick GTO thin film grown on top of LAO substrate (cf. schematic representation in d). HAADF TEM images, along the $\langle 110 \rangle$ -direction (a) and along the $\langle 100 \rangle$ direction (b). Insets in (a) are FFT images of (a) for the upper panel and (b) for the lower panel. EELS chemical maps are presented in (c) at all edges. In (b) defects are highlighted in red while the substrate-film interface is marked by a dashed blue line.

Along the $\langle 110 \rangle$ direction (cf. Figure C-8 a) the sample presents a high-structural quality with apparently no chemical defects. The symmetry is different from the one observed in bulk crystals (upper panel inset in (a) compared to Figure B-3 a), confirming the reduced monoclinic symmetry.

When looking along the $\langle 100 \rangle$ direction, the film is clearly presenting stacking faults (red rectangle in Figure C-8 b), that appears to accommodate the strain induced by chemical and structural cationic defects highlighted by the red circles in (b).

This small spherical region (cf. red circles in Figure C-8 b) brighter in the TEM images evidencing intermixing and segregation of brighter Gd ions over Ti ions. Just above this defect, the stacking fault develops all along the sample thickness. 2 nm left of this stacking fault, a series of oriented cation vacancies can be observed (dashed red line). This can be considered as the first stage prior to stacking fault formation.

Finally, this suggests that, as envisaged in [97], off-stoichiometry in RTO is accommodated by stacking faults or cation vacancies (also present in TEM pictures) rather than by oxygen vacancies.

From this picture we can estimate roughly 1.2 % of stacking faults in the sample. Below 7 u.c however no stacking fault was observed. EELS chemical maps show that beyond 7 high quality unit cells, the Gd/Ti ratio starts to get off-stoichiometric (Figure C-8 c). We will thus restrict sample thickness below 7 u.c. when growing heterostructures in chapter V.

In summary, we have reported on the various phases that are stabilized when growing GTO films by PLD as a function of temperature and pressure during the optimization process. We have shown that by appropriately choosing the fluence and frequency we are able to grow $\langle 110 \rangle_o$ -oriented fully strained GdTiO_3 films in layer-by-layer mode. The structural, electrical, and magnetic properties of the GdTiO_3 films grown by PLD were presented. We also characterized the type of defects observed in our GTO thin films. The synthesis of high-quality GTO films is a first step in the study of Mott physics in rare earth titanates as a function of strain and confinement, or at epitaxial interfaces with other perovskite oxides. In the next section, we will focus on the effect of strain on GTO thin films.

D - A strain engineering study

Strain engineering is a fantastic knob to investigate oxide properties that would not otherwise be present in bulk form. This technique has shown, for example, exceptional results in the context of ferroelectrics and multiferroics [98].

This section is devoted to study how strain-engineering would affect GTO thin films. By using exactly the same growth condition as the ones presented in the last section, GTO thin films were thus deposited onto many different substrates: PrScO_3 -PSO, NdScO_3 -NSO, GdScO_3 -GSO, SrTiO_3 -STO, $(\text{LaAlO}_3)_{0.3}(\text{Sr}_2\text{AlTaO}_6)_{0.7}$ -LSAT, SrLaGaO_4 -SLGO, LaAlO_3 -LAO, NdAlO_3 -NAO.

1 - Effect of strain on the growth orientation

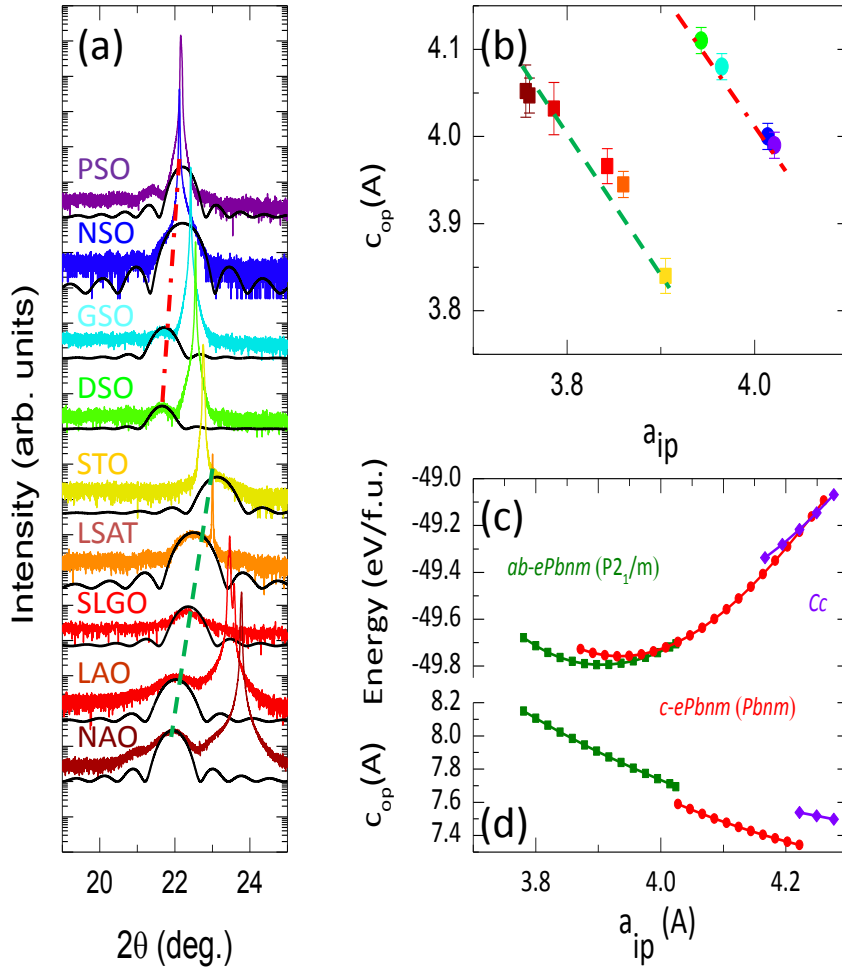


Figure D-1: (a) X-ray diffraction patterns of the $[001]_{pc}$ peak of GTO on different substrates. The black line is obtained from finite thickness Laue fringes fits (b) The extracted out-of-plane parameter as a function of the substrate in-plane lattice. (c) first-principle DFT calculations of the energy of different ground states as a function of the in-plane parameter (d) calculated out-of-plane parameter as a function of the in-plane parameter.

In Figure D-1 (a), we present XRD patterns of GTO thin films grown onto different substrates. We observe that GTO thin films $[001]_{pc}$ -peak position varies with the substrate. For substrates with in-plane parameter below 3.91 \AA , the peak position increases linearly from 22 degrees to almost 23 degrees. The peak position then jumps from 23 degrees to 21.6 degrees. This jump occurs between STO and RScO₃ (RSO) substrates. The peak position then linearly decreases again to a value close 22.2 deg.

Using Bragg's law, we could determine the out-of-plane lattice constant for all GTO thin films (Figure D-1 b). The out-of-plane lattice constant first decreases from a value close to 4.06 \AA for NdAlO₃ to 3.9 \AA for SrTiO₃ substrate, then back to 4.1 \AA for DSO and decreasing to 3.97 \AA for NSO and

PSO. All samples present a thickness which is around 10 nm and should thus all be strained.

Assuming that all samples are fully strained and variations of the in-plane parameter are small enough, elastic theory of solids applies. We can thus write:

$$\varepsilon_{\perp} = -2 \frac{c_{12}}{c_{22}} \varepsilon_{\parallel}$$

with ε_{\perp} and ε_{\parallel} , being the perpendicular and parallel strains, $\varepsilon_{\perp} = \frac{c_{measured} - c_{bulk}}{c_{bulk}}$ and $\varepsilon_{\parallel} = \frac{a_{ip} - a_{bulk}}{a_{bulk}}$, and c_{ij} the elastic constant in the i,j directions. This explains the negative linear relationship between the out-of-plane parameter and the substrate in-plane parameter observed in Figure D-1 (b). Indeed, according to the above formula, out-of-plane parameter varies proportionally with the in-plane parameter fixed by the substrate with a linear coefficient given by $-2 \frac{c_{12}}{c_{22}} \frac{c_{bulk}}{a_{bulk}}$.

As we already presented in the last section, there exists many possible orientations for GTO thin films. The jump and change of linearity regime upon crossing from STO to the scandate family may be related to this change of orientation. Indeed, the two out-of-plane parameters are either $\frac{1}{2}\sqrt{a^2 + b^2}$ in the ab - $Pbnm$ orientation or $c/2$ in the c - $Pbnm$ orientation. The change in out-of-plane parameters represents a change of 2.4 % from bulk values which is of the order of the observed jump (the slight difference can be explained by strain).

The change of slope can also be fully rationalized by the elastic theory developed above. In one case, for c - $Pbnm$, the c_{12} is the elastic constant between $\langle 110 \rangle$ and $\langle 001 \rangle$ -directions, and c_{22} is the elastic constant along the $\langle 001 \rangle$ -direction. In the other case, for ab - $Pbnm$, the c_{12} is the same but c_{22} is the elastic constant along $\langle 110 \rangle$ -direction. The linear coefficient expressed previously is proportional to $\frac{1}{c_{22}}$ and would thus be changed depending on the film orientation.

To confirm this idea, Hongjian Zhao performed theoretical density functional (DFT) calculations in the same general fashion as he did in the previous section of this manuscript. The results of the computed energies for the two phases are presented in Figure D-1 (c).

According to the calculations, at a certain point in tensile strain, the system rotates to accommodate the strain from ab - $Pbnm$ to a c - $Pbnm$, strongly supporting the experimental data. This change in orientation is also accompanied by a jump of the calculated out-of-plane parameter (cf. Figure D-1 d). Interestingly, DFT calculations are unable to reproduce the sign of the change that we observe. DFT predicts a diminution of the out-of-plane parameter when going from a ab - $Pbnm$ to a c - $Pbnm$, whereas the experiments point to an increase of this latest. We believe this is largely explained by the fact that the calculations are performed for square lattices with in-plane lattice constants being equal in both in-plane directions. However, we know that scandates are strongly distorted structures with in-plane parameter that can vary by more than 3% in PSO for example. Test calculations have proven that this discrepancy can reverse the sign of the variation in the

calculations.

We also completed this study by checking that changing the rare-earth in RTO from Gd to Tm did not change the physics describe above. We thus grew two TmTiO₃ (TTO) films on top of LAO and DSO.

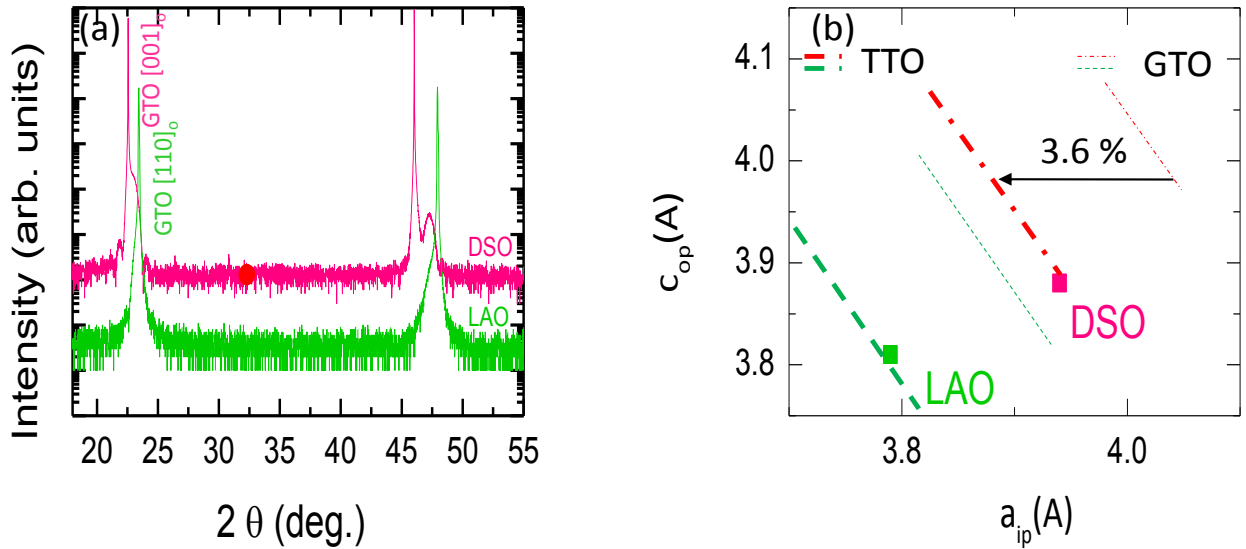


Figure D-2: (a) XRD patterns for TTO films grown on top of DSO and LAO with the same growth condition as GTO thin films. (b) out-of-plane parameters as a function of the in-plane lattice parameter. Very thin dashed line accounts for previous GTO dependence while the thicker dashed lines are the ones suspected for TTO.

In Figure D-2 (b), we extract the out-of-plane parameter as a function of the in-plane parameter. Assuming that the elastic constants are not modified when changing the rare-earth from Gd to Tm [39], we reported the linear slopes extracted from strain engineered GTO and used it for TTO. We see that, if true, the linear fit would have been shifted to the left (thick dashed lines). This displacement corresponds to a variation of 3.6 %. Remarkably, this value is exactly equal to the reduction of volume from GTO (236.4 Å³) to TTO (228 Å³), confirming the scenario of a strain-engineered control of the growth orientation in RTO thin films.

2 - Effect of strain on surface morphology

We then looked at the superficial morphology of the as-grown thin-films. The AFM topography images are presented in Figure D-3 for 6 different substrates: NAO, SLAO, LAO, NGO, LSAT, DSO, NSO, PSO

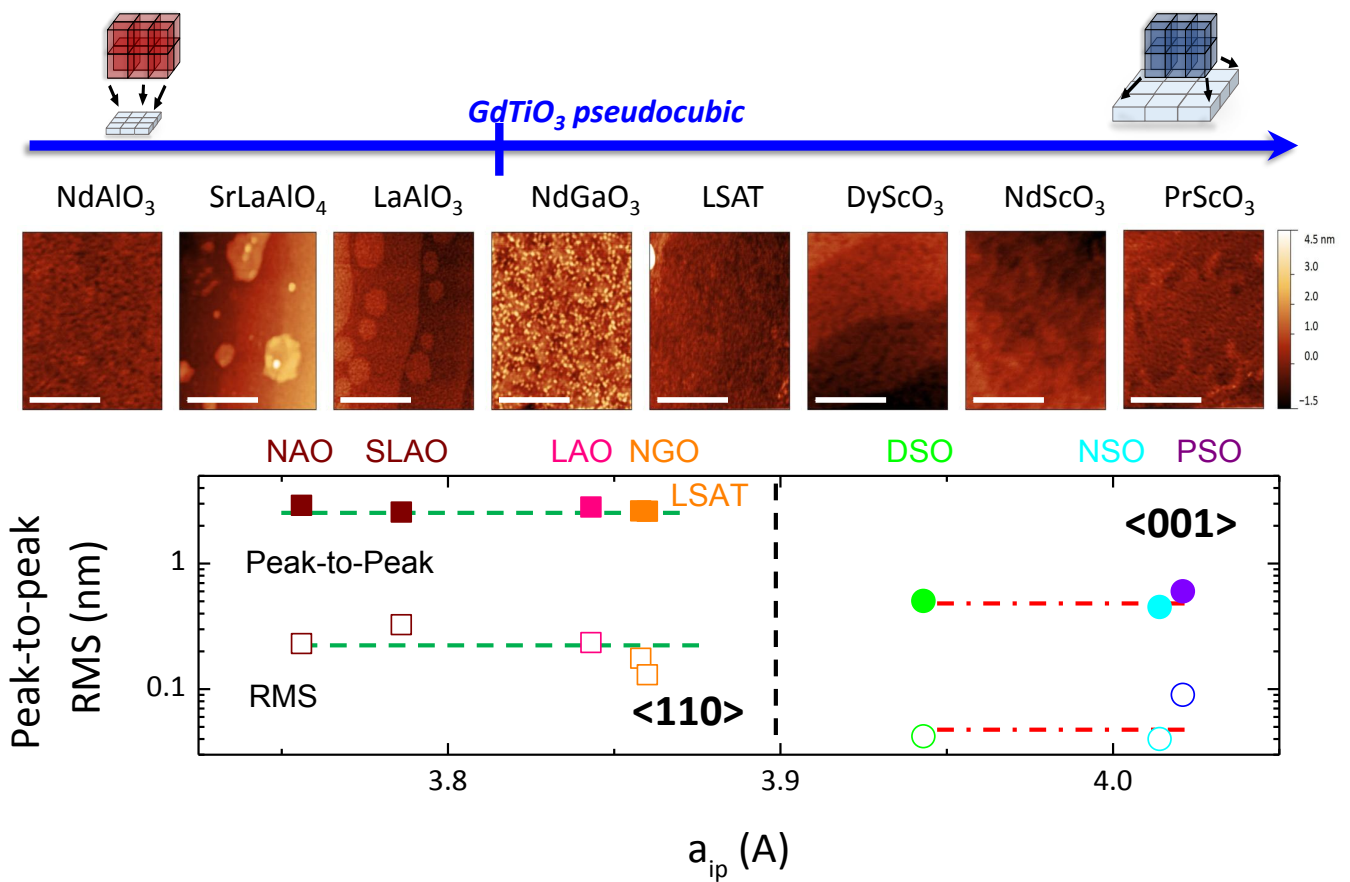


Figure D-3: (a-h) AFM images of the superfcies of GTO thin films deposited on different substrates. The images are all $1 \mu\text{m}^2$ in area and the white bare is equal to $0.5 \mu\text{m}$ in length. The scale for SLAO is different and goes from -20 nm to 9.5 nm due to large thermally activated SLAO crystallites forming at the substrate. The peak-to-peak height (full symbols) and the root-mean-square(RMS) roughness (open symbols) extracted from the AFM images presented above are displayed in (i).

All films present a root-mean-square roughness which is below 0.3 nm (cf. Figure D-3), accounting for a good superficial reconstruction, and morphology. This is expected from the nice epitaxial growth of the thin films on all these substrates (cf. Figure D-1). The sample terraces is apparent in SLAO, LAO, DSO, NSO, and PSO and can be distinguished in NAO.

However, it is clear that the sample present different roughness (cf. Figure D-3). As the samples change orientation, the RMS roughness (avergaed over the whole images) is strongly suppressed by more than 80%. This is also true for the peak-to-peak height which has been recorded for a profile extracted on a step terrace. Note that this is also observable in TTO grown samples where Laue fringes (cf. Figure D-2) are clearly visible, assessing that the roughness of the inner-layers are better defined when grown on DSO than on LAO.

The rougher surfaces of the *ab*-*Pbnm* films than for *c*-*Pbnm* films suggest an intrinsic

mecanism (not related to substrate miscut) during the formation of the few first layers of the oxide thin-films. We thus turn to RHEED to understand surface reconstructions happening during the growth. In the following, directions are given according to substrate orientation.

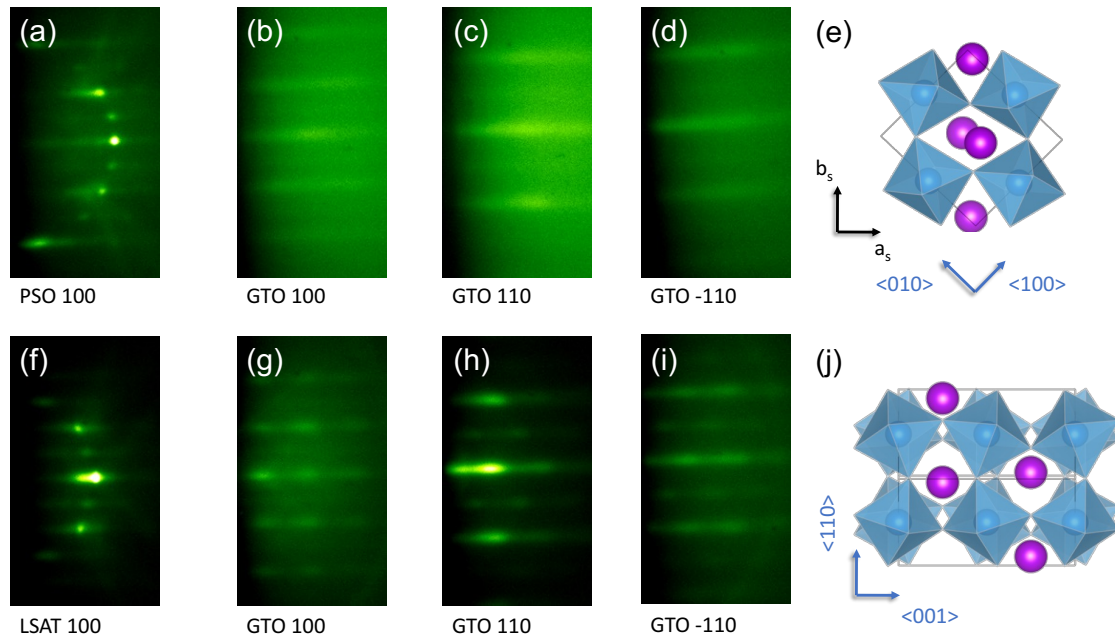


Figure D-4: in-situ RHEED patterns of (a) PSO substrate along the <100> direction, GTO thin film along the <100> direction (b), the <110> (c), and <-110> (d) grown on top of it. (e) Schematic crystal structure of a <001>_{GTO}-oriented GTO thin film. RHEED patterns for LSAT along the <100> direction (f), GTO thin film along the <100> direction (g), <110> (h) and <-110> (i) grown on top of it. (j) Schematic crystal structure of the in-plane view of a <110>_{GTO}-oriented GTO thin film.

The first observation is that RHEED suggests (as expected from RSMs) that films in both orientations are fully strained. Indeed, the interspacing between RHEED fringes in the substrate and in the film are identical, confirming that both present the same in-plane lattice constants (within experimental resolution). Second, RHEED patterns show very different behaviors in both orientations.

In the *c-Pbnm* orientation, GTO thin films present a 90 degrees-symmetry, as in [90], cf. Figure D-4 (e). This is confirmed by comparing for example RHEED patterns along the <110> and the <-110> direction that are identical (cf. Figure D-4 c-d). However, RHEED pattern along the <110> direction looks different compared with the one along the <100> direction for example (cf. Figure D-4 b-c). The form factor associated with the diffracted planes is indeed different, as visible on Figure D-4 (e).

In the *ab-Pbnm* oriented thin-films, however, the situation is very distinct as there is no in-plane symmetry. One can see that measurements along the three directions present completely

different RHEED patterns. This advocates that the film adopts a preferential in-plane orientation during growth (cf. Figure D-4 g-h-i) - there are no structural variants at 90° from one another.

The presence of such an in-plane anisotropy for films grown in the *ab-Pbnm* orientation may be the key to account for the morphology of their surfaces, which are much rougher than in *c-Pbnm* thin films. Indeed, *ab-Pbnm* films are monoclinic as we showed in the previous section. Nevertheless, RHEED also states that they are largely made of one single in-plane orientation. This implies that the monoclinic angle will spread throughout the thickness of the film, leading to an increase of the in-plane strain along the whole thickness of the film. In order to accommodate this strain, the sample will have to break locally by creating extended defects such as stacking faults - just like we observed in the previous section on LAO substrates (cf. Figure C-8). These defects would lead to a faster transition from a pure 2D growth-mode (which we can estimate below 7 unit cells from the TEM images of Figure C-8) to a mixed 2D-3D growth mode that increases the roughness as the sample gets thicker and thicker. This is also suggesting that samples grown in *c-Pbnm* orientations will be much more stable since less likely to experiment large internal strain gradient.

In this chapter we have presented our understanding of the properties of rare-earth titanates. We first looked at single crystals and proposed the first absorption spectroscopy experiment with magnetic circular dichroism on single crystal rare-earth titanate. We could quantify the effect of oxidation on the magnetic properties of our titanates and discuss the spin-orbital structure of late rare-earth titanates single crystals.

Then, we turned to the growth and characterizations of the first PLD grown GTO thin- films. We showed that we could succeed to grow nice epitaxial thin films with bulk properties. We also studied how strain-engineering affects the growth orientation of the thin-film that eventually present two possible variants *c-Pbnm* and *ab-Pbnm*, yielding distinct structural and morphological properties.

We will now turn to the other building block of our end-goal heterostructure : rare-earth nickelates.

IV. Rare-earth nickelates

In this chapter, we will discuss the physics of rare-earth nickelates. First, we will start by reviewing some basic properties of bulk crystals and recent studies on thin-films. Then, we will present our own theoretical description of the ground state of rare-earth nickelates. Finally, we will present some spectroscopic characterizations of the metal-insulator transition in SmNiO_3 .

A - Electronic and magnetic properties of RNiO_3 :

Among all perovskites (cf. chapter I), rare-earth nickelates $\text{R}^{3+}\text{Ni}^{3+}\text{O}_3$ ($\text{R}=\text{Lu-La, Y}$) might be considered as a prototypical system because they possess almost all possible degrees of freedom present in perovskites. Nickelates were intensively studied during the 1990's [99] and regained interest lately due to their great potential for engineering novel electronic and magnetic states [100–104]. Let us, first, start by reviewing the main properties of bulk nickelates.

1 - Bulk crystals

Perovskite rare-earth nickelates have a perovskite unit cell ($\text{RNiO}_3\text{-RNO}$) made of rare-earth ions sitting in the middle of cubes composed of Ni ions surrounded by oxygen octahedra. In this

configuration, Ni is trivalent and has a $3d^7 (t_{2g}^6 e_g^1)$ low-spin configuration.

Historically, nickelates were left apart in comparison with manganites and cuprates, although they present exceptional properties. This may be probably due to their extremely difficult synthesis [105], that requires very high temperatures and extremely high pressures [106,107]. Bulk single crystals are almost impossible to find (the largest being only 100 μm [108]). Hence powdered polycrystalline samples were often used to conduct preliminary research.

a) Structural properties

At room temperature nickelates present an orthorhombic structure with a tolerance factor varying from 0.93 for LuNiO_3 (LuNO) to 0.975 for PrNiO_3 (PNO). As we observed previously in the RTO family, lattice parameters depend on the rare-earth ionic radii as shown in Figure A-1 a. Interestingly, in the RNO structure, NiO_6 -octahedra cages remain practically undistorted throughout the series, the octahedra only tilt to accommodate the interstitial space appearing when rare-earths are replaced by smaller ones.

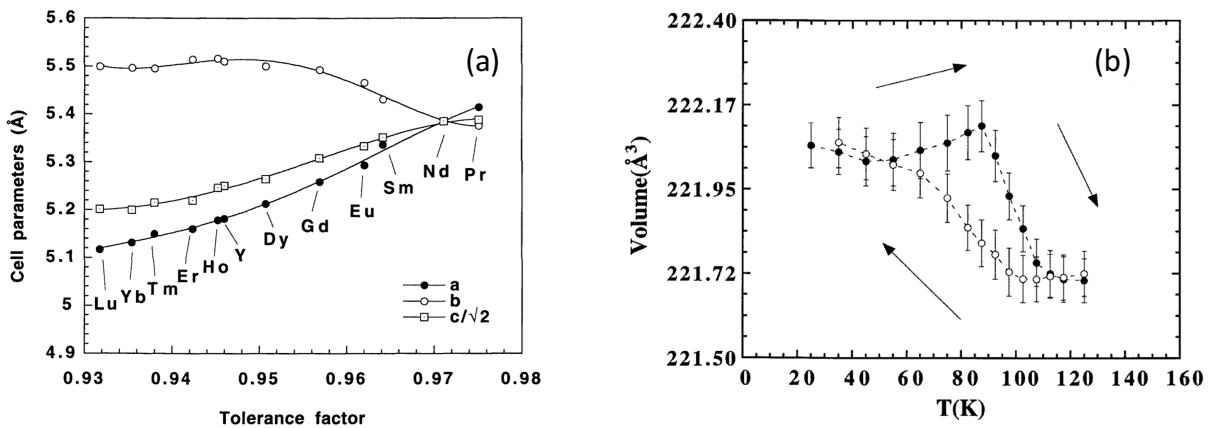


Figure A-1: (a) cell parameters for different rare-earth nickelates as a function of the tolerance factor (b) Temperature dependence of the volume for a $\text{La}_{0.3}\text{Nd}_{0.7}\text{NiO}_3$ sample. Adapted from [99]

One of the first remarkable properties of RNO is its temperature-dependent structural phase transition. At a certain temperature, the volume suddenly increases by roughly 0.2 %. In the case of PNO, NdNiO_3 (NNO), and any solid solution involving one of these two elements, the volume change is hysteretic upon cooling and warming (cf. Figure A-1 b). The variation of the unit cell volume results from a small increase of the Ni–O distance ($\sim 0.2\%$) and from a simultaneous decrease of the Ni–O–Ni superexchange angle ($\sim 0.4\%$) [99].

b) Magnetic properties

In nickelates, the rare-earth can be either diamagnetic (Lu, Y, La) or (para-)magnetic (Nd, Pr, Sm,...). In the latter case, they contribute enormously to susceptibility measurements. For that reason, the Ni magnetic configuration of polycrystalline nickelate samples has remained for long mysterious. However, at the beginning of the 1990s, muon rotation experiments showed a decrease of the paramagnetic fraction which, to the authors, was due to the appearance of a 3D magnetic ordering at $T_N = 130$ K (Pr), 200 K (Nd), 225 K (Sm) and 205 K (Eu) [109]. These results were later confirmed by neutron diffraction experiments [110] (see Figure A-2 a-b). Note that the Néel temperature in NNO coincides with the temperature at which the volume of unit cell expands.

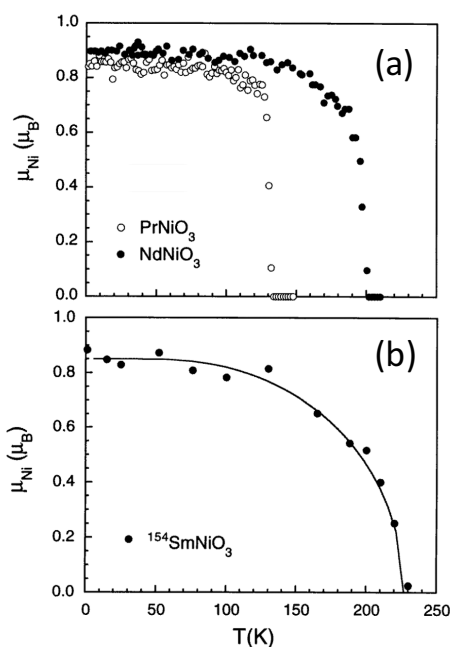


Figure A-2: Temperature dependence of the Ni magnetic moments for different nickelates: (a) $PrNiO_3$ (MIT = 130 K) and $NdNiO_3$ (MIT = 200 K); (b) $SmNiO_3$ (MIT = 400 K) adapted from [99]

Neutron experiments signaled the presence of small resonances that were indexed with the propagation vector $k = [1/2, 0, 1/2]$ ($k = [1/4, 1/4, 1/4]$ in the pseudo-cubic parent perovskite cell). The presence of a magnetic condensed mode at the $[1/4, 1/4, 1/4]$ resonance advocates for an antiferromagnetic alignment of the Ni ions. However, when decomposing the different magnetic coupling in the unit cells, the authors [111] found an equal proportion of anti-ferromagnetic and ferromagnetic coupling yielding a very unique $[\uparrow\downarrow\downarrow]$ -stacking that can be labelled either E, T or S depending on the direction (cf. Figure A-3), of the ferromagnetic coupling with respect to the

antiferromagnetic ones.

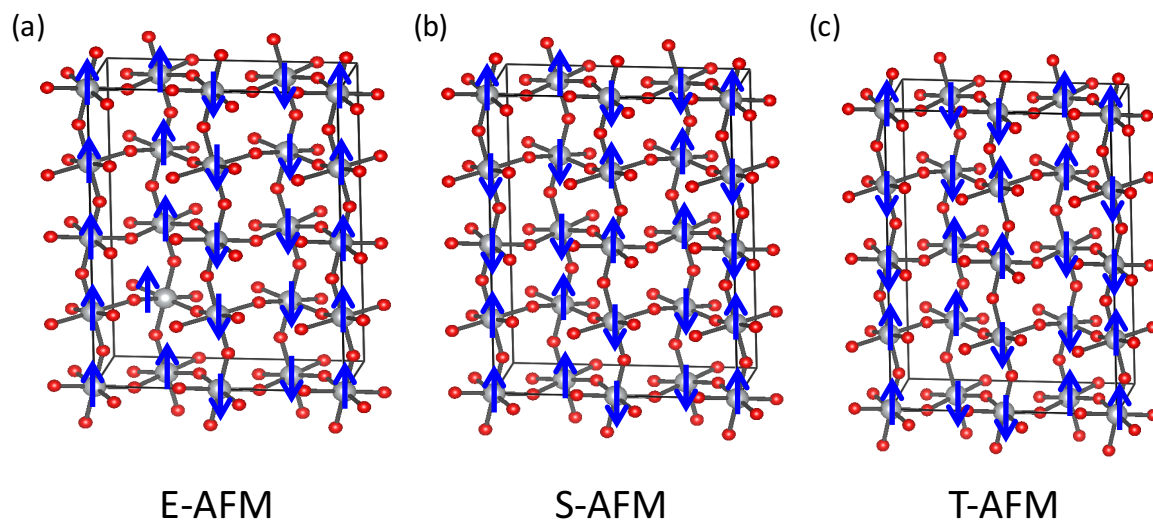


Figure A-3: magnetic structure of RNO presenting the $[\uparrow\uparrow\downarrow]$ -stacking with the three possible arrangements (a) E-AFM, (b) S-AFM, (c) T-AFM.

c) Transport properties

Nowadays nickelates are famous because of their extraordinary transport properties. Indeed, they present a temperature-activated metal-to-insulator transition (MIT). In Figure A-4 (a), we present the typical temperature-dependence of the resistivity for RNO: above a certain temperature corresponding to the MIT, the nickelates display a metallic behavior. At the MIT, the onset of resistivity is very abrupt and a sudden change from metallic to semiconducting-like behavior is observed. Remarkably, in Nd, Pr, and in any mixture of these two elements, the temperature dependence of the resistivity is hysteretic, reminding what was observed in temperature-dependent volume measurements.

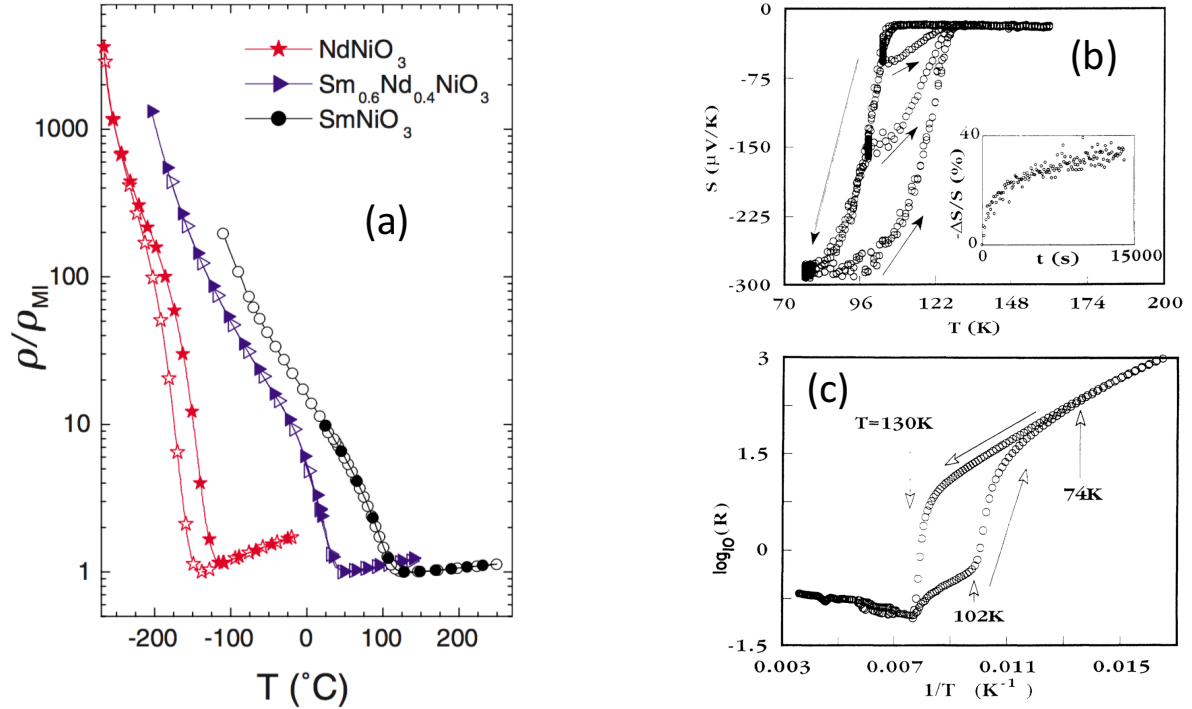


Figure A-4: (a) temperature-dependent resistivity for NdNiO_3 (red stars), SmNiO_3 (black circles), and a solid solution of 40% Nd-doped SmNiO_3 (purple triangles) adapted from [112] The hysteretic temperature dependence below MIT = 130 K of the Seebeck coefficient (b) and of the electrical log-resistance (c) of PrNiO_3 (adapted from [113])

In [113], the authors investigated carefully the electronic transition in PrNiO_3 (cf. Figure A-4 b-c). They have shown that the resistivity, and the Seebeck coefficient also display a temperature-dependent hysteretic behavior. Above the MIT, the Seebeck coefficient varies linearly with the temperature and presents a relatively small negative value of $\sim -10 \mu\text{V}/\text{K}$. However, at the MIT, the Seebeck coefficient suddenly drops down to much larger negative values such as $\sim -300 \mu\text{V}/\text{K}$. This variation of the Seebeck coefficient is accompanied by a strong decrease of the resistivity. Larger Seebeck coefficients are typical of semiconductor-like states with flat dispersion. The sign of the Seebeck coefficient (negative), which remains the same across the transition, indicates that electrons are the main carriers at any temperature.

Please note that authors in [113] also proposed to model the transport properties of PNO as a metastable mixture of metallic and semiconducting regions that would percolate at low temperature. The hysteresis would thus result from the simultaneous presence of both phases.

d) Electronic structure

These transport measurements suggest strong instabilities in the Fermi surface at the MIT.

Figure A-5 displays spectroscopic characterizations of these instabilities. In Figure A-5 (a), we present XAS measurement of the O K-edge in LNO, PNO, and NNO [18], whereas in Figure A-5 (b), we present XPS of the Ni 2p core levels [114]. In Figure A-5 (a), the pre-peak of the O K-edge, associated with the number of holes in the hybridized p-d bonds, is particularly pronounced. This result first established the strongly covalent nature of the p-d bonds in the RNO family. Noteworthy, the O K-edge peak intensity seems to evolve with the rare-earth size. It is larger in LNO than in PNO than in NNO, following the decrease of the ionic radius.

More recent studies [115] performed during this Ph.D. confirmed this trend and discussed it in terms of the level of covalence between the Ni and O ions that would be tuned by the size of the rare-earth ions.

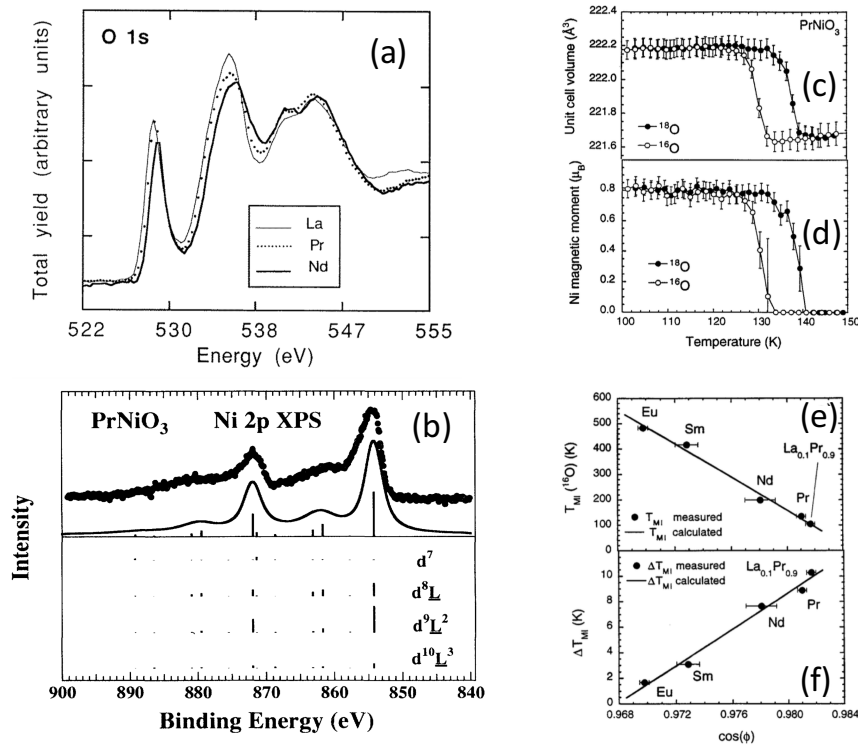


Figure A-5: (a) O K-edge of LNO, PNO and NNO extracted from [116] (b) Ni 2p XPS of PNO compared with cluster-model calculations. The theoretical spectrum is decomposed into high-order ligand-hole states [114]. Temperature dependence of the unit cell volume (c) and the Ni-magnetic moment (d) for two isotopic compositions $\text{PrNi}^{16}\text{O}_3$ and $\text{PrNi}^{18}\text{O}_3$. Evolution of the MIT (e) and of the MIT difference (f) between ^{16}O and ^{18}O isotopic nickelate compounds with the cosine of Ni-O-Ni angle. [117]

Fujimori et al., in [18], also discussed their XPS measurements in terms of the presence of oxygen holes in the Ni 2p core levels. Experimental spectra were well reproduced taking into account the presence of ligand holes ($d^{7+n}L^n$). Finally, an interesting point revealed by these measurements is that the analysis of the valence-band XPS spectra were among the firsts to support the charge-

transfer insulating nature of RNO (with the p-d energy excitation of $\sim 1\text{--}2$ eV being the smallest in the electronic structure).

Medarde et al. in [117] proposed to replace the natural oxygen ^{16}O isotope by the heavier one, ^{18}O , in PNO in order to investigate the effect of electron-phonon coupling onto the electronic structure and transport properties. They observed (cf. Figure A-5 c-d) that the MIT was shifted up by more than 10 K in presence of the heavier O isotope. The authors discussed this phenomenon in terms of Jahn-Teller polaron activation. Indeed, since nickelates were proven to be charge-transfer insulator by XPS measurements, the smallest excitation would be from an O p-state to empty Ni d-states (cf. chapter I): $\text{Ni}^{3+} + \text{O}^{2-} \rightarrow \text{Ni}^{2+} + \text{O}^-$. As a result, Ni^{2+} would follow the electronic excitation, yielding a strong electron-phonon (polaron) coupling. Medarde et al. believed that the enhancement of the MIT would then be associated with a polaron-induced band narrowing, modified by substituting ^{16}O by ^{18}O .

Interestingly, this study is one of the first to clearly link the MIT in nickelates with structural deformations and Ni-O-Ni bond angles specifically. They observed that the MIT was suppressed when the Ni-O-Ni angle increased (cf. Figure A-5 e-f). This result would also explain the correlation observed between volume and resistance change. We will see in the following that this represents a key parameter in understanding the physics of the nickelates ground state, as it links, structural mode activation, covalence and rare-earth ionic size.

e) Effect of hydrostatic pressure on rare-earth nickelates.

Following on the idea that electronic properties are strongly coupled to the lattice. Obradors [113] and Canfield [118] among others [119] applied hydrostatic pressure onto rare-earth nickelates (Pr, and Nd).

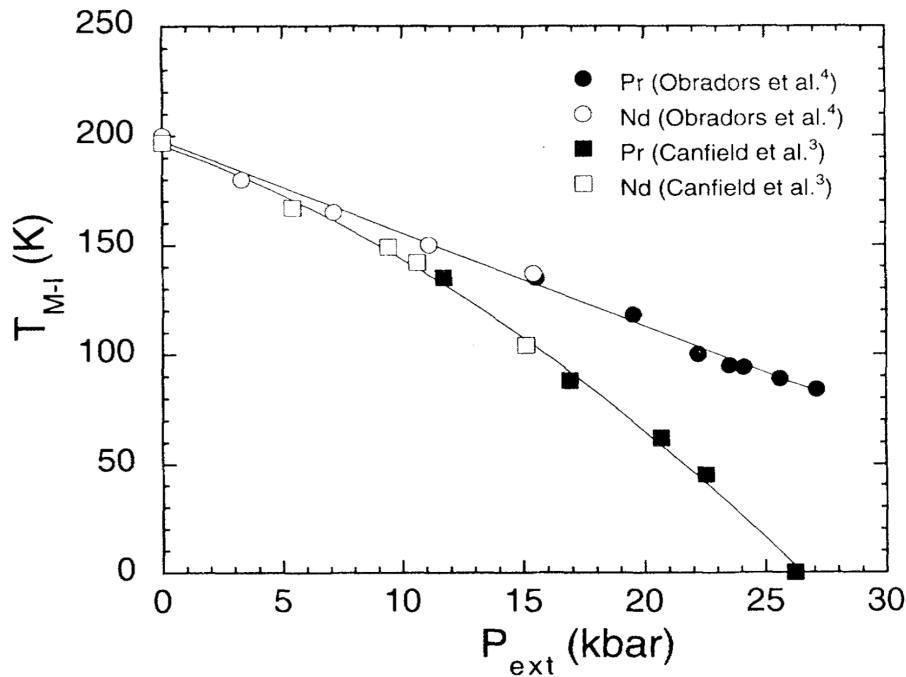


Figure A-6: Pressure dependence of the metal-insulator transition for PNO and NNO. Adapted from [119]. 3 and 4 in the figure stand for refs [113,118] resp.

Figure A-6 reports their results. The authors have been able to suppress the MIT in PNO by applying 25 kBar (2.5 GPa) [118], whereas the MIT was only linearly reduced in NNO.

Note that this behavior under pressure is the same as the one observed when continuously changing the rare-earth in bulk crystals. This follows the idea proposed by Medarde et al. [117] that the MIT is directly linked to the bond-angle between Ni-O-Ni that is increased under hydrostatic pressure (cf. Figure A-5 e-f).

2 - Thin films

As we have seen, it is very difficult to grow nickelates in bulk, yet, RNO single crystals were recently achieved in thin-film forms [120–122]. The vast majority of known studies on RNO thin films used R= La, Nd or Sm. To our knowledge, films with smaller rare-earth (except Eu [123]) radii have not yet been achieved.

a) Growth parameters and variability

Contrary to bulk crystals that require very high pressure conditions, thin films grow relatively

easily under moderate strain conditions. Several groups have succeeded in growing nickelates by means of sputtering [124], pulsed laser deposition [96,125], and molecular beam epitaxy [126].

However, the resistivity upturn, the MIT temperature, the room temperature sheet resistance and the activation energy differ from one growth technique (and study) to another. Indeed, as showed in Breckensfeld's thesis manuscript [127] or in recent works done by Stemmer's group [128], the transport properties of RNO are highly sensitive to cations and oxygen stoichiometry.

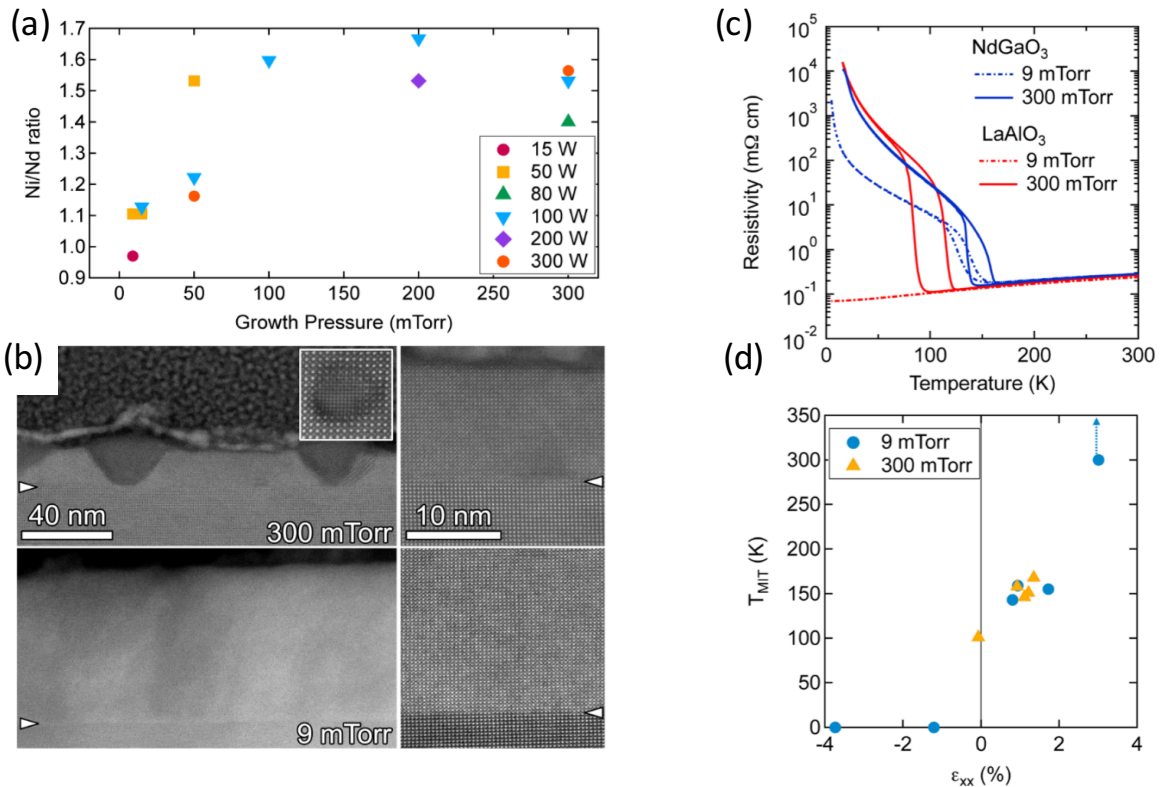


Figure A-7: (a) Ni/Nd ratios for different growth pressures and different RF sputter powers. (b) STEM images of NNO films grown on LaAlO_3 (LAO) for different total growth pressures. The inset shows a NiO inclusion. Arrows indicate the NNO/LAO substrate interface. (c) Temperature-dependent resistivity for NNO thin films grown on two different substrates (LAO and NGO) at different pressures. (d) MIT temperatures as a function of in-plane strain for films grown at total growth pressures of 300 mTorr (triangles) and 9 mTorr (circles). Adapted from [128]

Figure A-7 reports, for example, the difficulties for growing RNO by means of RF sputtering. The cationic stoichiometry depends strongly on the growth pressure and RF sputter power, as shown in Figure A-7 (a). This off-stoichiometry is consecutive of the presence of nickel oxide inclusions in the films grown at 300 mTorr for example (cf. Figure A-7 b). Remarkably, the presence of a MIT depends dramatically on the cationic ratio and stoichiometry.

Stemmer's work also indicates that in-plane lattice mismatch could affect the MIT and the

shape of the resistivity of the films very differently depending on the growth conditions and stoichiometry (cf. Figure A-7 c). In some cases, (the effective) strain has no effect as the sample is dominated by off-stoichiometry and defects (cf. Figure A-7 d).

Reproducibility is thus extremely challenging if one is pursuing the search for novel electronic phases in nickelates using strain engineering as instance [129].

b) Strain-engineering in rare-earth nickelates

This has prevented, for some time, the production of strain engineering studies. Prior to the beginning of this Ph.D., one of the unique strain engineering studies on nickelates was performed by Triscone's group in [129]. A figure of this study is reported below:

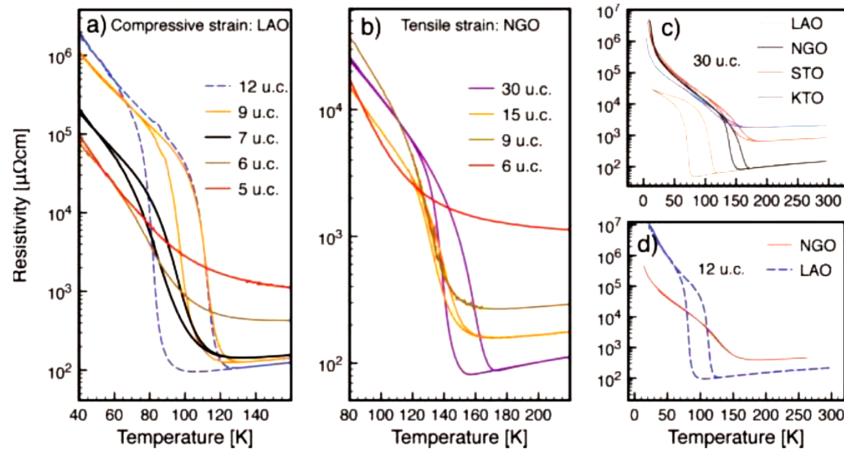


Figure A-8: Temperature dependence of the resistivity for different thicknesses on LAO (a) and on NGO substrate (b) and for 30 u.c thick NNO grown on various substrates (c). (d) comparison of temperature dependent transport measurement for 12 u.c. thick samples grown on top of NGO and LAO. Adapted from [129].

They showed that the resistivity was dramatically affected by strain. This is clearly visible from Figure A-8 (c) and (d), which present very distinct temperature dependent resistivity curves. For instance, a 12 u.c.-thick NNO thin film grown on LAO presents a large hysteresis whereas none is apparent when the sample is grown on NGO. The thickness dependence of the $R(T)$ in the samples is also modified under strain (cf. Figure A-8 a and b). Note that because of confinement effect (that we discuss just after), the hysteresis is eventually lost. However, the critical thickness at which the hysteresis vanishes depends on strain (7 u.c for LAO, and 15 u.c. for NGO).

During the course of this Ph.D., other nice studies have shown the great potential of strain-engineering for tuning nickelates magnetic and electronic properties.

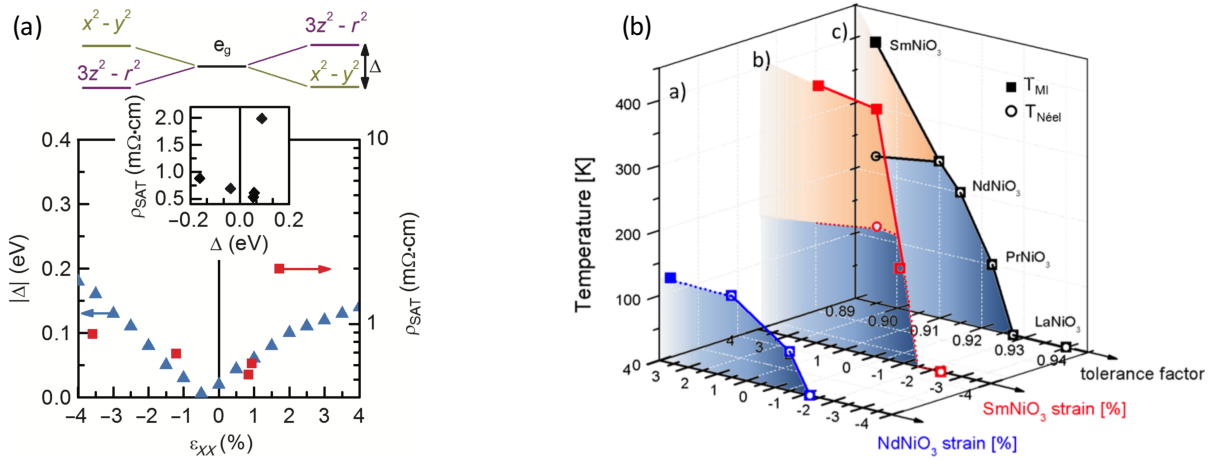


Figure A-9: (a) calculated e_g -orbital peak splitting (triangle) and saturation resistivity (square) depending on the in-plane strain state of the films. Inset presents the correlation between these two quantities. (a) is adapted from [130] (b) phase diagram of NNO (blue) and SNO (red) as a function of the strain, the bulk phase diagram is reported in black. (b) is adapted from [131]

In Figure A-9 (a), we report work by the Stemmer's group [130], where the authors calculated the orbital polarization of NNO thin films as a function of the in-plane strain state of the films. They clearly observe that strain can be used to nicely tune the orbital polarization from an in-plane polarized orbital (x^2-y^2) to an out-of-plane polarized orbital (z^2): When the in-plane strain is compressive the orbital occupancy is rather out-of-plane, whereas the opposite is obtained for tensile strain. They also noted a correlation between the orbital occupancy and the room-temperature resistivity of the films (cf. Figure A-9 (a)-inset).

Figure A-9 (b) shows how effective strain can be used for tuning both electronic and magnetic phase transitions. Indeed, SNO under compression exhibits a smaller MIT and antiferromagnetic transition, whereas tensile strain seems to be less effective at tuning these instabilities. Note that for compressive strain larger than 1%, SNO mimics the transport properties of NNO with simultaneous AFM ordering and MIT.

As we already observed in Figure A-8, confinement can also disturb the transport properties of nickelate thin films.

c) Confinement effects

Indeed, Triscone's group [132] also showed that LNO thin films grown on STO presented a MIT for thickness below 7 unit cells (cf. Figure A-10 a). For a same thickness (cf. Figure A-8), NNO

grown on LAO lost the hysteretic 1st order character of its MIT. They interpreted this phenomenon as due to weak localization of the charge carriers where impurity-induced quantum interference enhances backscattering and thus leads to a reduction of the conductivity.

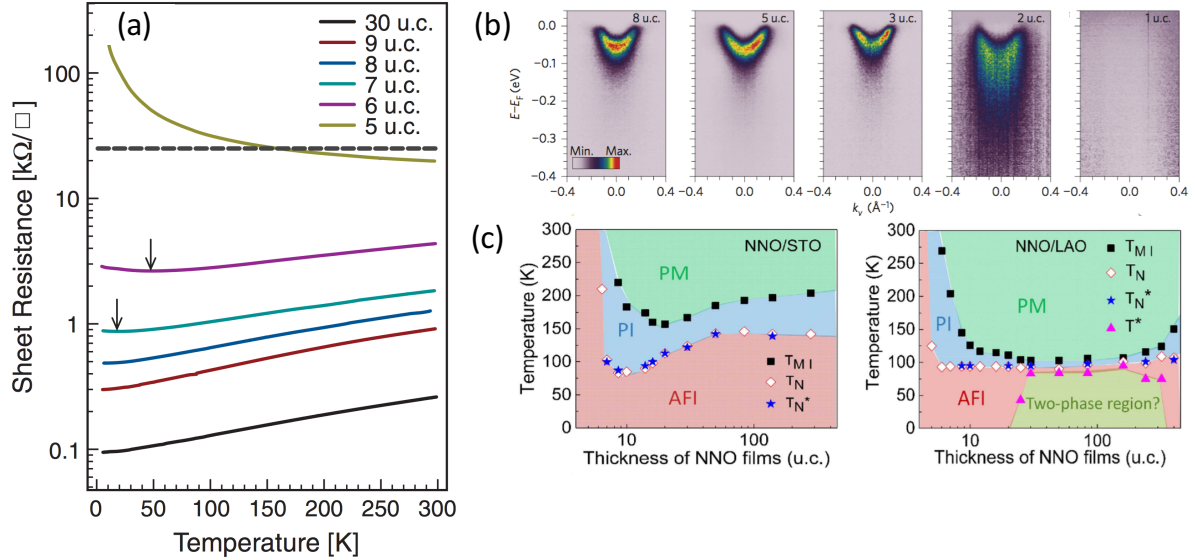


Figure A-10: (a) temperature dependence of the sheet resistance for different LNO thickness grown on STO substrate [132] (b) ARPES measurements near the Fermi level for different LNO thicknesses [133]. (c) Temperature-thickness phase diagram for NNO deposited on STO or LAO substrates [134]

This effect was later discussed in LAO by means of ARPES in [133]. If the authors of this study confirmed the presence of a 7 u.c. metal-insulator transition in LNO, they measure a momentum distribution of the ARPES peaks width at the Fermi level that was largely thickness independent from 8 Å down to 2 u.c.. This is not expected for a localization-driven MIT.

They argued instead that the MIT was rather correlated to a sudden breakdown of the Fermi-liquid picture and the appearance of quasi-particle peaks below 2 u.c. with the spectral weight being transferred to larger binding energies (cf. Figure A-10 b). Polar distortions in few u.c.-thick layers may indeed cause small structural rumpling close to the LNO surface yielding out-of-plane Ni-O bond lengths modifications that would result in the observed MIT.

In other RNO, confinement also plays a role as proven by [134]. Looking at the thickness dependence in Figure A-10 (c), the phase diagrams present two main regions regardless of the substrate: below ~ 20 u.c., dimensionality is dominant and the physics resembles the one discussed in LNO: metal-insulator and magnetic transitions increase quickly due to interference-induced localization. Above a certain critical thickness, they both decrease with thickness. This suggests a dominant effect of strain following what was reported in the previous sub-section.

d) A debated ground state

The phase diagram of rare-earth nickelates presented in Figure A-11 highlights nicely the richness and complexity of the RNO family. Indeed, nickelates (in bulk as much as in thin-films) exhibit an unusual metal-insulator transition, coupled to a paramagnetic-to-antiferromagnetic transition that may happen at different temperatures. As we saw both transitions can be strain- or dimensionally-engineered. However, the most efficient knob to tune magnetic and electronic coupling seems to be decreasing the rare-earth ionic radius in rare-earth nickelates, from La to Pr to Sm to Lu. Interestingly, the coupling between magnetic and electronic degrees of freedom in nickelates is exemplified by the concomitant increase of the Néel and metal-insulator transition temperatures, even in regions where they do not happen simultaneously. Indeed, apart from PNO and NNO, the Néel temperature is always lower than the MIT.

Surprisingly, LaNiO_3 does not fit in this picture. First, it does not adopt an orthorhombic ($Pbnm$) but rather a rhombohedral ($R-3c$) structure. Second, it does not present a MIT but rather a paramagnetic metallic behavior at all temperatures in the bulk.

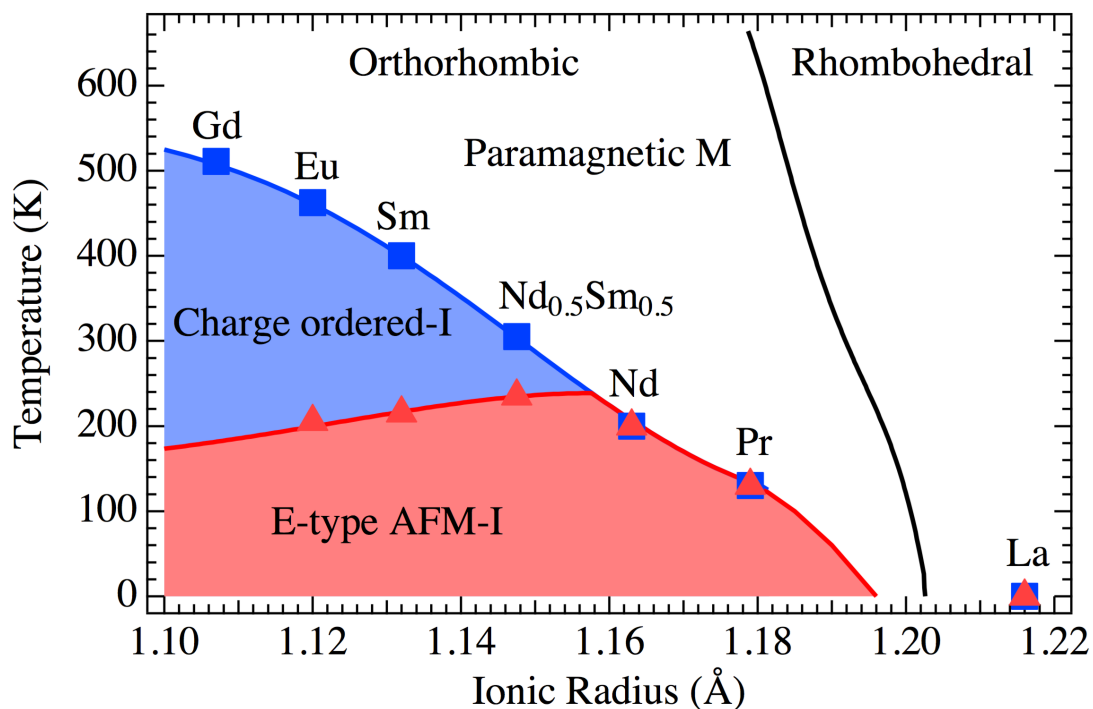


Figure A-11: phase diagram of rare-earth nickelates with the critical temperatures of the different phases as a function of the ionic radius adapted from [135]

In the other RNO compounds, the metal insulator transition (MIT) is accompanied by a

structural phase transition from a high temperature orthorhombic ($Pbnm$) phase to a low temperature monoclinic ($P2_1/n$) one (cf. Figure A-11 b) that exhibits a larger volume (cf. Figure A-1). The monoclinic distortion is quite small, but has been detected by X-ray diffraction and Raman scattering [14, 15]. The complexity of this tunable ground state has raised a lot of attention and debate over the years. Divergences also arise when dealing with identifying the primary order parameter that drives the MIT. In the following figure, we present the three main scenarios.

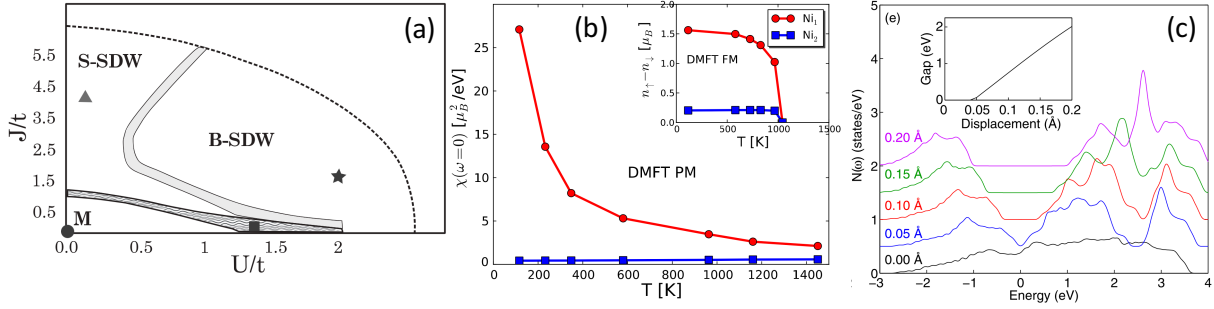


Figure A-12: (a) MIT phase diagram of bulk RNO depending on the Hund's coupling (J) and the d - d repulsion term (U) normalized to the hopping term in an idealized two band models adapted from [138]. B-SDW and S-SDW stand for "site-centered" (S-) and "bond-centered" (B-) Spin Density Waves. (b) temperature dependence of the local magnetic susceptibility of LuNiO_3 for disproportionated Ni_1 (red) and Ni_2 (blue) adapted from [139] (c) single-particle density of states as a function of the energy for different oxygen displacements (inset: gap as a function of the oxygen displacement) adapted from [140]

The three models are close in their conclusions but discuss different causes and consequences of the appearance of the MIT.

- Balents et al., [138,141] proposed an idealized two-bands model for describing "weakly coupled" nickelates as NNO and PNO. In this specific case, the authors argue that all disproportionation effects are caused by itinerant behavior of the carriers tight to Fermi-surface instabilities. They claim that flat bands in nickelates appear favorable for a nesting-based spin-density-wave instability. In the ideal cubic phase, they obtain two types of insulating ground states, corresponding to either "site-centered" (S-) and "bond-centered" (B-) SDWs (cf. Figure A-12 a). They believe that for symmetry reasons, in the orthorhombic phase, B-SDWs would be shifted off producing weak charge-ordering.
- Millis et al. [139] rather believe that due to translational symmetry breaking the Ni sites differentiate into a Ni_1 surrounded by long bonds leading to a decoupled sublattice and a Ni_2 encircled by short bonds, instead strongly coupled to O p-holes that eventually bound to form singlet states. In this vision, the long-bond Ni sites would have $S=1$ spin state, while the others would be screened by the O holes with

total value $S=0$. This is observed in the calculation of the local magnetic susceptibility (cf. Figure A-12 b).

- Sawatzky et al. [140,142], first, explain the absence of experimental evidence for Jahn-Teller or charge order [143] by a non-ionic ground state even at high temperature: Ni would not be purely $3d^7$ but rather $\alpha |3d^7 \rangle + \beta |3d^8L \rangle$, with $\alpha^2 + \beta^2 = 1$, and $\beta \gg \alpha$, which is backed up by some experimental evidences (cf. Figure A-5 b). According to this scenario, the oxygen holes would then couple to bond-stretching vibrations. This modulation would strongly link carriers with structural distortions. Even without charge movement, they claim that d^8L states would disproportionate into d^8L^2 and d^8 for a sufficiently large oxygen displacement (cf. Figure A-12 c inset). In this description, this would apparently look like charge disproportionation as oxygen holes would adopt the e_g symmetry of Ni 3d leaving Ni in a formal 4+ valence ($3d^6$).

Depending on whether structural, spin-based, or covalent degrees of freedom are the first order parameter, the description of the ground state and its properties at low temperature slightly differ. As stated by Balents [138], a crossover from weak to strong correlations takes place when changing the rare-earth which also accounts for the difficulty to produce one single theoretical framework in which all nickelates can be carefully reproduced. This probably also explains the huge diversity of U values used in DFT studies from weak to strong corrections that have been proposed in different works [139,144,145]. However knowing the end-goal of this Ph.D. work – studying the effect of different rare-earth nickelates when interfaced with GTO – finding such a theoretical framework is absolutely crucial in our quest for a better understanding of the physics of interfacial correlations.

e) Crossing from ionicity towards covalence

In the next section, we will discuss the construction of such a framework and discuss its main conclusions. This section is based entirely on DFT+ U calculations on various nickelates that were performed by J. Varignon, who was a PostDoc at CNRS-THALES during my Ph.D. Even if I did not perform any of the simulations, I helped in building the numerical experiments and was strongly involved in data analysis. I present these results here as they constitute the basic understanding on which we will base all future analysis.

1) Structure of the ground state

First, full geometry relaxations were performed for both possible $Pbnm$ and $P2_1/n$ structures with different magnetic orderings: ferromagnetic (FM) as well as complex E, S and T-type AFM orderings based on $[\downarrow\downarrow\uparrow\uparrow]$ -spin chains in the (ab)-plane with different stacking along the c axis (cf. Figure A-3). Several nickelates ($R=Y, Dy, Tb, Gd, Eu, Sm, Nd$ and Pr), covering all the phase diagram, have been considered. All nickelates relax to a $P2_1/n$ insulating ground state with complex antiferromagnetic structures (S or T-type depending on the rare-earth) and band gaps both compatible with experiments [114,146]. All $Pbnm$ phases favor a FM solution, which is the best approximation of a paramagnetic solution in DFT, and are metallic.

In the following, calculations were performed employing the PBEsol functional in combination with a U correction of 2 eV on Ni-3d states in order to account for electronic correlations. The reliability of the DFT+U calculations was checked by changing the U correction to either 0 eV or 5 eV in $SmNiO_3$. While the ground state is unchanged when no U- correction is applied – the gap is eventually decreased to 91 meVs –, imposing $U = 5$ eV yields a $P2_1/n$ ferromagnetic and insulating solution that is much more stable than the considered complex AFM orderings ($\Delta E \approx 160$ meV per 80-atom unit cell). This further supports the choice of a relatively small Hubbard correction for the Ni-3d electrons.

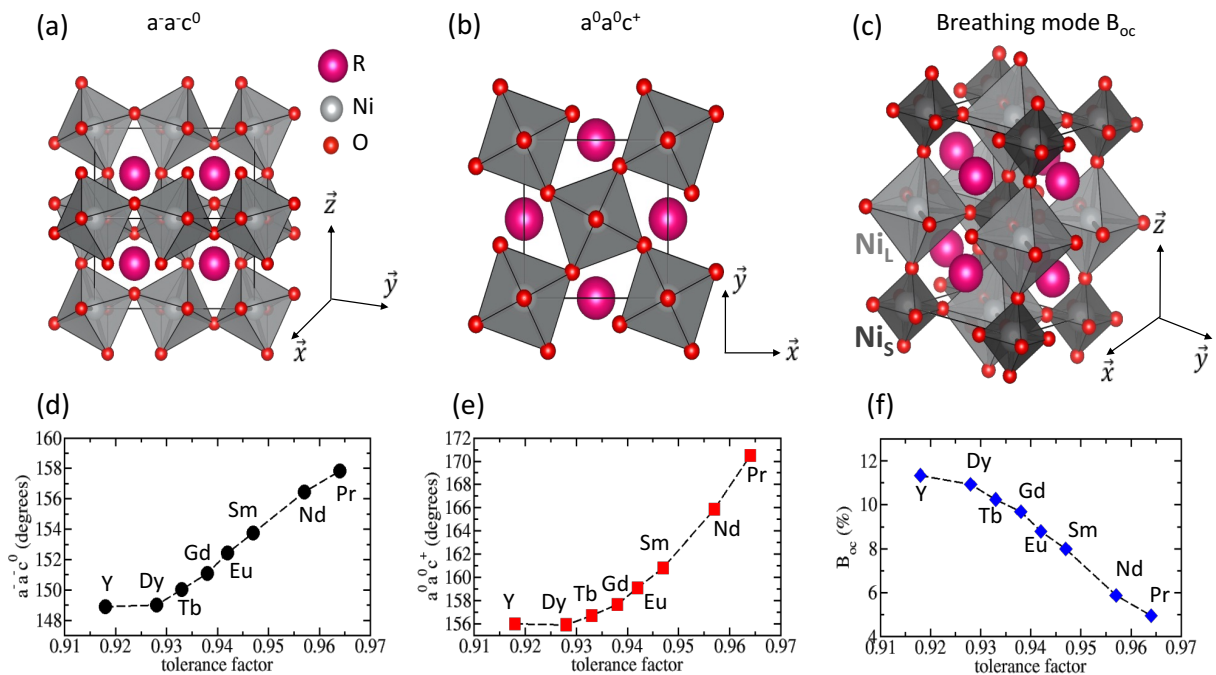


Figure A-13: Rare-earth nickelates ground state structural properties. (a, b and c) Schematic pictures of the three main lattice distortions appearing in the ground state of nickelates: $a^-a^-c^0$ antiferrodistortive motion (a), $a^0a^0c^+$ antiferrodistortive motion (b) and breathing of the oxygen cage octahedra B_{oc} (c). (d) and (e) Ni-O-Ni angles (in degrees) produced by the $a^-a^-c^0$ (d) $a^0a^0c^+$ (e) antiferrodistortive motions. (f) Oxygen cage octahedra volume expansion/contraction (in %) produced by the breathing mode.

The optimized ground state structures are described by three main lattice distortions (Figure A-13 a-c):

- two antiferrodistortive (AFD) motions denoted, in Glazer's notations [38]: $a^-a^-c^0$, meaning two antiphase rotations along a and b-axis with no rotation along the third direction, and $a^0a^0c^+$, meaning one single rotation along the c-axis, producing the intermediate $Pbnm$ symmetry
- a breathing of the octahedra B_{oc} (see Figure A-13 a, b and c) which only appears in the $P2_1/n$ symmetry and produces a rock-salt pattern of small and large NiO_6 octahedra leading to two different Ni sites (see Figure A-13 c). In the following sections, Ni_S and Ni_L will refer to the Ni sites located in the small and large NiO_6 octahedra respectively.

As usual in perovskites, the amplitude of Ni-O-Ni angles induced by oxygen rotations is governed by steric effects (see Figure A-13 d and e), and nickelates with low tolerance factors appear more distorted. The volume expansion/contraction of the oxygen cage induced by B_{oc} also appears to be modulated by the rare-earth (see Figure A-13 f), as smaller R cations produce larger breathing distortion. Finally, Jahn-Teller distortion in the ground state is one to two orders of magnitude smaller than B_{oc} or the two AFD motions respectively, in agreement with experimental evidence of an absence of Jahn-Teller active site [143].

2) Electrostatic properties of the ground state

The electrostatic properties of the optimized ground states were analyzed by three methods:

First, Figure A-14 (a) reports both Ni site occupancy as a function of the rare-earth. Although atomic charges are not uniquely defined in DFT calculations, sphere integrations around the Ni cations can provide some insight into the possible charge ordering despite the fact that they might not reflect the real site occupancies. Surprisingly, a weak and rather constant charge ordering is observed between both Ni sites ($Ni^{3+\delta} + Ni^{3-\delta}$), going from $\delta=0.13$ ($YNiO_3$) to $\delta=0.11$ ($PrNiO_3$), but this latter is opposite to expectations. Ni_S , sitting in the smallest cage octahedra, holds more

electrons than Ni_L , located in the largest NiO_6 octahedra. Since the breathing mode B_{oc} is an inter-site e_g levels splitting between both Ni_S and Ni_L [147,148], Ni_S should hold less electrons than Ni_L .

Then, Born Effective Charges (BECs) [149–151] which are better defined – and experimentally measurable – quantities, that characterize the amount of charge displaced upon the movement of individual atoms were used. In the representative case of SNO, BEC for Ni_L was $Z_{Ni_L} \approx +2.5$, which is not far from the nominal oxidation state of 2+ that is associated with Ni in the complete charge-disproportionation picture (Figure A-14 b). However, for Ni_S a similar $Z_{Ni_S} \approx +2.1$ was obtained, which severely deviates from the expected value (4+) in the charge-disproportionation picture. Figure A-14 (b) reports the same behavior across the various studied compounds. Hence, from the point of view of the effective charges, the two Ni sites behave similarly. The disproportionation effects being weak, the calculation does not comply with the usual picture of charge ordering in RNO.

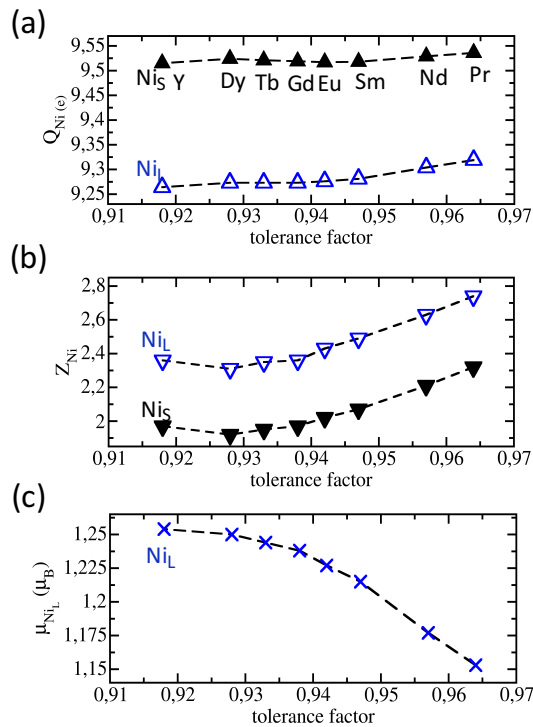


Figure A-14: (a) Total number of electrons Q_{Ni} ascribed to Ni_S (black filled up triangles) and Ni_L (blue unfilled up triangles) during the GGA+U sphere integrations as a function of the tolerance factor. (b) Computed average Born effective charges of both Ni_S (black filled down triangles) and Ni_L (blue unfilled down triangles) as a function of the tolerance factor. (c) Computed magnetic moment (in μ_B) of Ni_L site (blue crosses) as a function of the tolerance factor. The magnetic moment of Ni_S is exactly zero in the calculation.

Last, magnetic moments are computed for both Ni sites. it appears to be in contradiction with the conclusions of the charge analysis. Indeed, as shown in Figure A-14 (c), the large difference

between Ni_L – with a moment larger than 1 μ_B – and Ni_S – for which the magnetic moment is null – suggests two very different electronic states. The conclusion of this first analysis is that, in RNO compounds, all Ni atoms seem to display a similar oxidation state. Yet, the presence of a large breathing modes, added to the large deviation of magnetic moments seem to point to very different electronic states.

3) Imaging orbital occupancy in the ground state

Wannier functions helped grasping more visually the microscopic physics of the orbital occupancies. The Wannier90 package was used to determine the maximally-localized Wannier Functions that reproduce the occupied electronic manifold. Further, the analysis is run without having to make any assumption on the precise character of the occupied Ni and O orbitals, which complicated the choice of the initial atomic orbitals onto which the Kohn-Sham states are projected in order to extract the initial gauge matrix for the localization procedure. Nevertheless, the following robust strategy was used to proceed. The whole occupied manifold was considered in order to disentangle a set of 2×(144+10) MLWFs, where 2×144 = 2×3×48 is the total number of O-2*p* orbitals available in our 80-atom supercell and 2×10 = 2×5×2 is the number of Ni-3*d* orbitals corresponding to two specific Ni atoms. (Note that separate MLWFs optimizations were performed for the spin-up and spin-down channels.) Hence the following initial atomic orbitals were used : 3 generic *p* orbitals centered at each O anions and 5 generic *d* orbitals centered at two neighboring Ni cations; this couple of Ni cations were chosen to be first-nearest neighbors, so that one Ni_L and one Ni_S is observed. The basic qualitative results of this optimization were the same for all the nickelates considered, and thus the following discussion is not compound specific.

Figure A-15 (a) and (b) report the e_g orbitals obtained from the second set of calculations on two consecutive Ni sites in SNO ground state. One sees that very well defined $d_{x^2-y^2}^{\uparrow}$ and $d_{z^2}^{\uparrow}$ orbitals emerge on Ni_L site, only in the spin ↑ channel, while Ni_S site does not develop any e_g orbitals in both spin channels. Eventually, some tails of the Ni_L e_g[↑] orbitals are found on their surrounding oxygens, likely coming from the strong hybridizations between Ni 3*d* and O 2*p* states. The third set of calculations, including all O 2*p* orbitals during the construction of these e_g states yields the same conclusion.

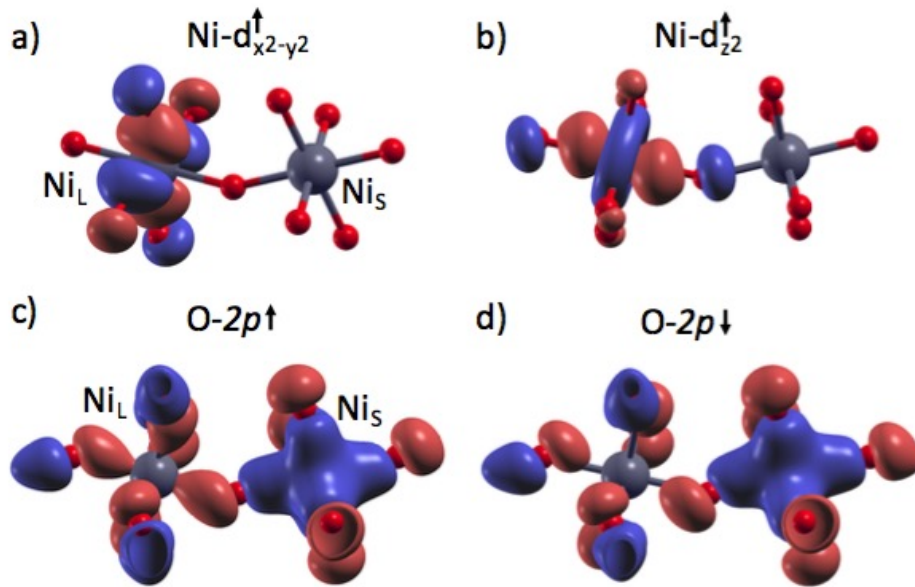


Figure A-15: Orbital occupancies in rare-earth nickelates. (a) $d_{x^2-y^2}^{\uparrow}$ maxi localized Wannier function on two consecutive Ni sites. The Ni_L site bears a spin \uparrow . (b) $d_{z^2}^{\uparrow}$ maxi localized Wannier function on two consecutive Ni sites. The Ni_L site bears a spin \uparrow . (c) O 2p maxi localized Wannier functions oriented along the Ni-O bonds on the two consecutive Ni sites in the spin \uparrow channel. (d) O 2p maxi localized Wannier functions oriented along the Ni-O bonds on the two consecutive Ni sites in the spin \downarrow channel.

As it is clearly visible in Figure A-15 for both O 2p spin channels, WFs have their centers significantly shifted towards the Ni_S cations and away from the Ni_L sites. Hence, Ni_S cations appear to be in a 4+ state because they receive a significant fraction of electrons coming from the surrounding oxygens, with which they are strongly hybridized. In the end, charge around the Ni_S ions renders results that are similar to those of the Ni_L, contradictory with disproportionation and suggesting valence state closer to 4+.

Across the series, O-2p centers get closer to the Ni_S cations for smaller rare earths, increasing the localization of the charge on Ni_S. Additionally, the O-2p WFs behave similarly irrespective of their spin polarization, so that their shifting does not result in any magnetic moment at the Ni_S sites.

The Wannier analysis therefore leads to the conclusion that a full disproportionation occurs in the system, with clearly distinct Ni⁴⁺ in the small octahedra (non-magnetic) and Ni²⁺ in the large octahedra (magnetic) sites. Simultaneously, the O-2p WFs approach the Ni⁴⁺ sites, ultimately yielding Ni_S and Ni_L that are nearly equivalent from the point of view of the charge (static and dynamics) around them.

4) Reconciling ionic and covalent scenarios

The results of these calculations thus appear to be compatible with the ionic disproportionation effects originally proposed to occur at the MIT [152,153]. They are indeed reminiscent of this picture, with the observation of a subsequent breathing distortion modulated by the rare-earth [154] – that should result in a varying magnitude of the charge disproportionation – and a charge disproportionation between Ni sites complying with numerous experimental works, and most notably with XAS and Mössbauer measurements [154,155].

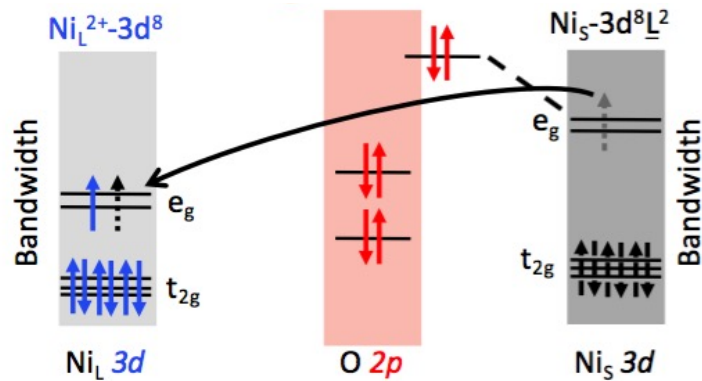


Figure A-16: Schematic picture of the electronic structure of rare-earth nickelates ground state.

Nevertheless, the results are also and mostly compatible with the model of Sawatzky [44], Mizokawa et al. [142] as well as with recent Dynamical Mean Field Theory (DMFT) studies [139,145,156] proposing a ligand-hole structure in rare-earth nickelates. Indeed, the Wannier analysis indicates that Ni_L cations have a $3d^8$ electronic configuration. More importantly, it is also compatible with the $3d^8 L^2$ configuration proposed for the Ni_S sites and backed up by XPS measurements [114]. Given that the integrated and dynamical Born charges suggest that the Ni_S and Ni_L sites host a similar number of electrons, results do in fact point to a situation in which each O_6^- cage shares approximately two electrons with the Ni_S at its center, exactly as in the ligand-hole picture. As for magnetic moments at the different Ni sites, these results are also clear and compatible with both proposed pictures: Ni_L bears a magnetic moment approaching $2 \mu_B$, as it corresponds to having Ni^{2+} in a high-spin configuration. Then, Ni_S has no magnetic moment associated to it, as it would correspond to a nominal Ni^{4+} low-spin configuration, also supporting Millis' conclusions [139]. The electronic structure is summarized in Figure A-16 and is based on having (i) a full charge disproportionation between Ni_L and Ni_S sites accompanied by a breathing mode and (ii) 2 electrons from surrounding oxygens shared with the depleted Ni_S site, leaving the impression of two similar Ni^{2+} sites in the system.

5) Role of the covalence

Finally, the covalent character of rare-earth nickelates seems to play a key role in the nature of the metal-insulator phase transition. Experimentally, it is observed that the MIT is different than the magnetic phase transition temperature T_N for all nickelates except for $R=Pr$ and Nd . This feature is well represented in the calculations as all geometry relaxations of the $P2_1/n$ phase with a ferromagnetic ordering yield an insulating phase. Regarding NNO and PNO, no opening of the band gap is observed with a FM solution. The complex antiferromagnetic ordering therefore appears to be crucial for the appearance of a MIT. As a consequence, a control of the electronic and magnetic phases can be achieved by controlling the level of covalence in the system.

B - Probing the metal-insulator transition in $SmNiO_3$

As we have seen in the previous section, a lot of work has been devoted to the description and the characterization of the electronic and magnetic ground state of rare-earth nickelates. Remaining issues in nickelates can be categorized depending on the temperature at which the phenomena of interest happen:

- A first type of problem arises at the ground state, where fundamental questions are yet to be answered. However, we believe that this latest point has reached a certain consensus among the community that agrees to consider nickelates ground state as resulting from a self-doping process, following disproportionation of Ni sites, into a $S=1$, $Ni\ 3d^8$ site, and a $S=0$, $3d^8L^2$ site.
- A second category of problems concerns the description of the appearance of the different magnetic and electronic order parameters at the Néel temperature and at the metal-insulator transition temperature respectively.
- Finally, a last question concerns the type of transition, either second-order (as in SNO and larger rare-earth) or first-order (as in NNO and PNO). This problem is intimately related to the coupling between the different degrees of freedom in the nickelates (namely the orbital, electronic and magnetic degrees of freedom).

Some recent experiments have been done on the temperature-dependence of the electronic and magnetic first-order transitions in PNO and NNO [135,157], however, the physics of the second

kind of nickelates (beyond SNO) has yet been overlooked.

In the next chapter, we will try to make up for this by analyzing charge and magnetic sensitive synchrotron radiation-based spectroscopic measurements performed at different temperatures on SNO thin films.

1 - Sample characterizations

We thus grew a 6 nm-thick SNO thin film on top of LaO-terminated LAO substrates by means of pulsed laser deposition. The sample was deposited at temperatures close to 650 °C for an oxygen pressure between 0.2 mbar and 0.4 mbar. The nickelates were previously optimized in our group by Dr. F. Bruno, a former post-doc in our lab, and we used the same conditions as the ones reported in [96]. Figure B-1 shows the temperature dependence of the resistivity.

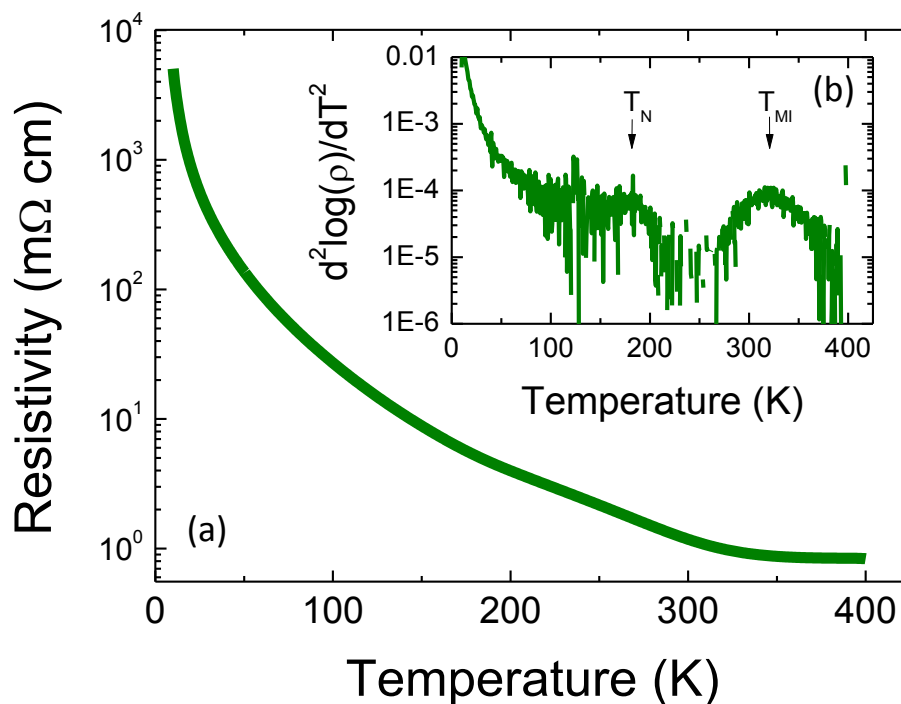


Figure B-1: (a) Temperature dependent resistivity of a 6 nm-thick SNO sample grown on top of LAO. (b) second-derivative of the log-resistivity

Following several studies [158–161], we characterized the MIT and the AFM transition by looking at kinks in the derivative of the log-resistivity (which is equivalent to looking for local maxima in its second derivative). We find that the MIT happens around 320 K while the Néel temperature is

around 180 K.

2 - Temperature dependence of isotropic XAS

The sample was first characterized by means of isotropic absorption spectroscopy in total electron yield (XAS-TEY) at high (HT) and low temperatures (LT) in the absence of magnetic field.

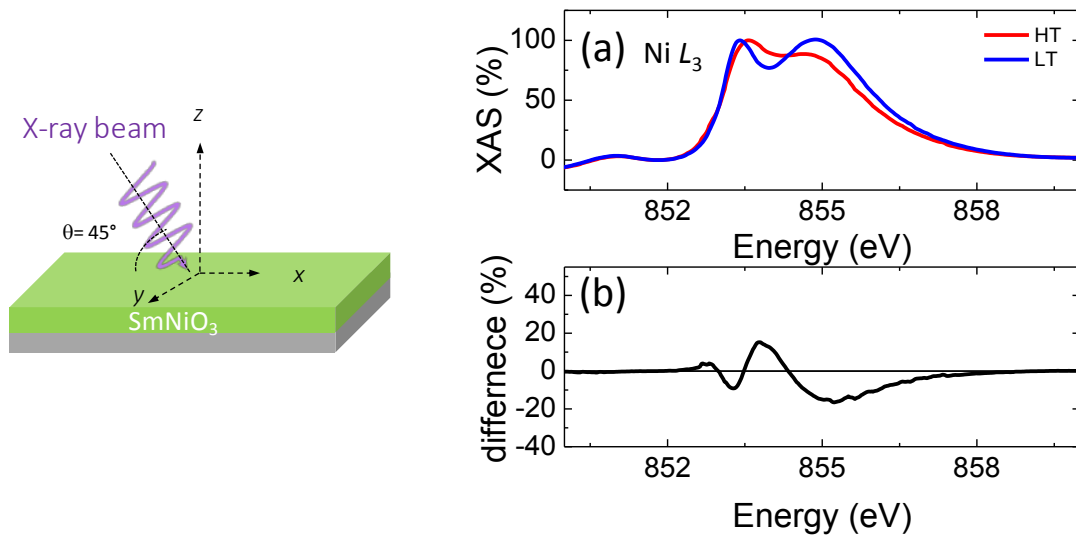


Figure B-2: (a) Ni L_3 edge at high (HT-red) and low temperature (LT-blue) in SNO (b) Difference of the High and Low temperature spectra. To amplify differences, the spectra were further normalized at the low-energy peak.

We present, in Figure B-2 (a), XAS spectra for high (red curves) and low temperature (blue curves) at Ni L_3 edge. The spectra display two features, at low (853.8 eV) and high energy (855 eV).

At low temperature, the low energy and high energy peaks are of almost equal intensity, meaning that their absorption coefficients are relatively similar. In a simplistic picture the L_3 edge is much more excitonic in nature and allows in first approximation (within the atomic $2p^53d^8$ excitonic picture) to discuss the intensity variation in terms of changes in level occupancy [8]. The change in spectral shape, in particular the intensity, is thus suggesting a change of electronic structure from high to low temperature. We will see that this is very useful to track down the metal-insulator transition.

The difference signal (black curve in Figure B-2 b) looks like the derivative of both peaks. This can be interpreted as a clear signature that both peaks are pushed apart at low temperature compared to their initial position at high temperature.

Van Veenendaal *et al.* [135,162] proposed that changes in the multiplet splitting of the Ni L_3

absorption edge (low- and high-energy peaks) can be used to estimate the level of covalence. Previous studies in bulk samples [162,163] have shown that progressing in the RNO series (decreasing the rare earth ionic radius) results in a larger splitting of the L_3 peaks, analyzed in terms of a decrease in covalence. This was recently confirmed by the work done by Bisogni et al. in [164], where the low energy peak at the Ni L_3 edge is ascribed to d-states while the one at larger energy is rather associated to p-holes states. Thus, a weaker splitting would correspond to a smaller p-d energy difference thus to a larger covalence.

3 - Temperature dependence of resonant X-ray diffraction

In order to complement charge-sensitive XAS measurements, the sample was then characterized by means of resonant X-ray diffraction (REXD) at the BESSY-II undulator beam line UE46-PGM1. The REXD was performed at the Ni L_3 edge (exactly at 853.49 eV) and Sm M_5 edge (at exactly 1078.95 eV), following a geometry in which the sample was mounted at 45 degrees in χ as in [125] in the absence of magnetic field. The beam was aligned along the diagonal of the substrate. Prior to measuring each resonant diffraction spectra, we realigned the sample in (x,y,z)-directions and performed ω -scans, to insure the perfect centering of the sample even in the presence of thermal dilatation. Results are presented in Figure B-3.

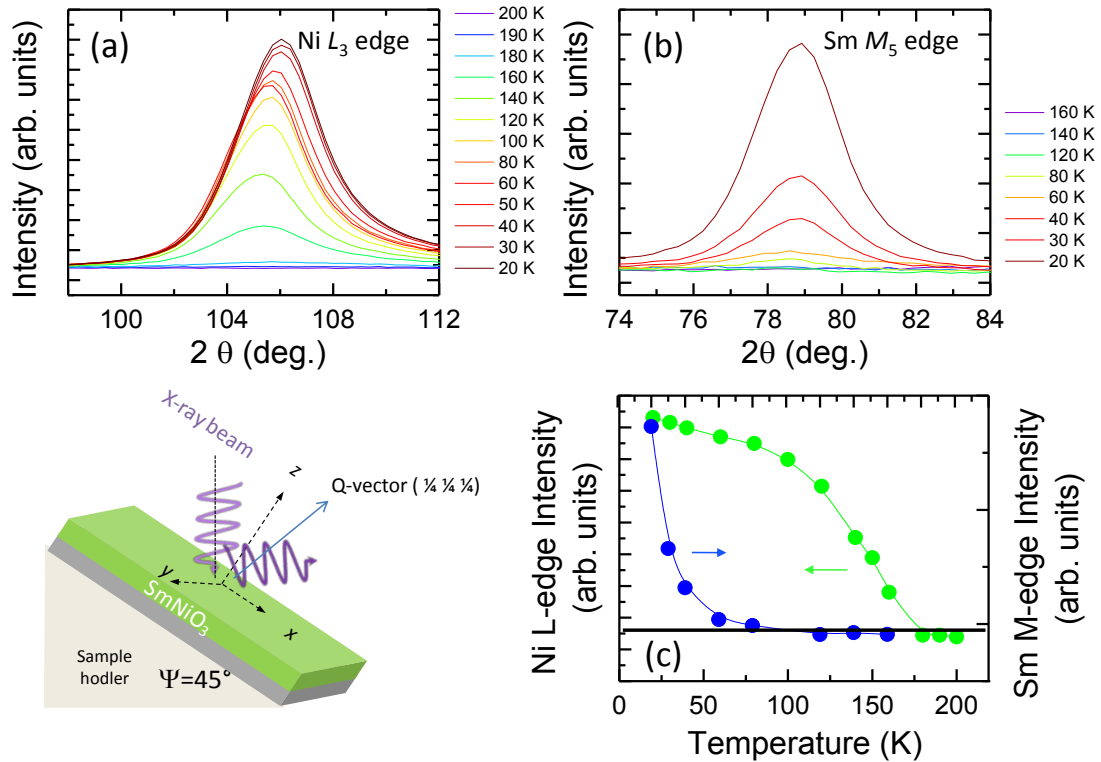


Figure B-3: Ni L-edge and Sm M-edge (b) resonant XRD at the $[\frac{1}{2} \frac{1}{2} \frac{1}{2}]$ -peak of the antiferromagnetic E-type order in SNO. (c) Temperature-dependent variation of the peak intensity at the Ni L-edge (in green) and at the Sm M-edge (in blue).

In Figure B-3 (a), when the energy is set at the Ni L₃-edge, we observe the appearance of a peak around 106 degrees whose intensity rises when the temperature is lowered. The same is observed at Sm M₅-edge, but at a position close to 79 deg. (cf. Figure B-3 b). In Figure B-3 (c), we report the intensity of both peaks as a function of the temperature. Ni ions antiferromagnetically align at ~ 180 K. This temperature is in agreement with resistive measurements (cf. Figure B-1 b) and with values reported for bulk samples [99]. The Sm sub-lattice aligns at the same resonant wave-vector but at a much lower T_N of about 50 K.

What is very surprising is that the AFM peak position moves from an initial $2\theta = 105.25$ degrees towards a final $2\theta > 106$ degrees when the temperature is decreased. This corresponds to a displacement from $Q=0.6911 \text{ \AA}^{-1}$ to $Q=0.6876 \text{ \AA}^{-1}$ corresponding to a variation of 0.51 %. Interestingly, the peak position is non linearly displaced which suggests that it is not due to thermal displacements or to any other stricitive effects (cf. Figure B-3 a) that would be linear in temperature.

4 - Temperature dependence of linearly polarized XAS

In order to probe both magnetic and charge degrees of freedom, we turn on the linear polarization of the X-rays using both vertical and horizontal polarization. We chose a 45 degrees X-ray incidence angle at $\chi=0$ degree in order to maximize linear dichroism (which is obtained as the difference between the two polarizations); we measured the signal in TEY in the absence of magnetic field. This configuration sets the vertical polarization of the X-ray light along the suspected low temperature $\langle 111 \rangle$ -direction of the magnetic order in SNO samples – but also provides the signal with both an in-plane and out-of-plane contribution in vertical polarization.

Figure B-4 summarizes the temperature dependent study. We observe two features in the signal both at the L_3 and L_2 edges in both polarizations. Note that in covalent nickel oxides, Haverkort et al. [8] mentioned that the physics at the L_2 edge is dominated by interferences between excitonic excitations of the L_2 edge and the continuum of states of the L_3 edge. As we discuss for isotropic XAS, we focus mainly on the L_3 -edge, which is much more excitonic than the L_2 edge. We can thus associate schematically the low energy-peak to d-states and the higher energy peak to the p-holes states.

Since the L_3 -edge low energy peak is barely changing with temperature, we will normalize the peak intensity difference calculated for the low (d-states) and high (p-states) energy peaks at the L_3 edge by the low energy peak (d-states). This will also remove any geometric contribution to the signal (due to the peculiar 45 degree-angle used here) when comparing horizontal and vertical polarization. We will label this quantity $\sigma_{x,z}$ depending on the polarization (vertical, z; horizontal, x).

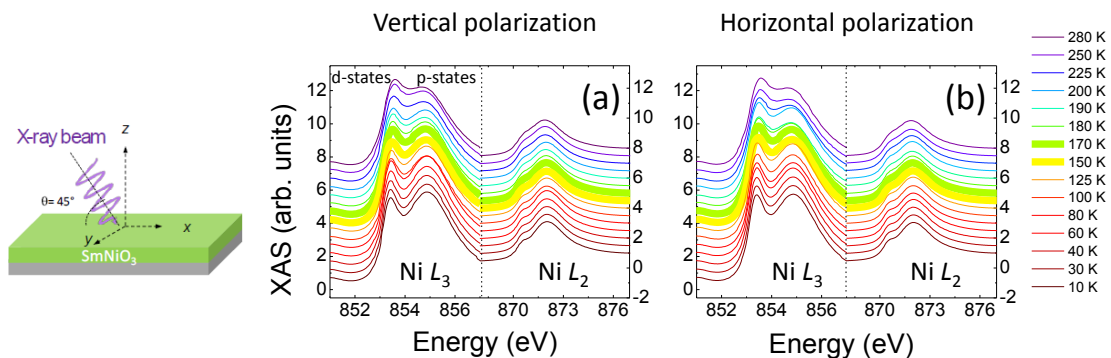


Figure B-4: Ni absorption spectra of a 6 nm-thick SNO grown on LAO. Ni L_3 edge and Ni L_2 -edge samples in vertical polarization (a) and in horizontal polarization (b) The thick curves are just above and below the Néel temperature.

At high temperature, in vertical polarization, the d-states peak is about 10 % more intense than the p-states peak. Nonetheless, at low temperature, the opposite situation is encountered and the p-states peak is now dominant by about 10 %.

For horizontal polarization, the d-states and p-states peak intensities are found to be similar

at low temperature although the relative intensity ratio was also virtually -10 % at high temperature.

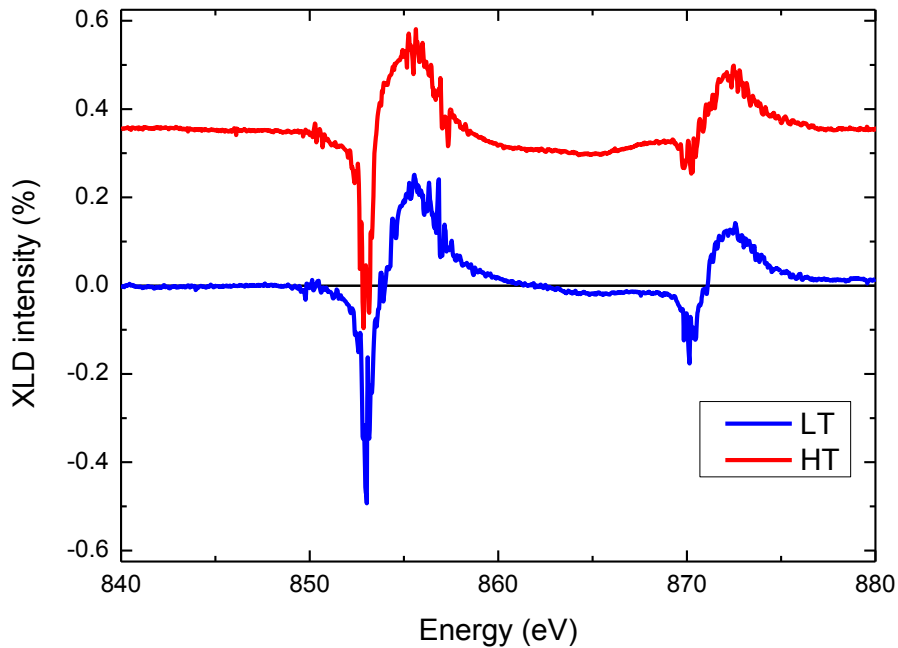


Figure B-5: Low (blue) and high temperature (red) X-ray linear dichroism (XLD) in SNO on top of LAO, normalized by the d peak intensity of the isotropic XAS spectra taken at the same temperature.

Figure B-5 presents the linear dichroism obtained from the difference between vertical and horizontal polarization at high (red) and low temperature (blue). No apparent variation is observed in the linear dichroic signal - which is surprising considering the changes in the relative p - d peak intensity ratio variations at the L_3 edge. The shape of the XLD is rather suggesting a weak compressive elongation of the octahedral cage weakly favoring the z^2 -orbital [96,165]. The strain state of nickelates on top of LAO substrates justifies the z^2 -orbital occupancy. Indeed, SNO is slightly compressively strained by -0.15 %. The compressive strain contracts the oxygens along the in-plane directions and expands it in the perpendicular direction. This recalls the mechanisms behind Jahn-Teller distortion (cf. chapter I) that would favor the out-of-plane polarized orbital over the in-plane polarized one. Note that this was also reported by Stemmer's group in [130].

5 - Discussion and conclusions

Figure B-6 summarizes all the different metrics that appeared to change in SNO upon varying temperature. The first panel Figure B-6 (a) presents the relative intensity ratio between the peaks

associated with the Ni L_3 edge p and d states for vertical (z) and horizontal (x) linear polarizations ($\sigma_{x,z} = \frac{p_{x,z} - d_{x,z}}{d_{x,z}}$), the second column gives the temperature dependence of the p-d states peak splitting. In Figure B-6 (c), we report the AFM peak position. And finally, in (d), we plot the orbital polarization ($P = \frac{n_{x^2-y^2} - n_{z^2}}{n_{x^2-y^2} + n_{z^2}}$) extracted from sum rules (cf. chapter II)

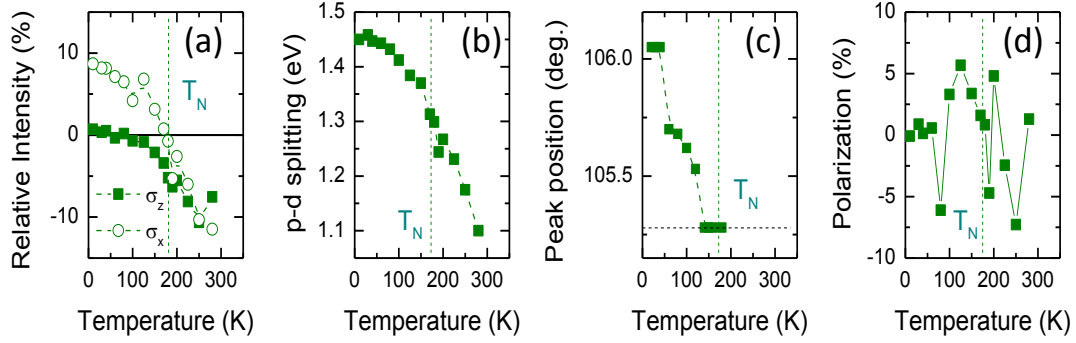


Figure B-6: Temperature dependence of (a) the relative $\frac{p-d}{a}$ intensity ratio at the Ni L_3 -edge for horizontal and vertical polarized X-ray light (b) p-d peak splitting. (c) AFM peak position (d) orbital polarization extracted from sum-rules for SNO.

In Figure B-6 (a), the peak-to-peak relative intensity fully reverses from -10 % to 10 % in vertical polarization (crossing 0 % at $T_N \sim 180$ K), σ_z , while in horizontal polarization, σ_x reaches 0 % at a temperature closer to 50 K.

Concomitantly, in Figure B-6 (b), the peak splitting increases from high to low temperature by more than 0.3 eV.

In the meantime, the peak position of the AFM resonance presents a non-linear displacement from incommensurate to the apparent $[\frac{1}{4} \frac{1}{4} \frac{1}{4}]$ -resonance. However, to fully determine the Q-value of the $[\frac{1}{4} \frac{1}{4} \frac{1}{4}]$ resonance we would need to perform further characterizations of the crystallographic unit cell of SNO deposited on top of LAO as a function of the temperature.

Finally, in Figure B-6 (d), we used sum rules (cf. chapter II) to compute the orbital polarization (P) value at different temperatures. We observe no clear dependence (within experimental signal-to-noise ratio) of the orbital polarization with temperature.

The peak splitting was already used in many studies [135,162,166] as a good metrics to track the level of covalence in rare-earth nickelates. Freeland et al. [135], go even further by stating that p-d peak splitting is actually a *measure* of how many O 2p holes are transferred to the empty Ni site. Interestingly, Figure B-6 (b) suggests that, in SNO, the on-site hole doping is a temperature activated process that increases from room temperature down to low temperature before reaching a saturation close to 50 K.

Let us now analyze in more details the evolution of $\sigma_{x,z}$ in Figure B-6 (a). The different temperature dependences between in-plane and out-of-plane seem to point toward a change of orbital occupancy. This behavior is however contradictory with the fact that no clear orbital polarization (cf. Figure B-6 d) is measured. We thus have to resolve that the discrepancy between the in-plane and out-of-plane orbital polarizations arises from another source of charge anisotropy.

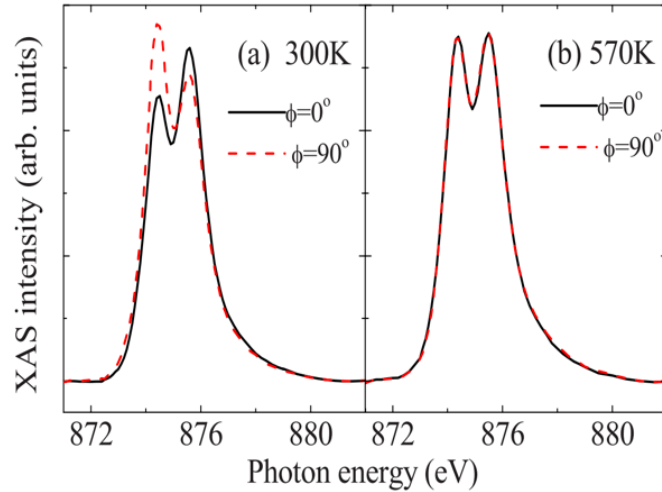


Figure B-7: Ni L_2 -edge XAS of 4.3 nm NiO films measured (a) at room temperature (AFM phase) and (b) at 570 K (paramagnetic) adapted from [167]

We believe that it may be due to spin-charge coupling. Indeed, it has been reported in many antiferromagnetic materials such as LaFeO_3 [168] or NiO [167] that spin-orbit coupling induces a deformation of the charge distribution along the direction of the magnetized spins. This deformation can then be detected through linear dichroism which is sensitive to any charge anisotropy. As one can see from Figure B-7, inversion of peak features in NiO looks very similar to what we observe in SNO. In NiO, this phenomenon has been solely ascribed to the presence of an AFM order, suggesting that the virtually identical inversion in SNO is also related to the appearance of AFM ordering. The difference between σ_x and σ_z can thus be interpreted as a difference in the amplitude of the local moments. If the amplitude of the spin moments is different for both orbitals in the magnetic unit cell, spin-orbit coupling would indeed affect differently each orbital resulting in an induced anisotropy.

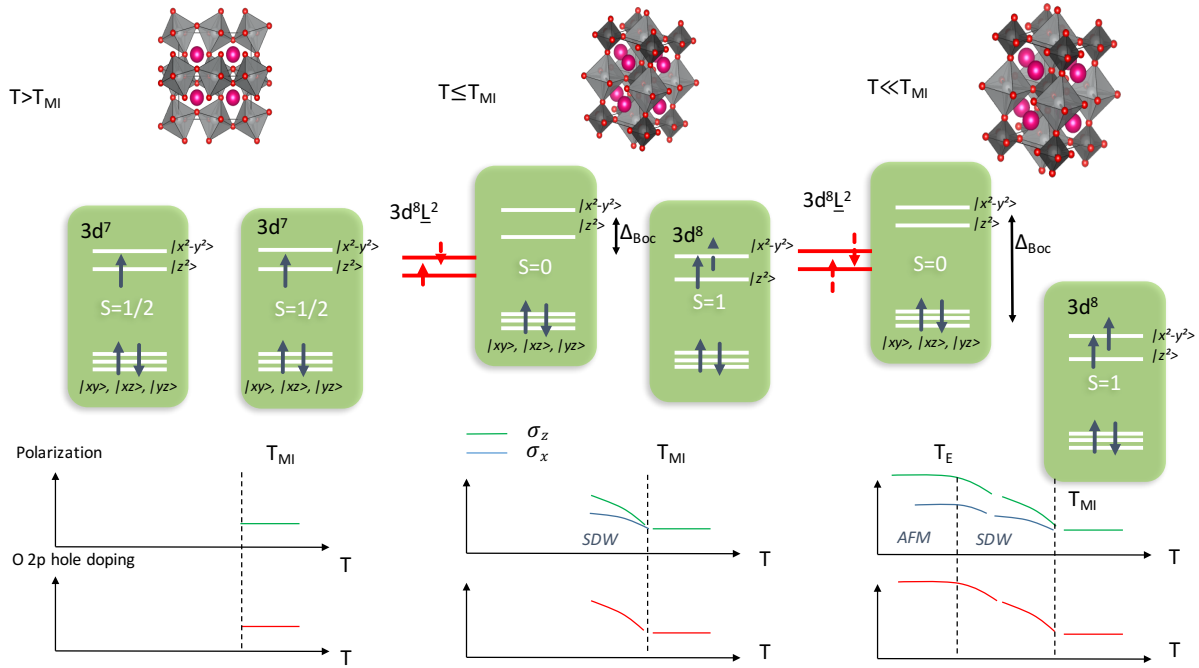


Figure B-8: sketch of the temperature dependence of the polarization, O 2p hole doping for SNO. Upper panels describe the exaggerated structure of the magnetic unit cell. Middle panels are diagrams of the energy hierarchy. Lower panels are sketches of the temperature dependence of the polarization (blue and green) and O 2p hole doping (red). SDW stands for spin-density wave and AFM stands for commensurate antiferromagnetism. The left column describes the situation for temperatures larger than the MIT, in the middle are presented a situation at intermediate temperatures (when the AFM peak position is still moving), on the right hand side stand panels at low temperature in the ground state when the AFM order is commensurate ($T_{N,c}$)

Based on the understanding that oxygen holes with opposite spins are progressively transferred to Ni d-orbitals (cf. Figure B-6 b), we sketched the temperature dependence of Ni orbital filling in Figure B-8.

At high temperature, $T < T_{MI}$, (left panels of Figure B-8), there should be almost no charge disproportionation. The in-plane compressive strain slightly favors the z^2 -orbital. This is confirmed by Figure B-6 (a), in which σ_x and σ_z are almost similar at high temperature.

At $T < T_{MI}$, (middle panels of Figure B-8), due to the appearance of the breathing mode, Ni electrons are transferred to a single Ni site, locating on the long-bond octahedra. Simultaneously, O 2p singlet starts to form which could be regarded as a filling of the Ni 3d states available (the O2p hole filling thus increases). Figure B-6 (b), which, as we explained, is a direct measure of the oxygen hole doping, indicates that this process happens progressively as the temperature is lowered. Above T_N , the difference in σ_x and σ_z is just a measure of the charge anisotropy (which can be considered negligible even if one can assume that z^2 -orbital occupancy would slightly dominate). Remembering that O 2p holes (n_h) is a singlet state and thus comes with two different spin orientations, the magnetic moment per orbital for two Ni sites (which is the elementary pattern in the G-AFM

magnetic unit cell), is $S_{z^2} = (1 + n_h)\frac{1}{2}$; $S_{x^2-y^2} = (1 - n_h)\frac{1}{2}$; below T_N , as the on-site charge transfer completes (middle panels in Figure B-8), the magnetic asymmetry between the x^2-y^2 and z^2 orbitals increases; eventually yielding $S_{z^2} = 1$ and $S_{x^2-y^2} = 0$. This difference of magnetic contribution at both orbitals reflects in the XLD signal (cf. Figure B-6 a). Indeed, at the Néel temperature, σ_z increases much faster than σ_x . Note that this scenario is reinforced by the fact that the evolution of σ_z fully correlates with the one of the p-d peak splitting, that directly gives the level of oxygen filling (cf. Figure B-9). We can look at σ_x as a measure of the charge arriving in the $x^2 - y^2$ orbital while the additional $\sigma_z (> 0)$ signal measures the spin-induced asymmetry between both orbitals.

Concerning the magnetic peak position displacement with temperature (cf. Figure B-6 c), we observe that the peak starts to displace exactly at the upturn of σ_z over σ_x . The AFM-peak displacement is reminiscent of temperature-dependent incommensurate antiferromagnetic orders, such as spin-density wave in Cr-based alloys [169] or in certain non-conventional superconductors [170–172]. From what we discussed, it is clear that, while the oxygen on-site doping process is taking place, the norm of the spin vector is indeed continuously increasing, resulting in a spin-density wave (SDW) like behavior. However, to fully ascertain this interpretation, we would need to discard any non-linear temperature-dependence of the crystallographic unit cell that may also account for the observed behavior.

However, for $T \ll T_M$, (right panels in Figure B-8), the oxygen holes on-site charge transfer should saturate. This would result in a locked spin amplitude for both Ni sites. Based, on the symmetry of the breathing mode, the AFM would thus lock at the commensurate $[\frac{1}{4} \frac{1}{4} \frac{1}{4}]$ -position. This is indeed what we observe around 50 K below which the peak position remains fixed (cf. Figure B-6 c). At the same temperature, the difference between σ_x and σ_z seems to saturate, suggesting that the on-site O hole doping has somehow stopped, as accounted by the similar saturation of the p-d peak splitting. Interestingly, this is also at this temperature that Sm sites order, supporting that, once fully developed, Ni spin moments magnetize Sm ions.

As a conclusion, in SNO, the correlation between orbital occupancy, oxygen on-site doping and non-commensurate spin ordering implies an intimate coupling between bond/orbital disproportionation waves and possible AFM coupled spin density waves. This is clearly apparent from the figure below in which we display all parameters as a function of the temperature.

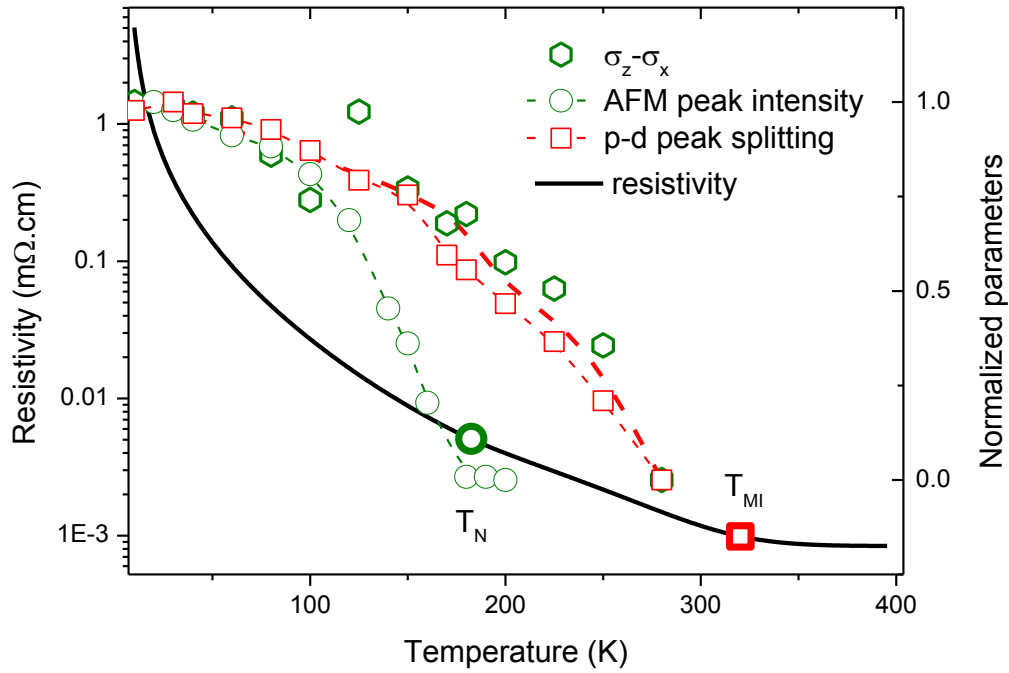


Figure B-9: resistivity (black curve) and normalized parameters at different temperatures.

It is clear that all transitions, either magnetic or electronic, are 2nd order. The temperature dependent oxygen hole filling recalls Sawatzky’s scenario [140] of bond-stretching vibrations coupled to the electronic carriers. Finally, we believe that SNO magnetic linear dichroism is also a clear (and the first) evidence for the anisotropic magnetic contribution of both Ni sites, strongly backing up Millis’ scenario of oxygen holes screening the short-bond Ni moments [139].

Based on this study of PLD grown rare-earth nickelates, we have been able to propose different methods to extract relevant experimental parameters (p-d peak splitting and σ_x/σ_z peak intensity ratio) to probe the physics of RNO. These experimental parameters rightfully fit the theoretical framework that we develop. As we will see in the next chapter, these parameters will reveal very useful for studying interfacial properties of titanate-nickelate heterostructures.

V. Correlated interfaces

This chapter constitutes the main part of this manuscript as it fulfills the initial end-goal of this work: combining titanates and nickelates into one single heterostructure to discover new phases of matter absent from the phase diagrams of the parent compounds.

We will begin this chapter by reviewing quickly the different types of oxides interfaces, starting with the canonical example of LAO-STO, before focusing on those built out of either titanates or nickelates. Then we will continue by describing the growth of the bilayer. Next we will describe the magnetic and electronic interfacial reconstructions. Finally, we will try to convey the idea that covalence is *the* key parameter in tuning these reconstructions.

A - Interfaces in oxides

Following the path opened by semiconductors, the oxide community has rapidly moved to the study of interfacial charge reconstructions between oxides. Besides the usual atomic and charge reconstruction also observed in semiconductors, the interplay between structural, charge, spin and orbital degrees of freedom in oxides yields a much richer physics - generating novel electronic states absent in the bulk constituents [173–175]. In the following, we present a rapid overview of oxide interfaces, highlighting important physical mechanisms and material systems. One of the most

striking example of the new physics that takes place at oxide interfaces is the canonical example of the $\text{LaAlO}_3\text{-SrTiO}_3$ interface.

1 - The canonical oxide interface: $\text{LaAlO}_3/\text{SrTiO}_3$

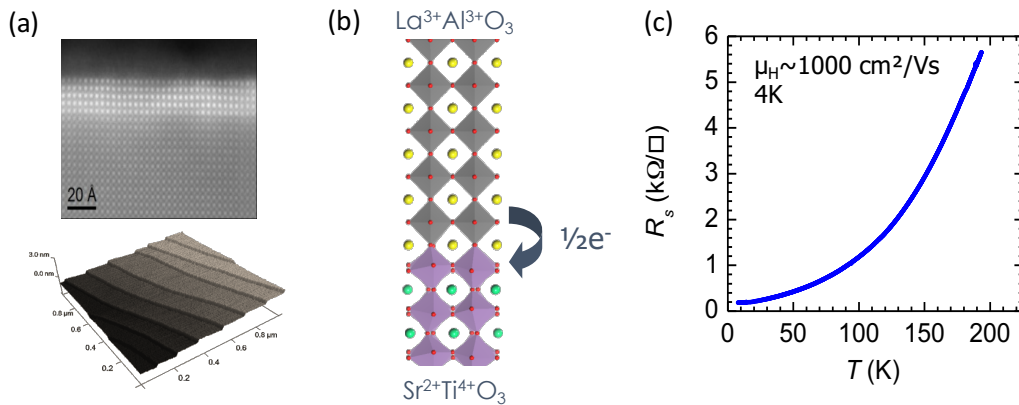


Figure A-1: (a) transmission electron microscopy of the $\text{LaAlO}_3\text{-SrTiO}_3$ interface (upper panel) and an AFM image (lower panel) of its topology. (b) schematic representation of the electronic reconstruction that takes place after the transfer of about half an electron from LaAlO_3 to SrTiO_3 . (c) An example of the exceptional properties of the resulting electron gas, that presents, besides superconducting properties, an extremely high mobility for 3d electrons up to $1000 \text{ cm}^2/\text{Vs}$

In 2004, Ohtomo and Hwang revealed unusual properties of the $\text{LaAlO}_3/\text{SrTiO}_3$ (LAO-STO) system [176]. It is a typical example of the marvel of oxide interfaces: although both compounds are wide band gap insulators, the interface shows two-dimensional conductivity with an electronic mobility up to $1000 \text{ cm}^2/\text{Vs}$ (cf. Figure A-1 c). The two-dimensional electron gas was found to be superconducting below 200 mK [177], and indications of magnetism [178–181] have also been reported. The most probable mechanism underlying the generation of this two-dimensional electron gas (2DEG) is charge transfer [182,183]. Indeed, LAO is built from alternating positively and negatively charged LaO^+ and AlO_2^- sub-planes while in SrTiO_3 both TiO_2 and SrO sub-planes are neutral. This makes the LAO-STO interfaces intrinsically polar. Consequently, an electrostatic potential develops from the interface into the LAO and diverges as the thickness of the polar material is increased. This phenomenon has been named the "polar catastrophe". The most efficient way to suppress this potential is to screen the built-in electric field by transferring electrons across the interface. Many mechanisms have been proposed :

- Either on-site doping [174], which is often possible in oxide-based heterostructures due to the mixed-valent character of the ionic species involved. For Ti, both 3+ and 4+ valences are possible. Traces of Ti 3+ were detected at LAO-STO interfaces [77]
- Or creation of vacancies and anti-site polar defects that act as electron donors. [184]

Whatever the mechanism, this electron doping occurs over nanometric distances [185] and does not involve dilute dopants (as it would be in bulk compounds or semiconductors), thereby minimizing chemical disorder. The LAO-STO system comprises an interface that demonstrates how oxides can host extraordinary proximity effects based on their mixed-valent cations and their intrinsic polar nature.

2- Interfacing nickelates or titanates

As we will see in the following few paragraphs, many authors have already studied interfacial properties between nickelates and titanates. We review interfaces that involve nickelates as one of the constituents.

a) Nickelates interfaces

As interfaces reconstructions relies mostly on band alignments, we can start by looking at heterostructures combining nickelates with conventional band insulators.

1) With a band insulator

Triggered by some theoretical predictions of possible cuprate-like physics and superconductivity in orbitally-engineered nickelates [103], people have started to investigate LNO-LAO interface.

In Figure A-2, we report some striking properties of this interface. In [186], Benckiser et al. constructed LNO-LAO superlattices. By performing reflectometry (as presented in chapter II) for linearly polarized light, they could probe the orbital occupancy as a function of the depth (cf. Figure A-2 b). They found that, in contact with the LAO layer, LNO orbitals are much more polarized in-plane close to the interface with LAO than deeper in the LNO layer. This specific orbital structure yields very

peculiar results. In [100], Boris et al. performed ellipsometry and muon spin rotation spectroscopy to probe the electronic and magnetic structure of such an interface.

They notice that LNO in contact with LAO developed a mass enhancement, yielding a metal to insulator transition. In parallel, a magnetic onset appeared at lower temperature upon cooling (cf. Figure A-2 b). The phase diagram for 2 u.c of LNO sandwiched in between LAO layers is presented in Figure A-2 (b). Note that for 4 u.c., the samples remained paramagnetic and metallic at all temperatures.

The authors claimed that higher electronic and magnetic fluctuations in two-dimensional systems probably reflects nesting in the LNO Fermi surface [100]. Note that for $N=2$, the orbitals are all polarized in the plane reducing strongly the overlap with the LAO layer and increasing the confinement and correlations of the LNO conduction electrons.

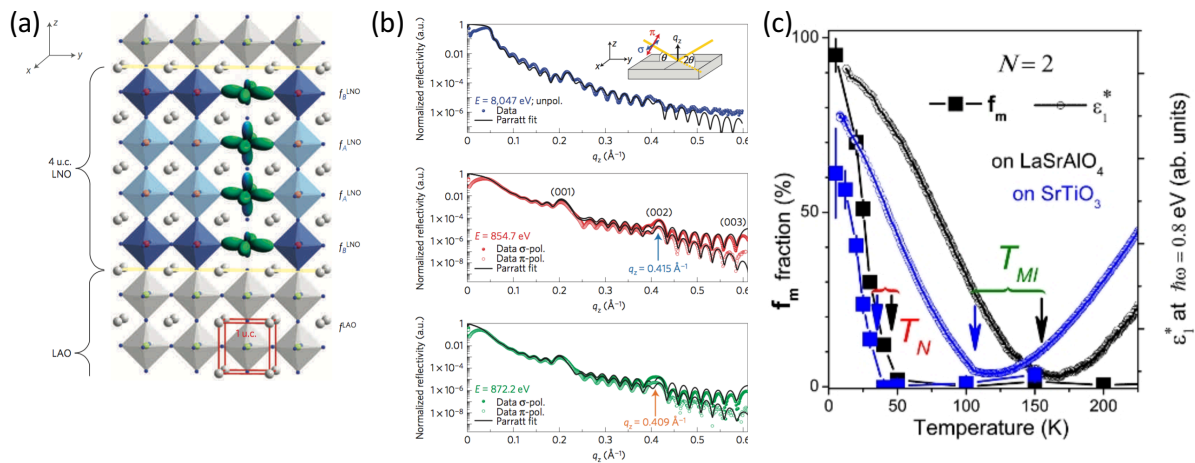


Figure A-2: Examples of interfaces involving LNO with LAO (a) schematic representation of the stacking sequence of LNO-LAO interface. LNO orbitals are displayed according to fits to the linearly polarized reflectometry measurements in (b). (a) and (b) are adapted from [186] (c) Temperature dependence of the fraction of muons experiencing static local magnetic fields in LNO-LAO superlattices on top of SLAO and STO substrates. (c) is adapted from [100]

In further studies, Keimer's group continued its investigations of the role of the large-band gap layer in the properties of such interfaces. They showed in [187] that good heterostructure quality with transition metal oxides can be extremely challenging due to the presence of strong polarity mismatch that can lead to the formation of divalent NiO precipitates (cf. Figure A-3 a-b).

The authors claimed that these precipitates were not a consequence of specific growth conditions, nor of specific strain states, but were rather formed at the interface with non-polar substrates (such as STO), and resulted from the effect of a polar mismatch which induces built-in electric fields.

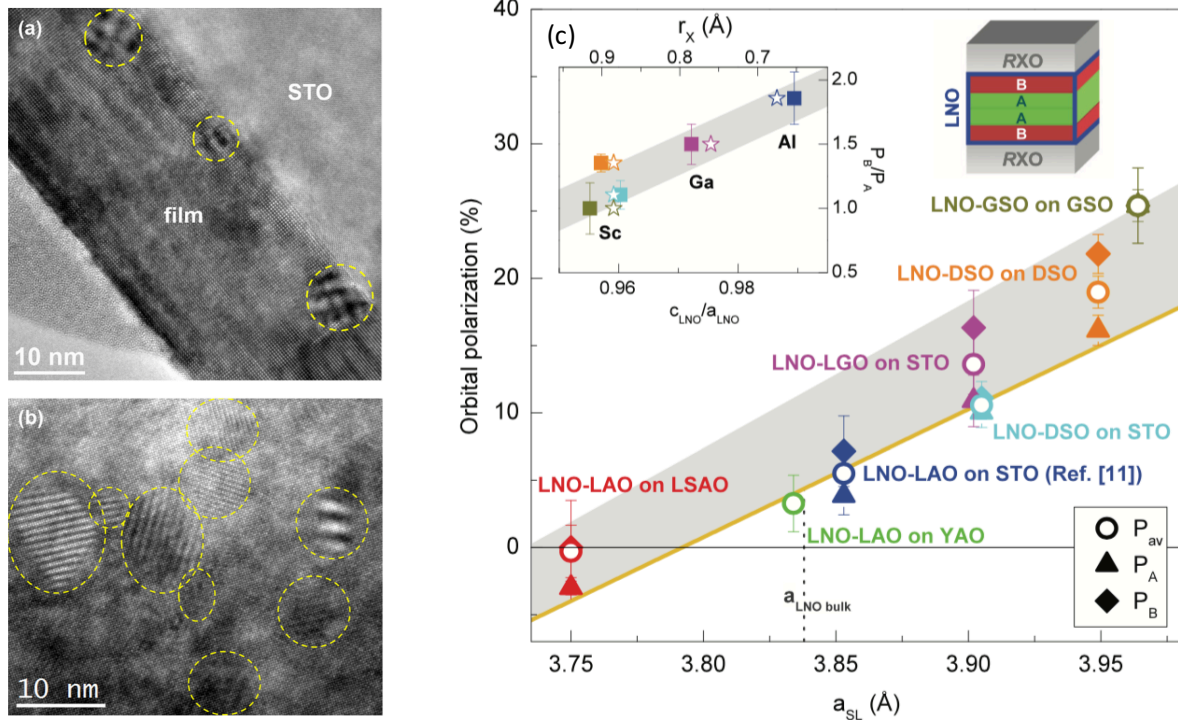


Figure A-3: (a-b) STEM images of LNO-LAO superlattices on top of STO substrates. The yellow dashed circles highlight NiO insertions close to the interface with the substrate. These images are adapted from [187] (c) orbital polarization for different interfacial stacking of LNO with large band gap insulators at different strain states [165].

However, by carefully stacking and terminating the substrate, they succeeded in growing by pulsed laser deposition heterostructures of LNO-LXO with $X = \text{Al, Ga, Sc}$ on different substrates [165]. They showed that the main effect was strain that allowed to tune the orbital polarization by 25%, whereas the interfacial engineering of the outer LNO layers contributed to 5% only (gray area in Figure A-3 c). Note that such a high-polarization was unexpected according to other experimental and theoretical work predicting that polarization could only be achieved through confinement [188–190]. They showed that the interfacial polarization (for the layer in contact with LAO) was essentially set by electrostatic confinement (related to the dielectric constant and, thus, to the band gap) and to X-s/O- p_z hybridization, which would influence the Ni-d/O- p_z .

Inspired by these promising results, other people tried to combine nickelates with more complex materials such as manganites that also belong to charge-transfer insulators.

2) With other charge-transfer insulators

In 2012, Gibert et al. combined LNO with LaMnO_3 (LMO) in superlattices grown on top of [111]-oriented STO substrate [104]. These heterostructures display very strong exchange-bias of the order of 800 Oe at 5 K. Note that this exchange bias scales with the temperature and disappears

around 30 K. This is very unexpected as exchange bias generally appears at the interface between a ferromagnet and an antiferromagnet [191], whereas, here, LNO is supposed to be paramagnetic. From the previous studies presented in Figure A-2, we know that interfacing LNO may produce the onset of magnetic fluctuations. However, no antiferromagnetism was ever reported.

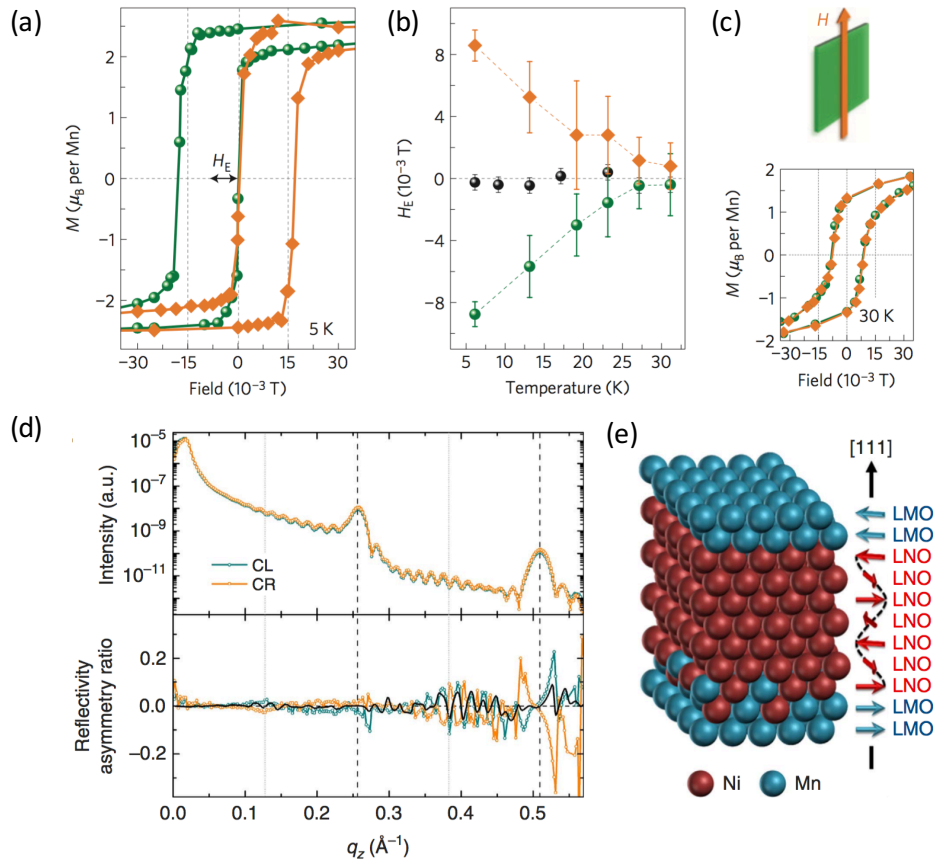


Figure A-4: Field dependence of the magnetization at 5 K (a) and 30 K (c) for a (7/7-LNO/LMO)-superlattice grown on [111]-STO after field-cooling at $+0.4$ T field (green circles) and at -0.4 T field (orange diamonds). (b) Temperature dependence of the exchange bias. In black the same is displayed for a LMO reference sample grown on (111)-STO is also shown for comparison (d) circularly polarized reflectivity and reflectivity asymmetry ratio for the same type of samples. (e) schematic representations of the spin orientations in the heterostructure. (a and b) are adapted from [104] while (d and e) are adapted from [192]

More recent studies by the same group [192,193], using magnetic dichroism in reflectometry measurements (cf. Figure A-4 d-e) showed that LNO presented complex in-plane spin spiral-structure that propagates parallel to the growth direction. This structure would ignite the kind of antiferromagnetic-like coupling needed in exchange bias systems. Interestingly, spin spirals develop only if LNO presents an odd number of monolayers. They also mentioned the importance of the

stacking sequence as the interface behaves differently whether LNO is grown on top of LMO or the opposite [193].

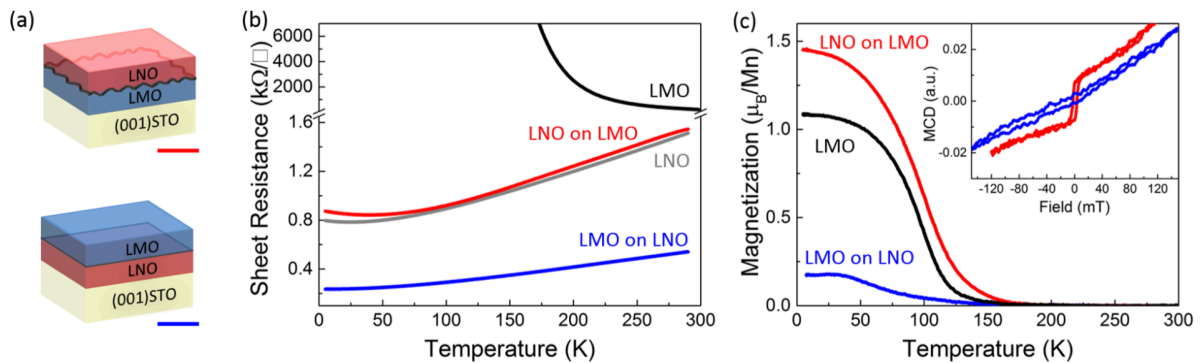


Figure A-5: (a) schematic representation of LNO-LMO (up) or LMO-LNO (bottom) grown on <001>-oriented STO. (b) Temperature dependent transport (b) and magnetic measurements (c) for these samples. In black is the same is displayed for a LMO reference sample. Figure adapted from [193]

Indeed, both the sheet resistivity and the magnetism (cf. Figure A-5) are reduced when LMO is grown on top of LNO. The reduction of the electronic and magnetic signals is associated with an increased interfacial roughness that allowed charge transfer (also reported in [192,194]) which eventually induces a coupling of Ni with Mn spins.

In our own work, we wish to push the interfacial properties a little further by combining charge-transfer with a material belonging to the other side of ZSA diagrams: a Mott insulator.

We believe that the prototypical system for that is GTO. In the following we review some studies combining RTO systems.

b) Titanates interfaces

1) With a band insulator

Stemmer's group, first, combined GTO with conventional band insulator STO in [57,195–200]. In Figure A-6, we present two figures extracted from [199]. In Figure A-6 (b) is reported the temperature-dependence of the sheet-resistance for different thicknesses of the STO layer grown below GTO. We observe that the sheet resistance decreases rapidly after the addition of a single STO layer below GTO.

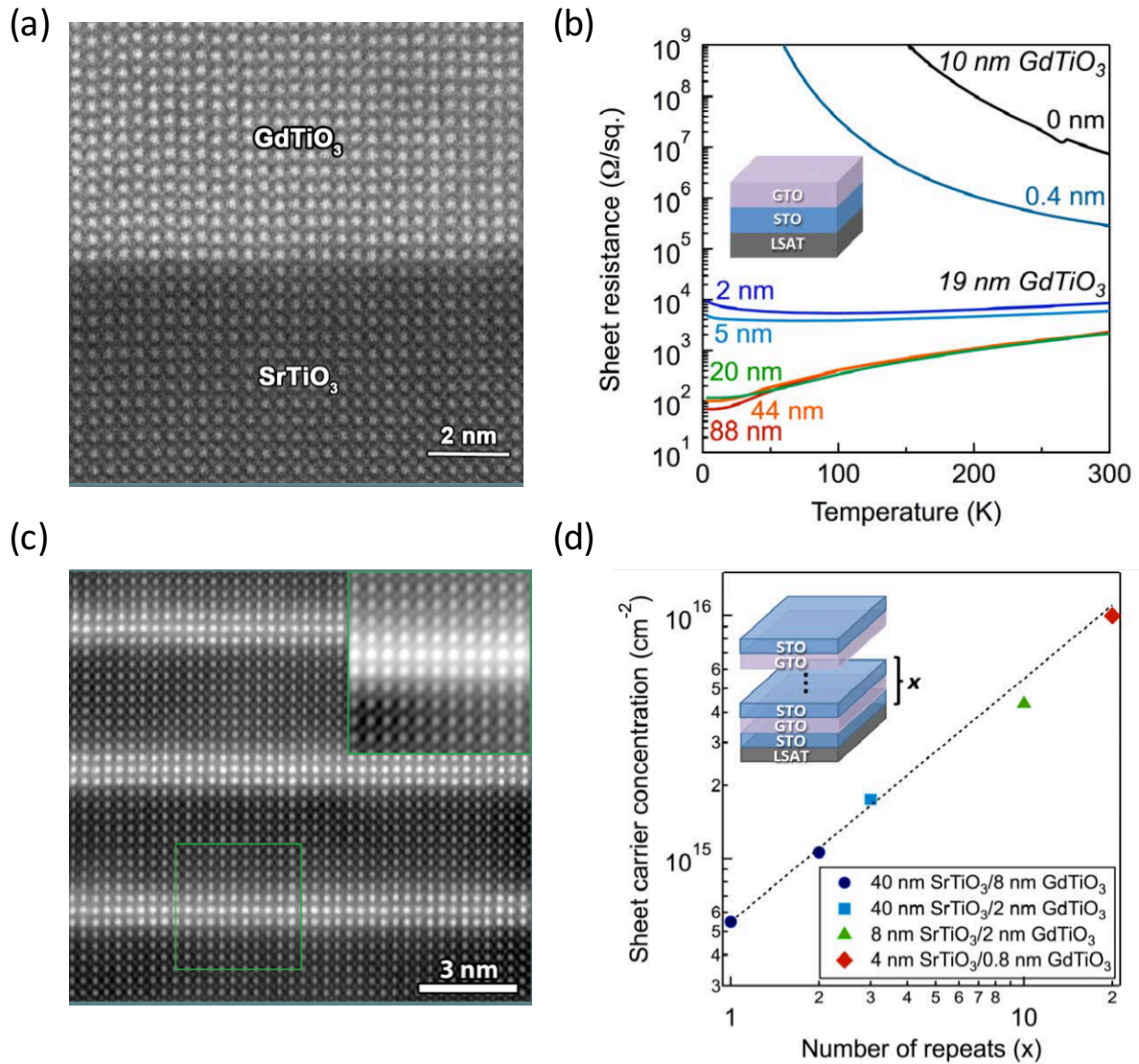


Figure A-6: In (b) Temperature dependence of the sheet resistance as a function of the STO thickness in a GTO-STO bilayer whose high-resolution STEM image is displayed in (a). In (c) sheet carrier concentration as a function of the number of repeated STO/GTO/STO trilayer. A high resolution STEM image of such GTO-STO stacking is presented in (c). This figure is adapted from [199]

Remarkably, the sheet resistance does not increase with increasing the number of STO layers as one would expect from oxygen deficient transport in the STO. The constant behavior for STO layers thicker than 20 nm suggest the presence of a conducting layer of constant thickness and finite carrier density. This is confirmed by stacking multiple STO/GTO interfaces. In Figure A-6 (d), we observe that the sheet carrier concentration linearly scales with the number of interfaces meaning that the behavior is reproduced at each interface.

GTO/STO heterostructures exhibit further interesting properties as they do also display ferromagnetism arising from the intrinsic ferromagnetic nature of GTO. Due to on-site interfacial

doping and confinement, the magnetization and critical temperature are reduced. The conjugation of ferromagnetism and conductivity leads to the appearance of magneto-resistance.

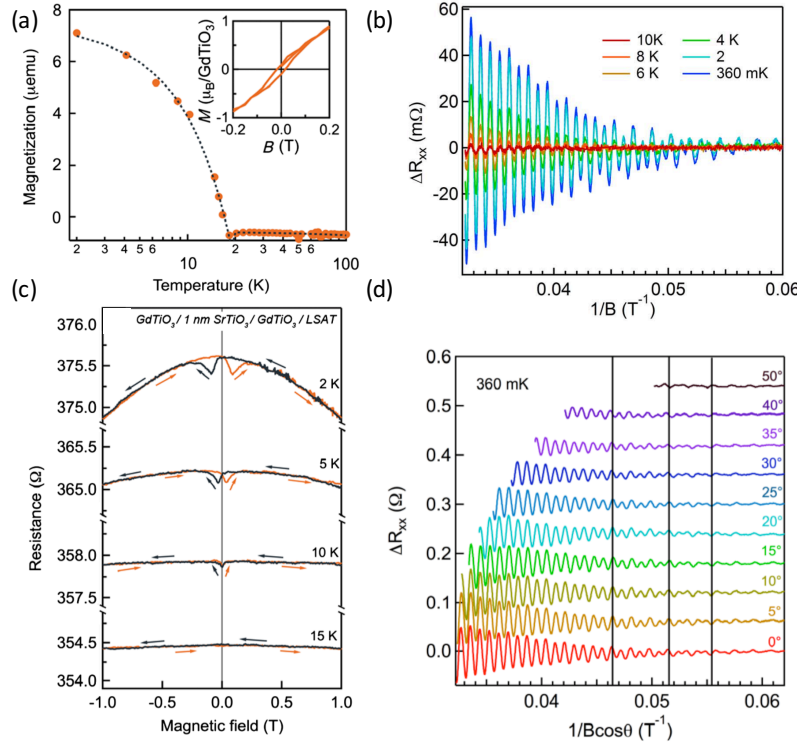


Figure A-7: temperature dependent magnetic properties (a) and magnetoresistance (b) at different temperatures of a 4-nm thick GTO/STO/GTO heterostructure grown on top of LSAT. Shubnikov-de Haas oscillations at different temperatures and (d) different in-plane field orientations. (a-d) are extracted from [201], whereas (b-c) are from [196]

Based, on the critical temperature and amplitude of the magneto-resistance, the authors claimed that the electron gas was in GTO. This was later confirmed by angle dependent rocking curves XPS analysis [202].

The two-dimensionality of the electron gas was established by the angle dependence of the Shubnikov-de Haas oscillations whose frequency times the cosine of the tilt angle of the external field is angle-independent. Note that the number of oscillations confirms the quality of the heterostructure. Finally, the temperature dependence and the different frequencies extracted from Shubnikov-de Haas oscillations are not in agreement with the one-electron t_{2g} d_{xy} -orbital configuration and differs from LAO-STO Shubnikov-de Haas measurements. A careful investigation of the Fermiology of the GTO/STO interface is still needed [196].

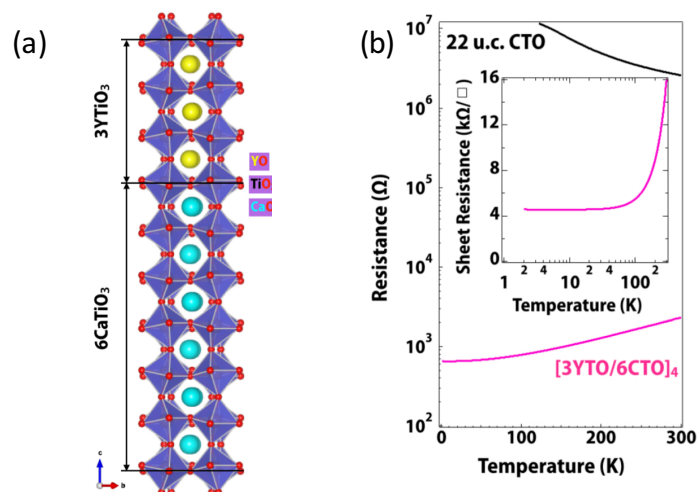


Figure A-8: (a) schematic representation of YTO/CaTiO₃ interface grown on top of NGO (b) temperature dependence of the resistance for YTO/CaTiO₃ superlattices and 22 u.c.-thick CaTiO₃ (black) reference samples. The figure is adapted from [203]

In 2015, Chakhalian's group grew YTO in non STO-based interfaces [203]. The results are reported in Figure A-8. The effect of stacking CTO with YTO is very strong since only 3 u.c. of YTO is enough to entail a metallic behavior, although both materials are supposed to be strong insulators. Thickness dependence of the sheet resistance indicates that this conductivity is mostly two-dimensional. However, the mobility was found to be about 2 orders of magnitude smaller than in STO-based 2DEGs [203].

In the next paragraph, we will see that other studies have already tried to combine RTO with other correlated oxides.

2) With other correlated oxides

During the first 2 years of this Ph. D., two main studies tried to combine RTO with other correlated oxides. In 2014, Kleibecker et al. combined LaTiO₃ with LaFeO₃ which is an antiferromagnetic charge-transfer insulator with a large charge-transfer gap of 2.2 eV [204]. XPS measurements are displayed in Figure A-9. Clear spectral changes were observed in the Fe 2p XPS while increasing the thickness of the LFO sandwiched between 2 u.c. of LTO. Angle dependent lab-XPS study enabled to extract depth-dependent profile of the Fe valence states. The valence of the Fe was indeed lowered close to the interface due to spontaneous charge transfer from the titanates to LFO layers.

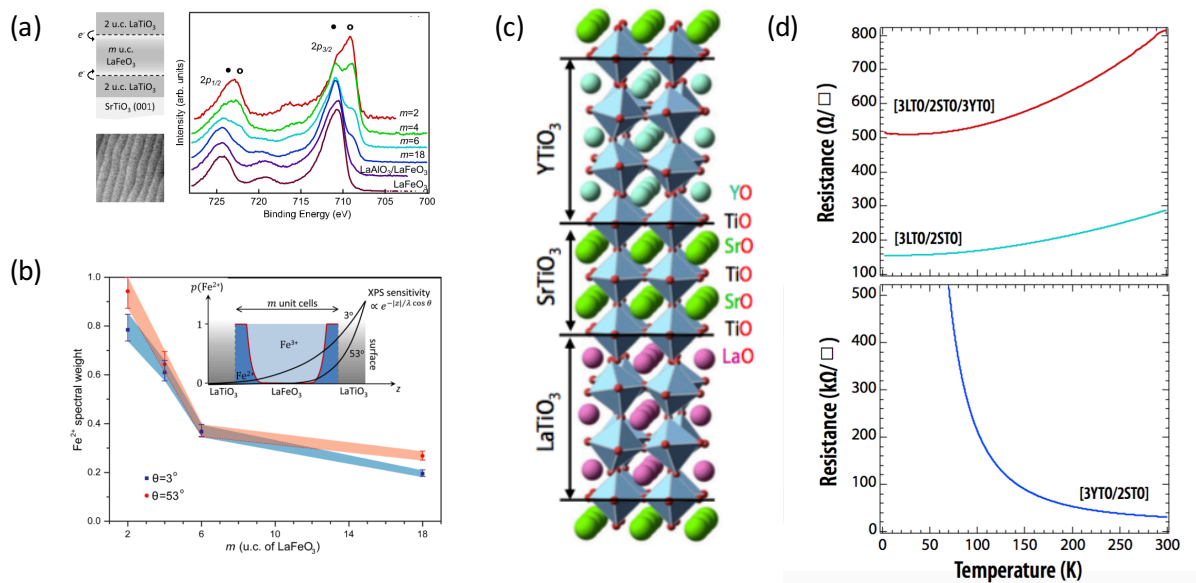


Figure A-9: (a) (upper left panel) schematic representation of the LaTiO₃/LaFeO₃/LaTiO₃ sample geometry. (lower left panel) 1 μm² wide AFM topography image of the LaTiO₃/LaFeO₃ heterostructure. (right panel) Fe 2p XPS spectra of a LTO/LFO/LTO heterostructure and various XPS spectra varying LFO thickness in LTO/LFO/LTO superlattices (b) normalized Fe²⁺ XPS spectral weight versus LFO thickness for both bulk (blue) and surface (red) sensitive XPS measurements. The inset presents the angle-dependent XPS sensitivity, and a sketch of the Fe valence distribution across the sample thickness. (c) schematic representation of tricolor LTO/STO/YTO grown on TbScO₃ substrate (d) temperature dependence of the heterostructure in (red), LTO/STO bilayer (cyan) and YTO/STO in blue. (a) and (b) are adapted from [204] and (c)-(d) are from [205]

Remarkably, XPS spectroscopy on LTO/LFO heterostructures for different LFO thicknesses is presented in Figure A-9 (a). The variation of spectral shapes in the Fe 2p spectra allowed for the first time to discuss the effect of charge reconstruction on the level of hybridization in the charge-transfer insulator LFO layer. The authors claimed that they witnessed a decrease of the O 2p-Fe 3d (e_g) hybridization following charge transfer, strongly suggesting the occurrence of Fe band rearrangement at the LTO/LFO interface [204].

Finally, Chakhalian's group proposed to build-up "tricolor" superlattices combining LTO/STO/YTO titanates [21] (cf. Figure A-9 c) on top of TbScO₃ substrate. The tri-color superlattices demonstrate a metallic behavior although all constituents are insulating over a wide range of temperatures. The authors excluded the presence of oxygen defects in any of the constituents which leaves the emergence of a conductive behavior as being solely ascribed to interfacial reconstruction. Comparing the resistivity cells in Figure A-9 (c-d), for the tricolor system and the reference heterostructures (3YTO/2STO, 3LTO/2STO) confirms that metallicity appears at the LTO/STO interface leaving YTO/STO insulating. Interestingly, the two types of Mott-Band/Mott-Mott interfaces

behave very differently opening new routes for the tuning of interfacial properties using buffer layers in tri-layer lattices.

B - Titanate-Nickelate bilayers

1 - Growing the bilayer

In this work, we took a slightly different direction compared to these studies, as we decided to combine two very different oxide materials with rich and complex phase diagrams (cf. Figure B-1): titanates grow at very low pressure while nickelates grow at high pressure with very distinct tolerance factors (0.85 and 0.95 respectively), nevertheless, they have relatively close lattice parameters, implying a small lattice mismatch, as shown in Figure B-1.

The strong diversity of phases in both phase diagrams let us hope that very peculiar electronic and magnetic reconstructions will occur as degrees of freedom should go continuously from one ferromagnetic insulating phase (in the titanates) to a complex antiferromagnetic phase displaying electronic instabilities (in the nickelates). Additionally, some preliminary theoretical studies on these types of interfaces mentioned the eventual appearance of new spin and orbital states [206].

For this study, we were helped by Dr. J. Varignon for DFT calculation and Dr. J. Rault, a Beamline scientist from Soleil synchrotron, for performing Hard X-ray Photoemission spectroscopy measurements.

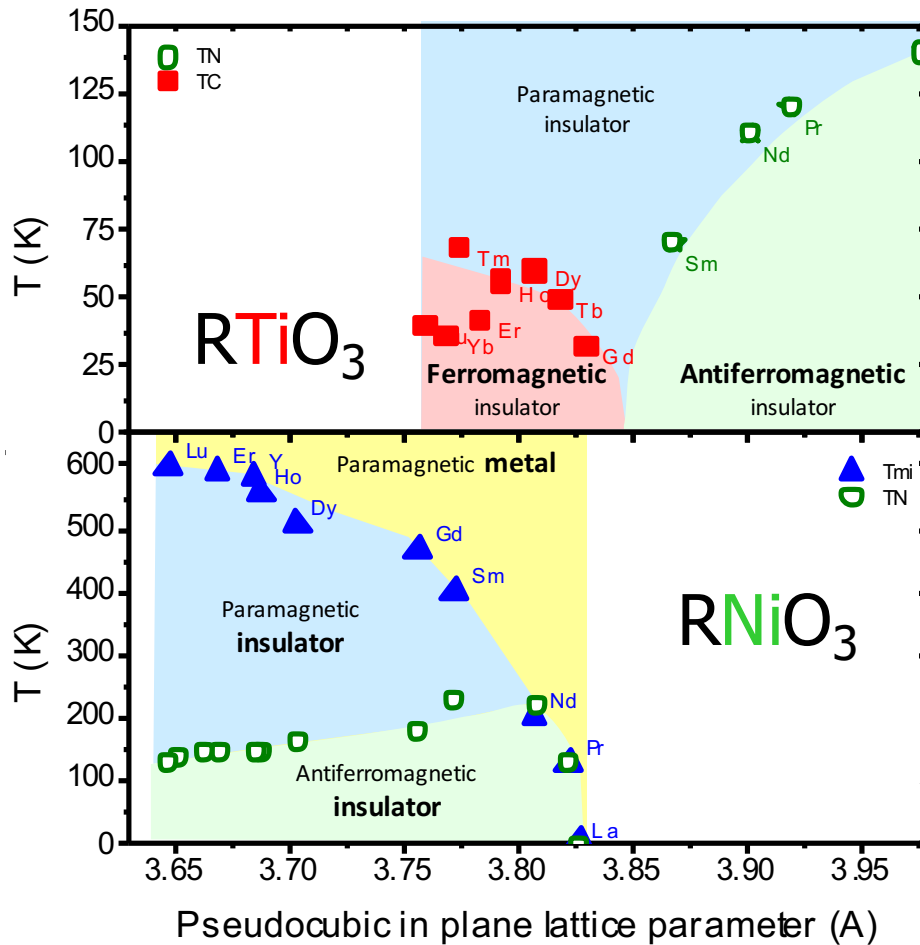


Figure B-1: Phase diagrams of RTO and RNO as a function of the pseudo-cubic in plane lattice parameters. The RNO phase diagram is adapted from [49] while RTO phase diagram is borrowed from [99].

To study the growth mechanism of RTO-RNO bilayers, we relied on in-situ RHEED monitoring. Any other techniques such as XRD, or AFM would not have provided interesting results as the layers are too thin and their parameters too close for the XRD spectra to be correctly interpreted.

In Figure B-2, we illustrate examples of RHEED patterns observed when growing bilayers. We could probe the quality of the growth by comparing the measured RHEED patterns with the ones of individual layers, which were characterized in the previous two chapters. For example, we found that depositing LNO before GTO (cf. Figure B-2 d) induces immediately a 3D-growth. Indeed, LNO is unable to sustain the low pressure/high temperature growth conditions required for GTO. Indeed, no matter what quality of sample is achieved after the first stage of the growth, LNO always developed 3D structures according to the evolution of the RHEED patterns and the AFM images. Besides, we could observe in combination with XRD on thicker nickelate samples that these 3D structures were associated with the appearance of parasitic phases with reduced stoichiometry at high temperatures and low pressures. During this work, we could not perform the growth of GTO on top of LNO.

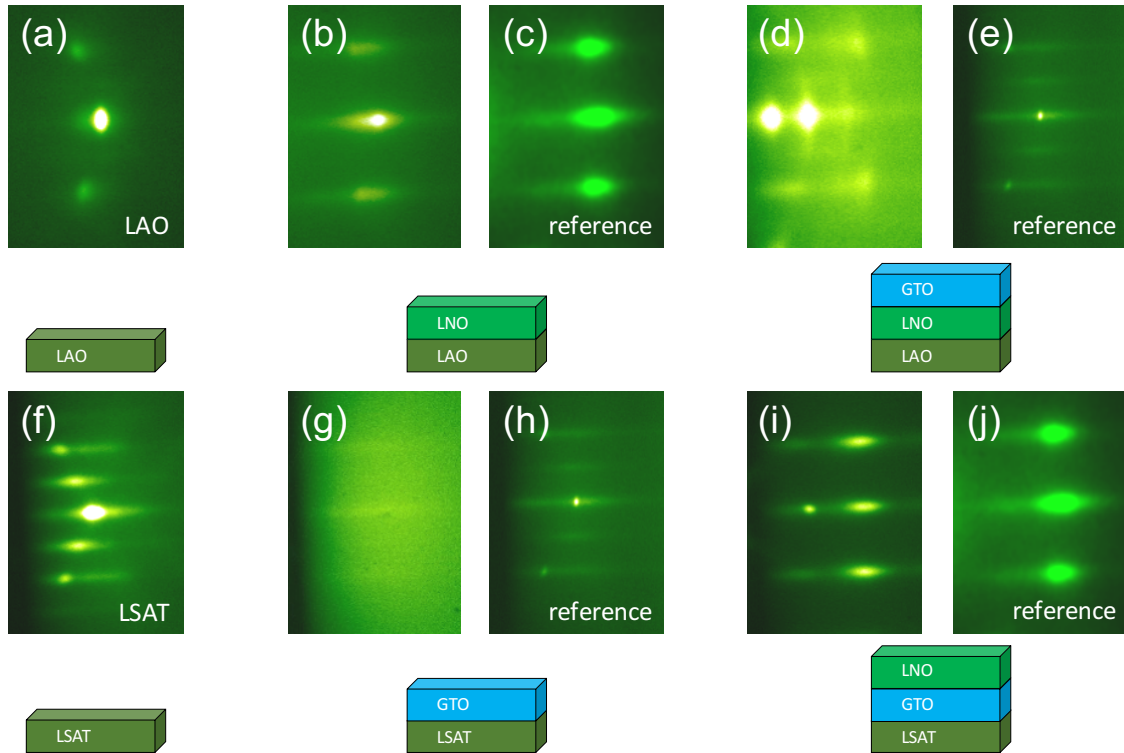


Figure B-2: RHEED patterns at different stages in the growth of GTO/RNO bilayers. In (a) and (f) are examples of substrate LAO and LSAT resp. RHEED patterns. RHEED patterns of LNO deposited on top of a substrate of LAO in (b) or on top of GTO in (i), with references of RHEED patterns for LNO (c and j). RHEED patterns of a GTO sample deposited either on LNO (d) or directly onto the substrate (in g) with references in (h and e)

Nevertheless, when exchanging the order of the layers, we succeeded good growth quality. As we see in Figure B-2 (f-j), the RHEED patterns remain indeed similar to the ones of the reference thin films observed during a single growth stage. The RHEED patterns show, at each stage of the growth, a good 2D-morphology with an interspace between fringes remaining the same as the one of the substrate all along the growth process, which suggests that the films are epitaxial (within experimental errors).

The samples for the rest of the study were grown on LAO substrates that were cleaned in acetone and propanol and annealed prior to deposition, in order to insure single termination. All targets were pre-ablated in their respective growth conditions for 15 min. The GTO was then deposited by pulsed laser deposition at $PO_2 = 2.10^{-6}$ mbar and $T_{dep} \sim 700$ °C. The thickness was monitored by intensity oscillations of *in situ* RHEED and stopped after 7 u.c. From chapter III, we know that for GTO grown on LAO beyond 7 u.c., defects may appear. Then the temperature was slowly decreased in the titanate growth pressure to the growth temperature of the nickelates (600-650 °C). While the temperature was reduced, we monitored the evolution of the titanate layer with

RHEED and no structural modification was observed. Right after depositing the nickelate layer at 0.4 mbar, the samples were annealed in situ for 30 min at 500°C and 300 mbar of oxygen. RHEED did not show any modification after the annealing process.

Following this study, we have grown nickelate (LaNiO_3 - LNO, NdNiO_3 - NNO, SmNiO_3 - SNO) films on top of GTO films using pulsed laser deposition using LAO substrates (cf. Ref. [67,96]).

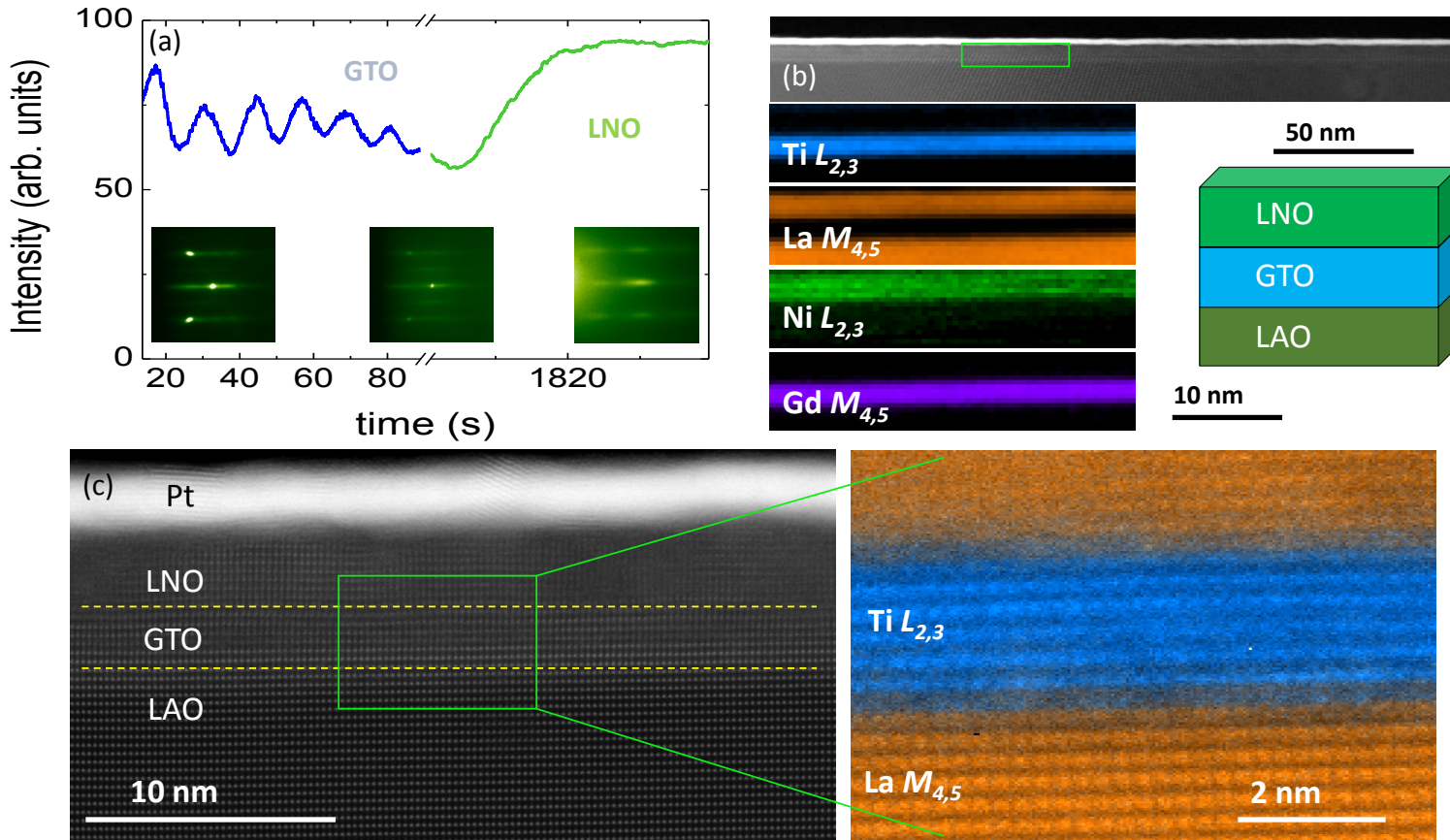


Figure B-3: (a) RHEED monitoring during growth with intermediate RHEED images at each stage: LAO substrate before growth (left), GTO layer before deposition of the nickelate (middle), LNO layer at the end of growth (right). (b) Low magnification Z contrast image of the LNO/GTO heterostructure (top), and EELS maps from an area such as the one marked with a green rectangle (bottom). From bottom to top maps corresponding to the Ti $L_{2,3}$, La $M_{4,5}$, Ni $L_{2,3}$ and Gd $M_{4,5}$ edges are shown. (c) Atomic resolution Z contrast image of the same sample along the $\langle 110 \rangle$ direction. The panel on the right shows the Ti $L_{2,3}$ (blue) and La $M_{4,5}$ (orange) EELS maps acquired on an area such as the one highlighted with a green rectangle.

Figure B-3 (a) displays reflection high-energy electron diffraction (RHEED) patterns before growth (LAO substrate, left), after growth of the GTO film (center) and after deposition of the LNO film (right), indicative of two-dimensional growth. Clear RHEED oscillations were observed while growing the GTO film, which we used to fix the GTO thickness to 7 u.c. in all samples. For LNO, no oscillations were observed but a large RHEED intensity was recovered during deposition. Through

growth rate calibrations using X-ray reflectometry, the nominal thickness of the nickelate layers was set to 7 u.c. as well (Figure B-4 left upper panel).

Figure B-3 (b) shows a high resolution Z-contrast scanning transmission electron microscopy (STEM) image of a LNO/GTO sample. Low magnification images and compositional EELS maps obtained from the analysis of the Ti $L_{2,3}$, La $M_{4,5}$, Ni $L_{2,3}$ and the Gd $M_{4,5}$ signals reveal layers that are flat and continuous over long lateral distances. Occasional defects are observed in high magnification images (Fig. Figure B-3 c) but the samples are epitaxial and sample quality is high. Elemental maps with atomic resolution reveal sharp interfaces between the LAO substrate and the GTO film, and between the GTO film and the nickelate layer. As expected, the LNO and GTO thicknesses were equivalent, within about one unit-cell.

This high epitaxial quality with no extended defect is also true for all other bilayers for which we present the TEM characterizations with the AFM surface morphology in Figure B-4. Azimuthal RHEED analysis also supported the epitaxial character of all three bilayers (LNO/GTO, NNO/GTO and SNO/GTO) within experimental errors. As observed in Figure B-4, the thickness of the nickelate films was comparable in all three bilayers, within 1 unit cell.

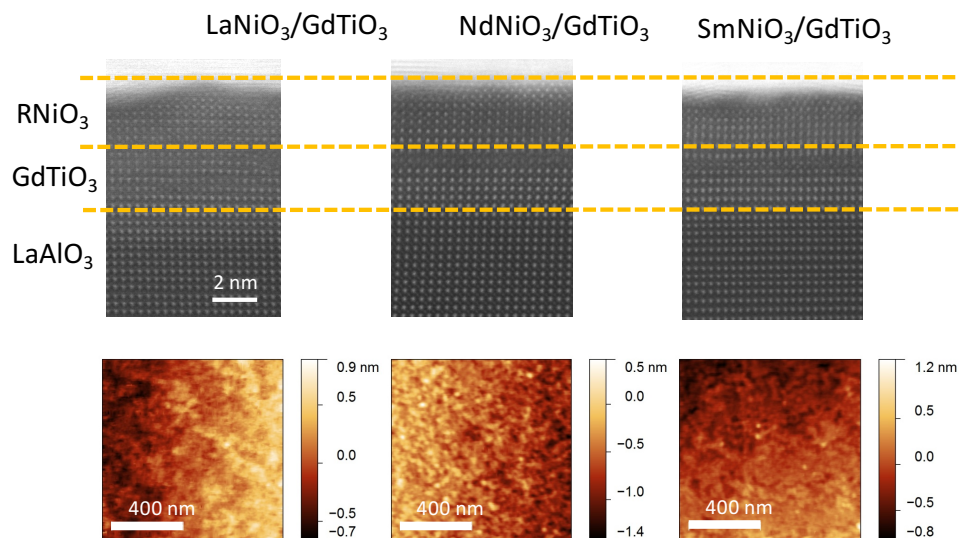


Figure B-4 (above) Low magnification Z contrast image (below) AFM topography of the of the LNO/GTO (left panels) – NNO/GTO (middle panels) – SNO/GTO (right panels) heterostructures.

Nevertheless, the RHEED reported in Figure B-3 (a) is characteristic of 2D + islands growth with a decrease of the oscillatory intensity due to an increased roughness. The AFM images account for very flat surface morphologies with RMS roughness below 1 u.c. (0.21 nm in the case of

GTO/SNO, 0.17 nm for GTO/LNO and 0.22 nm for GTO/NNO) but with visible mounts confirming the scenario of a growth mode that combines pure 2D growth with some 3D islands.

We should recall that the roughness of GTO on LAO substrates with no capping layer was also about 0.2 nm (cf. chapter III). We also discussed the fact that *ab-Pbnm* orientation of GTO on top of LAO substrate was prone to island formations because of its intrinsic single in-plane oriented growth. This is however minimized by the very-thin layers of GTO. Thicker samples would however result in more defects (cf. chapter III).

We thus succeeded to reach a satisfactory quality with no chemical intermixing nor extended structural defects. Based on this, we can move to characterizing the electronic properties of this interface. For that, we will use absorption spectroscopy, and photoemission spectroscopy in connection with ab-initio calculations.

2 - Interfacial charge transfer

a) In LNO/GTO

We start by looking at the interfacial properties of a single bilayer: LNO-GTO. Since the interface of interest is buried below 7 u-c of NNO, we performed angle-dependent hard X-ray photoemission (HXPS) experiments in collaboration with Dr J. Rault from SOLEIL.

Indeed, performing HXPS measurement (cf. chapter II) for different incidence angles of the X-ray beam with respect to the sample surface enables to probe the sample at different depths. We calculated the depth dependence of the X-ray electric field strength as a function of the incidence angle (cf. Figure B-5). Close to total reflection (grazing incidence), photons are barely penetrating the surface leading to a very surface sensitive measurement. On the contrary, for higher incidence angle (here 10 degrees), the photons penetrate deeper in the sample and the probing depth is only limited by the electron mean free path (*i.e.* approximately 9 nm probing depth, which is larger than the total thickness of the heterostructure, which is around 5.5 nm).

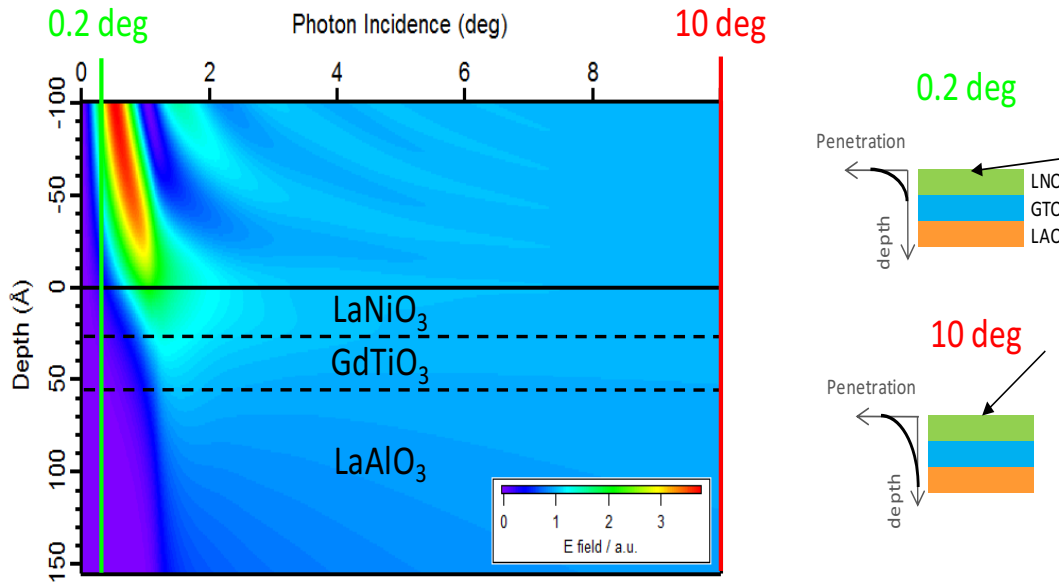


Figure B-5: (left) Depth dependence of the electric field of the incoming X-rays as a function of the incidence angle and (right) sketches of the measurement geometry in grazing incidence 0.2 deg. and at 10 deg.

To detect possible changes in the Ni valence near the interface, we conducted valence band HXPS of a LNO/GTO bilayer at 0.2 and 10 deg. incidence angles. Note that this is however not ideal because the nickelate is on top of the GTO and thus the contrast in sensitivity of the interface region between 0.2 and 10 deg. experiments is much weaker than it would be for GTO (as we would see later on).

Figure B-6 shows valence band HXPS of single films of LNO at 0.2 deg. and 10 deg. incidence angles (green and red respectively). The signal at 10 deg. is very typical of valence band photoemission of this material [133,207] and the peaks “a” and “b” corresponding to t_{2g} and e_g states are easily recognizable. At 0.2 deg., the intensity of those two peaks is reduced, which possibly reflects some reduced metallicity at the surface. This is better visualized in Figure B-6 (c) that plots the difference between signals acquired at 10 deg. and 0.2 deg. incidence angles.

Figure B-6 (b) shows similar data for the LNO/GTO bilayer. Compared to data from Figure B-6 (a), peak “a” appears broader and peak “b” is much less intense. Such a progressive weakening of the quasiparticle peak and the depletion of spectral weight at the Fermi level has been observed for LNO in the 3 to 6 unit-cell thickness range (close to the thickness of our LNO films, 7 unit-cells) [133,207]. Peak “a” is further weakened at 0.2 deg. compared to that at 10 deg. (compared to LNO single films), but what is remarkable is that peak “b” is now weaker at 10 deg. than at 0.2 deg. (this is clearly visible from the difference plotted in Figure B-6 (d) that is negative at the energy of peak “b”). This suggests a transfer of spectral weight to lower energies consistent with an increase in the number of

electrons, in other words a reduction of the Ni valence from 3+ to 2+. Because here HXPS is more sensitive to the interface with the GTO at 10 deg. than at 0.2 deg., this suggests a change of the Ni valence towards 2+ near the interface and not close to the surface of the LNO.

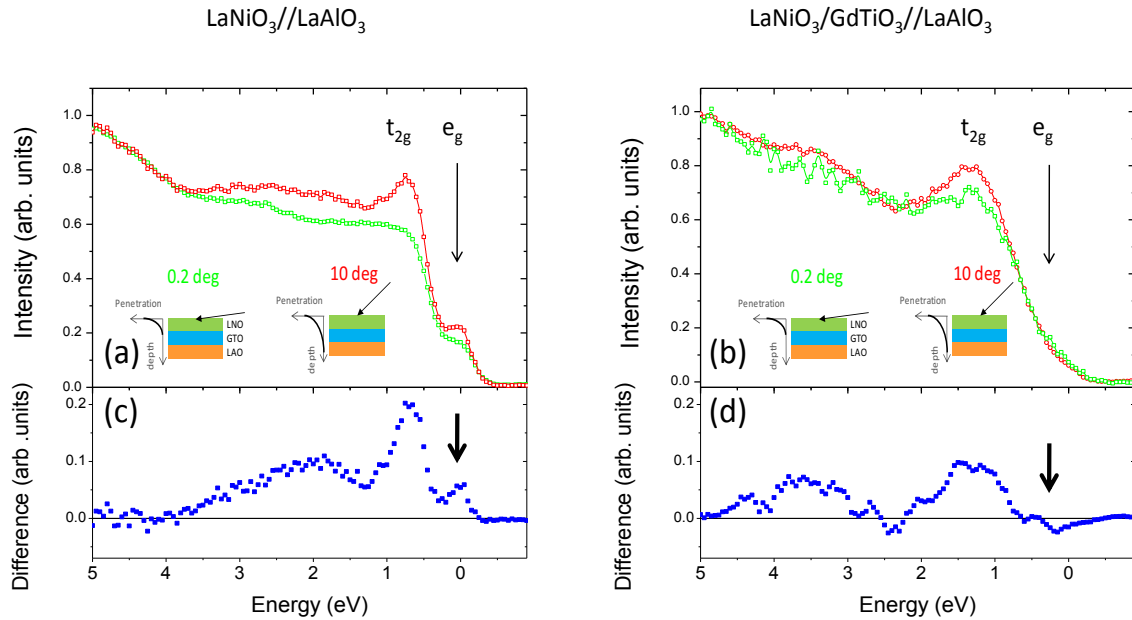


Figure B-6: Valence band HXPS of a single LNO layer (a) and a LNO/GTO bilayer (b) at 10 deg. and 0.2 deg. incidence angles. Panels (c) and (d) show the difference between the signals acquired at 10 deg. and at 0.2 deg.

To fully ascertain the absence of superficial Ni^{2+} due to oxidation, we performed angle dependent core level HXPS at the Ni edges (Figure B-7 a). Al $2p$ core-level coming from the LAO substrate is even visible at 10 deg., confirming the ~ 9 nm probing depth at this photon energy. The Ni $3p$ core-levels are virtually identical for both incidence angles. Any surface Ni^{2+} , would have induced a strong difference in the surface-sensitive data. This is confirmed by simulations of the evolution of the spectral shape assuming the presence of some Ni^{2+} at the surface (here an hypothetical 2 nm-thick layer, see Figure B-7 c) for the same incidence angles - we use the difference in binding energies between Ni^{2+} and Ni^{3+} from [208], rescaled to our binding energy calibration. The large peak at ~ 63 eV in the simulations of Figure B-7 (c) is due to Ni^{2+} and dominates the signal at both 0.2 deg and 10 deg, but the peak due to Ni^{3+} is visible at 68 eV only in the 10 deg configuration which probes deeper into the nickelate. This drastically differs from our experimental observations and confirms the absence of Ni^{2+} at the surface of the nickelate.

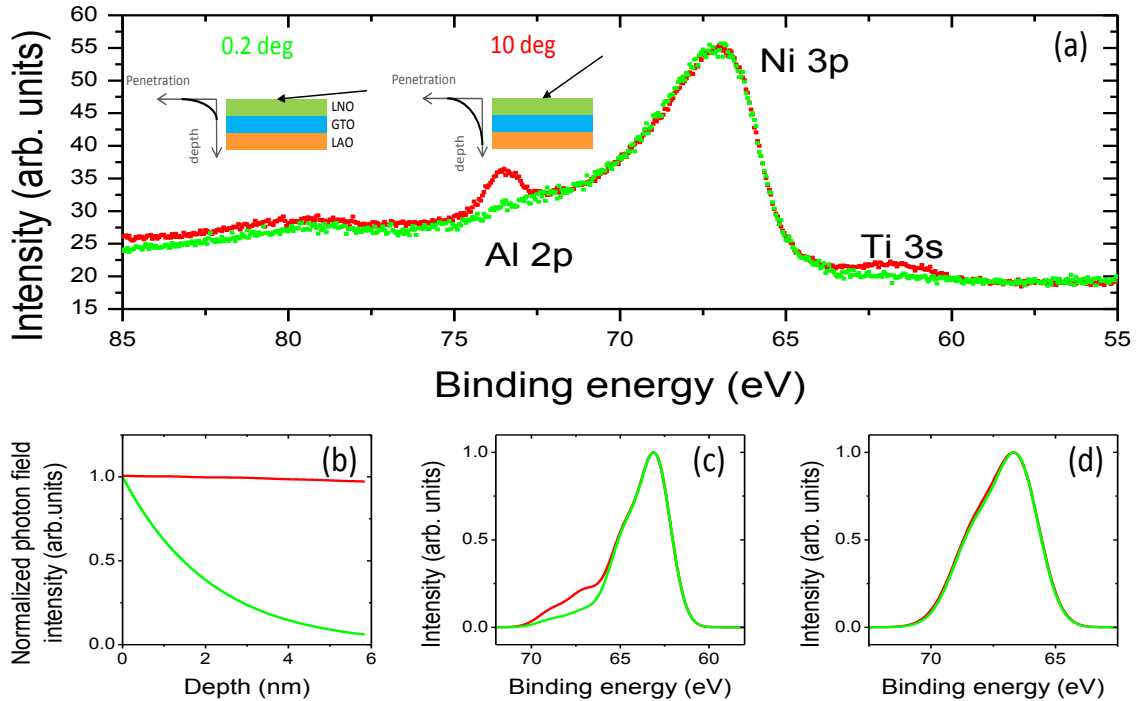


Figure B-7: (a) HAXPS spectra of a LNO/GTO/LAO sample at 0.2° (surface) and 10° (bulk) incidence angles, at 300 K, with a photon energy $h\nu=2300$ eV. (b) Normalized photon field intensity at 0.2° (green) and 10° (red) (computed using YRXO software [37]). (c) Simulation of HXPS spectra for a signal comprising 2 nm of Ni^{2+} at the surface probed at 0.2° (green) and 10° (red) incidence angles (d) Simulation of HXPS spectra in case of charge transfer induced Ni^{2+} at the interface with GTO probed at 0.2° (green) and 10° (red) incidence angles

We now turn to the investigation of the Ti valence changes at the interface. For that, we also measured HXPS of Ti $2p_{3/2}$ core-levels on a LNO/GTO sample at two different photon incidence angles. At 0.2 degrees incidence, we probe mainly the very first planes in the GTO layer whereas at 10 degrees, the whole bilayer is surveyed, see the cyan and blue dots in Figure B-8 (a). Both spectra clearly consist of multiple components. Those peaked at low binding energies are strongly enhanced in grazing incidence, which we interpret as reflecting the presence of a built-in electric field shifting the core levels of interfacial Ti ions to higher energies. To fit the experimental spectra we assume that the signal from each Ti plane has a Gaussian line shape, progressively shifted in binding energies, assuming a potential drop of 1.6 eV over ~ 3 u.c. in the GTO close to the interface (consistent with the 1.69 eV drop predicted from DFT-calculations). Figure B-8 (c) shows the dependence of the energy shift as a function of the position in the GTO film. In a rigid band model, this upward band bending results from a progressive depletion of the $3d$ band as one gets closer to the interface *i.e.* it corresponds to an increase of the Ti valence from $3+$ towards $4+$ near the interface.

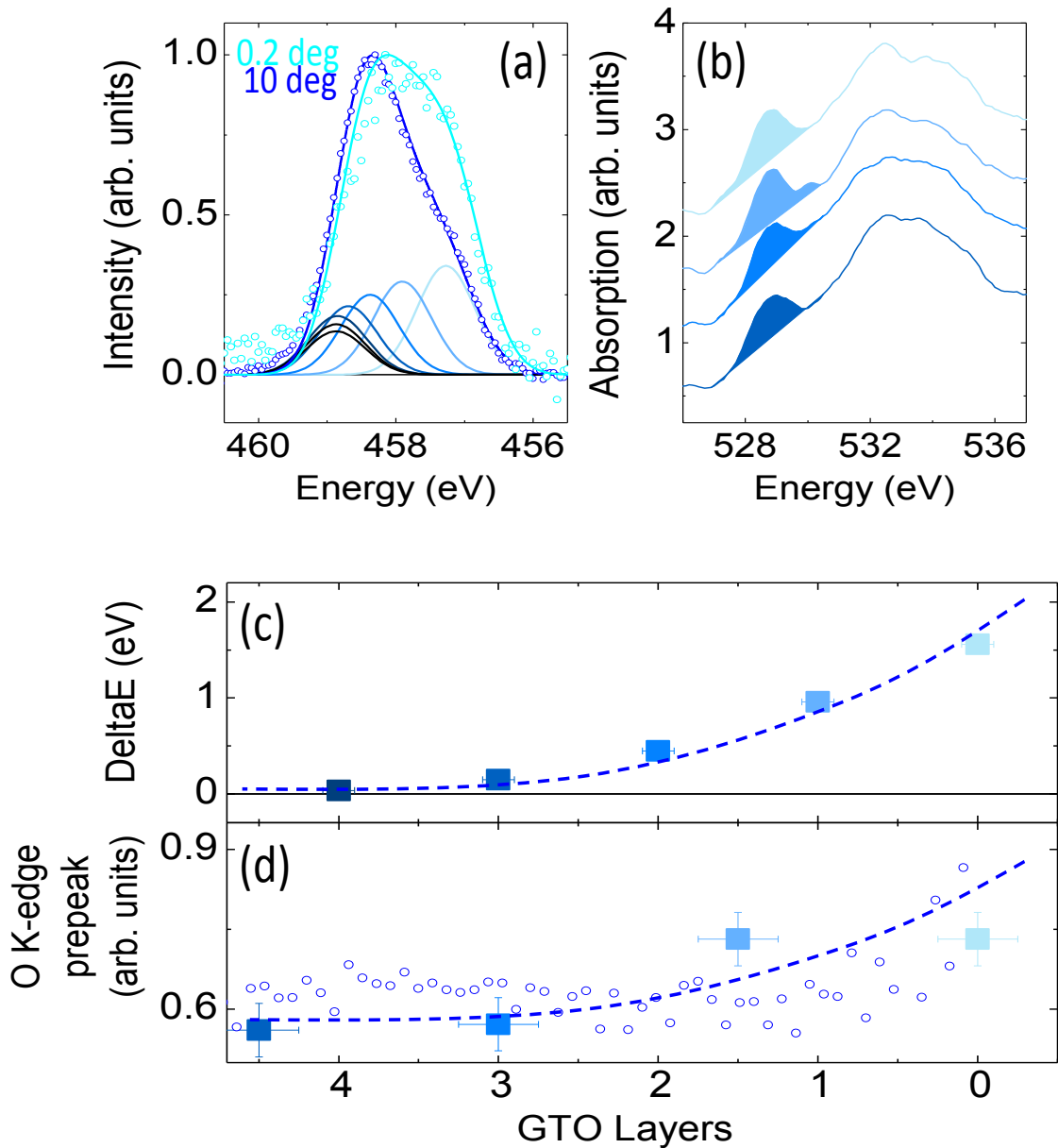


Figure B-8: (a) Experimental data (dots) and fit (thick solid lines) of the Ti 2p_{3/2} spectra measured at 0.2 deg and 10 deg (cyan and blue). The thin Gaussian lines show the individual simulated Ti 2p_{3/2} spectra for each Ti plane used to reproduce the experimental data. (b) EELS at the O K-edge at different positions in the GTO (lighter blue: closer to the interface) (c) Variation of the Ti 2p_{3/2} binding energy in each Ti layer extracted from fitting the HXPS spectra shown in (a). (d) Variation of the O K-edge pre-peak area (large squares) and energy shift (small blue dots) resolved for each layer and extracted from the EELS spectra presented in (b). In (c-d), the blue dotted lines are guides to the eye.

We confirm this trend observed by HXPS, using EELS at the O K-edge. Indeed, the intensity of the pre-peak in the O K-edge spectra is proportional to the number of holes in the hybridized *p-d* band. In titanates, in which the conduction band is more *d*-like, it is directly related to the number of holes in the *d* band, set by the oxidation state [209] *i.e.* the peak is enhanced for Ti⁴⁺ compared to

Ti³⁺. Figure B-8 (b) shows O K-edge spectra collected at different distances from the interface in the GTO layer. The peak area appears to increase as one approaches the interface (from darker to lighter blue). The data are plotted as solid squares in Figure B-8 (d), along with the normalized height of the O K-edge pre-peak (blue open dots). Both sets of data indicate an increase of the pre-peak intensity near the interface with the nickelate, consistent with a Ti valence increasing towards 4+. Interestingly, a "bulk-like" response is also recovered beyond 2 to 3 GTO planes (cf. chapter III). Both HXPS and EELS data thus point to an increase of the Ti valence towards 4+ occurring over 2 to 3 unit-planes near the interface with the nickelate.

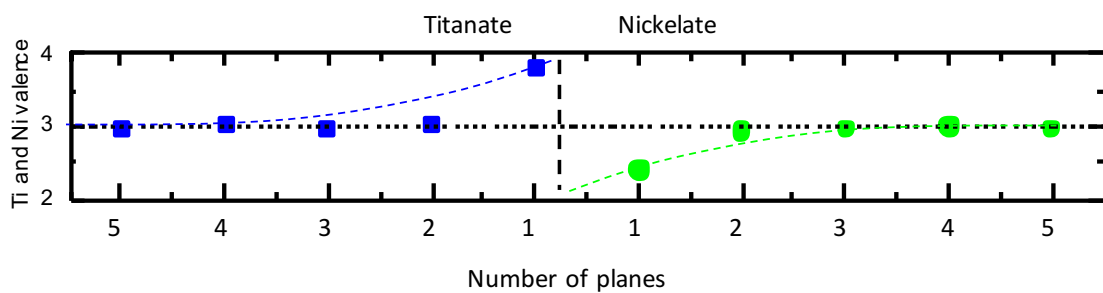


Figure B-9: Evolution of the Ti and Ni valence across the interface from first-principles calculations.

This opposite trend from 3+ to 4+ and 2+ to 3+ respectively for Ti and Ni across the interface was also established using first-principles calculations based on parameters that reproduce correctly the bulk properties of both titanates and nickelates (see previous chapters). Geometry relaxations were performed on a (GdTiO₃)₇/(GdNiO₃)₇ superlattice strained on a LAO substrate. The computed average valence per BO₂ plane of Ti and Ni atoms along the growth direction is summarized in Figure B-9.

Away from the interface between GTO and the nickelate, the Ti valence is close to 3+ as in the bulk but closer to the interface, the Ti valence increases from 3+ to 4+. An opposite behavior is observed on the nickelate side: the nickel valence decreases from 3+ towards 2+ upon approaching the interface. This clearly indicated charge transfer, which spreads over 2-3 u.c. with a main contribution coming from the interfacial plane.

b) In RNO/GTO

We now move on to study the influence of the rare earth in the nickelate on the interfacial charge transfer. We have used XAS at the Ti and Ni $L_{2,3}$ edges in LNO/GTO, NNO/GTO and SNO/GTO bilayers and different reference samples.

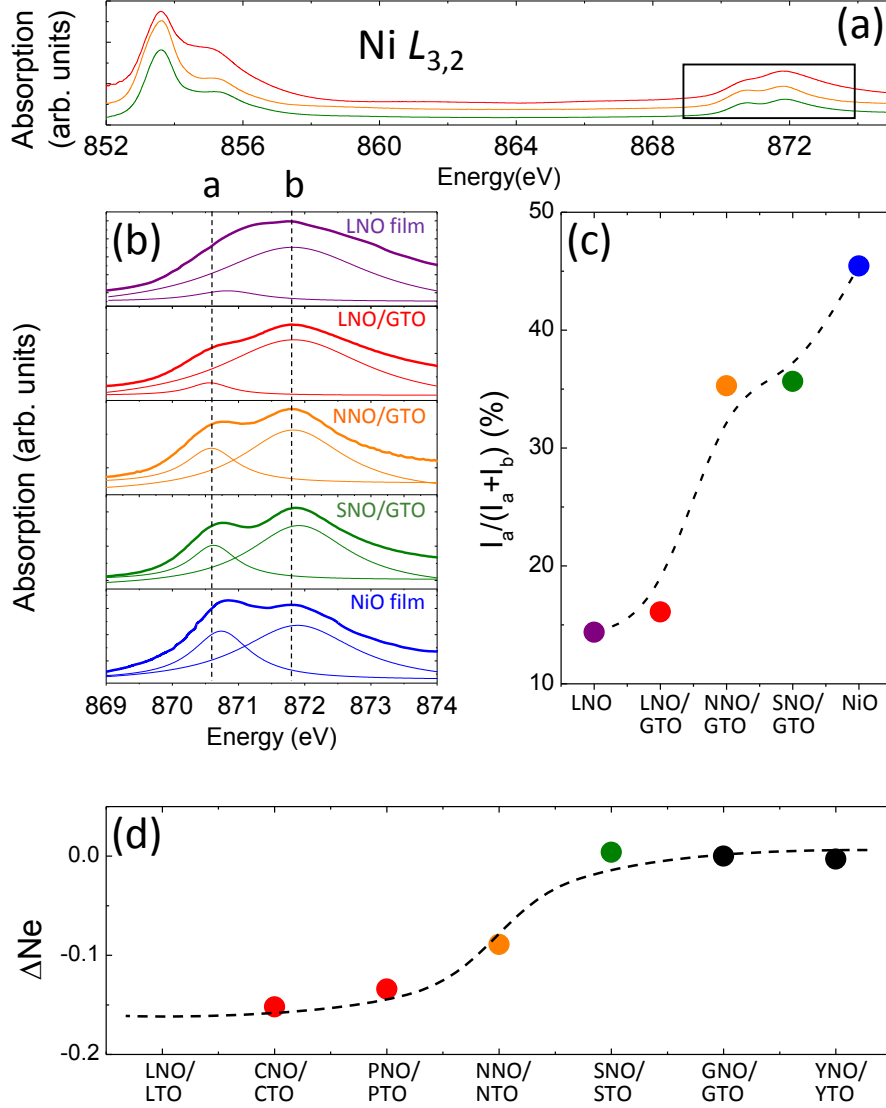


Figure B-10: (a) XAS at the Ni $L_{2,3}$ edge for LNO/GTO (red), NNO/GTO (orange) and SNO/GTO (green). The black rectangle highlights the Ni L_2 edge. (b) Detailed view of the Ni L_2 experimental spectra (thick lines) in (from top to bottom) a LNO single film (violet), the three bilayers and a NiO reference (blue, from Ref. [210]). All spectra were fitted with two Gaussian peaks (shown as thin lines). (c) Relative intensity of peak "a" in Fig. 3b plotted for the different samples (the dashed line is a B-spline passing through the data). (d) DFT calculations of amount of transferred electrons ΔN_e from the Ti ions across the interface in $(RTO)_2/(RNO)_1$ (for $R = Ce, Pr, Nd, Sm, Gd, Y$) relative to the value for $R=Gd$.

In Figure B-10, we plot the XAS at the Ni $L_{2,3}$ edge for the three bilayers, corrected for the overlap of the La $M_{4,5}$ signal. In Ni oxides, the spectral shape of the Ni L_2 edge strongly varies with the

Ni oxidation state [116,210]. We thus use it to gain insight into the Ni valence in our samples. As we discussed in the previous chapter, Ni L_2 is intrinsically more complex than Ni L_3 on which we based our analysis in chapter IV. Even if we may be tempted to call these peaks t_{2g} and e_g , mixed-valence would blur such distinction as atomic excitonic states from both valence states may interact. We would rather label these peaks: "a" and "b". As visible in Figure B-10 (b), the shape of the spectra in our bilayers clearly deviates from that of a reference LNO film (top panel), which readily indicates a different formal Ni oxidation state. The enhancement of the low energy peak (labelled "a") is reminiscent of the signature of Ni^{2+} in the NiO reference [210] (bottom panel). We analyze the valence change in the different bilayers by comparing the relative intensity of the two peaks ("a" and "b"). Figure B-10 (c), summarizes these results and suggests that the Ni valence is reduced towards $2+$ for the three samples, with a stronger change for the NNO/GTO and SNO/GTO samples. This behavior is further confirmed by DFT calculations on a set of different RTO/RNO superlattices (Figure B-10) revealing a strong effect of the sole rare earth in the nickelate on the amount of transferred electrons.

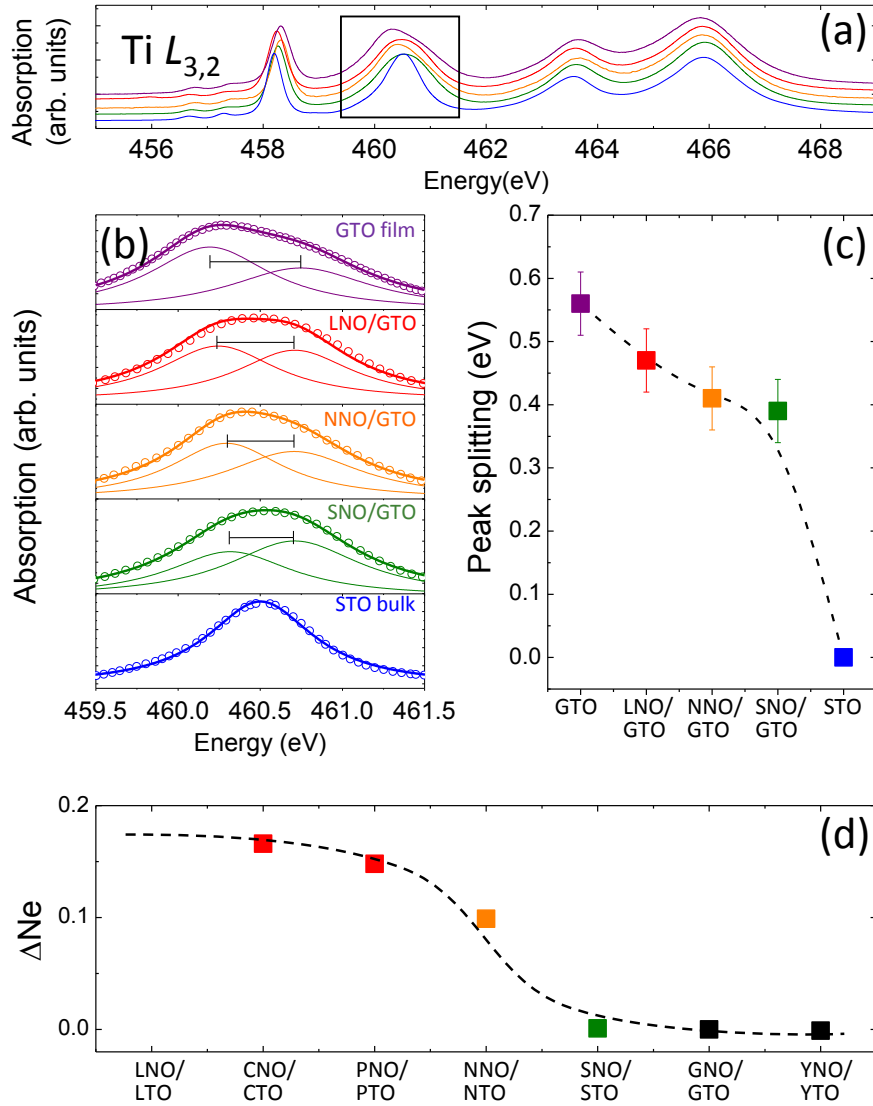


Figure B-11: (a) XAS at the Ti $L_{2,3}$ edge for a GTO film (purple), LNO/GTO (red), NNO/GTO (orange), SNO/GTO (green) and a STO crystal (blue). The black rectangle highlights the second peak of Ti L_3 edge used for the analysis. (b) Detailed view of the experimental XAS (symbols) at the second peak of the Ti L_3 edge for (from top to bottom) a GTO film, the three bilayers and a STO crystal. Except for STO, all spectra were fitted with two gaussian peaks (shown as thin lines; the resulting spectra are shown as thick lines). The horizontal bar indicates the energy separation between the peaks. (c) Energy difference between the two gaussian components (the dashed line is a B-spline passing through the data). (d) DFT calculations of the variation of transferred electrons ΔN_e to the Ni ions across the interface in $(RTO)_2/(RNO)_1$ (for $R= Ce, Pr, Nd, Sm, Gd, Y$) relative to the value for $R=Gd$.

In parallel, we looked for variations in the Ti valence by analyzing the XAS at the Ti $L_{3,2}$ edge, cf. Figure B-11. Literature on XAS in rare-earth titanates is scarce [211] especially for strongly distorted compounds such as GTO. Trends in the XAS spectra can however be inferred from the electronic structure of perovskite titanates [49]. There are several important differences in the Ti $3d$

levels of a Ti^{3+} perovskite compared to those of a Ti^{4+} perovskite, including the finite d level occupancy and the splitting of both t_{2g} and e_g levels due to oxygen cages and orthorhombic GdFeO_3 distortions for Ti^{3+} (Ref. [49]). As a result, the spectral shape and width of the absorption peaks are expected to be broader in rare-earth titanates than in Ti^{4+} perovskites such as SrTiO_3 (STO), cf. Ref. [211,212]. In chapter III, we also observed that the presence of superficial over-oxidation (presence of Ti^{4+}) on GTO monocrystal could be quantified by a broader width of the second feature of the L_3 -peak.

In Figure B-11 (a), we plot the high-energy Ti L_3 peak for LNO/GTO, NNO/GTO and SNO/GTO bilayers, along with those of a GTO single film and a STO crystal. While the peak for STO can be well fitted by a single component, two components are needed for the GTO film and the three bilayers. The total width of the experimental peak as well as the energy splitting between both components decreases upon going from the GTO film through the bilayers series (see Figure B-11 c). Because the structural parameters of GTO in the different bilayers are the same, this variation is unlikely to be associated with changes in the crystal field splitting. Rather, this finding suggests a mixed $\text{Ti}^{3+/4+}$ character for the bilayers, with an increase of the Ti valence towards 4+ for smaller rare-earths. Again, this behavior is reproduced by our first-principles calculations (Figure B-11 d). Remarkably, the trend is opposite and complementary to that of the Ni valence inferred from Figure B-10 a-d, strongly suggesting that the transfer of electrons from the titanate to the nickelate is controlled by the sole rare-earth in the nickelate, in agreement with the calculations. Because, here, XAS probes the whole nickelate and titanate thickness, the valence changes that we deduce correspond however to weighted averages within each layer.

c) Effect of polar termination

An arresting result of the interfacial properties of our bilayer is that the interface configuration may not play a major role in the charge transfer. Indeed, in both subsystems, whatever the termination is, the charge configuration is in principle exactly the same and the interface is non-polar: $\text{GdO}^+-\text{TiO}_2^- - \text{LaO}^+-\text{NiO}_2^-$ or $\text{GdO}^+-\text{NiO}_2^- - \text{LaO}^+-\text{TiO}_2^-$. Note that from Figure B-3, we can estimate that the nickelate film is LaO-terminated.

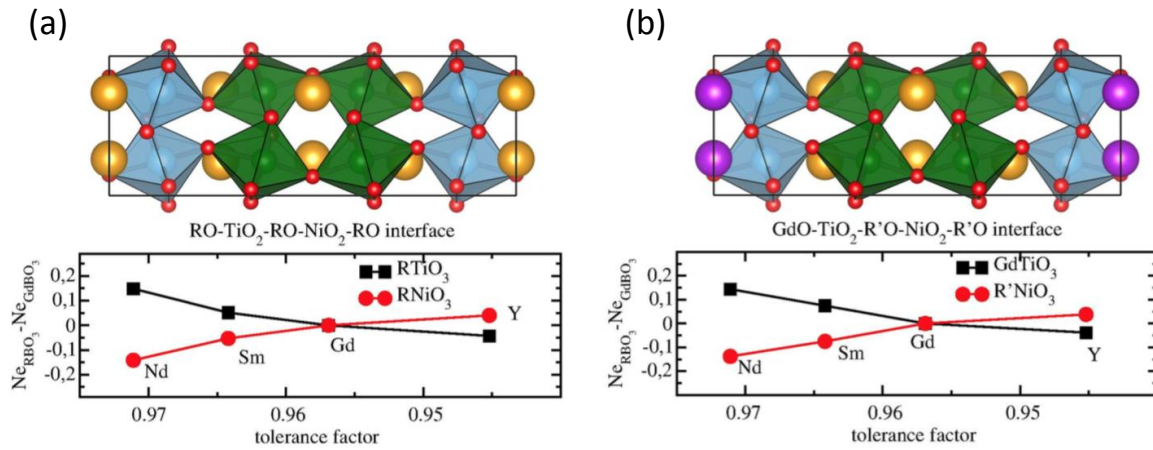


Figure B-12: Variation of number of electrons in each subsystems RTO/RNO ($R=\text{Nd, Sm, Gd, Y}$) compared to the ideal case of $(\text{GTO})_2/(\text{GNO})_2$ superlattice with similar interfaces (a) and asymmetric interfaces for subsystems GTO/RNO ($R=\text{Nd, Sm, Gd, Y}$) (b) compared to the ideal case of $(\text{GTO})_2/(\text{GNO})_2$ superlattice.

However, since we could not reverse the stacking of the heterostructures, cf. Figure B-2, we checked this possibility using DFT calculations on a set of $(\text{RTiO}_3)_2/(\text{R}'\text{NiO}_3)_2$ superlattices ($R=\text{Y, Gd, Sm}$ and Nd). The two possible interfaces were modeled $\text{RO-TiO}_2\text{-RO-NiO}_2\text{-RO}\dots$ and $\text{GdO-TiO}_2\text{-R}'\text{O-NiO}_2\text{-R}'\text{O}\dots$, taking care of not creating an artificial polarization through asymmetric interfaces in the superlattice. Clearly, the trend of the number of electrons transferred as a function of the rare earth is very similar whatever the termination is (see Figure B-12). As the tolerance factor increases, the number of electrons transferred across the interface is decreased. We should emphasize that calculations were intentionally restricted to symmetric interfaces (Figure B-12 a) with only one type of R-cation in order to avoid any propagation of GTO rotations to the nickelate layer due to the relative small size of the system (2/2 superlattices).

Please note however, that after charge transfer, the interface does become polar with a strong dipole electric field forming across the interface as TiO_2 is now neutral while NiO_2 bears now a 2+ charge.

As a conclusion, charge is transferred across the interface of RNO-RTO bilayers. We have been able to show that the amount of charge transferred is controlled by the presence of the rare-earth (La, Nd, or Sm) on the RNO side of the interface rather than by polar discontinuities as in LAO-STO interfaces [176]. In line with recent results on $\text{LaTiO}_3/\text{LaFeO}_3$ interfaces [213] the total charge transferred from the GTO to the nickelate is large, particularly for the NNO/GTO and SNO/GTO

samples. For LNO/GTO, however, charge transfer is strongly thwarted by strong covalence effects as we shall see in the last section of this chapter. But before coming back on the mechanism controlling the charge transfer, let us first turn to the magnetic properties of the heterostructures.

3 - ferromagnetic phase in RNO

Magnetism in transition metal insulators such as nickelates and titanates is ruled by super-exchange interactions [4]. Strongly distorted rare-earth titanates such as GTO are ferromagnetic [49] – for more information please refer to chapter III. However, as we saw in chapter IV, nickelates can be viewed as alternating ferromagnetic and antiferromagnetic exchange paths along the [111] direction in a way determined by the ionic (antiferromagnetic) or covalent nature (ferromagnetic) of the bonds [99]. At the interface between GTO and a nickelate there is a Ti^{3+} -O-Ni antiferromagnetic super-exchange path mediated by t_{2g} electrons which will locally induce a ferromagnetic-like moment in the nickelate. This path will be interrupted for non-magnetic Ti^{4+} if charge transfer occurs at the interface. Thus, looking at the magnetic interactions in the nickelates provides further information about the charge transfer and electronic reconstructions.

a) Magnetism in NNO/GTO

In Figure B-13, we present XAS, XMRS and XMCD measured at low temperature and 5 T in a NNO/GTO bilayer. A magnetic signal is detected at the Gd $M_{4,5}$ (we estimate $M_{\text{Gd}}=5.8 \mu_{\text{B}}$) and Ti $L_{2,3}$ edges, consistent with the ferromagnetic character of GTO. Surprisingly, although bulk NNO is antiferromagnetic, a sizeable dichroic signal is measured at the Ni $L_{2,3}$ edge (sum rules leads to a value of about $M_{\text{Ni}}=0.1-0.2 \mu_{\text{B}}$ averaged over the whole 7 u.c. thickness).

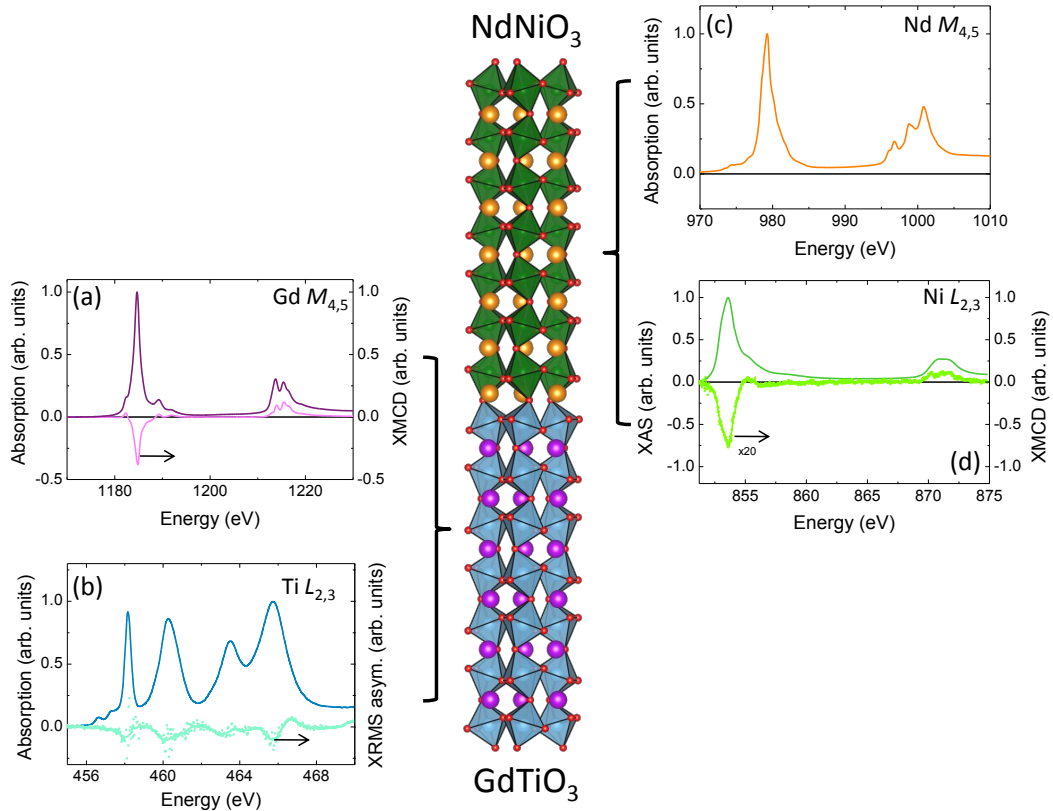


Figure B-13: X-ray absorption, X-ray resonant magnetic scattering and X-ray magnetic circular dichroism spectra obtained at 8 K and 5 T in a NNO/GTO bilayer. XAS spectra were collected at the Ti (b) and Ni $L_{2,3}$ (d) edges and at the Gd (a) and Nd $M_{4,5}$ (c) edges. XMCD at the Gd $M_{4,5}$ and Ni $L_{2,3}$ edges are shown in panels (a) and (d), right axes. The asymmetry of the XMRS signal with respect to photon helicity measured at the Ti $L_{2,3}$ edge is also presented in panel (b), right axis.

The magnetic field dependence of the dichroic response at the Ni L_2 edge for this sample is shown in Figure B-14 (a-h). Panels Figure B-14 (a) to Figure B-14 (f) show XRMS asymmetry spectra measured at different fields ramping the field down from 3T (darker graphs) and up from -3T (lighter graphs). A first observation is that at high magnetic field the spectra for both sweep directions virtually superimpose (Figure B-14 a and f), while they are different at low magnetic field (see for instance Figure B-14 d and e). This indicates hysteresis and a ferromagnetic-like behavior.

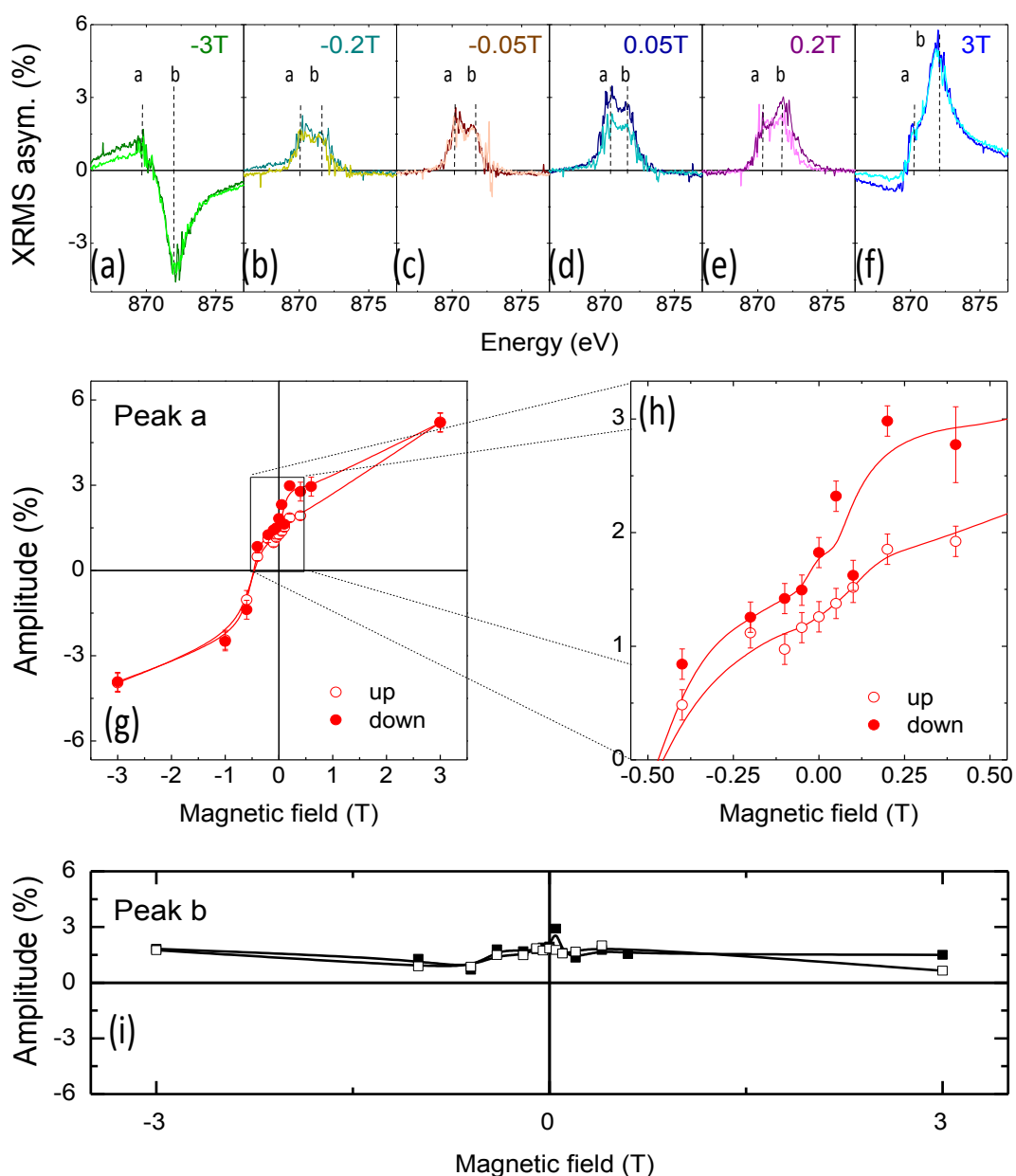


Figure B-14: (a-f) XRMS spectra measured at different fields ramping the field down from 3 T (darker graphs) and up from -3 T (lighter graphs). Amplitude of peak “a” (g) and “b” (i) extracted from the XRMS spectra as a function of the magnetic field. (h) Zoom of the low field region of graph (g).

Secondly, the shape of the signal changes with the magnetic field, which strongly suggests that several magnetic components are present in the sample, and that they respond differently to the magnetic field. This is not unexpected because Ni is in a mixed 2+/3+ valence state and Ni^{2+} and Ni^{3+} may show different behavior under the application of an external magnetic field. Even with multiplet calculations, decomposing the experimental spectrum at each magnetic field into two dichroic signals unambiguously ascribable to Ni^{2+} and to Ni^{3+} would be very delicate (notably due to

the depth dependence of both Ni species). Here we simply fit the spectra with two Lorentzian components for which we allow the width and position to vary only in a narrow range (cf. Figure B-15).

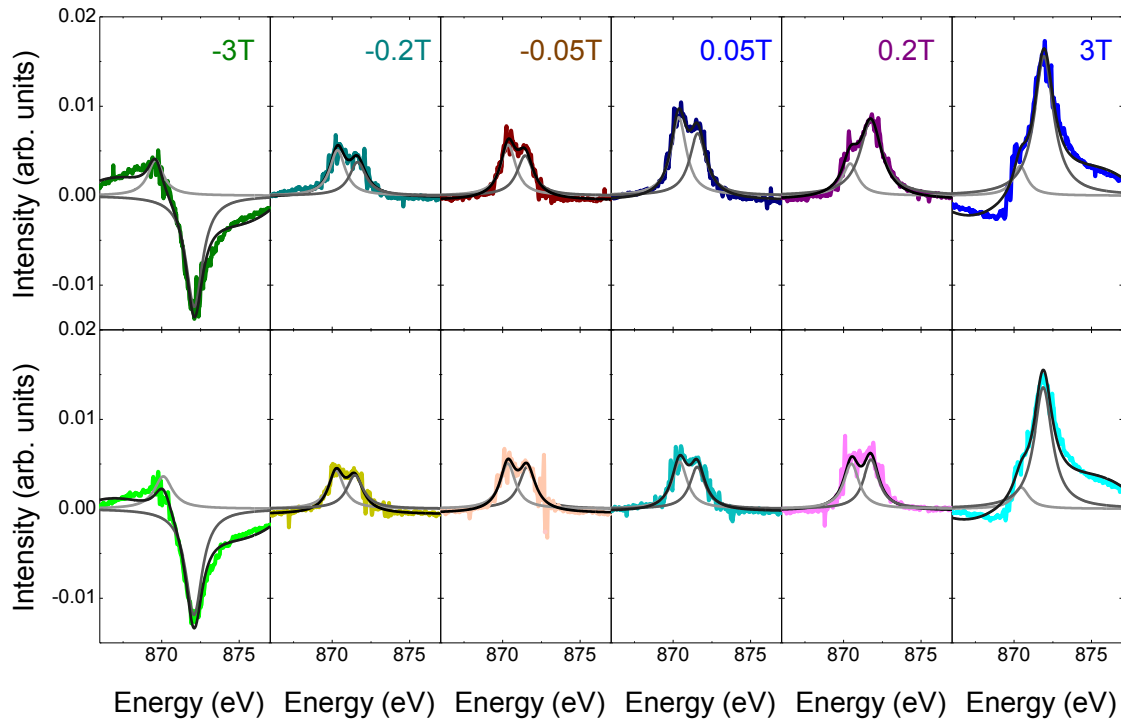


Figure B-15: Lorentzian decomposition for different fields ramping up (upper panel) and ramping down (lower panel).

The first peak ("a") amplitude (centered near 870 eV) shows little magnetic field dependence and is always positive (cf. Figure B-14 i). The second peak ("b") shows a much stronger dependence of its amplitude with the magnetic field, corresponding to an hysteresis loop that is open at low positive fields, see Figure B-14 (g-h). The asymmetry in the hysteresis loop is possibly reminiscent of exchange bias [191] which occurs at interfaces between a ferromagnet and an antiferromagnet [214]. In some exchange bias systems, a vertical shift of the hysteresis loop of one magnetic component accompanies the horizontal shift of the loop of the other component [215], as in our observations. We note that exchange bias has also been observed in nickelate/manganite multilayers [216].

Additionally, the magnetic behavior of peak "a" in the AXRMS spectra suggests the presence of pinned moments (also referred to as "frozen spins", since large magnetic fields are necessary to change their direction). These frozen spins may be at the origin of the phenomenon of exchange bias and are found in different materials ranging from oxides, to metals, to core-shell nanoparticles [215,217]. Some of these frozen spins produce uncompensated moments that are also blocked and, within the theory of exchange bias, are expected to produce vertical shifts of

magnetization loops (in other words, the measured magnetization is the sum of the rotating moments and of the pinned moments).

Such vertical shifts have been observed in a broad range of systems [215,218,219]. Olhdag et al in [215] have reported vertical shifts in Mn XMCD hysteresis in IrMn/Co bilayers. In that study, the vertical shift, corresponding to the presence of pinned moments, is observed up to 3 kOe. However, in other systems [218,219], large vertical shifts persisting up to several teslas have been reported. We believe that this pinned moments are responsible for the magnetic response observed at peak “a” and are the origin of this peculiar asymmetry that we observed in Figure B-14 (g), reminiscent of exchange bias signals.

b) Magnetism in RNO/GTO

To explore the influence of interfacial charge transfer on magnetism in the nickelate, we compare XMCD at the Ni $L_{2,3}$ edge for the three bilayers after normalization at the L_3 peak of the respective XAS spectra, *cf.* Figure B-16 (a-b). As visible in Figure B-16 (i), a large XMCD signal is observed for all samples. In Figure B-16 (b), we highlight the signal at the Ni L_2 edge. As in the XAS (see Figure B-10), the spectral shape varies with the rare-earth, suggesting an influence of the Ni valence change on its magnetic response. The intensity of the low energy peak “a” increases when going from LNO/GTO to SNO/GTO, as summarized in Figure B-16 (c). The parallel between Figure B-10 (c) and Figure B-16 (c) indicates that Ni^{2+} ions strongly contribute to the overall magnetic signal (namely in the region of peak “a”).

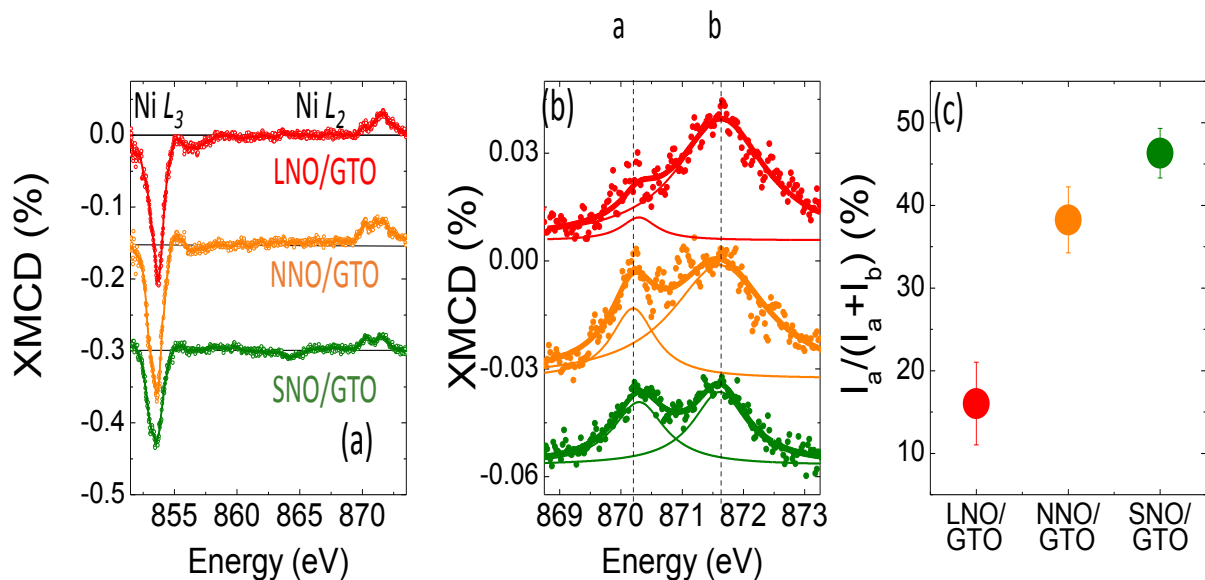


Figure B-16: (a) Full Ni $L_{2,3}$ XMCD spectra acquired at 8 K for LNO/GTO (red), NNO/GTO (orange) and SNO/GTO (green). (b) Ni L_2 edge experimental spectra (symbols) for all three bilayers. The spectra were fitted by two Gaussian components shown as thin lines, with the resulting fit displayed as a thick line. (c) Relative intensity of peak “a” plotted for the different bilayers.

From this parallel between XAS and XMCD, it is tempting to associate the pinned moments observed in Figure B-14 (i) with interfacial Ni^{2+} that would exchange bias a majority of magnetized Ni^{3+} further away from the titanate interface, leading to the magnetic response in Figure B-14. However, further work is required to fully confirm this scenario. Extra work is needed to determine the temperature-dependent properties of this ferromagnetic-like state and in particular its Curie temperature

In this section, we have thus unveiled a ferromagnetic-like phase in nickelates at the interface with GTO. It is clear from XMCD and XAS characterizations that this magnetic phase is fully correlated to the amount of charge transferred across the interface. Interestingly, we believe to have uncovered magnetic Ni^{2+} states which are pinned and present very strong anisotropy up to several Teslas.

We now turn to investigate the mechanism driving how the transferred charge and magnetic spins are distributed in the hybridized bands of the nickelate.

4 - A new knob for tuning oxide properties: Covalence

As we saw in the previous chapter, changes in the multiplet splitting of the Ni L_3 absorption edge can be used to estimate the level of covalence.

a) Measuring covalence in RNO/GTO

Previous studies in bulk samples, confirmed by our own low temperature study on SNO thin films, have shown that progressing in the nickelate series (decreasing the rare earth ionic radius) results in a larger splitting of the L_3 peaks, analyzed in terms of a decrease in covalence [162,163]. We have analyzed and fitted the XAS at the Ni L_3 edge for LNO, NNO and SNO reference films as well as for LNO/GTO, NNO/GTO and SNO/GTO bilayers. Results for LNO and LNO/GTO, as well as for SNO and SNO/GTO are shown in Figure B-17 (a) and (b), respectively. The energy splitting between both components of the fit are plotted in Figure B-17 (c). The peak splitting increases upon going from LNO/GTO to NNO/GTO to SNO/GTO, reflecting a decrease in covalence, as found in bulk nickelates with decreasing rare-earth size [162]. In addition, we also find that the splitting values are similar between the bilayers and reference single films (fully strained on LAO).

We will describe the hybridization between the oxygen $2p$ band to the $3d$ band – that we thoroughly investigate in the previous chapter – as a superposition of the form $|\Psi\rangle =$

$\alpha|3d^7> + \beta|3d^8L>$ where L stands for the ligand (oxygen) holes ($\alpha^2 + \beta^2 = 1$), following Sawatzky's description [140]. RNO systems are now partly covalent, and the degree of covalence is given by the ratio between β^2 and α^2 . In the strongly covalent limit ($\beta^2/\alpha^2 \gg 1$), conduction has a dominant p character (in contrast, in ionic Mott-Hubbard insulators $\beta^2/\alpha^2 \ll 1$) [21,116,139,140,142]. Hence, similar splitting between bilayers and reference single films indicates that the relative weights (probability) in the hybridized states $|\Psi\rangle = \alpha|3d^7> + \beta|3d^8L>$ are comparable in films and in bilayers, suggesting that for a given rare-earth nickelate, the proportion $\beta^2/(\beta^2 + \alpha^2)$ is characteristic of the chemical Ni^{3+} state.

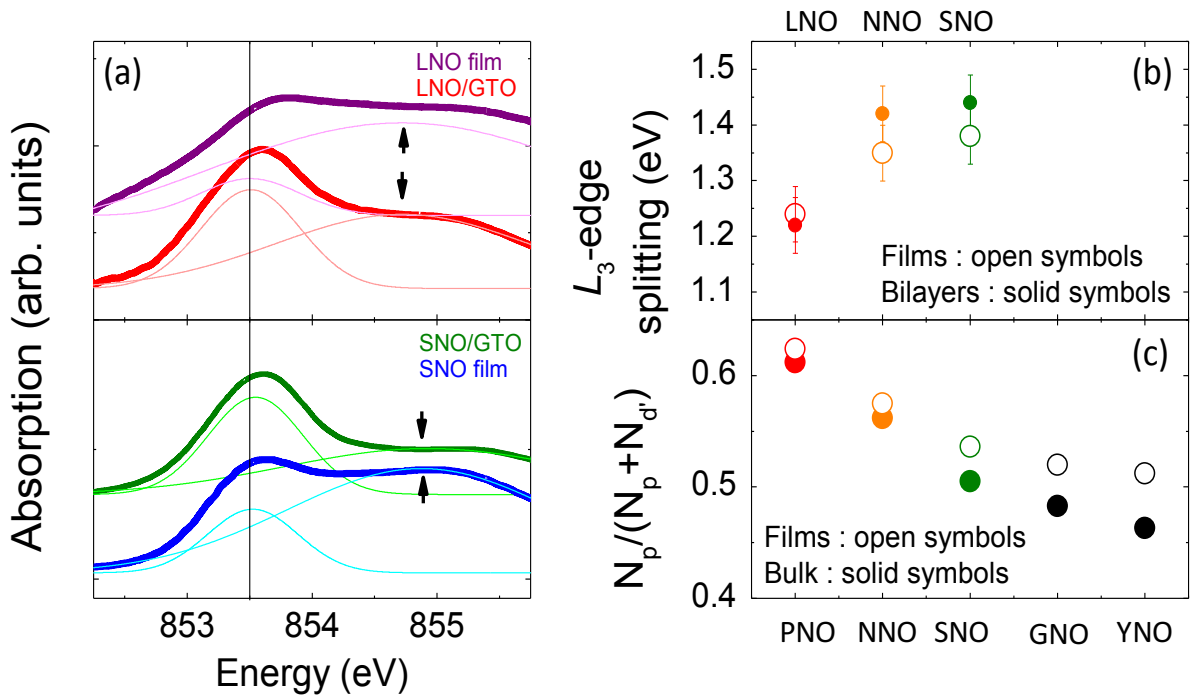


Figure B-17: Experimental XAS signal (thick line) at the Ni L_3 edge for a LNO film and a LNO/GTO bilayer (a) and a SNO film and a SNO/GTO (b). All spectra were fitted with two peaks (thin lines) and shifted in energy to align the first component at 853.5 eV. The arrows indicate the position of the second peak. (c) Energy difference between the two components in (a), (b) and for a NNO film and a NNO/GTO bilayer analyzed similarly (not shown). (d) Covalence extracted from first-principles calculations of density of states in nickelate films strained on LAO (open symbols) and bulk (solid symbols)

To reinforce this interpretation, the electronic structure of single films of nickelates (bulk and strained on LAO) was calculated. We report the density of states of $GdNiO_3$ ground state (T-type AFM ordering) in Figure B-18. Two peaks near the Fermi level (between -0.5 eV and 0 eV), well separated from deeper levels, are observed. Contributions to these peaks come from the d -orbitals of the two types of Ni sites with differences linked to the charge ordered phase as well as O p -orbitals, revealing strong covalence effects.

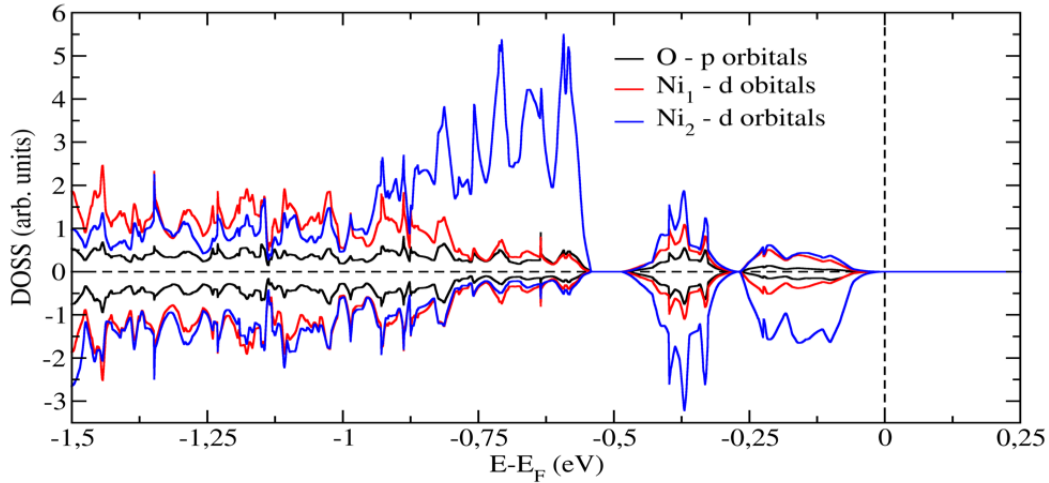


Figure B-18: Density of states of bulk GdNiO_3 (T-type AFM). The total density of states projected on d levels of the two independent Ni sites is reported (red and blue curves) as well as the total density of states projected on p levels of one O atom belonging to the same NiO_2 plane.

As addressed by [220], the charge in DFT calculations is ill-defined while magnetic properties are more reliable in the case of spin polarized systems. This discrepancy arises from the difficulty to separate charges between species (particularly in heterostructures), coming from a non-unique method to perform this partitioning. Here, we thus extract the covalence from the calculation by estimating how much the magnetic moment coming from the d electrons in these two peaks spreads on the nearest-oxygen sites located in the NiO_2 plane.

In our definition, covalence is thus proportional to $(N \text{ p-electrons}) / (N \text{ p-electrons} + \text{net magnetic moment in } d \text{ orbitals})$, see Figure B-18. This analysis was then performed for various nickelates and the behavior is reported on Figure B-17 (c). As the tolerance factor of bulk nickelates increases, calculations show that the covalence is strongly increased. Going to strained compounds, a similar behavior is observed, even if the covalence is increased for compounds with small tolerance factor. However, the trend is still present and large R cations remain more covalent than small rare earth elements.

To conclude on this point, it is important to state that all structural and spectroscopy data point to a fully strained structure for all bilayers (cf. Figure B-4). An analysis of the out-of-plane lattice parameter of the GdTiO_3 in the different bilayers yields similar values for all films (3.87 \AA). Thus, each experimental tool, added to DFT calculations indicate that in the large rare-earth limit, the rare-earth size is the dominant parameter determining the level of covalence, while strain acts as a secondary

effect. This confirms the idea that covalence is mostly a local and intrinsic property of the Ni-O-Ni bond (with strain playing a minor role in the low strain limit of larger rare-earth nickelates on LAO).

b) Charge transfer in RNO/GTO at the O K-edge

In Figure B-19 (a), we plot the spectra for three bilayers and two reference samples (purple: SNO single film, blue: GTO single film). Bilayers display two pre-peaks at 529 eV and 531 eV, associated with oxygen hybridization with Ni and Ti, respectively. Upon going from LNO/GTO to NNO/GTO and SNO/GTO, the Ni pre-peak intensity globally decreases while that of the Ti pre-peak increases (see Figure B-19 b and c). This latter trend is a direct confirmation of the change in the Ti valence discussed in Figure B-11 (c) and Figure B-11 (g). The decrease in the Ni pre-peak intensity as the rare earth is varied from La to Sm is much stronger than that found in bulk RNO (Ref. [115]) and thus cannot be attributed to a simple decrease in the covalence.

To understand this variation, it is helpful to consider that charge transfer from GTO causes a change from $Ni^{3+} = \alpha|3d^7\rangle + \beta|3d^8L\rangle$ towards a $Ni^{2+} \approx \alpha'|3d^8\rangle$ (which is mostly a non-covalent state due to the very high correlation energy cost of states with $3d^9$ components). In the bilayers nickel can thus be described as a mixture of Ni^{3+} and Ni^{2+} , *i.e.* $\alpha|3d^7\rangle + \beta|3d^8L\rangle + \alpha'|3d^8\rangle$, with now $\alpha^2 + \beta^2 + \alpha'^2 = 1$. Charge transfer from GTO increases α'^2 , thereby reducing $\alpha^2 + \beta^2$ and in fact *both* α^2 and β^2 since, as discussed above, the ratio $\beta^2/(\alpha^2 + \beta^2)$ is fixed for a given nickelate (*cf.* Figure B-17 c).

This *rehybridization* process [221] requires a redistribution of electrons between the $|3d^7\rangle$ and the $|3d^8L\rangle$ states, which occurs at an energy cost Δ for each electron transferred from $|3d^8L\rangle$ to $|3d^7\rangle$. Their relative proportion is β^2 and thus the resulting energy cost is proportional to $\beta^2\Delta$.

Figure B-19 (c) also presents the full width at half maximum (FWHM) of both prepeaks [222], characterizing the hole bandwidths for Ti – that increases as the Ti 3d band is depleted – and for Ni – that decreases as the Ni mixed states are filled. This observation definitely confirms the transfer of charge from the GTO to the nickelate, controlled by the rare earth size.

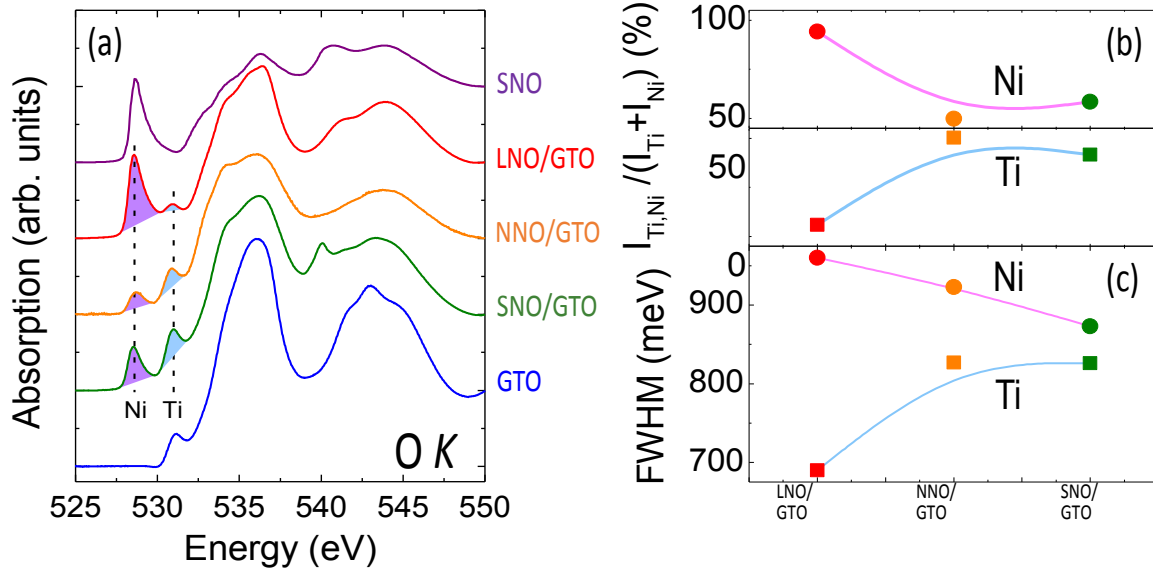


Figure B-19: (a) O K-edge for reference thin films of SNO (violet) and GTO alone (blue) along with the same bilayers. In the bilayers data the integrated area for the Ni and Ti pre-peaks are shaded in purple and blue, respectively. (b) Relative integrated area for the different bilayers. (c) FWHM of the Ni and Ti pre-peaks.

We summarize these ideas in Figure B-20. The top panels correspond to a schematic representation of the electronic structure of "bulk" GTO (left) and nickelate (decomposed into $\alpha|3d^7\rangle + \beta|3d^8L\rangle$ states, right). The rare earth size decreases from left to right, causing a progressive decrease of the bandwidth of the $3d^7$ state and a reduction of the covalent character (decrease of β^2). When an interface is built between GTO and the nickelate (bottom panels), the system attempts to transfer electrons in order to align the electrochemical potentials and this leads to the *rehybridization* process discussed above.

For large rare-earth size, the nickelate has a strong covalent character, which increases the cost of *rehybridization*. This mechanism competes with the energy gain associated with the difference in electron affinity, thereby limiting the amount of charge that can be transferred across the interface. This scenario can also be viewed as a decrease of the effective electron affinity difference, $\delta\phi$, for larger rare earth radii.

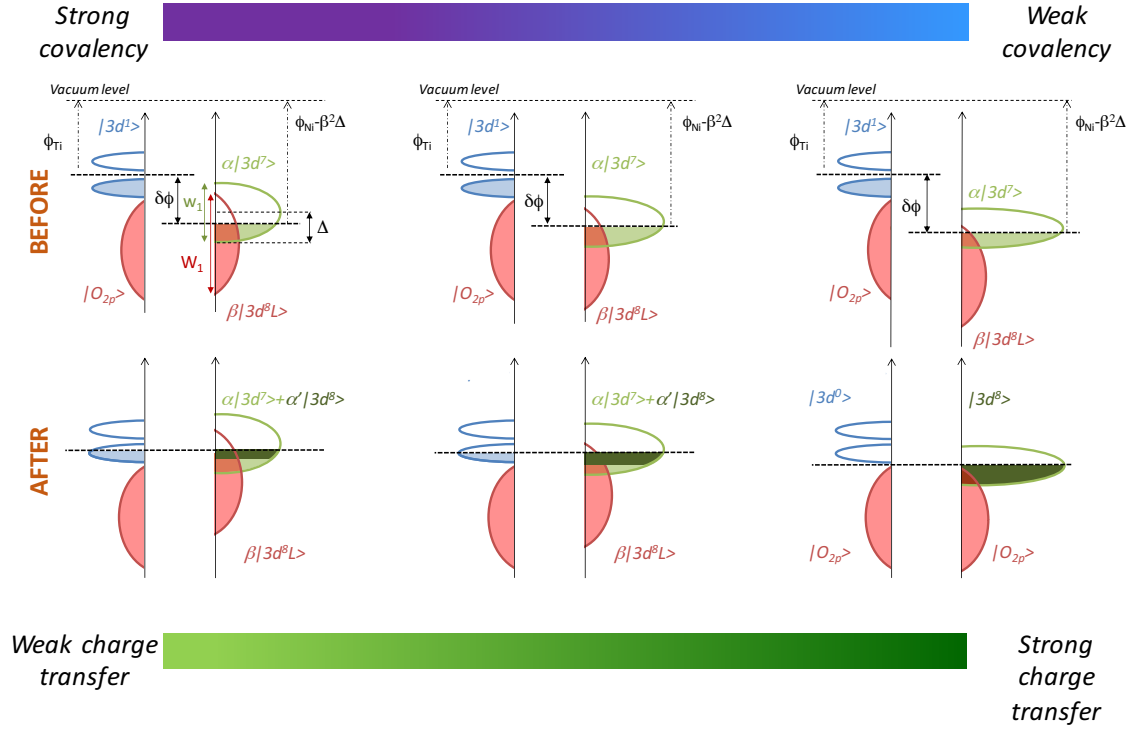


Figure B-20: Schematic representation of the interfacial charge transfer and the rehybridization processes in the covalent bond represented as two independent bands ($|3d^7\rangle$ and $|3d^8L\rangle$) for decreasing rare-earth size (from left to right). The upper panels represent the two parts of the heterostructure before contact and lower panels depict the resulting electronic state after charge transfer and rehybridization.

c) Origin of the covalence in RNO/GTO bilayer

In the following, let us try to extract from DFT calculations the factors affecting the covalence at a microscopic level and try to relate them to what we understood from the ground state of nickelates in the previous chapter. Since the charge transfer is mainly located at the interface, calculation was performed only on a $(\text{GdTiO}_3)_1/(\text{GdNiO}_3)_1$ system. The ground state of this (1/1) superlattice exhibits three main distortions: two antiferrodistortive (AFD) motions ($a^-a^-c^0$ and $a^0a^0c^+$ oxygen cage rotations) and one anti-polar X_5 motion whose atomic displacement is in the (xy) -plane. The different distortions in an ideal cube $P4/mmm$ structure were then condensed individually. The variation of the magnetic moment was then extracted in both subsystems (see Figure B-21 left panel). As discussed previously, this variation is homogeneous to a variation of electron transferred between the titanate and the nickelate.

The anti-polar (X_5) and especially the $a^-a^-c^0$ AFD motions have nearly no effect on the charge transfer across the interface, whatever their magnitude in the structure. However, tuning the $a^0a^0c^+$

AFD motion affects in consequence the number of electron transferred between the two subsystems. This may be achieved by changing the rare-earth involved in the system, hence changing the covalent character of the nickelate.

The independent role of the $a^0a^0c^+$ oxygen cage rotations in both subsystems was then checked by fixing this latter in one subsystem and freezing-in some amplitude in the other subsystem (see Figure B-21 right panel).

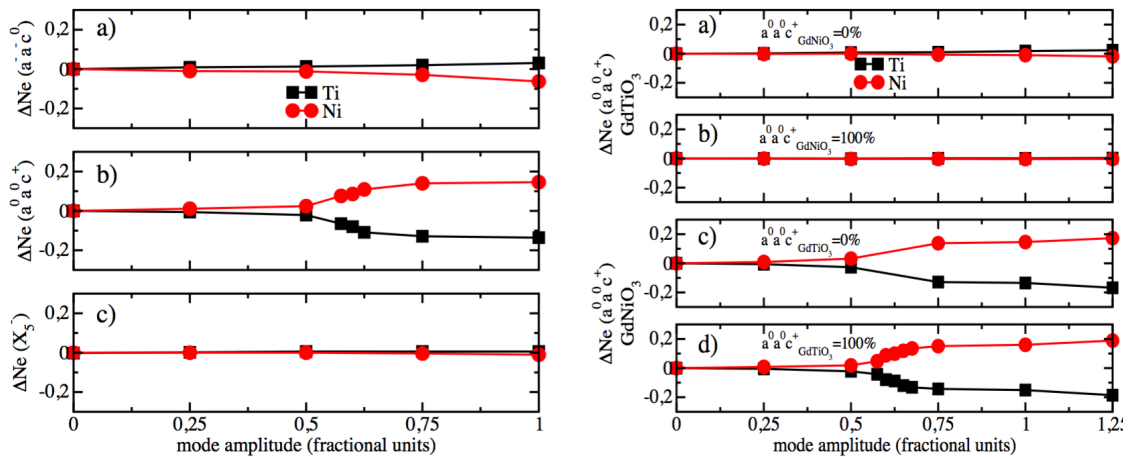


Figure B-21: (Left panel) Influence of the three main distortions appearing in a $(GdTiO_3)_1/(GdNiO_3)_1$ superlattice on the amount of charges transferred between the titanate and the nickelate: the $a^-a^-c^0$ AFD motion (top panel), the $a^0a^0c^+$ AFD motion (middle panel) and the anti-polar X_5^- motion (bottom panel); (right panel) Influence of the $a^0a^0c^+$ rotation in GTO or GNO by imposing 0% or 100% of this distortion in the nickelate or titanate respectively.

The oxygen rotations in the titanate have clearly no impact on the amount of charge transferred, whatever the magnitude of the AFD motion is in the nickelate. The trend is totally different for the nickelate $a^0a^0c^+$ rotation. Indeed, as the magnitude of this rotation increases, the amount of electron transferred increases, whatever the magnitude of the rotation is in the titanate. This results totally demonstrates that tuning the sole rotation in the nickelates, by R-cation substitutions, may alter the charge transfer, independently of the rotation in the titanates. Since the $a^0a^0c^+$ AFD motion might tune the covalence of the nickelate (as the tolerance factor increases, the $a^0a^0c^+$ may decrease). This observation strongly supports the scenario of a covalence-controlled charge transfer.

d) Role of the covalence on magnetism in RNO/GTO

In the last paragraphs of this chapter, we will try to quantify the impact of covalence on the magnetic properties of bilayers interfaces. By using XMCD sum rules (cf. Chapter II) and applying them to the XMCD spectra presented in Figure B-16 (a), we are able to extract the magnetization at Ni site in the three bilayer. We observe that the magnetization increases from LNO/GTO to NNO/GTO before it decreases again from NNO/GTO to SNO/GTO (cf. Figure B-23). Further work is needed to ascertain the exact nature of the exchange paths at play at this complex interface, but one may speculate that covalent exchange, proposed as the source of ferromagnetism in $\text{Li}_{1-x}\text{Ni}_{1+x}\text{O}_2$ (Ref. [223]), is an important ingredient to produce the observed Ni dichroism. Indeed, any other super-exchange paths between Ni ions either $\text{Ni}^{3+}\text{-Ni}^{3+}$ or $\text{Ni}^{2+}\text{-Ni}^{2+}$ or $\text{Ni}^{2+}\text{-Ni}^{3+}$ yields strong antiferromagnetic behavior. Only the exchange between a Ni^{3+} covalently bonded to a Ni^{2+} can lead to a strong ferromagnetic exchange. The measure of the magnetization thus informs on the distribution of the charge across covalent bonds.

In order to reinforce the qualitative trend presented in Figure B-10 and Figure B-11, we have performed simulations of the XMCD of both Ni^{2+} and Ni^{3+} in Figure B-13 using the CTM4XAS software [72]. The simulations are presented in Figure B-22 (f-j) below, and compared with experimental results at 5 T for the three bilayers (Figure B-22 b-d) and for two reference samples (LaNiO₃ for Ni^{3+} – Figure B-22 a – and a NiFe₂O₄ film for Ni^{2+} – Figure B-22 e).

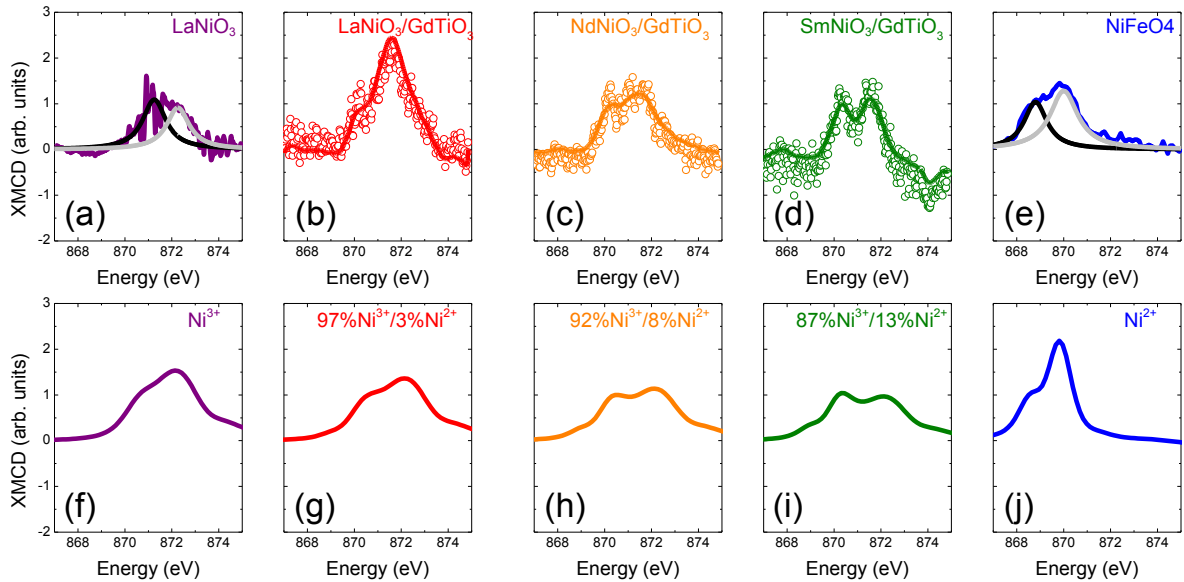


Figure B-22: XMCD for reference samples (a, e), RNO/GTO bilayers (b-d) and their simulations with CTM4XAS assuming a $10Dq=1.4$ eV in an O_h environment (f-j).

As one can appreciate, the experimental spectra are well reproduced by multiplet calculations (using a $10Dq$ of 1.4eV). For both pure Ni^{2+} and pure Ni^{3+} , the XMCD can be interpreted

as composed of two main peaks, the peak at low energy always remaining less intense than that of higher energy. However, because there is a shift in energy between the XMCD of pure Ni^{2+} and that of pure Ni^{3+} , the XMCD of mixed-valent $\text{Ni}^{2+/3+}$ may show a multiple-peak shape, with a lower energy peak as intense as (or even more intense than) the higher energy peak, cf. Figure B-22 (g-i). Remarkably, the relative proportion of Ni^{2+} required to reproduce the experimental spectra of Figure B-22 (b-d) increases upon changing the rare-earth from La to Nd to Sm in the nickelate, in agreement with the amount of charge transferred from the GTO thin film.

Assuming, in a simplistic 2D percolation model (since charge transfer mainly occurs at the interface), that only Ni^{2+} shared by a majority of Ni^{3+} will magnetize, one can reproduce the non-monotonous trend observed for the magnetization in the three bilayers. Indeed, for a small amount of transferred charges, the Ni configuration is mainly made of pairs of Ni^{3+} that yield strong AFM coupling. While increasing the amount of transferred charges (for weaker covalence), the number of covalently shared Ni^{2+} - Ni^{3+} couple increases, to reach a maximum. This corresponds to the maximum magnetization in NNO. When the charge transfer is increased further, the magnetization drops down because of the very strong Ni^{2+} - Ni^{2+} AFM coupling (as in SNO for instance).

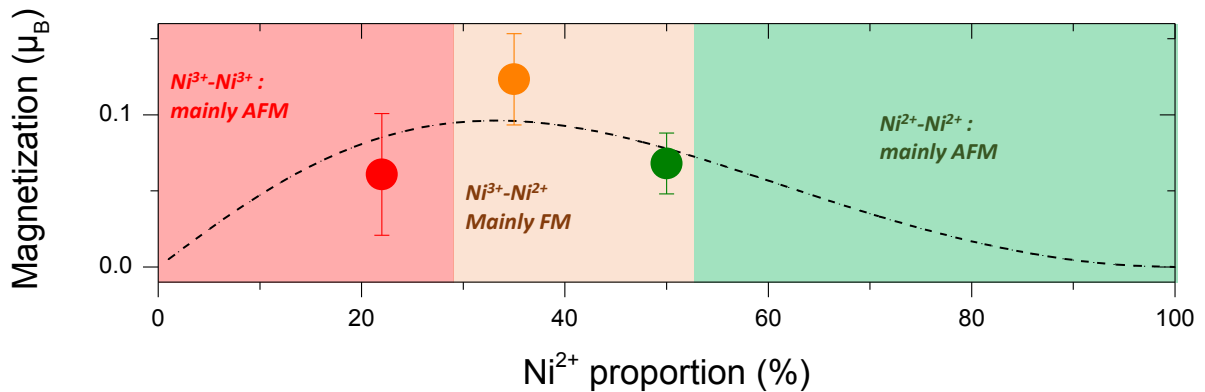


Figure B-23: Magnetization as a function of the magnetic Ni^{2+} proportion. Magnetization is extracted from XMCD sum rules.

In summary, we have discovered that at interfaces between strongly correlated oxides, the covalent character of the transition metal / oxygen bonds plays a key role in determining the amount of charge transferred across the interface, and the resulting charge density in the different available bands. The situation is thus very different from the one found at weakly correlated interfaces [176] where, conventionally, differences in electron affinity and possible polar discontinuities control the interfacial doping.

Our results suggest novel strategies to engineer two-dimensional states in correlated oxides by playing on both the electron affinity mismatch and the level of covalence. In bulk nickelates, the latter can be adjusted by changing the rare-earth size, but any mechanism altering the electron bandwidth should play the same role. For instance, strain-engineering in the large strain limit seems quite promising as an additional knob to craft interfacial properties. Another means of tuning covalence could be to move from oxygen to other ligands such as S or Se.

In the last chapter of this manuscript, we will present other perspectives opened by this work. Indeed, now that we highlighted the specific role of covalence as a new knob to control the amount of charge transferred and induced magnetism in correlated interfaces, we will try to provide novel routes towards the external control of covalence without changing the rare-earth in titanates-nickelate-heterostructures.

VI. Versatile manipulation of covalence in rare-earth nickelates

In the previous chapter, we have highlighted the role of covalence in tuning the properties of interfacial reconstructions in nickelate-titanate interfaces. We have shown that by changing the rare-earth in rare-earth nickelates, we were able to tune the level of covalence which controls the interfacial charge transfer and induced magnetism. However, changing the rare-earth in nickelate is not very functional and we would like to find a more versatile handle producing similar effects. In this chapter, we will try to demonstrate a new route to enhance covalence in rare-earth nickelates through illumination. But, first, let us start by reviewing illumination experiments in oxides in general, with a special emphasis on cuprates.

A - Illumination experiment in oxides

Most of illumination experiments are performed in a very simple fashion: light is shined onto a sample whose resistance is measured in Van-der-Pauw configuration (cf. experimental part and Figure A-1 a). Usually, photoconductivity can arise via two mechanisms:

- the creation of electron-hole pairs through inter-band (intrinsic) absorption. This typically occurs at photon energies close to the energy of the gap.
- the excitation of electrons (or holes) from donor (or acceptor) impurities into the conduction (valence) band. This generally happens at much smaller energies ~ 5 meV to 50 meV

Depending on the process involved and the band structure, the relaxation can vary from 600 fs in direct band semiconductors (such as nanocrystalline Si films [224]) to hours in the case of $\text{Al}_x\text{Ga}_{1-x}\text{As}$ [225]. However, in the following, we will be highlighting the effect of illumination in the special context of cuprates.

1 - In cuprates

Doping is essential for reaching superconductivity in cuprates [226]. Thus, photo-induced doping has rapidly been applied to the field of High- T_c superconductivity.

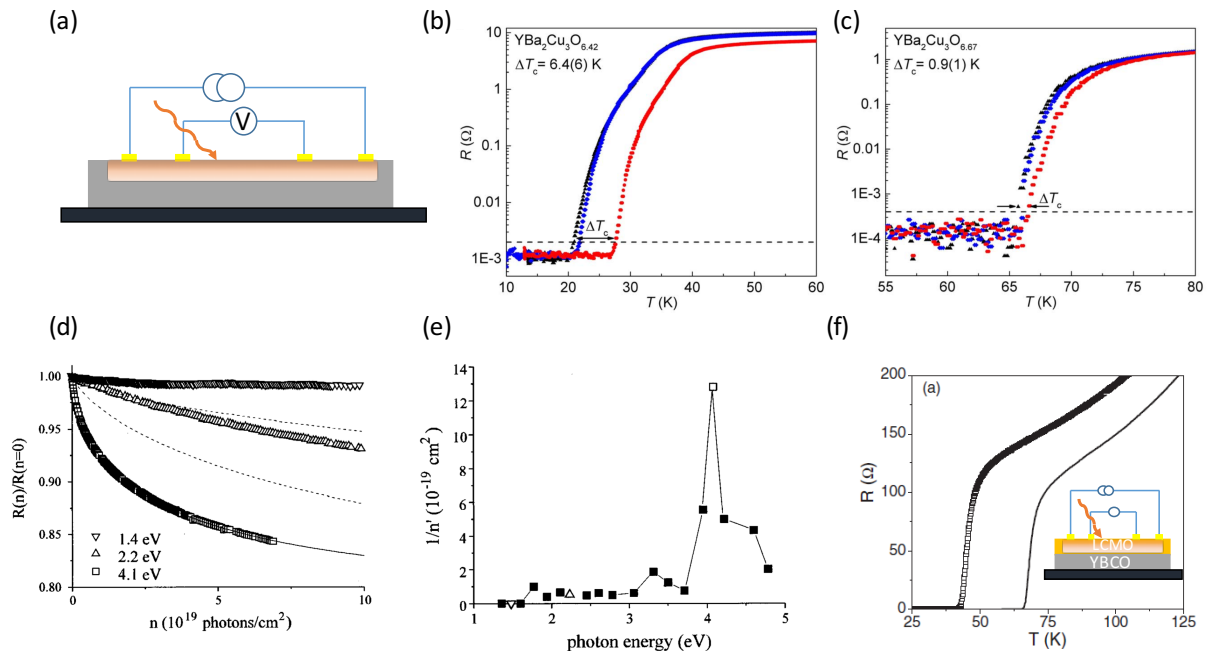


Figure A-1: (a) sketch of the measurement set-up. Temperature-resistance measurement for different oxygen content under illumination (in red) and without (in blue) in (b) $\text{YBa}_2\text{Cu}_3\text{O}_{6.42}$ and in (c) $\text{YBa}_2\text{Cu}_3\text{O}_{6.67}$. (b) and (c) are adapted from [227] (d) fluence dependence of the normalized resistance variation of $\text{GdBa}_2\text{Cu}_3\text{O}_{6.5}$ at different photon energies (e) inverse variation of the number of photons per unit area necessary for a 2% change in the resistance for different photon energies. (d-e) are adapted from [228] (f) temperature dependent resistance in $\text{LaCaMnO}_3/\text{YBa}_2\text{Cu}_3\text{O}_7$ adapted from [229]

It has been shown indeed that, in under-doped $\text{YBa}_2\text{Cu}_3\text{O}_{6-x}$ with reduced oxygen content ($x < 1$), the electrical conductivity can be significantly enhanced after continuous illumination with visible light, in thin films [230] as well as in single crystals [231]. We present in Figure A-1 (d) an example of such an enhancement in the conductivity of $\text{GdBa}_2\text{Cu}_3\text{O}_{6.5}$ [228].

The critical temperature at which the sample becomes superconductor can also be modified and shifted to higher temperatures under illumination. This shift can reach 15 K for $x > 0.4$. The magnitude of the shift strongly depends, however, on the oxygen content x (cf. Figure A-1 b and c), and the photon dose [232].

Interestingly, in [228], authors also studied the efficiency of the photoconductivity enhancement as a function of the photon energy. Two main peaks are visible in the signal: one at relatively low energy, 1.8 eV, and another one, much more efficient, at 4.1 eV (Figure A-1 e).

The changes in resistivity and T_c can persist until the temperature is raised above 270 K. Then the resistivity relaxes slowly on time scales of the order of hours to days depending of the temperature at which the sample is maintained [230]. The effect, recalling the physics of $\text{Al}_x\text{Ga}_{1-x}\text{As}$, is often referred to as photo-persistent conductivity (PPC).

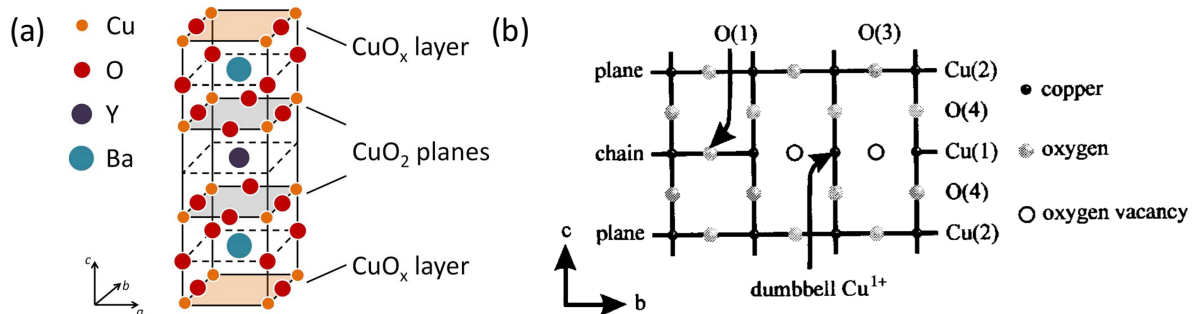


Figure A-2: (a) sketch of the unit cell structure of high- T_c YBCO superconductors adapted from [227] (b) Schematic structure of $\text{YBa}_2\text{Cu}_3\text{O}_{7-d}$ in the (b,c) plane. The label (1) denotes ions in the Cu-O chains, label (3,4) stands for apical oxygens between the chains and the planes, while (2) refers to atomic sites in the CuO_2 planes.

Before discussing more on the still-debated origin of PPC, let us first come back on the structure of YBCO. The anisotropic structure of YBCO systems is made of CuO_2 planes separated by CuO_x layers that rearrange in Cu-O chains along the b axis for larger doping levels, x (Figure A-2 a). For sufficient amounts of oxygen holes, electrons are transferred from the CuO_2 planes to CuO chains, leaving mobile holes in CuO_2 planes that contribute at low temperature to superconductivity (cf. Figure A-2 b). Based on this, two main scenarios have been proposed: (i) photo-induced charge

transfer and (ii) photo-assisted oxygen ordering. Both mechanisms would indeed result in enhanced conductivity and T_c , mimicking the physics taking place at larger doping levels:

- In (i), photo-induced charge-transfer results in the creation of electron-holes pairs. Electrons are trapped at oxygen vacancies, impeding recombination, while holes are transferred to CuO_2 planes.
- In (ii), oxygen ordering at CuO_x facilitates longer Cu-O chains.

Pure photo-doping can also be used in heterostructures as, in [229], where the authors combine manganites and YBCO. In this example, the authors have succeeded to obtain similar shift although YBCO was placed under a LCMO capping layer, suggesting that photo-doping can also change electro-static boundary conditions and allows band (and thus, charge-transfer) engineering in oxide heterostructures. Interestingly, PPC was also observed in other non-superconductive oxide systems.

2 - In other oxides

The main system in which PPC, or large illumination effects were also reported are doped manganites ($\text{A}_{1-x}\text{B}_x\text{MnO}_3$). Manganites are also well known to be very sensitive to doping [233].

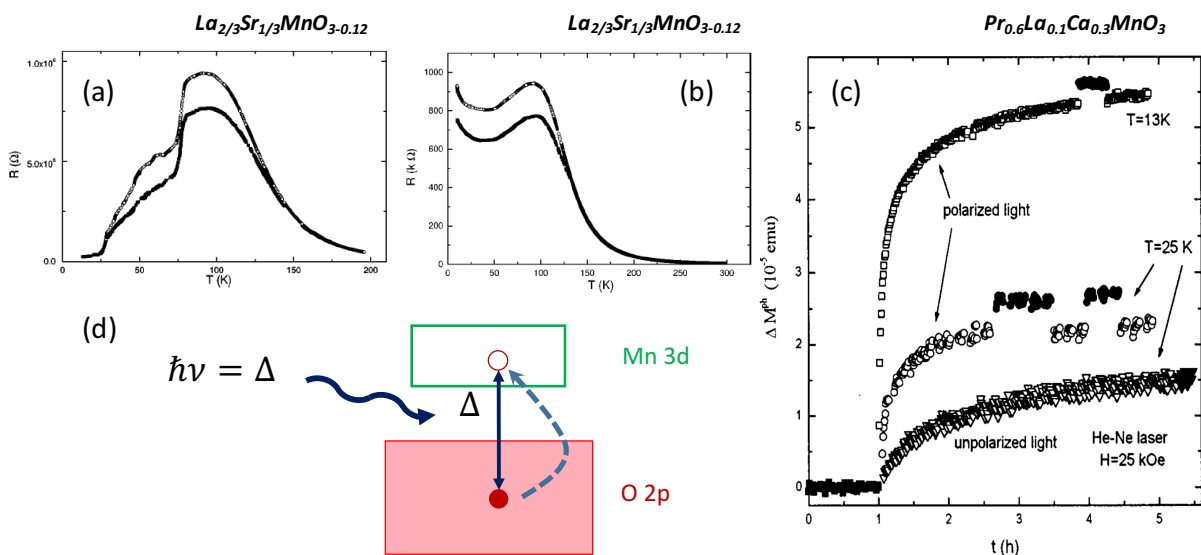


Figure A-3: Temperature dependence of the resistance under an applied magnetic field of 0.48 T solid squares and without open circles (a) under illumination and in darkness (b). a and b are extracted from [234] (c) Temporal dependence of the magnetization at 25 kOe under (open dots) and without (full dots) illumination. Light was turned-on after 1 h. The light is provided by an He-Ne laser and is linearly polarized (circles: 25 K, squares: 13 K) or non-polarized (triangles: 25 K) (d) Sketch of the on-site oxygen hole doping of the 3d level of Mn sites. [235]

In Figure A-3, we report the main magneto-transport properties in mixed-valence doped manganites. Figure A-3 (a) and (b) compares the giant magneto-resistance behavior under illumination (a) and in darkness (b). Authors in [234] claim that the physics in oxygen-deficient LSMO is very similar to what happens in cuprate PPC. One of the main arguments is that in both systems, PPC disappears when the temperature is sufficiently raised suggesting a rearrangement due to thermal activation of the ionic oxygen defects throughout the whole sample. The observed photo-induced changes in the magneto-resistance response are believed to be related to photo-induced disorder which would be sufficient to localize the electronic wave functions.

Figure A-3 (c) gives an example (from [235]) of the effect of photo-doping in other manganites, namely $\text{Pr}_{0.6}\text{La}_{0.1}\text{Ca}_{0.3}\text{MnO}_3$. Here, authors nicely take advantage of the interplay between spin and charge degrees of freedom. By inducing holes in the manganite, the authors are able to control its magnetization as they move in the phase diagram that naturally exhibits ferromagnetic regions associated with an increase of conductivity. In manganites, the highest efficiency is reported for photon-energies that correspond to the energy required for transferring an oxygen hole in the d-band of the Mn ions (cf. Figure A-3 d).

In the following chapter, we will show that similar effects can happen in rare-earth nickelates mimicking the physics of oxygen hole doping, and consecutively, covalent control.

B - Illumination properties in nickelates

1 - Photo-excited transport properties in SNO

As we have seen in chapters IV and V, a key parameter for controlling the level of covalence in nickelates is the presence of oxygen 2p holes in 3d bands. The study of illumination in RNO, was motivated by the idea that photo-excitation at a specific wavelength, corresponding to the p-d energy difference, would reproduce the physics of on-site oxygen doping happening below the metal-insulator transition. In the following, we focus our attention on SNO, in which we could clearly highlight oxygen hole-doping by means of polarized XAS (cf. chapter IV-B).

Before presenting our preliminary research using visible light, we would like to mention that several authors have proposed another route for tuning the metal-insulator transition in RNO [148,236,237]. Their proposal is based on the use of Terahertz-pulses that non-linearly couple to

specific phonon modes in the Brillouin zone. Terahertz-pulses can thus ignite the MIT by exciting specific modes involved in the disproportionation of Ni sites.

a) Experimental setup

For photo-conductivity measurements, I have designed a particular labview interfaced magneto-transport measurement system with He-gas cryogenic compressor that is presented below. The system has a large temperature range from 5 K to 350 K.

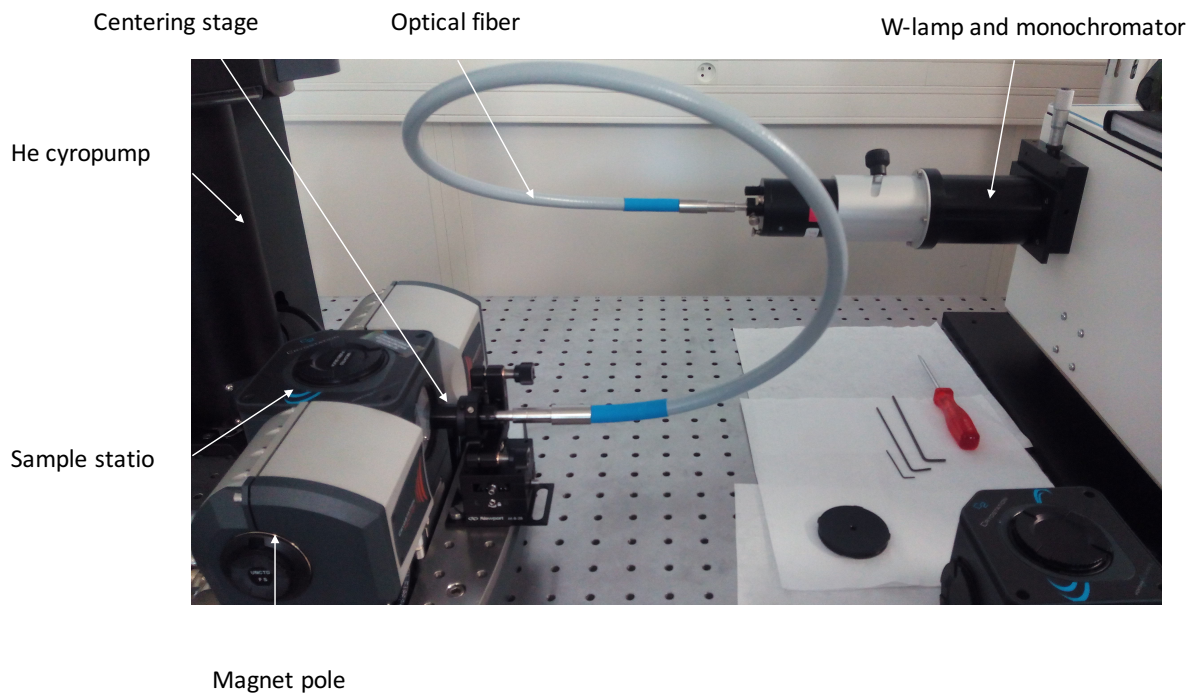


Figure B-1: experimental setup for photoconductive experiment at low temperature and low magnetic field.

As one can see from Figure B-1, the sample can be illuminated through a glass window, which stands 5 cm away from the sample. The glass windows are almost fully transparent in the wavelength range that we have used in our experiments. Depending on what we were measuring, we used three different light sources:

- A halogen white lamp Schott KL 1500 with a maximum power of 500 mW. The light is brought in contact via a flexible light guide, 1-branch PURAVIS \varnothing 5mm/1600mm. This setup was used to provide a large power when measuring $R(T)$ under illumination
- A LOT halogen-tungsten light coupled to a MSH 300 monochromator with a wavelength selectivity of ~ 1 nm. The wavelength can be varied from 200 nm to 1200

nm. The light is then transmitted to the glass windows by flexible quartz optical fibers. The power at the end of the optical line is around 4 mW power. This setup is designed to study the spectral dependence of photoconductivity.

- A OSRAM Golden dragon blue light emitting diode (LED) centered around 470 nm. The maximum output power was measured at 500 mW in contact mode. The light was focused thanks to a lens (ILS 15°, diameter of 6.3 mm) that confines the emitted light, yielding a fluence of 140 mW/cm² in contact mode. This setup was used to look for the power dependence of photoconductivity at a specific wavelength.

b) Transport measurements under illumination

1) Photo-conductivity

We first measured conventional (in darkness) transport properties of 23 nm-thick epitaxial SNO sample grown on LAO. The sample presents a good temperature-dependent resistance (Figure B-2 a-blue curve), with activated-behavior, confirming the sample quality and stoichiometry.

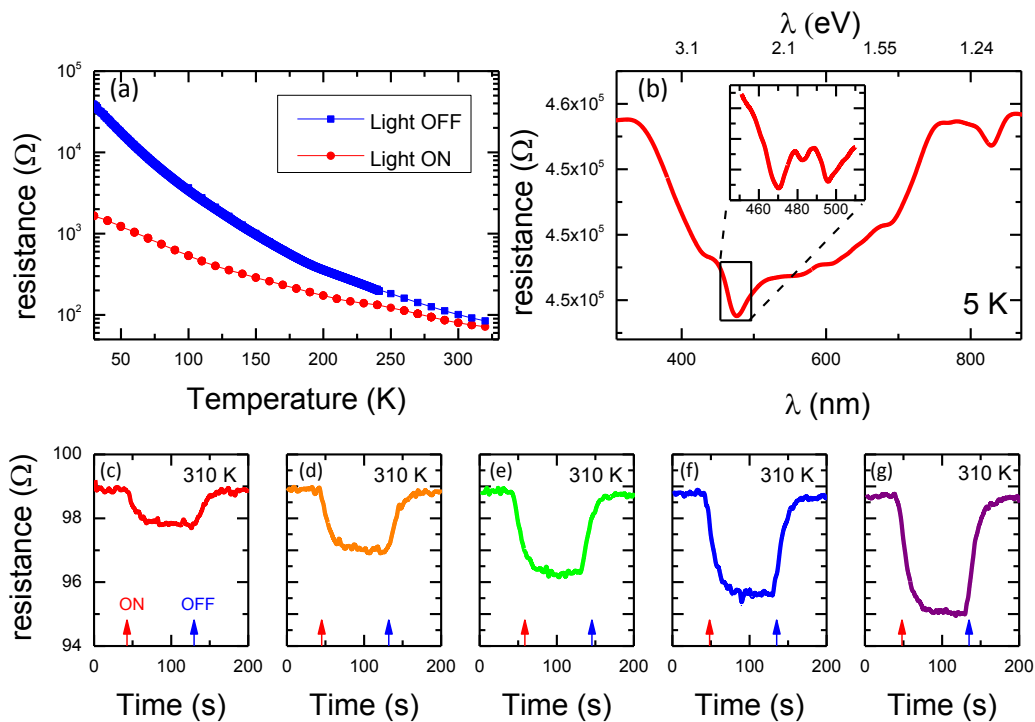


Figure B-2: (a) temperature dependence of the resistance of a 23 nm thick SmNiO_3 sample deposited on LaAlO_3 in darkness (blue) and under illumination at 0.5 W white light (red). (b) variation of the resistance as a function of the illumination wavelength at 4 mW. (Inset) Zoom between 450 and 550 nm. (c-g). Variation of resistance as a function of time after illumination at 470 nm from 20 s to 120 s (red arrow) and with no light after 120 s (blue arrow) for different currents passing through the diode centered at 470 nm (c) 0.2 A (d) 0.4 A (e) 0.6 A (f) 0.8 A (g) 1 A. The red and blue arrows indicate when the illumination was turned on and off.

We then illuminated the sample *in-situ* with the first illumination setup using a Schott KL 1500 white lamp. The illumination power is around 0.5 W. We observe a sudden drop of resistance (Figure B-2 a-red curve). Interestingly, the diminution of resistance is not linear with the temperature. The resistance is indeed divided by 32 at 20 K whereas it is only divided by 2 at 200 K. This behavior reminds what was observed by Xiang et al. in [238] when SmNiO_3 was hole-doped with Ca. In this latest case, the effect was assumed to be due only to pure hole doping (as the u.c. is not modified upon adding Ca ions. Based on their measurements, and the resistance variation that they measured, we can estimate that our effective “photo-doping” is slightly smaller than 1 %.

In order to quantify the heating power of the white lamp at 500 mW/cm^2 , we measured the effect of light on a Gold stripe attached to a nickelate sample. The behavior of the Gold stripe resistance at different temperatures is presented in Figure B-3. Whilst it can be observed that the resistance increases upon exposure to light, we note, however, that this increase depends on the temperature at which the experiment is performed as the cooling power of the Montana cryostation is larger at high temperatures. At 300 K, the heating is found to be $\sim 18 \text{ K}$ whereas it is $\sim 44 \text{ K}$ at 100 K. In contrast, in SNO, the heating should be of at least $\sim 110 \text{ K}$ to reproduce the photoconductive effect observed in Figure B-2. This suggests that not all the observed changes are due to heating and that a pure photoconductive effect is likely happening in SNO upon exposure to white light.

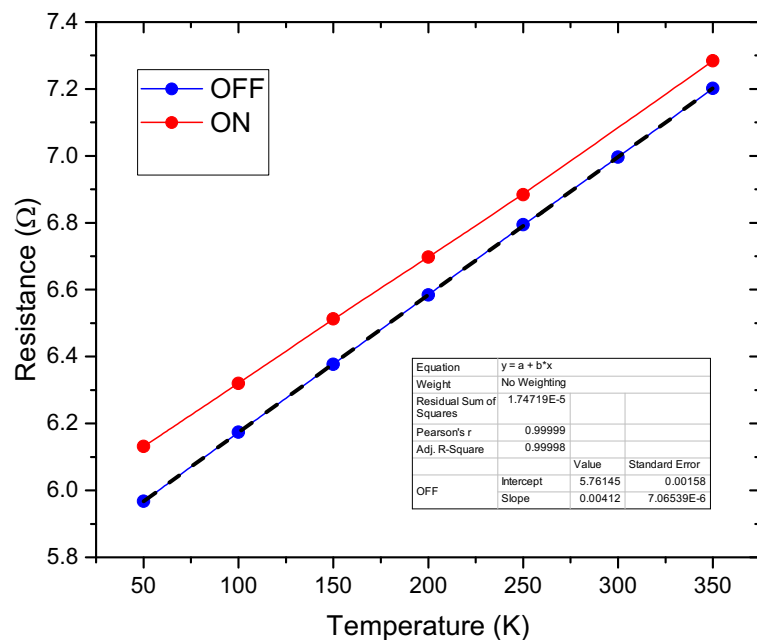


Figure B-3: $R(T)$ of a gold stripe in the montana cryostation under exposure (red) to white light at 500 mW/cm^2 and in darkness (blue). The dashed black line is a linear fit for the extraction of the Gold stripe parameter allowing for a measure of the temperature shift under exposure

2) Spectral dependence

We then turned to the spectral dependence of the photo-resistivity. For that, we probed the resistance at 5 K as a function of the wavelength of the photo-excitation using the second illumination setup for a 23 nm step size at 4 mW illumination power.

We observe that the resistance is strongly affected by the wavelength (Figure B-2 b). Indeed, the resistance suddenly drops at 370 nm (3.35 eV) with a global minimum around 480 nm (2.58 eV) before it returns to a value close to the initial one around 750 nm (1.65 eV). The resistance presents a second drop around 810 nm (1.53 eV) before coming back to the initial value for larger wavelength.

Zooming into the minimum at 480 nm (2.58 eV) by performing scans with smaller step size of the order of 1 nm, we observe that the gap is actually made of 3 local minima at respectively 477 nm (2.6 eV), 481 nm (2.58 eV) and 490 nm (2.53 eV) - cf. inset Figure B-2 (b). Interestingly, the two main gaps (resp. at 1.3 eV and 2.6 eV) have been clearly identified in nickelates by means of near UV-visible and infrared spectroscopy (whose results [148,239] are reproduced below).

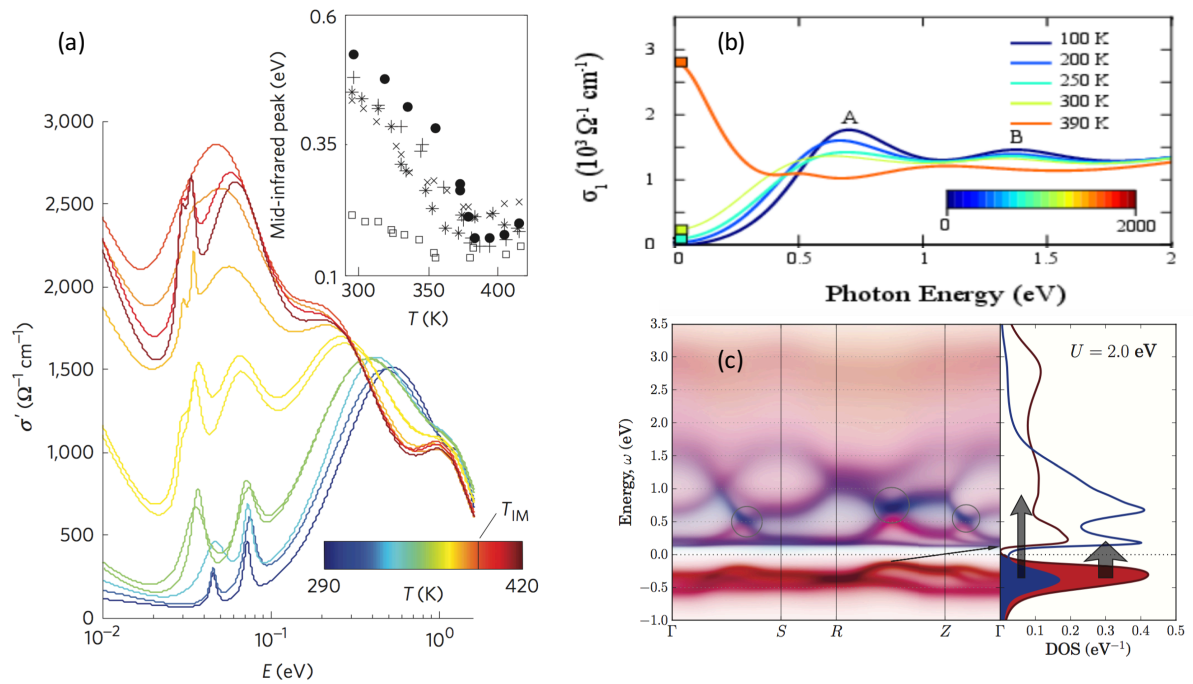


Figure B-4: (a) real part of the optical conductivity for SNO on top of LAO substrates at different temperatures (inset) mid-infrared peak as a function of the temperature adapted from [239] (b) Spectral dependence of the real part of the optical conductivity (c) color-coded momentum resolved spectral functions. (b) and (c) are Adapted from [148]

Authors in [148] associated respectively the two peaks at low energy (< 1.3 eV) to d-d excitation between Ni sites (cf. Figure B-4 b-c). The peak at 2.6 eV corresponds exactly to p-d excitations between Ni d-states and O p-states [240].

Remarkably, due to Laporte's orbital selection rules [241], there should be no optical absorption between pure d levels. The presence of a gap at this specific energy (810 nm / 1.3 eV) in the photo-resistivity response is a further proof of the intrinsic covalent nature of d-levels in nickelates. Based on the description that we developed in the previous chapter in which Ni 3d states were viewed as $Ni^{3+} = \alpha|3d^7\rangle + \beta|3d^8L\rangle$, where $\alpha^2 + \beta^2 = 1$, we can rationalize the absorption as occurring only between $|3d^7\rangle$ and $|3d^8L\rangle$ states. This explains also why this gap in the photo-response is thus less deep than the one occurring between p and d states at 480 nm / 2.58eV.

The decomposition of the 480 nm / 2.58 eV-gap in 3 local minima (cf. inset Figure B-2 b) is more mysterious. We may however ascribe these gaps to absorption from p levels to different d levels. Previous spectroscopic investigations of SNO samples grown on top of LAO [239] also reported the presence of 3 peaks that are separated by 20 meV and 60-90 meV respectively, in close agreement to what we observed. In [148], Subedi et al. proposed that the 2 higher energy peaks were related to absorption in the e_g subsets of disproportionated Ni sites (cf. Figure B-4). Indeed, the breathing mode leads to a Peierls-like gap opening of approximately 50 meV, hence resulting in the splitting of the e_g states. This has also been invoked by [239] to account for the three features of the spectra in Figure B-4 (a).

3) Power dependence

We then fixed the wavelength around 470 nm (2.64 eV) by using a OSRAM-dragon blue centered light-emitting diode (LED) and looked at the power dependence of the photo-induced effect (Figure B-2 c-g) at room temperature. We first performed some characterizations of the LED in different configurations (cf. Figure B-5).

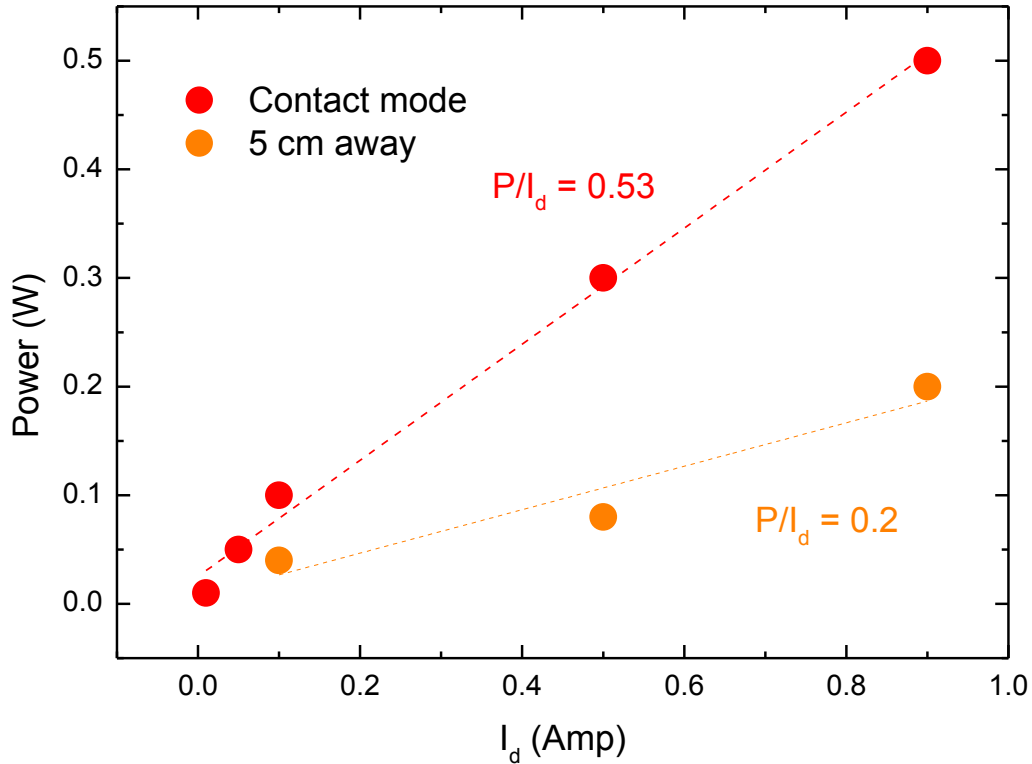


Figure B-5: Power measured in contact mode (red) and 5 cm-away (orange) as a function of the AC input current in the OSRAM Golden dragon blue LED

The output power delivered by the diode is almost linear in current. In contact mode, the power is equal to half the current passing through the diode, $P_{\text{output}}(\text{W}) = 0.53 I_{\text{input}}(\text{Amp})$. The power decreases rapidly with the distance as the focus lens does not allow to fully collimate the emitted light. The output power received 5 cm-away from the source is half the one in contact, $P_{\text{output}}(\text{W}) = 0.2 I_{\text{input}}(\text{Amp})$.

For simplicity, in the following we will discuss the results in function of the input current passing through the LED. In Figure B-2 (c-g), we report time-dependent resistance changes at different powers. For this experiment, the LED is placed in contact with the glass window (at 5 cm-away from the sample). For a current of 0.2 A (0.04 W), we observe a rapid decrease of the resistance measured at room temperature (starting from the red arrow). When the photo-excitation is turned off (blue arrow) the resistance increased also rapidly until it reaches the initial value.

Ramping up the current intensity from 0.2 A to 1 A (0.2 W), we uncover a linear dependence of the resistance (Figure B-2 c-g). The resistance decreases by a little less than 4% at RT for a fluence of 0.8 mW/cm^2 (cf. Figure B-6).

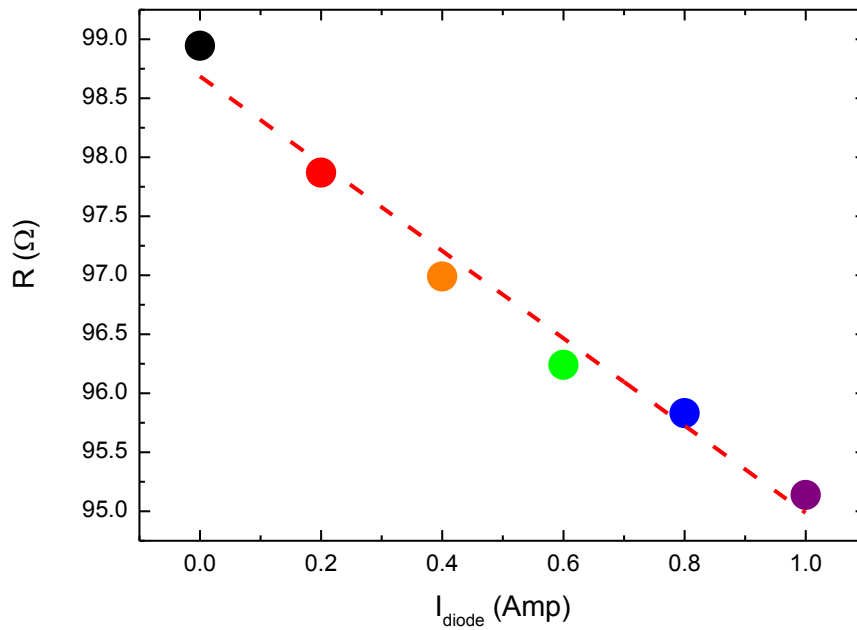


Figure B-6: linear relationship between the resistance variation and the diode intensity at 300 K around 470 nm.

We believe that the decrease of resistance under illumination is a very promising indicator that the level of covalence is increased.

Even if we cannot yet completely rule out heating, we also observed the same features with the white light from the lab room ceiling at 5 K, which delivers a very weak power unable to heat up the sample (cf. Figure B-7).

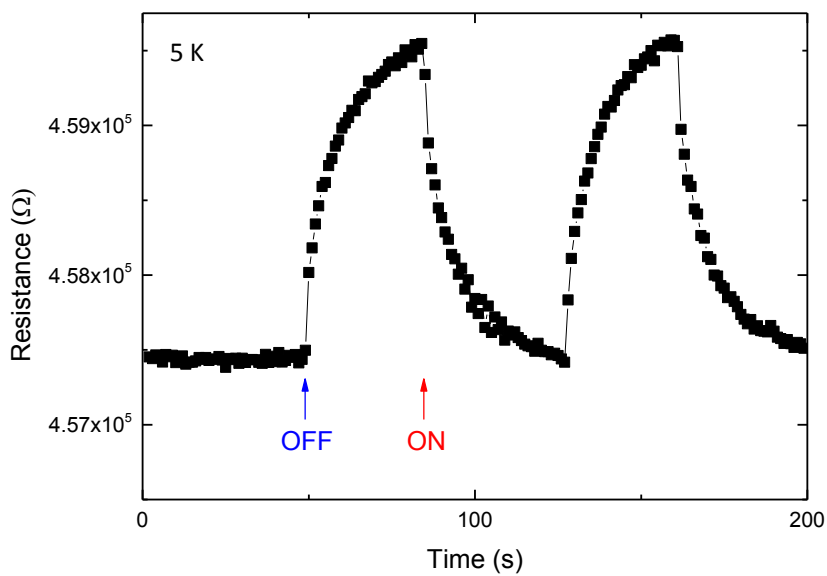


Figure B-7: temporal dependence of the resistance at 5 K when the room ceiling white light is turned on and off.

4) Relaxation times

In Figure B-2 c-g and Figure B-7, we observed that the timescales for reaching equilibrium do not seem to depend neither on the illumination power nor on the temperature. The timescales to reach equilibrium either from an on or off state look also equivalent.

We carefully measured the temporal dependence of the resistance at 5 K for p-d excitation (470 nm/2.64 eV) and d-d excitation (810 nm/1.53 eV). We observe in Figure B-8 that the drop in resistance can be fitted by a double exponential decay: one short decay of the order of ~ 2.5 seconds, and another taking place on a much longer time scale of ~ 13 seconds (cf. fits in Figure B-8). Interestingly, the timescales are the same at both wavelengths and do not vary with temperature. We also note that the fact that timescales do not depend on the illumination power suggests that the effect is not related to heating phenomena but rather to different photo-activated behaviors.

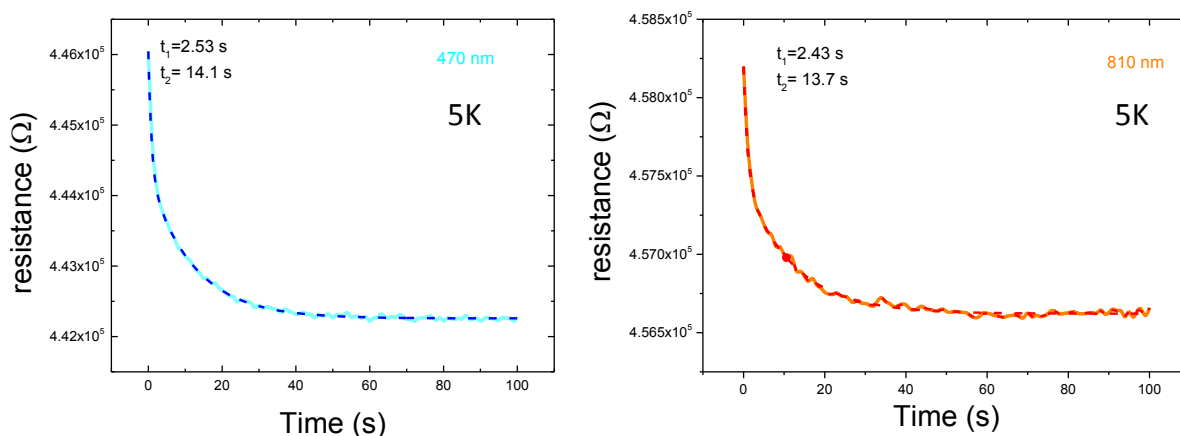


Figure B-8: temporal dependence of the resistance at 470 nm (left) and at 810 nm (right) at 5 K for 4 mW illumination power. Double decay exponential fits are presented in dashed line.

In order to separate the effect of heating from those of pure photo-doping, we plan on performing synchronous detection with the photoexcitation being locked onto the detection frequency. This would allow to perform the detection at tens or even hundreds of Hz, much faster than the timescales on which heating processes usually take place.

In conclusion we have been able to tune the level of covalence in SNO by mimicking the covalent oxygen hole doping process through specific photo-excitation. This has resulted in a rapid decrease of the resistance under illumination (as observed when going from SNO to NNO to LNO). Let us now see whether the other covalent-related properties of SNO are modified.

2 - Photo-excited structural properties in SNO

As we discussed extensively in chapter IV, covalence and MIT are tightly linked to structural changes in the RNO family. Indeed, the MIT is characterized by an increase of covalence and disproportionation of Ni sites. This disproportionation is itself consecutive of a breathing mode, resulting in alternating large and small octahedra surrounding the Ni ions. This breathing mode breaks a mirror symmetry and lowers the symmetry from orthorhombic to monoclinic. This change in symmetry is accompanied by a unit-cell expansion of roughly -0.2 %, cf. [99].

a) X-ray reflectivity under illumination

To detect possible photo-induced structural changes, we performed illumination inside the X-ray diffraction setup. To maximize the possible structural contrast (that should linearly scale with the number of unit cells), we used 100 nm-thick samples grown on SrLaGaO₄. Note that due to the very large thickness, we may expect the sample to be relaxed.

Figure B-9 displays X-ray reflectivity for illuminated (red curve) and in darkness (blue curve) samples. For this specific experiment at very grazing incidence we used the halogen white lamp at full power (0.2 W), emitting approximately 10 cm away from the sample. A clear discrepancy is observed at very low angle (< 0.75 degrees). Indeed, the critical angle is shifted to larger value when the light is on (cf inset in Figure B-9).

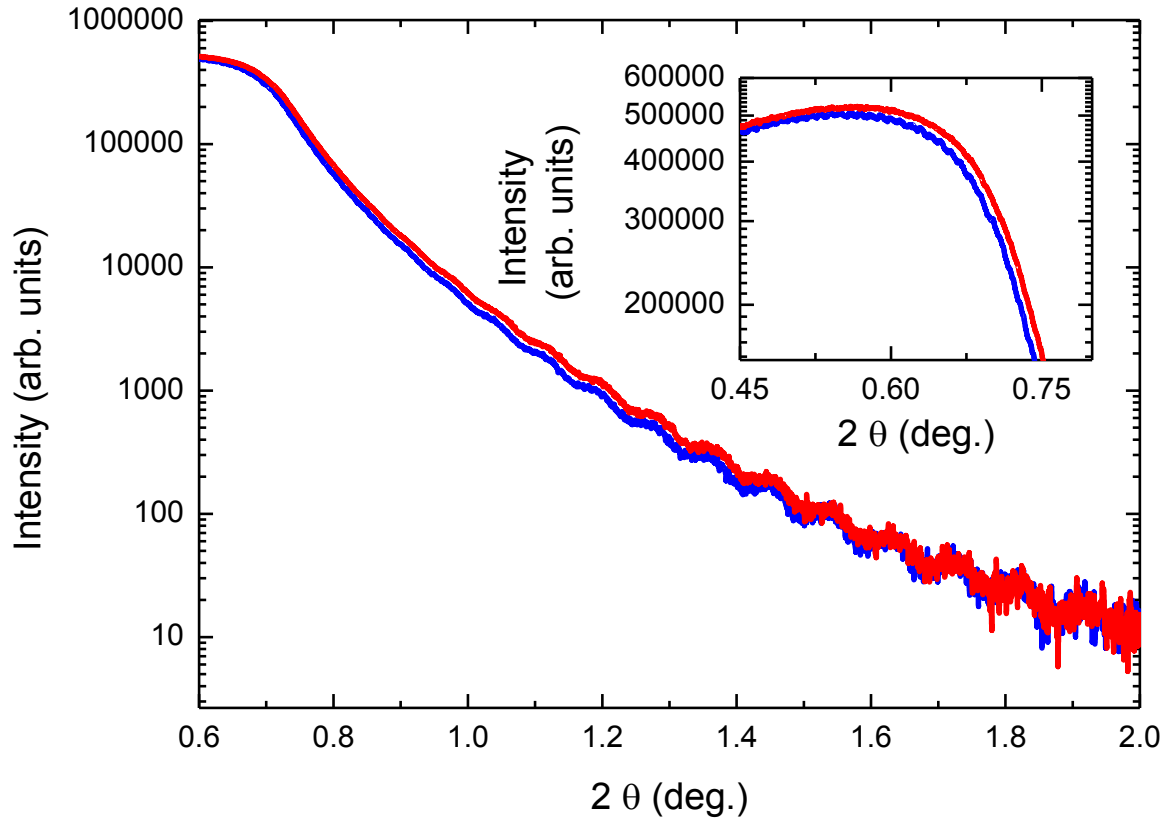


Figure B-9: X-ray reflectivity with 0.2 W power light ON (red) and light OFF (blue) (inset) Zoom on the X-ray intensity plateau near the critical angle.

Taking into account the relationship between the critical angle (θ_c) and the electronic density, δ , $\theta_c = \sqrt{2\delta}$, we find that δ varies by 2.41 % when the light is on. Considering that changes in resistance reflects only changes in the electronic density, this variation of the electronic density extracted from the X-ray optical index is in complete agreement with Figure B-6 (which states a 2.5 % resistance variation for a similar output power of 0.5 W/cm²).

What is more surprising is that the intensity decay of the XRR curve seems to change under illumination. We believe that this is due to the fact that photo-induced effects are rather superficial. This would thus explain that the XRR signal is different at low angle (0.6 - 1.2 deg.) – when the X-rays barely penetrate into the samples – before recovering the same modulation at larger angles (> 1.4 deg.) – when the X-rays penetrate deeper into the samples. Note that at low angles, the first two oscillations seem to have larger periods when the light is turned on (suggesting a compression of the film). However, considering the noise level, and the small number of oscillations available, a careful characterization of this variation remains out of reach.

b) Reciprocal space maps under illumination

We performed On/Off characterizations of the symmetric [002]-reflexion, but observed that the peak position changed only negligibly.

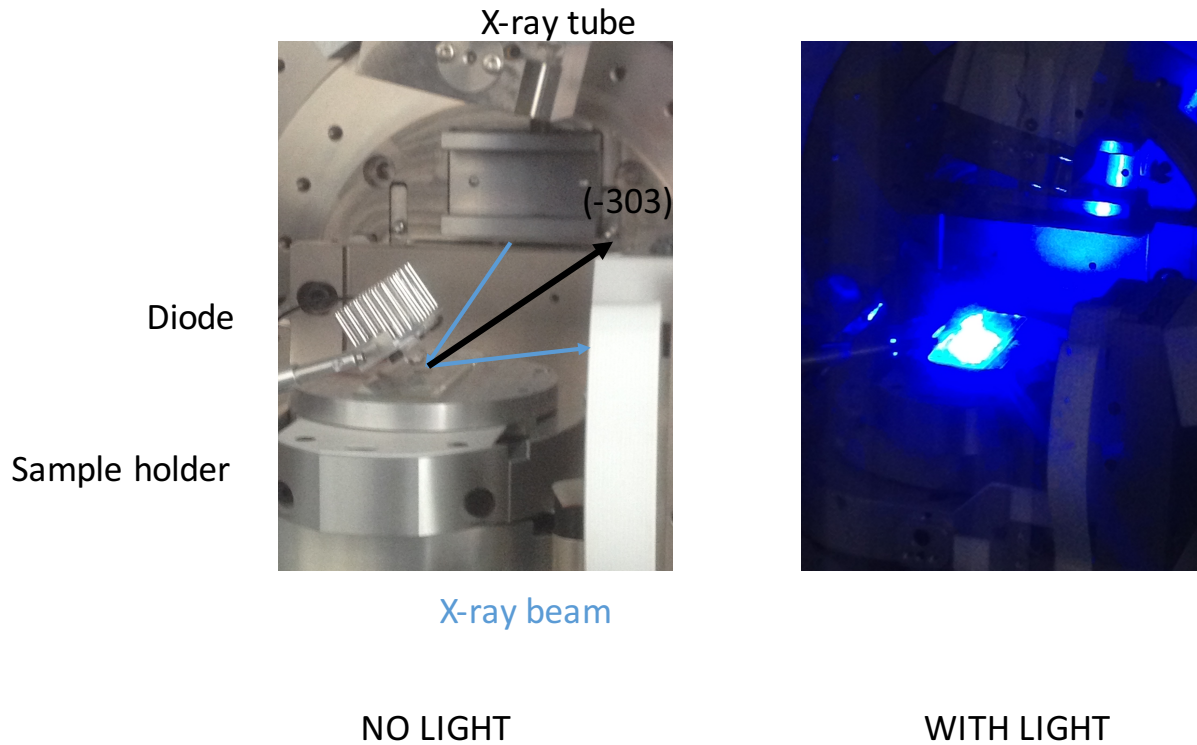


Figure B-10: Reciprocal space map configuration for maximal illumination of SNO 50 nm-thick sample on SLGO substrate.

We then turned to the characterizations of asymmetric reflexions. We used SLGO [-307]-reflection to quantify the effect of heating. Under 0.5 W illumination, the SLGO peak was displaced, due to thermal dilation. This heating is associated with an elevation of the substrate temperature by approximately 20 K.W^{-1} , in very close agreement to the heating obtained from the white lamp observed from Figure B-2. Based on that, we could thus correct the SNO [-303]_{pc}-peak displacement due to heating. Figure B-11 presents cuts of the SNO [-303]_{pc} peak, after correction, extracted from 2θ - θ at different ω -values (cf. chapter II). The peak intensity, coded by the diameter of the circles in Figure B-11, appears to be shifted down in both in-plane and out-of-plane direction.

The peak is displaced by -0.028 % along the out-of-plane direction and by -0.008 % along the in-plane direction. The in-plane displacement can be explained by substrate dilation which slightly expands, inducing a similar displacement on the fully-strained sample. However, the out-plane variation is much larger than the thermally-induced tensile strain (which is one order of magnitude smaller). The total peak displacement in the RSM corresponds to a variation of $\frac{\Delta L}{L} = -0.03 \%$. This contraction is the largest ever observed in photo-strictive materials for this incident power and can

be considered a record for oxide materials. Previous record in oxides was obtained for piezo-electric materials which displayed a dilatation 100 times smaller for 4 times more illumination power [242].

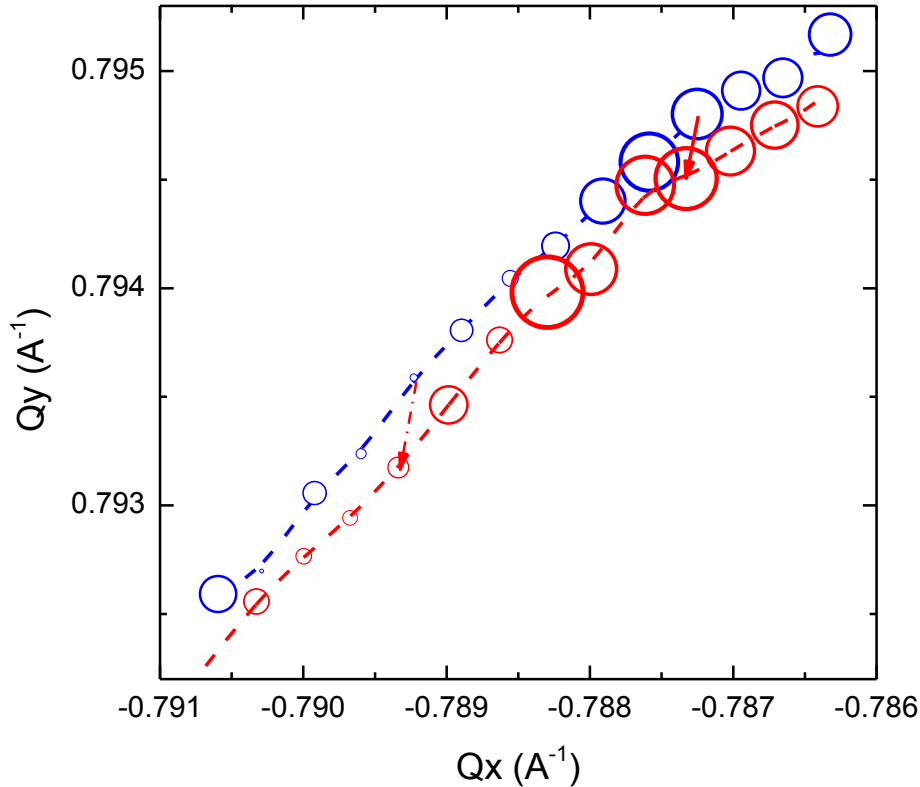


Figure B-11: Reciprocal line scans of $[-303]_{pc}$ SmNiO_3 peak of a 50 nm-thick sample deposited onto SLGO under 470 nm illumination with a 1 Amp focused blue LED (red) and without illumination (blue) at room temperature. The diameter of the circles codes for the intensity of the peak.

As a conclusion, we observed a decrease of the $[-303]_{pc}$ vertical component of the peak position while the $[002]_{pc}$ reflection was negligibly affected by light exposure. As the experimental temperature is well below the metal insulator transition, the system is monoclinic. A modification of the vertical component at the $[-303]_{pc}$ order (along with the absence of variation at the $[002]_{pc}$ order) can thus be explained through a reduction of the monoclinic angle by 0.012 degrees. This is a surprisingly large reduction that would correspond to the replacement of 50 % of Sm ions by larger Nd ions at low temperature.

These results, both from transport and structural point of view, are very encouraging in using illumination at the p-d energy as an effective handle to mimic the effect of the rare-earth replacement in controlling the MIT and level of covalence in RNO system. Indeed, through illumination at 480 nm/2.58 eV at a constant temperature, we have been able to force the system

closer to the metallic region (as if we had replaced Sm by Nd or La). This was concomitantly accompanied by a reduction of the monoclinic angle by 0.012 degrees similar to what is observed when going from the low temperature monoclinic phase to the high-temperature orthorhombic one. The agreement between resistance variation and structural change strongly suggests that this strategy is efficient for modifying the level of covalence in rare-earth nickelates.

By providing an external knob to control the amount of oxygen hole doping at the d-levels, illumination could open new routes for the external fine tuning of correlated systems involving charge transfer insulators in next-generation (spin)-electronic systems.

VII. Conclusions, and perspectives

In this last chapter, we will come back on the different studies conducted during this Ph.D. Then we will discuss eventual follow-ups for this work from fundamental perspectives. Finally, we will try to convey the idea that this work may bring new functionalities to correlated oxide interfaces from a more applied point of view.

A - Conclusions and summary

After briefly reviewing, in the first chapter, the basics of oxide physics and correlated matter, we presented, in chapter II, the different characterization tools used during this Ph.D. In chapter III, we studied GTO single crystals. We were able to measure the spin and orbital moments by using XAS and XMCD measurements combined with STEM-EELS characterizations. It led us to the conclusions that Ti ions present a orbital moment. However, the measured crystal field and magnetic anisotropy were rather supporting a quenched orbital moment. We finally reconcile these elements by considering an orbitally unquenched combination of the three 3d-orbitals.

We then turned to the study of GTO thin-films that we optimized by means of pulsed laser deposition. Our films displayed bulk-like properties but presented a monoclinic symmetry (whereas the bulk is orthorhombic) when strained on SLGO substrates. Next, we discussed how the orientation of the samples was influenced by the substrate in-plane lattice constant. The in-plane lattice mismatch induces a rotation of the unit-cell from ab -Pbnm ($a_{ip} < a_{STO}$) to c -Pbnm ($a_{ip} > a_{STO}$). The induced monoclinicity of the samples grown with $a_{ip} < a_{STO}$ produces an in-plane anisotropy which is believed to lead to the appearance of a thickness-dependent strain gradient throughout the film. STEM was useful to discuss how this strain gradient was apparently accommodated by stacking faults that emerge after 7 u.c. Remarkably, the samples grown with the c -Pbnm orientation were found to present a different morphology, probably due to their more symmetric in-plane growth.

In chapter IV, we studied nickelates thin-films. Based on DFT calculations, we discussed and reconciled the so-far debated ground state of rare-earth nickelates. We could show that nickel sites are disproportionated at low temperatures in an alternating rock-salt pattern. This disproportionation is accompanied by a breathing mode that alternatively contracts and distorts

oxygen cages. Surprisingly, the expected $3d^6/3d^8$ disproportionation is apparently suppressed by oxygen holes filling of the e_g holes of the $3d^6$ nickel sites, resulting in a final ground state made of alternating $3d^8L^2/3d^8$.

After, we measured the electronic and magnetic properties of SNO by means of XAS and XLD combined with resonant X-ray scattering at the Ni L-edge. We could bring spectroscopic evidences backing-up the above theoretical scenario. We showed that polarized XAS could probe the onset of antiferromagnetic order, while the $t_{2g}-e_g$ peak splitting was associated with oxygen hole filling of the Ni 3d levels. The e_g-t_{2g} peak intensity ratio also provided a good measure of the “effective” valence that changed upon cooling the sample from $3d^7$ to $3d^8$. Its polarization-dependent behavior offered one of the first evidence of the magnetic singlet state formed by oxygen holes populating Ni 3d levels. Not only did this study show that all those parameters were intrinsically coupled but it revealed valuable for characterizing the electronic and magnetic state of the nickelates when interfaced with titanates.

In chapter V, we combined nickelates and titanates into heterostructures. Despite some intrinsic difficulties in growing titanates on top of nickelates, we were able to perform the opposite stacking. The bilayers presented a good morphology and a good epitaxial quality. We did not detect extended structural defects over distances larger than hundreds of nanometers.

First, we used XAS to characterize LNO/GTO bilayers. We observe a large charge transfer from the interfacial titanate layer to the nickelate layer. This was not unexpected knowing the large electron-affinity difference (of approximately 1.2 eV). However, the surprise came when we repeated the experiment after replacing La by other rare-earths - Nd and Sm - in the RNO layer. The charge transfer was found to be enhanced by more than 20%.

Second, we used XMCD to characterize the eventual magnetic reconstruction at the interface between GTO and RNO. We found that magnetism in GTO was maintained, as expected from the ferromagnetic nature of GTO. However, we detected a strong Ni dichroic signal in all bilayers. The field dependence of the dichroic signal led to the unambiguous conclusion that some ferromagnetic-like coupling between Ni sites was present. Additionally, a deeper analysis of the field dependence points to the presence of two different Ni magnetic sub-systems: one presents barely no magnetic field dependence and seems completely frozen even up to several Teslas. The other, in contrast, presents an asymmetric hysteretic cycle, reminiscent of exchange bias. We believe that this asymmetry in the hysteresis may be linked to the presence of these Ni frozen spins. The correlation between the variation of the absorption spectra and the one of the dichroic signals from bilayers made of La, Nd and Sm suggests that the frozen spins are mainly divalent in nature. However, further work needs to be done to confirm this scenario.

Finally, we have been able to ascribe the fine tuning of the charge transfer and induced magnetism to the evolution of the covalence throughout the nickelate series. Indeed, when changing the rare-earth, the level of covalence in the hybridized p-d bands is strongly reduced upon closing the Ni-O-Ni angle, which controls the p-d orbital overlap. In our scenario, the level of covalence is competing with the energy gain associated with the reduction of the electron affinity difference. This scenario has been further confirmed and reinforced by density functional theory. At that point, we have been able to exhibit the role of a new handle in tuning the interfacial properties of correlated interfaces: the level of covalence in (negative) charge transfer insulators.

In the last chapter of this manuscript, we discussed some preliminary results on photo-induced changes in the covalent level of rare-earth nickelates. We have been able to show that both the resistivity and the structure were modified when the samples were illuminating at a specific wavelength corresponding to the p-d energy difference (~ 2.7 eV) in nickelates. At this wavelength, the density of states at the Fermi level, that we associated with oxygen holes in the 3d band, increased by more than 3 % for 0.8 mW/cm^2 , suggesting that we successfully photo-induced oxygen holes in the 3d band. This was also confirmed from XRD based measurements of the electronic density. We also reported that under the same illumination condition, we could measure a a reduction of the monoclinic angle by 0.012 degrees.

All these results comfort us in believing that we have found an efficient way to externally tune the level of covalence in rare-earth nickelates.

B - Perspectives

In the next section, we will discuss studies and potential directions of interest following up on this work.

1 - Future research

a) Other titanates and nickelates

First, due to lack of time, we were only able to focus on some specific nickelates (Nd, Sm, and La) and almost exclusively on GTO. Developing new materials in these families would allow us to probe the effect of the rare-earth on rare-earth titanates in titanate-nickelate heterostructures.

Our group is currently trying to develop new titanates such as DyTiO_3 and TmTiO_3 which present larger coercive fields and magnetization saturations that would greatly facilitate magnetic measurements. The behavior of magnetic properties of RTO thin films indeed remains an open question.

As for nickelates, the synthesis of other rare-earth nickelates such as GdNiO_3 , DyNiO_3 would be also interesting in terms of application as their MIT is well beyond room temperature.

Not only do we want to study more RTO and RNO samples but we would also like to be able to increase the thickness of the samples (up to hundreds of nanometers) which still requires some growth optimization.

b) Strain engineering physical properties in titanates

We are also very much interested in measuring the effect of strain on physical properties of rare-earth titanates. Even if we have been able to measure the effect of strain onto the growth orientation and the surface morphology, measuring physical properties across the different substrates remains challenging. Indeed, all rare-earth containing substrates pollute the magnetic analysis. We are currently investigating other routes to measure magnetic properties such as XMCD at the Ti (which would probably require thicker samples), or Kerr magnetometry.

The effect of strain in different rare-earth titanates (for different thicknesses) would also teach us a lot about the role of the different structural modes involved in tuning the magnetic properties of rare-earth titanates.

c) Growing superlattices

During this work, we were not able to reverse the order of the layers in the bilayer (RTO on top of RNO), which prevented the possibility to grow superlattice. Growing superlattice would allow to probe the effect of coupled interfaces, and probably bring up new physics such as non collinear spin order [192]. Superlattices also enable the use of other experimental techniques to probe interfacial properties such as angle dependent XPS [202], or magnetic or/and orbital sensitive X-ray reflectivity [186]. This would be of a great help in understanding the complex magnetic coupling happening at our interfaces.

Building superlattices of different R'TO or RNO made out different rare-earths may also break mirror symmetries and force the system to adopt a monoclinic phases resulting in the appearance of an in-plane polarization [243]. This polarization can then couple to other structural parameters such as Jahn-Teller, antiferrodistortive motions, etc. [244,245] This paves the way for new magneto-electric control of orbital polarization (and magnetism) for instance, that could be of interest in the context of titanates.

More generally, we could envision new routes using either octahedral control or non-centrosymmetric structures.

d) Octahedral control

Very recently, it has been shown that at the interface between two different oxides, octahedra rotations can propagate on distances of the order of a few unit cells [246–248]. This very local interfacial coupling can yet strongly affect the physical properties of the entire films [247]. As octahedra seem to be the key parameter controlling the physics of RNO (and probably of GTO), using well-engineered buffer layers as in [249] may allow to control interfacial properties between nickelates and titanates

e) Looking for topological properties

Finally, combining titanates and nickelates which present rich correlated physics may lead to the discovery of new topological phases at their interface. First, in confined RNO layers, theory works have predicted superconductivity [103,188]. Second, topologically non-trivial states have also been

predicted in triangular lattices of strongly *d*-correlated electrons [250–252]. These exotic phases in [111]-oriented heterostructures are very exciting and largely unexplored.

Very recently, [111]-oriented NNO was proved to be polar [253]. This also opens a lot of possibilities for spin-orbit induced coupling through Dresselhaus-like interactions [254]. At the interface with magnetic systems such as titanates or in non-collinear spin structures observed at the oxide interfaces, this coupling may produce very exotic magnetic phases.

2 - New “covalentronic” architectures

Apart from fundamental perspectives, we believe this work also offers interesting outlooks for applications. Indeed, a natural evolution of this work would be to take advantage of this new covalent knob into next-generation electronic devices. Researchers have already proposed to take advantage of the filling dependent MIT in Mott insulators into so-called “Mottronic” devices [255,256]. To our knowledge, the charge-transfer sector of the ZSA diagram has remained overlooked in terms of potential applications.

As we have shown in the previous chapter, we can tune the charge transfer across the titanate-nickelate interfaces by acting on the level of covalence of rare-earth nickelates. Field-effect in nickelates have dramatic influence on the properties of MIT in RNOs as shown by Scherwitzl et al. [129]. It would be interesting to analyze this result in light of a modification of the covalent proportion of Ni-O bonds. Indeed, modification of the strength of the ground state would accordingly diminish the MIT. This kind of field effect, if really affecting the level of covalence in RNO, could be advantageously used in a planar geometry for tuning the charge transfer across nickelate-titanate interfaces (cf. Figure B-1 a).

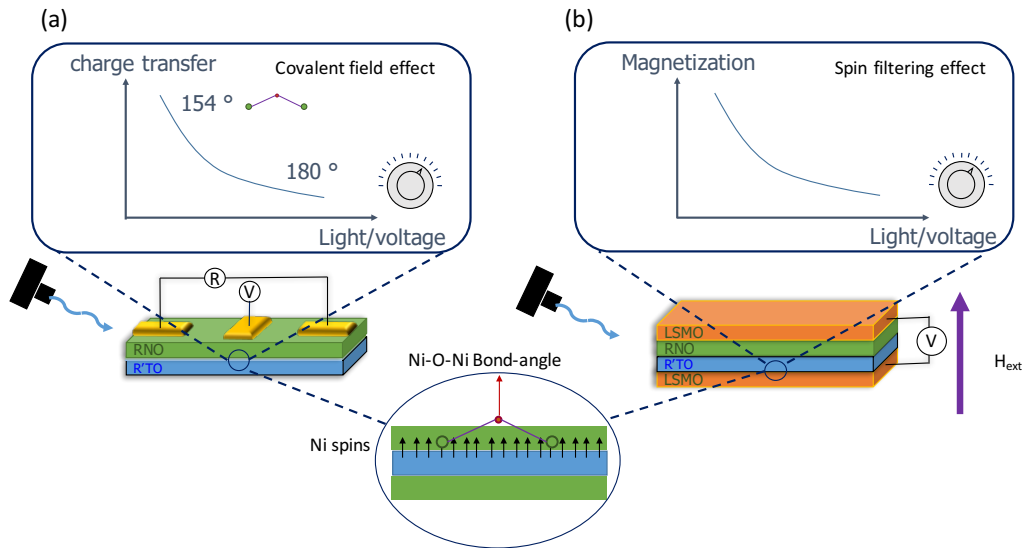


Figure B-1: (a) lateral 3-terminal devices (b) vertical tunnel junctions where the bond angle and the interfacial Ni spins are controlled either by an external voltage or by illumination.

Interestingly, covalence tuning also affects magnetic properties as ferromagnetic Ni spins appear at the interface. The potentiality of tuning the magnetic properties of an interface paves the way towards new spin-filtering architectures. Indeed, we have demonstrated in other correlated interfaces comprising charge-transfer insulators ($\text{LaFeO}_3/\text{La}_{0.7}\text{Sr}_{0.3}\text{MnO}_3$) that the control and fine tuning of interfacial spins can have dramatic influence on the properties of tunnel magnetoresistance. [257]

In RTO/RNO interfaces, we could benefit from the multiple spin components present in the system: the frozen spin that would still spin-polarize the tunneling electrons, but would be insensitive to the external magnetic fields, or the exchange biased ferromagnetic-like Ni that would also depend on the level of charge transferred and probably, the density of interfacial frozen spins (cf. Figure B-1 b).

Similarly, field effect could be replaced by illumination. Indeed, we have shown in the last chapter that illumination was a very efficient way for tuning the level of covalence. The same kind of devices (cf. Figure B-1 a and b) that take advantage of covalent tuning could thus also be controlled via light-induced oxygen hole doping of the 3d levels, as we demonstrated in the previous chapter.

Bibliography

- [1] M. Imada, A. Fujimori, and Y. Tokura, *Rev. Mod. Phys.* **70**, 1039 (1998).
- [2] E. O. Wollan and W. C. Koehler, *Phys. Rev.* **100**, 545 (1955).
- [3] A. von Hippel, R. G. Breckenridge, F. G. Chesley, and L. Tisza, *Ind. Eng. Chem.* **38**, 1097 (1946).
- [4] J. B. Goodenough, *Phys. Rev.* **100**, 564 (1955).
- [5] J. G. Bednorz and K. a. Muller, *Zeitschrift Für Phys. B Condens. Matter* **64**, 189 (1986).
- [6] M. Wu et al., *Phys. Rev. Lett.* **58**, 908 (1987).
- [7] V. M. Goldschmidt, *Naturwissenschaften* **14**, 477 (1926).
- [8] M. W. Haverkort, M. Zwierzycki, and O. K. Andersen, *Phys. Rev. B - Condens. Matter Mater. Phys.* **85**, 1 (2012).
- [9] H. A. Jahn and E. Teller, *Proc. R. Soc. A Math. Phys. Sci.* **161**, 220 (1937).
- [10] J. H. de Boer and E. J. W. Verwey, *Proc. Phys. Soc.* **49**, 59 (1937).
- [11] N. F. Mott and R. Peierls, *Proc. Phys. Soc.* **49**, 72 (1937).
- [12] J. Hubbard, *Proc. R. Soc. A Math. Phys. Eng. Sci.* **281**, 401 (1964).
- [13] J. Hubbard, *Proc. R. Soc. A Math. Phys. Eng. Sci.* **277**, 237 (1964).
- [14] J. Hubbard, *Proc. R. Soc. A Math. Phys. Eng. Sci.* **276**, 238 (1963).
- [15] E. Dagotto, *Science (80-.)*. **309**, 257 (2005).
- [16] J. F. Mitchell et al., *J. Phys. Chem. B* **105**, 10731 (2001).
- [17] S. Nakatsuji et al., *Phys. Rev. Lett.* **93**, 146401 (2004).
- [18] S. Nakatsuji and Y. Maeno, *Phys. Rev. Lett.* **84**, 2666 (2000).
- [19] P. Hansmann, N. Parragh, A. Toschi, G. Sangiovanni, and K. Held, *New J. Phys.* **16**, 33009 (2014).
- [20] H.-B. Schüttler and A. J. Fedro, *Phys. Rev. B* **45**, 7588 (1992).
- [21] J. Zaanen, G. A. Sawatzky, and J. W. Allen, *Phys. Rev. Lett.* **55**, 418 (1985).
- [22] B. C. Chakoumakos, D. G. Schlom, M. Urbanik, and J. Luine, *J. Appl. Phys.* **83**, 1979 (1998).
- [23] J. H. Ngai et al., *Adv. Mater.* **22**, 2945 (2010).
- [24] F. Sánchez et al., *Chem. Soc. Rev.* **43**, 2272 (2014).
- [25] R. Bachelet, C. Ocal, L. Garzón, J. Fontcuberta, and F. Sánchez, *Appl. Phys. Lett.* **99**, 51914 (2011).
- [26] D.-W. Kim et al., *Appl. Phys. Lett.* **74**, 2176 (1999).
- [27] J. Yao, P. B. Merrill, S. S. Perry, D. Marton, and J. W. Rabalais, *J. Chem. Phys.* **108**, 1645 (1998).
- [28] H. Krebs et al., in *Adv. Solid State Phys. SE - 36* (2003), pp. 505–518.
- [29] H. M. Christen and G. Eres, *J. Phys. Condens. Mat.* **20**, 264005 (2008).
- [30] J. Fink, E. Schierle, E. Weschke, and J. Geck, *Reports Prog. Phys.* **76**, 56502 (2013).
- [31] P. Ohresser et al., *Rev. Sci. Instrum.* **85**, (2014).
- [32] B. T. Thole, P. Carra, F. Sette, and G. van der Laan, *Phys. Rev. Lett.* **68**, 1943 (1992).
- [33] P. Carra, B. T. Thole, M. Altarelli, and X. Wang, *Phys. Rev. Lett.* **70**, 694 (1993).
- [34] G. van der Laan, *J. Phys. Soc. Japan* **63**, 2393 (1994).
- [35] B. T. Thole and G. van der Laan, *Phys. Rev. Lett.* **70**, 2499 (1993).
- [36] J. P. Rueff et al., *J. Synchrotron Radiat.* **22**, 175 (2015).
- [37] S.-H. Yang et al., *J. Appl. Phys.* **113**, 73513 (2013).
- [38] A. M. Glazer, *Acta Crystallogr. Sect. B Struct. Crystallogr. Cryst. Chem.* **28**, 3384 (1972).
- [39] A. C. Komarek et al., *Phys. Rev. B - Condens. Matter Mater. Phys.* **75**, 1 (2007).
- [40] H. D. Zhou and J. B. Goodenough, *J. Phys. Condens. Matter* **17**, 7395 (2005).
- [41] M. Heinrich, H.-A. Krug von Nidda, V. Fritsch, and A. Loidl, *Phys. Rev. B* **63**, 193103 (2001).
- [42] H. D. Zhou and J. B. Goodenough, *Phys. Rev. B - Condens. Matter Mater. Phys.* **71**, 1 (2005).
- [43] G. Amow, J.-S. Zhou, and J. B. Goodenough, *J. Solid State Chem.* **154**, 619 (2000).
- [44] E. Pavarini et al., *Phys. Rev. Lett.* **92**, 176403 (2004).
- [45] F. Iga et al., *Phys. Rev. Lett.* **93**, 1 (2004).
- [46] I. V. Solovyev, *Phys. Rev. B* **74**, 54412 (2006).
- [47] G. Khaliullin and S. Okamoto, *Phys. Rev. B* **68**, 205109 (2003).
- [48] S. Okatov, A. Poteryaev, and A. Lichtenstein, *Europhys. Lett.* **70**, 499 (2005).
- [49] M. Mochizuki and M. Imada, *New J. Phys.* **6**, 1 (2004).
- [50] J. Akimitsu et al., *J. Phys. Soc. Japan* **70**, 3475 (2001).
- [51] G. Khaliullin and S. Maekawa, *Phys. Rev. Lett.* **85**, 3950 (2000).
- [52] J. P. Goral and J. E. Greedan, *J. Magn. Magn. Mater.* **37**, 315 (1983).
- [53] B. Keimer et al., *Phys. Rev. Lett.* **85**, 3946 (2000).
- [54] Y. Okimoto, T. Katsufuji, Y. Okada, T. Arima, and Y. Tokura, *Phys. Rev. B* **51**, 9581 (1995).
- [55] T. Katsufuji and Y. Tokura, *Phys. Rev. B* **50**, 2704 (1994).
- [56] Y. Tokura et al., *Phys. Rev. Lett.* **70**, 2126 (1993).
- [57] P. Moetakef et al., *Appl. Phys. Lett.* **98**, 112110 (2011).
- [58] P. Moetakef et al., *J. Cryst. Growth* **355**, 166 (2012).

- [59] B. Jalan, R. Engel-Herbert, N. J. Wright, and S. Stemmer, *J. Vac. Sci. Technol. A Vacuum, Surfaces, Film.* **27**, 461 (2009).
- [60] V. Avrutin et al., *J. Cryst. Growth* **311**, 1333 (2009).
- [61] L. L. H. King, K. Y. Hsieh, D. J. Lichtenwalner, and A. I. Kingon, *Appl. Phys. Lett.* **59**, 3045 (1991).
- [62] L. Bjaalie et al., *Appl. Phys. Lett.* **106**, 232103 (2015).
- [63] P. Moetakef and T. A. Cain, *Thin Solid Films* **583**, 129 (2015).
- [64] J. Y. Zhang, C. A. Jackson, S. Raghavan, J. Hwang, and S. Stemmer, *Phys. Rev. B - Condens. Matter Mater. Phys.* **88**, 1 (2013).
- [65] C. Ulrich et al., *Phys. Rev. B* **77**, 113102 (2008).
- [66] Y. Cao et al., *Appl. Phys. Lett.* **107**, 112401 (2015).
- [67] M. N. Grisolia et al., *Appl. Phys. Lett.* **105**, 172402 (2014).
- [68] A. Ohtomo, D. A. Muller, J. L. Grazul, and H. Y. Hwang, *Appl. Phys. Lett.* **80**, 3922 (2002).
- [69] N. N. Kovaleva et al., *Phys. Rev. B - Condens. Matter Mater. Phys.* **76**, 1 (2007).
- [70] M. Abbate et al., *Phys. Rev. B* **44**, 5419 (1991).
- [71] M. W. Haverkort et al., *Phys. Rev. Lett.* **94**, 1 (2005).
- [72] E. Stavitski and F. M. F. de Groot, *Micron* **41**, 687 (2010).
- [73] H. W. Jang et al., *Science* **886**, 886 (2011).
- [74] M. N. Grisolia et al., *Nat. Phys.* **12**, 484 (2016).
- [75] J. E. Greedan, *J. Less Common Met.* **111**, 335 (1985).
- [76] J. Garcia-Barriocanal et al., *Nat. Commun.* **1**, 82 (2010).
- [77] J.-S. Lee et al., *Nat. Mater.* **12**, 703 (2013).
- [78] M. Salluzzo et al., *Phys. Rev. Lett.* **111**, 87204 (2013).
- [79] C. W. Turner, M. F. Collins, and J. E. Greedan, *J. Magn. Magn. Mater.* **23**, 265 (1981).
- [80] C. W. Turner and J. E. Greedan, *J. Solid State Chem.* **34**, 207 (1980).
- [81] J. P. Goral and J. E. Greedan, *J. Solid State Chem.* **43**, 204 (1982).
- [82] C. Chen et al., *Phys. Rev. Lett.* **75**, 152 (1995).
- [83] A. Scherz et al., *Phys. Rev. B* **66**, 184401 (2002).
- [84] A. Scherz et al., *Phys. Scr.* **T115**, 586 (2005).
- [85] M. Mochizuki and M. Imada, *Phys. Rev. Lett.* **91**, 167203 (2003).
- [86] M. Cwik et al., *Phys. Rev. B* **68**, 60401 (2003).
- [87] C. Ulrich et al., *Phys. Rev. Lett.* **89**, 167202 (2002).
- [88] R. Rückamp et al., *New J. Phys.* **7**, 1 (2005).
- [89] T. Mizokawa, D. I. Khomskii, and G. a Sawatzky, *Phys. Rev. B* **60**, 5 (1999).
- [90] P. Moetakef, J. Y. Zhang, S. Raghavan, A. P. Kajdos, and S. Stemmer, *J. Vac. Sci. Technol. A Vacuum, Surfaces, Film.* **31**, 41503 (2013).
- [91] C. J. Eklund, C. J. Fennie, and K. M. Rabe, *Phys. Rev. B - Condens. Matter Mater. Phys.* **79**, 1 (2009).
- [92] Q. Gan, R. a Rao, C. B. Eom, L. Wu, and F. Tsui, *J. Appl. Phys.* **85**, 5297 (1999).
- [93] G. Amow, N. P. Raju, and J. E. Greedan, *J. Solid State Chem.* **155**, 177 (2000).
- [94] M. Reedyk, D. A. Crandles, M. Cardona, J. D. Garrett, and J. E. Greedan, *Phys. Rev. B* **55**, 1442 (1997).
- [95] D. A. Crandles, T. Timusk, J. D. Garrett, and J. E. Greedan, *Phys. Rev. B* **49**, 16207 (1994).
- [96] F. Y. Bruno et al., *Phys. Rev. B* **88**, 195108 (2013).
- [97] T. Ohnishi, K. Shibuya, T. Yamamoto, and M. Lippmaa, *J. Appl. Phys.* **103**, (2008).
- [98] H. Béa et al., *Phys. Rev. Lett.* **102**, 217603 (2009).
- [99] M. L. Medarde, *J. Phys. Condens. Matter* **9**, 1679 (1997).
- [100] A. V Boris et al., *Science* **332**, 937 (2011).
- [101] G. Giovannetti, S. Kumar, D. Khomskii, S. Picozzi, and J. van den Brink, *Phys. Rev. Lett.* **103**, 156401 (2009).
- [102] H. J. Zhao et al., *Nat. Commun.* **5**, 4021 (2014).
- [103] J. Chaloupka and G. Khaliullin, *Phys. Rev. Lett.* **100**, 3 (2008).
- [104] M. Gibert et al., *Nat. Mater.* **11**, 195 (2012).
- [105] G. Demazeau, A. Marbeuf, M. Pouchard, and P. Hagenmuller, *J. Solid State Chem.* **3**, 582 (1971).
- [106] J. K. Vassiliou, M. Hornbostel, R. Ziebarth, and F. J. Disalvo, *J. Solid State Chem.* **81**, 208 (1989).
- [107] P. Lacorre et al., *J. Solid State Chem.* **91**, 225 (1991).
- [108] J. A. Alonso et al., *J. Phys. Condens. Matter* **16**, S1277 (2004).
- [109] J. B. Torrance, P. Lacorre, A. I. Nazzal, E. J. Ansaldo, and C. Niedermayer, *Phys. Rev. B* **45**, 8209 (1992).
- [110] J. L. García-Muñoz, J. Rodríguez-Carvajal, and P. Lacorre, *Phys. Rev. B* **50**, 978 (1994).
- [111] J. L. García-Muñoz, J. Rodríguez-Carvajal, and P. Lacorre, *Europhys. Lett.* **20**, 241 (1992).
- [112] C. Girardot, J. Kreisler, S. Pignard, N. Caillault, and F. Weiss, *Phys. Rev. B* **78**, 104101 (2008).
- [113] X. Obradors et al., *Phys. Rev. B* **47**, 12353 (1993).
- [114] T. Mizokawa et al., *Phys. Rev. B* **52**, 13865 (1995).
- [115] J. Suntivich et al., *J. Phys. Chem. C* **118**, 1856 (2014).
- [116] M. Medarde et al., *Phys. Rev. B* **46**, 14975 (1992).
- [117] M. Medarde, P. Lacorre, K. Conder, F. Fauth, and a. Furrer, *Phys. Rev. Lett.* **80**, 2397 (1998).
- [118] P. C. Canfield, J. D. Thompson, S.-W. W. Cheong, and L. W. Rupp, *Phys. Rev. B* **47**, 12357 (1993).

- [119] M. Medarde et al., Phys. Rev. B **52**, 9248 (1995).
- [120] K. M. Satyalakshmi et al., Appl. Phys. Lett. **62**, 1233 (1993).
- [121] G. Catalan, R. M. Bowman, and J. M. Gregg, J. Appl. Phys. **87**, 606 (2000).
- [122] F. Conchon et al., Appl. Phys. Lett. **91**, 192110 (2007).
- [123] D. Meyers et al., Phys. Rev. B **88**, 75116 (2013).
- [124] R. Scherwitzl, P. Zubko, C. Lichtensteiger, and J.-M. Triscone, Appl. Phys. Lett. **95**, 222114 (2009).
- [125] A. Frano et al., Phys. Rev. Lett. **111**, 106804 (2013).
- [126] L. Feigl et al., J. Cryst. Growth **366**, 51 (2013).
- [127] BRECKENFELD, Thesis Manuscr. (2014).
- [128] A. J. Hauser et al., Appl. Phys. Lett. **106**, 0 (2015).
- [129] R. Scherwitzl et al., Adv. Mater. **22**, 5517 (2010).
- [130] E. Mikheev et al., Sci. Adv. **1**, e1500797 (2015).
- [131] S. Catalano et al., APL Mater. **2**, 0 (2014).
- [132] R. Scherwitzl et al., Phys. Rev. Lett. **106**, 3 (2011).
- [133] P. D. C. King et al., Nat. Nanotechnol. **9**, 443 (2014).
- [134] L. Wang et al., Sci. Rep. **5**, 18707 (2015).
- [135] J. W. Freeland, M. van Veenendaal, and J. Chakhalian, J. Electron Spectros. Relat. Phenomena **208**, 56 (2016).
- [136] M. Zaghrioui, A. Bulou, P. Lacorre, and P. Laffez, Phys. Rev. B **64**, 81102 (2001).
- [137] J. a. Alonso, M. J. Martínez-Lope, M. T. Casais, and M. T. Fernández-Díaz, Phys. Rev. B **61**, 1756 (2000).
- [138] S. Lee, R. Chen, and L. Balents, Phys. Rev. B - Condens. Matter Mater. Phys. **84**, 1 (2011).
- [139] H. Park, A. J. Millis, and C. A. Marianetti, Phys. Rev. Lett. **109**, 156402 (2012).
- [140] S. Johnston, A. Mukherjee, I. Elfimov, M. Berciu, and G. A. Sawatzky, Phys. Rev. Lett. **112**, 1 (2014).
- [141] S. Lee, R. Chen, and L. Balents, Phys. Rev. Lett. **106**, 7 (2011).
- [142] T. Mizokawa, D. I. Khomskii, and G. a Sawatzky, Phys. Rev. B **61**, 4 (1999).
- [143] Y. Bodenthin et al., J. Phys. Condens. Matter **23**, 36002 (2011).
- [144] J. van den Brink and D. I. Khomskii, J. Phys. Condens. Matter **20**, 434217 (2008).
- [145] Z. He and A. J. Millis, Phys. Rev. B **91**, 195138 (2015).
- [146] T. Arima, Y. Tokura, and J. B. Torrance, Phys. Rev. B **48**, 17006 (1993).
- [147] I. I. Mazin et al., Phys. Rev. Lett. **98**, 176406 (2007).
- [148] A. Subedi, O. E. Peil, and A. Georges, Phys. Rev. B - Condens. Matter Mater. Phys. **91**, 1 (2015).
- [149] X. Gonze, D. C. Allan, and M. P. Teter, Phys. Rev. Lett. **68**, 3603 (1992).
- [150] R. D. King-Smith and D. Vanderbilt, Phys. Rev. B **47**, 1651 (1993).
- [151] J. D. Axe, Phys. Rev. **157**, 429 (1967).
- [152] J. A. Alonso, M. J. Martínez-Lope, M. T. Casais, M. A. G. Aranda, and M. T. Fernández-Díaz, J. Am. Chem. Soc. **121**, 4754 (1999).
- [153] M. Medarde, M. T. Fernández-Díaz, and P. Lacorre, Phys. Rev. B **78**, 212101 (2008).
- [154] M. Medarde et al., Phys. Rev. B **80**, 245105 (2009).
- [155] M. T. Ferna, J. A. Alonso, M. J. Marti, and A. Mun, J. Solid State Chem. **182**, 1982 (2009).
- [156] J. Ruppen et al., Phys. Rev. B - Condens. Matter Mater. Phys. **92**, 1 (2015).
- [157] M. Hepting et al., Phys. Rev. Lett. **113**, 1 (2014).
- [158] J. Pérez-Cacho et al., J. Phys. Condens. Matter **11**, 405 (1999).
- [159] J. Pérez-Cacho, J. Blasco, J. García, and J. Stankiewicz, Phys. Rev. B **59**, 14424 (1999).
- [160] P.-H. Xiang et al., Appl. Phys. Lett. **97**, 32114 (2010).
- [161] F. Y. Bruno et al., Appl. Phys. Lett. **104**, (2014).
- [162] C. Piamonteze et al., Phys. Rev. B - Condens. Matter Mater. Phys. **71**, 2 (2005).
- [163] J. Liu et al., Phys. Rev. B **83**, 161102 (2011).
- [164] V. Bisogni et al., arXiv:1607.06758 (n.d.).
- [165] M. Wu et al., Phys. Rev. B **88**, 125124 (2013).
- [166] A. V Ushakov, S. V Streltsov, and D. I. Khomskii, J. Phys. Condens. Matter **23**, 445601 (2011).
- [167] Y. Z. Wu et al., Phys. Rev. B **78**, 64413 (2008).
- [168] J. Lüning et al., Phys. Rev. B **67**, 214433 (2003).
- [169] E. Fullerton, S. Bader, and J. Robertson, Phys. Rev. Lett. **77**, 1382 (1996).
- [170] M. H. Hamidian et al., Nat. Phys. **12**, 150 (2015).
- [171] W.-L. Zhang et al., Phys. Rev. B **93**, 205106 (2016).
- [172] M. Liu et al., Nat. Phys. **8**, 376 (2012).
- [173] M. Bibes, J. E. Villegas, and A. Barthélémy, Adv. Phys. **60**, 5 (2011).
- [174] H. Y. Hwang et al., Nat. Mater. **11**, 103 (2012).
- [175] P. Zubko, S. Gariglio, M. Gabay, P. Ghosez, and J.-M. Triscone, Annu. Rev. Condens. Matter Phys. **2**, 141 (2011).
- [176] A. Ohtomo and H. Y. Hwang, Nature **427**, 423 (2004).
- [177] N. Reyren et al., Science **317**, 1196 (2007).
- [178] A. Brinkman et al., Nat. Mater. **6**, 493 (2007).
- [179] Ariando et al., Nat. Commun. **2**, 188 (2011).
- [180] J. A. Bert et al., Nat. Phys. **7**, 767 (2011).

- [181] L. Li, C. Richter, J. Mannhart, and R. C. Ashoori, *Nat. Phys.* **7**, 762 (2011).
- [182] N. Nakagawa, H. Y. Hwang, and D. a. Muller, *Nat. Mater.* **5**, 204 (2006).
- [183] R. Pentcheva and W. E. Pickett, *J. Phys. Condens. Matter* **22**, 43001 (2010).
- [184] L. Yu and A. Zunger, *Nat. Commun.* **5**, 5118 (2014).
- [185] M. Basletic et al., *Nat. Mater.* **7**, 621 (2008).
- [186] E. Benckiser et al., *Nat. Mater.* **10**, 189 (2011).
- [187] E. Detemple et al., *Appl. Phys. Lett.* **99**, (2011).
- [188] P. Hansmann et al., *Phys. Rev. Lett.* **103**, 1 (2009).
- [189] P. Hansmann, A. Toschi, X. Yang, O. K. Andersen, and K. Held, *Phys. Rev. B* **82**, 235123 (2010).
- [190] M. J. Han, C. A. Marianetti, and A. J. Millis, *Phys. Rev. B* **82**, 134408 (2010).
- [191] J. Nogués et al., *Phys. Rep.* **422**, 65 (2005).
- [192] M. Gibert et al., *Nat. Commun.* **7**, 11227 (2016).
- [193] M. Gibert et al., *Nano Lett.* **15**, 7355 (2015).
- [194] C. Piamonteze et al., *Phys. Rev. B* **92**, 14426 (2015).
- [195] D. G. Ouellette et al., *Sci. Rep.* **3**, 3284 (2013).
- [196] P. Moetakef et al., *Appl. Phys. Lett.* **101**, 151604 (2012).
- [197] J. Y. Zhang, J. Hwang, S. Raghavan, and S. Stemmer, *Phys. Rev. Lett.* **110**, 1 (2013).
- [198] T. A. Cain, P. Moetakef, C. A. Jackson, and S. Stemmer, *Appl. Phys. Lett.* **101**, 111604 (2012).
- [199] P. Moetakef et al., *Appl. Phys. Lett.* **99**, 232116 (2011).
- [200] C. a Jackson, J. Y. Zhang, C. R. Freeze, and S. Stemmer, *Nat. Commun.* **5**, 4258 (2014).
- [201] P. Moetakef et al., *Phys. Rev. X* **2**, 21014 (2012).
- [202] S. Nemšák et al., *Appl. Phys. Lett.* **107**, 231602 (2015).
- [203] X. Liu et al., *Appl. Phys. Lett.* **107**, 1 (2015).
- [204] J. E. Kleibeuker et al., *Phys. Rev. Lett.* **113**, 1 (2014).
- [205] M. Kareev et al., *Appl. Phys. Lett.* **103**, 1 (2013).
- [206] H. Chen, C. A. Marianetti, A. J. Millis, and C. A. Marianetti, *Phys. Rev. Lett.* **2**, 2 (2013).
- [207] E. Sakai et al., *Phys. Rev. B - Condens. Matter Mater. Phys.* **87**, 1 (2013).
- [208] L. Qiao and X. Bi, *EPL (Europhysics Lett.)* **93**, 57002 (2011).
- [209] A. Fujimori et al., *Phys. Rev. B* **46**, 9841 (1992).
- [210] S. Middey et al., *Sci. Rep.* **4**, 6819 (2014).
- [211] G. Lucovsky, L. Miotti, K. P. Bastos, C. Adamo, and D. G. Schlom, *J. Vac. Sci. Technol. B* **29**, 01AA02 (2011).
- [212] E. Lesne et al., *Nat. Commun.* **5**, 4291 (2014).
- [213] J. E. Kleibeuker et al., *Phys. Rev. Lett.* **113**, 237402 (2014).
- [214] M. Ali et al., *Nat. Mater.* **6**, 70 (2007).
- [215] H. Ohldag et al., *Phys. Rev. Lett.* **91**, 17203 (2003).
- [216] M. Gibert, P. Zubko, R. Scherwitzer, J. Iñiguez, and J.-M. Triscone, *Nat. Mater.* **11**, 195 (2012).
- [217] J. Wu et al., *Phys. Rev. Lett.* **104**, 3 (2010).
- [218] M. Ungureanu et al., *Phys. Rev. B* **82**, 174421 (2010).
- [219] Y. Shiratsuchi et al., *Phys. Rev. Lett.* **109**, 77202 (2012).
- [220] Y. Quan, V. Pardo, and W. E. Pickett, *Phys. Rev. Lett.* **109**, 1 (2012).
- [221] C. Marianetti, G. Kotliar, and G. Ceder, *Phys. Rev. Lett.* **92**, 196405 (2004).
- [222] J. Liu et al., *Nat. Commun.* **4**, 2714 (2013).
- [223] J. B. Goodenough, *J. Solid State Chem.* **127**, 126 (1996).
- [224] E. Lioudakis, A. Othonos, C. B. Lioutas, and N. Vouroutzis, *Nanoscale Res. Lett.* **3**, 1 (2008).
- [225] R. J. Nelson, *Appl. Phys. Lett.* **31**, 351 (1977).
- [226] K. M. Shen and J. C. S. Davis, *Mater. Today* **11**, 14 (2008).
- [227] E. Stilp et al., *Sci. Rep.* **4**, 6250 (2014).
- [228] T. Endo, A. Hoffmann, J. Santamaria, and I. K. Schuller, *Phys. Rev. B* **54**, R3750 (1996).
- [229] C. Visani et al., *Phys. Rev. B - Condens. Matter Mater. Phys.* **84**, 1 (2011).
- [230] V. I. Kudinov et al., *Phys. Lett. A* **157**, 290 (1991).
- [231] G. Yu, A. J. Heeger, G. Stucky, N. Herron, and E. M. McCarron, *Solid State Commun.* **72**, 345 (1989).
- [232] K. Tanabe, S. Kubo, Hosseini Teherani F, H. Asano, and M. Suzuki, *Phys. Rev. Lett.* **72**, 1537 (1994).
- [233] J. M. D. Coey, M. Viret, and S. von Molnár, *Adv. Phys.* **48**, 167 (1999).
- [234] R. Cauro et al., *Phys. Rev. B* **63**, 174423 (2001).
- [235] M. Baran et al., *Phys. Rev. B* **60**, 9244 (1999).
- [236] A. Subedi, A. Cavalleri, and A. Georges, *Phys. Rev. B* **89**, 220301 (2014).
- [237] M. Först et al., *Nat. Mater.* **14**, 883 (2015).
- [238] P. H. Xiang et al., *Appl. Phys. Lett.* **97**, 6 (2010).
- [239] R. Jaramillo, S. D. Ha, D. M. Silevitch, and S. Ramanathan, *Nat. Phys.* **10**, 304 (2014).
- [240] T. Katsufuji, Y. Okimoto, T. Arima, Y. Tokura, and J. B. Torrance, *Phys. Rev. B* **51**, 4830 (1995).
- [241] O. Laporte and W. F. Meggers, *J. Opt. Soc. Am.* **11**, 459 (1925).
- [242] B. Kundys, *Appl. Phys. Rev.* **2**, 1 (2015).
- [243] N. A. Benedek and C. J. Fennie, *Phys. Rev. Lett.* **106**, 107204 (2011).

- [244] N. C. Bristowe, J. Varignon, D. Fontaine, E. Bousquet, and P. Ghosez, *Nat. Commun.* **6**, 6677 (2015).
- [245] J. Varignon, N. C. Bristowe, and P. Ghosez, *Phys. Rev. Lett.* **116**, 57602 (2016).
- [246] A. Borisevich et al., *Phys. Rev. Lett.* **105**, 87204 (2010).
- [247] E. Bousquet et al., *Nature* **452**, 732 (2008).
- [248] Z. Liao et al., *Nat. Mater.* **15**, 425 (2016).
- [249] H. Y. Qi et al., *J. Mater. Sci.* (2016).
- [250] S. Kourtis, J. W. F. Venderbos, and M. Daghofer, *Phys. Rev. B - Condens. Matter Mater. Phys.* **86**, 1 (2012).
- [251] A. Rüegg and G. A. Fiete, *Phys. Rev. B* **84**, 201103 (2011).
- [252] K. Y. Yang et al., *Phys. Rev. B - Condens. Matter Mater. Phys.* **84**, 2 (2011).
- [253] T. H. Kim et al., *Nature* **533**, 68 (2016).
- [254] G. Dresselhaus, *Phys. Rev.* **100**, 580 (1955).
- [255] Y. Zhou and S. Ramanathan, *Proc. IEEE* **103**, 1289 (2015).
- [256] Z. Yang, C. Ko, and S. Ramanathan, *Annu. Rev. Mater. Res.* **41**, 337 (2011).
- [257] F. Y. Bruno et al., *Nat. Commun.* **6**, 6306 (2015).